

**Analysis of Defects in Block Copolymer  
Thin Films**

by

**Jeffrey Nathaniel Murphy**

A thesis submitted in partial fulfillment of the requirements for the  
degree of

**Doctor of Philosophy**

**Department of Chemistry**

**University of Alberta**

© Jeffrey Nathaniel Murphy, 2015

# Abstract

2015 marks the 50<sup>th</sup> anniversary of Moore's law, which has described the exponential progress in semiconductor patterning technologies, enabling creation of smaller circuitry features at greater densities. These continued hardware developments, economically mass manufactured, have made possible computer technologies which have revolutionized daily life. The continued shrinking of features has largely been enabled *via* conventional photolithography, however inherent limitations due to the wavelength of light used mean that alternative technologies are required to continue the trend.

Block copolymers are a self-assembling material which can be used as a stencil (or mask) to pattern arrays of periodic nanoscale surface features, in a manner which would complement photolithography and conventional CMOS manufacturing, while preserving economic mass production. Defects in block copolymer structures could limit adoption of this technology, as industry targets strive for less than 1 defect per 100 mm wafer. Consequently numerous efforts have sought to address the issue with various annealing techniques and guiding

structures employed to enable quick, uniform, defect-free patterning of large areas.

This thesis describes the computer-automated analysis of defects in striped patterns formed using block copolymers: focusing on topological defects (disclinations and dislocations), pattern orientation, and irregularity of features through line-edge and line-width roughness. The tool, *ADABlock*, has been developed for use with ImageJ and is open source and free for anyone to use and to modify. The tool has been made freely available online, with the intent that as an open-source tool, it can lead to greater accessibility of the analysis and uniformity of data between research groups.

While defects in lamellar polystyrene-*block*-poly(methyl methacrylate) line patterns have been widely studied, the embedded nature of cylindrical domains has limited their analysis. Here, we focus primarily on defects in polystyrene-*block*-poly(2-vinylpyridine) cylinders arranged in monolayers on the native oxide surface of silicon wafers, with the P2VP domains metallized with platinum to enable SEM imaging. The analysis performed by *ADABlock* is applied to develop a better understanding of surface morphology and how film thickness affects defectivity within the monolayer regions and as a function of distance from the edge of islands. .

# Preface

Chapter 1 provides a brief overview of emerging lithographic technologies, in order to situate the manufacturing potential of block copolymers. This is followed, in Chapter 2, by a brief examination of the major challenge to the application of block copolymers: defects in the pattern. A description of the algorithm used to determine defects, orientation, correlation lengths, and line-edge or line-width roughness is laid out in Chapter 3. Chapter 4 applies the algorithm to a thorough study of the effect of initial film thickness on the morphology and defectivity of cylinder-forming polystyrene-*block*-poly(2-vinylpyridine). Finally, Chapter 5 summarizes the findings of this thesis and proposes future directions for the ongoing development of this research.

The work presented in Chapter 3, describing the *ADABlock* tool and its application, including the two Appendices, A and B, has been published in *PLOS One* in an article co-authored with Prof. Jillian M. Buriak and Dr. Kenneth D. Harris.<sup>[1]</sup> I wrote the initial draft of the text, per-

formed the calculations, and prepared all of the figures. All co-authors contributed to subsequent editing of the text. The *ADAblock* code was written in its entirety by me, with some input from Dr. Harris.

Chapter 4 was also written as an article, co-authored with Prof. Buriak. I performed all experiments described and calculations performed, created each figure, and wrote the initial manuscript. Prof. Buriak co-conceived some of the experiments, and contributed significant edits to the text.

This thesis is dedicated to my mother, *Brenda*.

# Acknowledgements

First and foremost, I would like to thank my supervisor, Prof. Jillian Buriak. She has been a pleasure to work with and has provided continual encouragement and support for me to strive to be the best scientist that I am able to be.

The numerous, positive interactions working with colleagues in the Buriak Group have enriched my time here immensely. None of this would be possible without these coworkers with whom I've collaborated on block copolymer research, including Dr. Kenneth Harris, Dr. Hidenori Mizuno, Dr. Xiaojiang Zhang, Dr. Nathanael Wu, Dr. Erik Luber, Fenglin Liu, Cong Jin, and Minjia Hu. I also had the privilege of supervising two keen, bright undergraduates, Andrew Wong and Isabella Tu, who assisted me in advancing the microwave and solvent annealing projects. The other members of group have also kept me sharp, provided assistance, and asked the right questions: Jennifer Ozdoba, Tate Hauger, Brian Olsen, Dr. Brian Worfolk, Dr. Anne Slaney, Torsten Doerschel, Dr. Sayed Sayed, Dr. David Rider, Dr. Weiwei Li, Dr. Tonggang Jiu, Dr. Usama Al-Atar, Dr. Qun Chen, Dr. Lawrence Huck, Dr. Ibrahim Al-Rafia,

Dr. Xiaoming He, Dr. Gang He, and Dr. Delwar Sikder.

The staff of the National Institute for Nanotechnology (NINT), the University of Alberta NanoFab, and ACSES have also rendered assistance: Keith Franklin, Stephanie Bozic, and Scott Munro of the NanoFab; Dr. Anquang He of ACSES; and Mike Xia, Daniel Solomon, and Kai Cui of NINT. Likewise, the staff of the Department of Chemistry have assisted me on numerous occasions, in particular Jason Dibbs (Glass Shop), Dieter Starke (Machine Shop), and Allan Chiltron (Electronics Shop).

The faculty of the Department of Chemistry have also been of particular help, including my committee members past and present: Profs. Jonathan Veinot, Michael Serpe, and Steven Bergens. As well as those professors whom have enabled me to learn through their courses, whether for credit or informal audit.

My research has also been greatly facilitated by scholarships which have funded me, including NSERC and the Killam Trusts. I offer my appreciation to the agencies and reviewers.

Many friends have also cheered me on and provided encouragement and fellowship along the way, whether in together as fellow students and colleagues, as volunteers, or for no apparent reason other than their pleasure.

Finally, I thank my family for their love and unwavering support in every goal that I pursue.

# Contents

<b>1</b>	<b>Introduction to Lithographic Patterning</b>	<b>1</b>
1.1	Introduction: Technology & Moore's Law . . . . .	1
1.2	Optical Lithography . . . . .	4
1.3	Emerging Lithography Methods . . . . .	8
1.3.1	Extreme UV . . . . .	9
1.3.2	Electron Beam Lithography . . . . .	10
1.3.3	Nanoimprint Lithography . . . . .	12
1.3.4	Scanning Tip Methods . . . . .	13
1.3.5	Block Copolymer Lithography . . . . .	16

1.4	Fundamental Challenges and the ITRS Objectives for Block Copolymer Lithography . . . . .	26
1.5	Application to Bit-Patterned Media . . . . .	31
1.6	Scope of the Thesis . . . . .	35
<b>2</b>	<b>Analysis of Defects in Block Copolymer Thin Film Structures</b>	<b>37</b>
2.1	Introduction . . . . .	37
2.2	Structure of Thin Films . . . . .	38
2.3	Defects and their Characterization . . . . .	41
2.3.1	General Considerations for Characterization of Defects . . . . .	42
2.3.2	Topological Defects . . . . .	44
2.3.3	Line-Edge Roughness and Line-Width Roughness . . . . .	46
2.3.4	Feature Size Variation . . . . .	50
2.3.5	Orientation and Registration . . . . .	52
2.3.6	Wetting and Misorientation . . . . .	57
2.3.7	Contamination by Particulate Matter . . . . .	59
2.3.8	The Internal Structure of BCP Domains . . . . .	59
2.3.9	Tracking Sources of Defects . . . . .	63

2.4	Means of Eliminating Defects . . . . .	66
2.4.1	Thermal Annealing . . . . .	66
2.4.2	Solvent Annealing . . . . .	68
2.4.3	Annealing Combinations . . . . .	72
2.5	Using and Controlling Defects . . . . .	73
2.5.1	Volume Fraction Modification and Blending . . . . .	76
2.6	Challenges . . . . .	79
2.6.1	Minimum Level of Defects . . . . .	79
2.6.2	Timescale for Annealing . . . . .	80
2.6.3	Multilayer Structures . . . . .	80
2.6.4	Flory-Huggins Parameter Trade-offs . . . . .	81
2.6.5	New Topologies and Large BCPs . . . . .	82
2.6.6	Effects of polydispersity on defects . . . . .	82
2.6.7	How the deposition method influence the evolu- tion of defects . . . . .	83
2.6.8	What is the minimum thermodynamic level of de- fects? . . . . .	83
2.7	Additional Open Questions . . . . .	84

2.8	Conclusions . . . . .	85
<b>3</b>	<b>Automated Defect Analysis of Block Copolymer Thin Film Nanopatterns</b>	<b>86</b>
3.1	Introduction . . . . .	86
3.2	Results and Discussion . . . . .	92
3.3	Outline of the Analysis . . . . .	94
3.3.1	Stages 1 and 2: Input of original image and smooth- ing . . . . .	95
3.3.2	Stage 3: Threshold to binary . . . . .	100
3.3.3	Stage 4: Initial Line-Width Analysis . . . . .	101
3.3.4	Stage 5: Particle analysis . . . . .	106
3.3.5	Stage 6: Skeletonization . . . . .	107
3.3.6	Stage 7: Groom and analyze . . . . .	110
3.3.7	Stage 8: Output and confirmation images. . . . .	137
3.4	Application of <i>ADAblock</i> . . . . .	139
3.4.1	Effect of Resolution and Sampling Area . . . . .	141
3.4.2	Feature Relationships . . . . .	147
3.4.3	Limitations of the code . . . . .	148

3.5	Conclusions . . . . .	151
3.6	Materials and Methods . . . . .	152
3.6.1	Substrate Preparation . . . . .	152
3.6.2	Solutions and Spin Coating . . . . .	153
3.6.3	Annealing . . . . .	154
3.6.4	Metallization . . . . .	154
3.6.5	Plasma processing . . . . .	155
3.6.6	Computation . . . . .	155
3.7	Abbreviations . . . . .	156
<b>4</b>	<b>Effect of Film Thickness on Defect Density of Monolayers of Self-Assembled Block Copolymers</b>	<b>157</b>
4.1	Introduction . . . . .	157
4.2	Results and Discussion . . . . .	161
4.2.1	Polymer Film Structure . . . . .	163
4.2.2	Brush Coating Thickness . . . . .	170
4.2.3	Metallized P2VP Domains . . . . .	176
4.2.4	Assessing Defectivity . . . . .	184
4.2.5	Defectivity Near Island Features . . . . .	189

4.3	Summary . . . . .	196
4.4	Materials and Methods . . . . .	197
4.4.1	Substrate Preparation . . . . .	198
4.4.2	Solutions and Spin Coating . . . . .	198
4.4.3	Ellipsometry Measurements . . . . .	199
4.4.4	Annealing . . . . .	200
4.4.5	Metallization and Plasma Processing . . . . .	200
4.4.6	AFM Imaging . . . . .	202
4.4.7	TOF-SIMS Data . . . . .	205
4.4.8	SEM Imaging . . . . .	208
4.4.9	Computation . . . . .	208
<b>5</b>	<b>Summary and Outlook</b>	<b>210</b>
5.1	Thesis Summary . . . . .	210
5.1.1	Chapter 1 . . . . .	211
5.1.2	Chapter 2 . . . . .	212
5.1.3	Chapter 3 . . . . .	212
5.1.4	Chapter 4 . . . . .	213

5.2	Directions for Future Work . . . . .	214
5.2.1	Further Refinement of ADABlock . . . . .	214
5.2.2	Use of Image Stitching . . . . .	220
5.2.3	Controlling Island Defects . . . . .	220
5.2.4	Pattern Transfer Fidelity . . . . .	222
5.2.5	Defects and LER . . . . .	223
5.2.6	Effects of Composition, Polydispersity, and Tacticity	224
5.3	Conclusion . . . . .	225
	<b>References</b>	<b>225</b>
	<b>A Particle Analysis Calculation of Line-Width</b>	<b>246</b>
	<b>B Summary of the "ADABlock" Defect Analysis Code</b>	<b>251</b>

# List of Figures

1.1	Moore's Law illustrated by an exponential increase of transistors per IC . . . . .	3
1.2	Schematic of a single lithographic process step using a photoresist. . . . .	5
1.3	Schematic illustrating contact, proximity, and projection printing techniques in photolithography. . . . .	7
1.4	Nanoimprint lithography process schematic. . . . .	14
1.5	Polystyrene- <i>block</i> -poly(2-vinylpyridine), a diblock BCP. . .	17
1.6	Bulk phases of diblock copolymers. . . . .	19
1.7	Structures formed by thin films of block copolymers. . . .	20

1.8	Scheme depicting process for making rectangular bits from lamellar BCPs. . . . .	23
1.9	Rectangular bits templated from PS- <i>b</i> -PMMA. . . . .	24
1.10	Irregular structures templated using lamellar BCPs with chemoepitaxy. . . . .	25
1.11	Exponential decrease in hard drive prices, measured in USD/GB. . . . .	32
2.1	Bulk morphologies of diblock copolymers. . . . .	40
2.2	Simulated morphologies for diblock copolymers confined between two similarly attractive surfaces. . . . .	41
2.3	Typology of defects observed in PS- <i>b</i> -P2VP thin films. . . . .	45
2.4	Defect annihilation in BCP thin films. . . . .	47
2.5	Undulation roughness and peristaltic roughness. . . . .	48
2.6	Computer simulation interrogating LER of diblock copolymers. . . . .	49
2.7	The ability of BCPs to rectify LER in chemical surface patterns demonstrated with SEM and PSD. . . . .	51
2.8	Example of variation in line width and spacing. . . . .	52
2.9	Distributions of position and size for cylinder features. . . . .	53

2.10 Optical set-up for finding defects in large BCP textures. . .	54
2.11 FFT sampling of orientations in ordered and disordered regions of BCP textures. . . . .	55
2.12 Fourier filtering of an SEM image to enhance contrast. . .	56
2.13 Microdroplet formation during rapid thermal processing of PS- <i>b</i> -PMMA thin films. . . . .	58
2.14 Preferential wetting induced using photopatternable in- terfacial layers. . . . .	60
2.15 Modelling the through-plane structure of lamellar PS- <i>b</i> - PMMA on guiding patterns using res-CDSAXS. . . . .	62
2.16 Reconstructed 3D volume of PS- <i>b</i> -PMMA/Al <sub>2</sub> O <sub>3</sub> film using TEM data. . . . .	63
2.17 Whole-wafer defect analysis. . . . .	64
2.18 Effect of white spots in the interfacial layer on DSA pat- terns. . . . .	65
2.19 Effect of degree of swelling on the morphology of fea- tures in a PS- <i>b</i> -P2VP thin film annealed with a THF-water mixture. Reprinted with permission from ref. <sup>[2]</sup> . Copy- right ©2012 American Chemical Society. . . . .	69

2.20	Experimental phase diagram for PS- <i>b</i> -PDMS annealed using heptane and toluene. . . . .	70
2.21	PS- <i>b</i> -PMMA directed to form bends using chemoepitaxial guiding patterns. . . . .	74
2.22	Disclinations generated at regular intervals along a tapered channel. . . . .	75
2.23	Line period and defectivity in a binary blend of two PS- <i>b</i> -P2VP BCPs. . . . .	78
2.24	Topologically distinct lamellar patterns PS- <i>b</i> -PMMA. . . . .	79
3.1	Four SEM images and defect analysis of of platinum line patterns derived from cylindrical P2VP domains of PS- <i>b</i> -P2VP. . . . .	93
3.2	Outline of the analysis algorithm carried out by <i>ADAblock</i> . . . . .	97
3.3	Necessity of filtering and the advantage of media filtering over Gaussian for BCP line patterns. . . . .	99
3.4	Feret measurement for curved objects. . . . .	102
3.5	Determination of line width from binary patterns using particle analysis. . . . .	104
3.6	Skeletonization of both phases of binary patterns. . . . .	110

3.7	Tendency of defects to prefer one polymer phase over the other. . . . .	111
3.8	Table of topological defects typically observed, with examples. . . . .	113
3.9	Pixels in a junction and determination of connectivity. . .	115
3.10	Equivalency of junctions for determining defect values. .	116
3.11	Pairing of defects and view of quadrupoles as a defect unit cell. . . . .	119
3.12	Rules for counting defects within an image frame . . . . .	120
3.13	Grooming the skeleton to remove apparent junctions resulting from LER. . . . .	122
3.14	Diagrams of line-edge roughness and line-width roughness.	124
3.15	Determining the positions and distances for line edges using points from a binary, skeletonized line. . . . .	127
3.16	Histograms showing the smoothing process used on binary lines and its effect on the distribution of edge positions. . . . .	129
3.17	Straightened line showing smoothing process used on curved binary lines and its effect on the distribution of edge positions. . . . .	131

3.18 Correlation length plots and cropped orientation maps for six SEM images. . . . .	135
3.19 Images of full defect analysis and orientation maps for Figures 3.15 and 3.18. . . . .	136
3.20 SEM images of metallized PS- <i>b</i> -P2VP line patterns and cor- responding defect analysis. . . . .	138
3.21 Persistence length as a function of normalized defect den- sity. . . . .	140
3.22 Periods of 5 BCPs, measured using FFT, as a function of magnification. . . . .	143
3.23 Effect of sampling area and resolution on LWR, LER, de- fect density, and correlation length. . . . .	145
3.24 Grain count affects estimates of correlation length. . . . .	146
3.25 Line-width, LER, and LWR measurements for 5 BCP films.	149
4.1 Illustration of the effect of thickness on the structure of cylindrical block copolymers films. . . . .	161
4.2 Schematic of the methodology used in studying the effect of thickness on topological defects. . . . .	162

4.3	AFM images and line profiles of PS- <i>b</i> -P2VP films in a thickness series. . . . .	165
4.4	Subtle differences in the height distribution in PS- <i>b</i> -P2VP films show heterogeneity when less than 1 nm below ideal thickness before metallization and after. . . . .	166
4.5	Schematic of cylinder-forming PS- <i>b</i> -P2VP film structure for polymer film and metallized structures. . . . .	167
4.6	3D projections of AFM images of metallized and polymer PS- <i>b</i> -P2VP films with heterogeneous orientation of cylinders. . . . .	169
4.7	AFM images of polymer films with holes, scratched to expose the substrate. . . . .	172
4.8	Height profiles extracted from AFM images of scratched films. . . . .	173
4.9	TOF-SIMS data for PS- <i>b</i> -P2VP with horizontal cylindrical P2VP domains on Si/SiO <sub>x</sub> . . . . .	174
4.10	Illustration of P2VP in association with the SiO <sub>x</sub> surface via hydrogen bonding. . . . .	175

4.11 AFM images of metallized PS- <i>b</i> -P2VP films, annealed from a series of initial thicknesses, showing overall heterogeneity and monolayer regions. . . . .	177
4.12 AFM line profiles and associated images of metallized PS- <i>b</i> -P2VP films. . . . .	179
4.13 AFM images of monolayer films showing homogeneity in metallized PS- <i>b</i> -P2VP at multiple length scales. . . . .	180
4.14 SEM images used to measure coverage of each texture in metallized films, along with high resolution images of each feature. . . . .	183
4.15 High resolution SEM images of metal nanostructures in monolayer regions, analyzed for defectivity. . . . .	186
4.16 Graphs for the area fraction of each feature, defect density of the monolayer regions, and measured period as a function of initial film thickness. . . . .	188
4.17 Schematic model of structures found in PS- <i>b</i> -P2VP thin films and associated thicknesses. . . . .	190
4.18 AFM images and line profile showing protrusion of vertically oriented cylinders near the hole edge. . . . .	192

4.19 Influence of islands on the defectivity of neighbouring regions. . . . .	193
4.21 Examples of plots used for semi-automated fitting of line profiles for the determination of height differences. . . . .	203
4.22 Kernel density estimates for distributions of plateau heights, measured from AFM profiles. . . . .	206
4.23 SEM image of thick film showing dot regions covering majority of thick regions. . . . .	207
5.1 PS- <i>b</i> -P2VP BCP pattern with a grain boundary highlighted.	215
5.2 Spirals and loops in PS- <i>b</i> -P2VP patterns. . . . .	217
5.3 Broken line patterns and matching terminal points. . . . .	218
5.4 Proposal for controlling island nucleation. . . . .	222
A.1 Line segments in all-junction structure. . . . .	246
A.2 Lines with semi-circular tips. . . . .	248
A.3 Lines with square tips. . . . .	249
A.4 Effect of deleting junctions. . . . .	250

# List of Tables

1.1	Challenges to industrial implementation of BCP DSA according to the ITRS, 2013 edition. . . . .	29
1.2	Numerical targets for BCP DSA. . . . .	31
3.1	Data for defect features (LER, LWR, correlation length, and defect density) in each of the 4 SEM images. . . . .	94
4.1	Estimated contributions to thickness and coverage by structure type, based on SEM, AFM, and ellipsometry data. . .	170
4.2	Ellipsometry measurements of spin coated films and substrates. . . . .	201

4.3	Height measurements for each plateau, determined from AFM profiles. . . . .	204
4.4	Summary of step-height measurements for each plateau.	205

# List of Abbreviations

Abbreviation	Meaning
AFM	Atomic force microscopy
-b-	<i>-block-</i>
LER	Line-edge roughness
LWR	Line-width roughness
GISAXS	Grazing-incidence small-angle X-ray scattering
PMMA	Poly(methyl methacrylate)
PS	Polystyrene
P2VP	Poly(2-vinylpyridine)
P4VP	Poly(4-vinylpyridine)
SAXS	Small angle X-ray scattering
SEM	Scanning electron microscopy
STM	Scanning tunneling microscopy
TEM	Transmission electron microscopy
XRD	X-ray diffraction

# 1

## Introduction to Lithographic Patterning

### **1.1 Introduction: Technology & Moore's Law**

Modern, 21<sup>st</sup> century society and the technological advancements which have shaped it, is driven by the continued advancements in computing and fabrication technologies. Chiefly, the continued rapid development of smaller, more powerful devices that now bear little physical similarity to the computers of decades past. This is primarily accounted for by the continued development of integrated circuits and

the materials, processes, equipment, and metrology required to assemble them.

Since the dawn of the microprocessor, transistor counts have continued to increase, roughly in accordance with a doubling every two years, shown in Figure 1.1. This observation was first synthesized in 1965 by Gordon Moore, co-founder of Intel, in the aptly named article, “Cramming More Components onto Integrated Circuits”.<sup>[3]</sup> His observation has become a self-fulfilling prophecy, as it subsequently spurred industry targets<sup>[4]</sup> in a race to the “bottom”.

This continued drive toward miniature features was broadly predicted by Richard Feynman in his December 1959 lecture, “There’s Plenty of Room at the Bottom”,<sup>[5]</sup> which described the potential for new frontiers in science accessible through creating and in studying the world at the nanoscale. There indeed remains much room and much to discover at the bottom of the scale, even today 56 years after Feynman’s proposal and 50 years after Moore’s prediction, and today we’re still racing to the bottom with every advance in the fields of nanotechnology and semiconductor fabrication.

The ongoing progress has meant that “Everything good about computers gets an order of magnitude better every five years,” according to one of the co-founders of the innovative and award-winning computer animation studio, Pixar.<sup>[7]</sup> Around 1986, computation time and

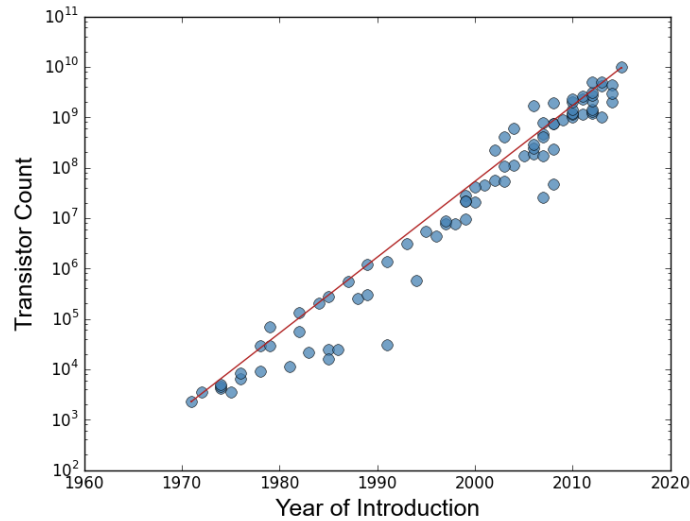


**Figure 1.1:** Moore's Law illustrated by data on transistor counts for microprocessors, of various sizes, by year of introduction. The line fit for doubling of transistor count every 2 years. Adapted from data collected in ref.<sup>[6]</sup>

production costs were deemed too high to make a computer-animated feature, but the expectation set in place by Moore's law provided the necessary direction, focus, and patience for Pixar to wait 5 years: In 1991, when microprocessors had reached the necessary level of maturity, and it was financially and technically feasible, they began making the world's first fully computer-animated feature, *Toy Story* (1995).<sup>[7,8]</sup> One can only imagine what future developments and innovations will result from continued extension of exponentially faster and cheaper computers, but it is certain that they will further transform human culture and experience.

## 1.2 Optical Lithography

The primary process used in creating modern integrated circuits is optical lithography, or photolithography. Lithography derives from the combination of the Greek roots, “*lithos*”, stone, and “*graphein*”, to write, hence this is a process whereby we are able to write patterns on a solid substrate, in this case, silicon wafers. One can conceptualize optical lithographic processes as a subtractive analogue of using a stencil: instead of adding material, such as paint, to create a pattern, photolithography relies on the removal of material to form a pattern.

Combined with various methods of layer deposition and doping, optical lithography can create highly complex architectures. Wafers lithographically patterned using complementary metal-oxide semiconductor (CMOS) technology will undergo the photolithographic cycle, shown in Figure 1.2, numerous times, in order to create fully functional, complex architectures typical of current microprocessors.

Current lithographic technology employs chemically amplified photoresists, originally developed by Ito, Frechet, and Wilson,<sup>[9]</sup> which undergo reaction upon exposure to light below 250 nm – more specifically to ArF 193 nm emission. This provided greater resolution over previous technologies which used larger wavelengths. Shorter wavelength allows pushing toward smaller feature dimensions, as limited

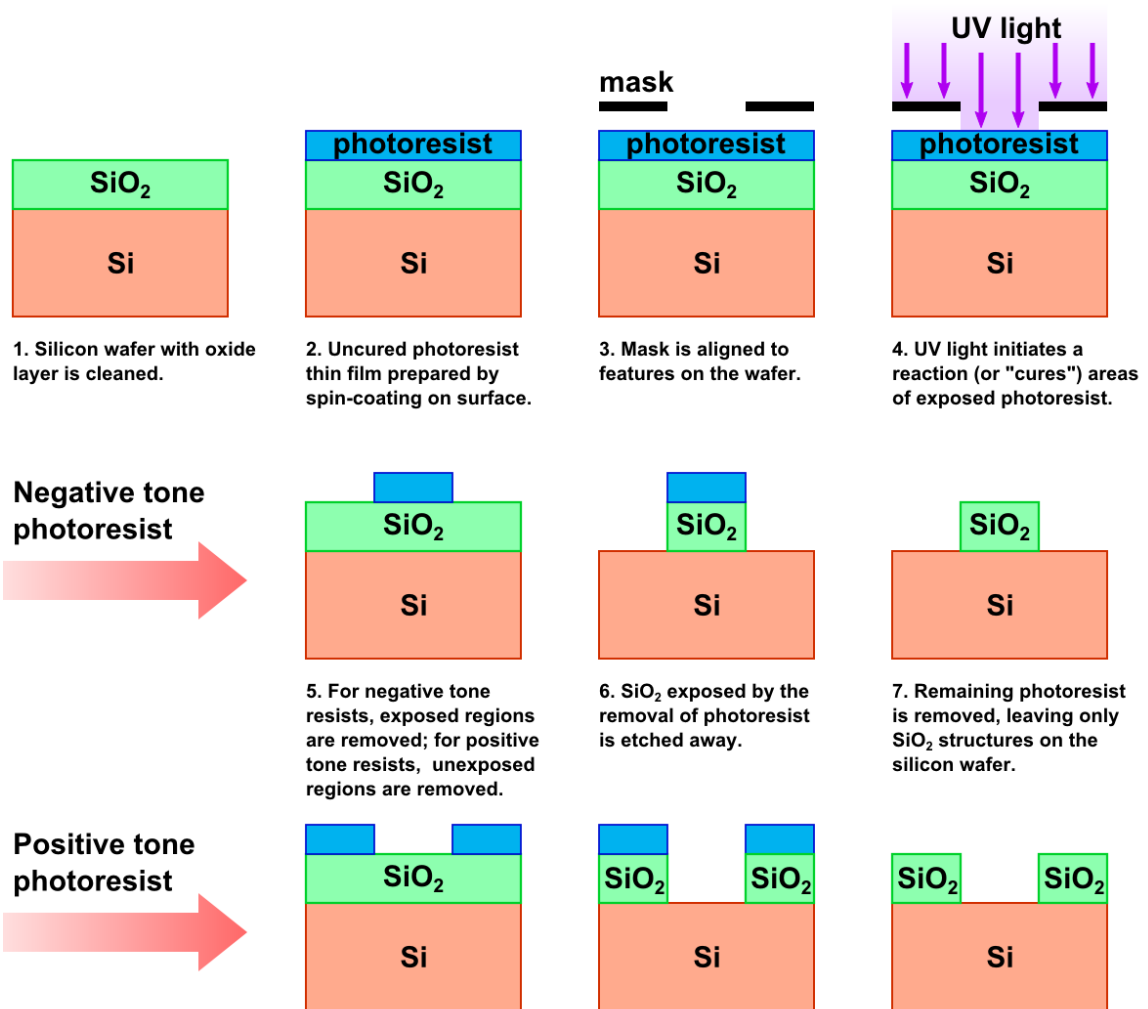


**Figure 1.2:** Schematic of a lithographic process. A silicon wafer coated with a silicon oxide (SiO<sub>2</sub>) thin film, is coated with photoresist, and a mask used to control the exposure of the photoresist to ultraviolet (UV) light. For negative tone photoresists, the exposed regions become fixed, whereas for positive tone photoresists, the exposed regions become soluble. After removing labile photoresist, the oxide is exposed and can be etched in according to the photoresist pattern. Finally, fixed photoresist is removed.

by diffraction, given by the Rayleigh equation:

$$R = k \frac{\lambda}{n \sin \theta} = k \frac{\lambda}{NA} \quad (1.2.1)$$

For the equation,  $R$  represents the resolution or critical dimension which can be attained;  $k$  is the Rayleigh coefficient;  $\lambda$  is the wavelength of light;  $\theta$  is the angular aperture of the lens; and  $n$  is the index of refraction in the medium above the substrate. As given in the equation,  $n \sin \theta$  is equivalent to the numerical aperture,  $NA$ , of the system.

The photomask pattern can be projected using one of three methods: contact printing, proximity printing, or projection printing, which are all shown in Figure 1.3. Contact printing often results in damage to the mask; whereas, proximity printing<sup>[10]</sup> limits feature resolution to the 2–4  $\mu\text{m}$  range. What about projection printing? One way to overcome the diffraction limit is to expose the pattern multiple times. Double patterning has stretched 193 nm lithography by aligning two different masks and etching independently. The alignment requires a high degree of precision in mask placement, as the tolerance is extremely low.

Projection printing suffers mainly from the effects of diffraction due to the greater distance between the mask and the resist, however this can be partially adapted for by utilizing phase-shifting masks and increasing the numerical aperture of the projection lens. Phase-shifting

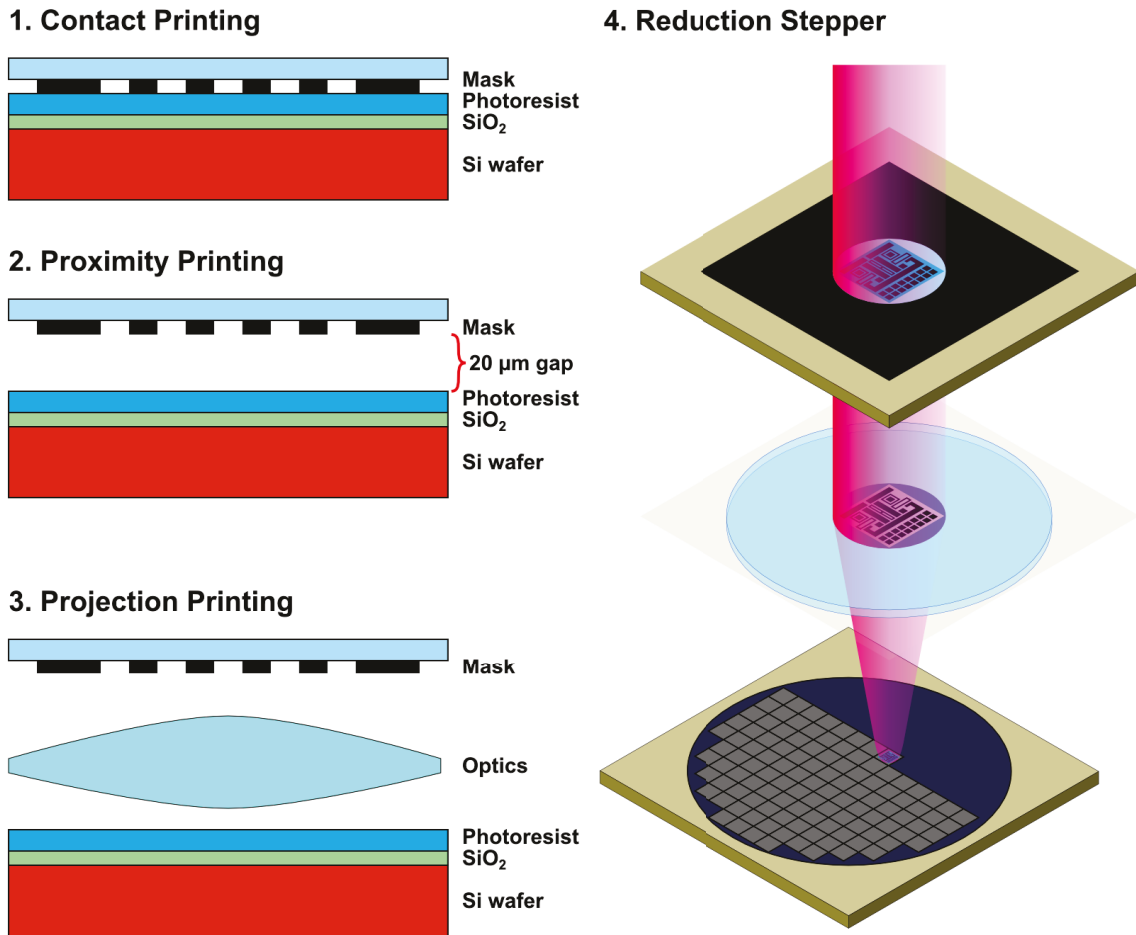


**Figure 1.3:** Schematic of (1) contact printing, where the mask is placed in direct contact with the resist surface; (2) proximity printing, where the mask is near the resist surface; and (3) projection printing, where size-reducing optics are placed between the mask and the resist. (4) Projection printing uses a reduction stepper, which projects the mask onto the wafer, reducing the feature size, through means of a system of lenses. This is repeated numerous times across the entire wafer, as each wafer produces on the order of 100 devices.

masks, go beyond the conventional binary intensity (shadow/light) masks by having light-transmitting regions with an intermediate thickness that results in phase of transmitted light having a new phase. With alternating 180 ° phase shifts, destructive interference with adjacent patterns can result in greater contrast and sharper intensity profiles. Still, this can only be manipulated with features of the same order as the wavelength of light used.

Ultimately, conventional photolithography is constrained by physical limitations—size limitations resulting from the 193 nm wavelength and resist chemistry—which bring us to “the end of the road” in terms of advancing to smaller and smaller dimensions reaching into the bottom end of the nanoscale. As previously described, these limitations have been repeatedly stretched and pushed, but a bridge is required to create features in the range of 5 to 20 nm.

### **1.3 Emerging Lithography Methods**

A variety of advanced techniques remain in development with potential to replace or complement existing lithographic technologies. These are dubbed by some as “next generation lithography”<sup>[11]</sup> for the goal of replacing, or rather complementing, the current 193 nm optical lithography. Several candidate technologies are available, each with advan-

tages and drawbacks. At present, there is significant industry focus on employing extreme ultraviolet lithography, however other techniques may yet be viable or yet complementary to that technology as well.

### **1.3.1 Extreme UV**

The shorter the wavelength of light, the smaller the features which can be projected. Extreme ultraviolet (EUV) photolithography, at 13.5 nm, is able to create features on the order of  $\sim 10$  nm. The technology was originally of interest because suitable reflectors and filters were already available for light at that wavelength, hence it was pursued with the aim of developing the other necessary components to the required performance thresholds, specifically: a bright light source for 13.5 nm light and photoresists sensitive to that wavelength.

Reflectors of approximately 60% to 70% efficiency can be constructed using multilayer stacks; with layer thicknesses satisfying the Bragg condition, it is possible to efficiently reflect light in the range of 11-14 nm. This permits both projection optics and reduction imaging. Currently, Mo/Si multilayer film stacks are preferred, with an optimal reflectance of 67.5% achieved for a normal incidence of light with 13.4 nm wavelength.

EUV lithography requires an extremely intense light source as a conse-

quence of the reflective losses incurred due to widespread absorption of short wavelength light by the mirrors. Dim light sources and losses within the optical system results in a longer exposure time, thus lower throughput, however higher power light sources could overcome this issue. 13.5 nm light can be produced via plasma emission, however this technology has faced many complications and has yet to mature to 80 W intensity, despite industry-desired targets of 1000 W.

The major disadvantage with extreme UV lithography, even were it to prove successful, is that it requires vacuum conditions, due to the absorption of 13.5 nm light by air. This will necessitates additional processing time for pump-down and transfer procedures.

### **1.3.2 Electron Beam Lithography**

Photolithography is limited fundamentally by the wavelength of light, hence lithography using species with shorter wavelengths is an avenue to creating smaller features. Electrons and ions, on account of their mass, have much smaller wavelengths and can thus pattern significantly smaller features. In the de Broglie equation, which gives the wavelength for these particles,  $h$  is Plank's constant,  $m$  is the mass of the particle, and  $E$  is the energy of the beam:

$$\lambda = \frac{h}{2mE} \quad (1.3.1)$$

For high voltage electron beams, with energies ranging from 10 to 100 keV, the wavelength of electrons ranges from 0.1 nm to 0.01 nm. This is the basis for both scanning electron microscopy (SEM) and its lithographic analogue, electron beam lithography (EBL), which rasters a beam of electrons accelerated toward a surface, either to collect data about the surface (imaging, in the case of SEM) or to write data on the surface (patterning, in the case of EBL).

Electron beam lithography is attractive for the ability to routinely create features down to a few nanometres. It offers complete flexibility in the design of 2-dimensional patterns; however, its primary drawback is that it writes features in serial fashion. Moreover, scanning to create a pattern with pitches on the order of  $\sim 20$  nm over an area of  $\sim 100$  cm<sup>2</sup> requires an inordinate amount of time. Similarly, focused ion beams can be used to write high-resolution patterns, however the serial nature also presents exceptionally long write times. One means of addressing the issue of slow serial scanning is to implement a multi-beam system: Electron optics capable of splitting the electron beam into multiple parallel beams could have the potential to pattern up to 10 wafers per hour.

E-beam patterns are resolution limited by forward scattering in the resist medium; however, in practice a 1 nm diameter beam can produce features with widths as small as 5 nm. Alignment is another major patterning issue for using EBL: as the field of view is limited to 100  $\mu\text{m}$  to 1 mm, patterning an entire surface requires translation of the stage. This demands precise alignment of the patterns to achieve proper pattern overlay.

### **1.3.3 Nanoimprint Lithography**

Nanoimprint lithography (NIL) utilizes mechanical contact of a polymer stamp bearing nanoscale topographic features, which are replicated through imprinting on a soft polymer thin film (the resist) on the substrate. Relief structures imprinted can be effectively 2-dimensional or 3-dimensional, depending on the features of the stamp. The resist must be hardened prior to demolding; this is typically achieved either by cooling a thermally softened resist below its glass transition temperature or by curing the stamp using ultraviolet light. The process for this follows three steps: imprinting, demolding, and etching; the process is outlined in Figure 1.4.

NIL is a commercialized technology, through Molecular Imprints, Inc. (now a subsidiary of Canon, Inc.). By design, NIL is a parallel, high-

throughput technology with minimal costs (that you have to pay to set something up) compared to conventional photolithography. Widespread application and commercial implementation has been found with use in patterning biochip arrays and display technologies such as LCDs, for which the pressures of keeping up with Moore's law are irrelevant. While feature dimensions of 5 nm and line spacings of 14 nm can be attained, repeat use of stamps leads to degradation in pattern quality and increasing levels of defects.

Related to NIL is nanoelectrode lithography,<sup>[12]</sup> which uses a conductive stamp to transform the surface chemically by applying a voltage between the mould and the substrate while they are in contact. This can be used to create a mask either by electrochemical oxidation, such as anodic oxidation of Si to produce SiO<sub>2</sub> patterns,<sup>[13]</sup> or sputtered Al metal to produce Al<sub>2</sub>O<sub>3</sub>. Subsequent etching can create relief structures using the electrochemically deposited mask.

### **1.3.4 Scanning Tip Methods**

Scanning probe microscopy (SPM) methods such as atomic force microscopy (AFM) or scanning tunnelling microscopy (STM) can be used to modify a surface, hence are applicable as a form of lithography. The major drawback is that serial production of features as a tip rasters

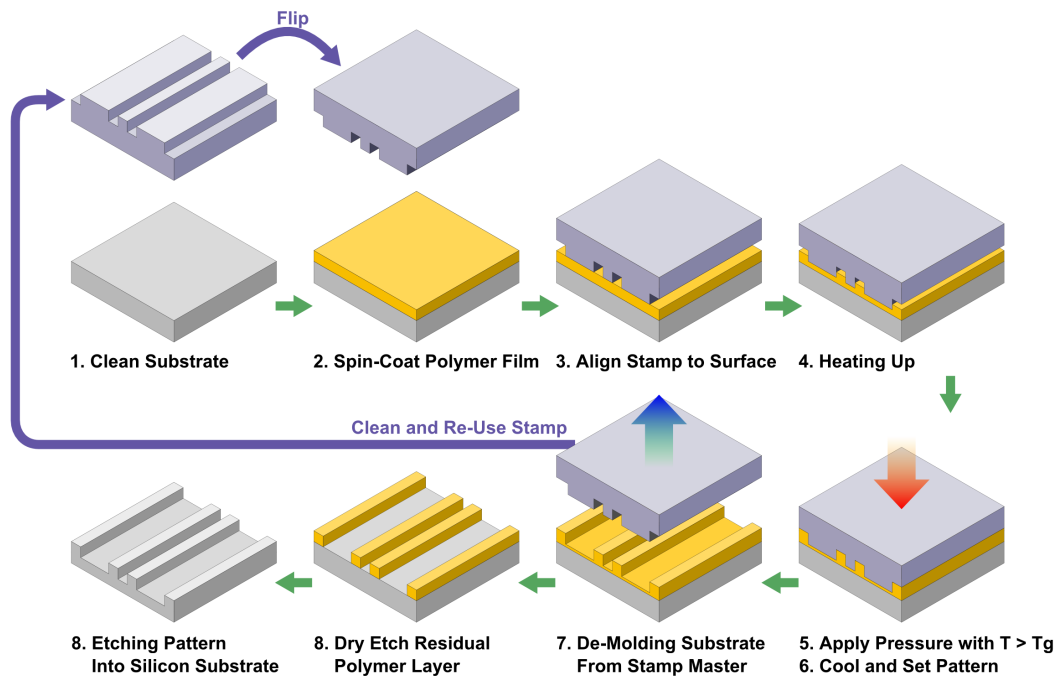


**Figure 1.4:** Schematic diagram of the process of nanoimprint lithography. The substrate is coated with a polymer film, which is placed in contact with a stamp that is aligned to the surface. The polymer is heated, and with the temperature above the polymer's glass transition temperature ( $T_g$ ), the stamp is pressed together with the substrate. After cooling, the substrate is de-moulded from the stamp; in order to remove the thin residual polymer layer coating, the surface is etched to reveal the underlying bare silicon areas. Finally, the mask formed is used to etch the pattern into the underlying silicon substrate.

across the surface is a slow and time-consuming process.

A classic example is the manipulation of individual atoms using an STM tip to create patterns with individual atoms on a surface, which represents both the highest resolution possible and the greatest spatial control. However the time required is enormous: Patterning a 45 nm x 25 nm copper <111> surface using CO molecules required roughly 180 hours to get each pattern exactly right, for the 242 frame, 60 second animation, "A Boy And His Atom".<sup>[14-16]</sup>

An AFM tip can cover a much larger area although with lower resolution. Pattern transfer can be applied via several ways: electrochemical reaction, deposition of material, scratching or etching, and indentation. In each case, an effort to parallelize the operation by creating arrays or lines of tips has made headway in patterning, despite the tips' propensity to break.

Dip pen nanolithography (DPN) is a commercialized process which deposits a self-assembled monolayer at the surface using a water meniscus at the tip, analogous to the operation of a fountain pen(10). Parallelization using 55,000 cantilever arrays can increase throughput to create half a billion sub-100 nm features in under 30 minutes.

Using an array of cantilevers to perform thermomechanical indentation, IBM's "millipede" technology was originally developed as a mo-

bile storage technology to compete with flash memory, however it subsequently found application in lithography.<sup>[17]</sup> Each cantilever tip in the array can heat up to form indentations in a PMMA or polycarbonate polymer film, creating a mask for etching, in a highly parallel process as it scans across the surface.

### **1.3.5 Block Copolymer Lithography**

Block copolymer lithography is the focus of this thesis. As a complementary technology, it has the potential to enable large area patterning with uniform features as small as 5 to 10 nm. Moreover, as a process it is extremely fast, able to apply a pattern to an entire wafer simultaneously in relatively short periods of time.<sup>[11]</sup> As noted in the ITRS: “Block copolymer self-assembly can easily define a limited set of highly symmetric patterns, *i.e.* repeating lines/spaces or hexagonal arrays of cylindrical holes, that may be useful in defining circuit elements.”

Block copolymer self-assembly represents the ideal of “bottom-up” patterning technology, wherein molecules organize to form nanoscale structures of defined shape and dimensions. This stands in contrast to “top-down” processes, wherein some larger object directs the selective deposition or removal of material from specific places. Bottom-up processes are attractive for the potential to pattern large areas in paral-

l with high throughput and minimal energy requirements. The most promising candidate materials available, at present, for bottom-up patterning are block copolymers.

In their simplest structural incarnation, block copolymers are comprised of two homopolymer chains covalently linked, which forms a diblock copolymer, such as that shown in Figure 1.5. The two phases are enthalpically driven to associate with other segments of the same type. The preferential association results in nanophase segregation below the critical temperature.

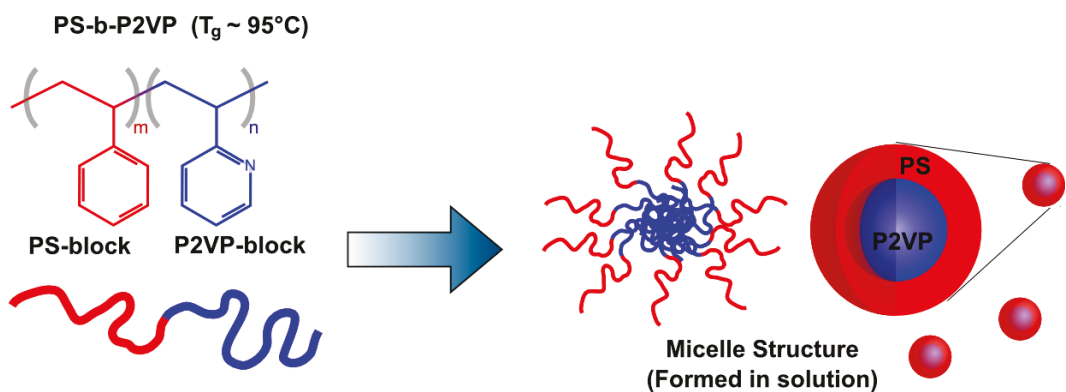


**Figure 1.5:** Polystyrene-block-poly(2-vinylpyridine), or PS-b-P2VP, as an example of a diblock copolymer. Polystyrene units, chains, and domains are shown in red, while poly(2-vinylpyridine) units are shown in blue. In toluene solution these typically form a micellar structure with a P2VP core and a PS shell, suitable for uniform spin coating of a surface.

Such polymers have been extensively studied, with bulk phases determined both theoretically and empirically using fractionation to pro-

duce multiple compositions of low polydispersity BCPs with a given molar mass and volume fraction, in conjunction with diffraction/scattering studies. The structures produced depend on the volume fraction of each block. Extremely low volume fraction of one block will result in a homogeneous mixture. Increasing the volume fraction of the lesser block will result in phases (depending on the degree of polymerization and the Flory Huggins parameter) going from homogeneous to close packed spheres; hexagonally packed cylinders; possibly a gyroidal phase; and lamellar when the volume fractions are approximately equal (see Figure 1.6).

When confined to a thin film, we can create a “monolayer” — a single layer, confined to 2 dimensions, of the bulk 3D structure, uniformly oriented with respect to the substrate surface — shown in Figure 1.7, of whichever structure is present. The actual structure depends on interfacial interactions between the polymer blocks and the two confining surfaces (usually substrate and air), in addition to the thickness of the film and the volume fraction of the blocks, which expands the range of structures possible.

Numerous methods capable of synthesizing well-defined diblock copolymers with narrow polydispersity (as well as other, more complicated systems) have been further developed and refined in recent years, expanding the range of monomers and initiating groups which can be

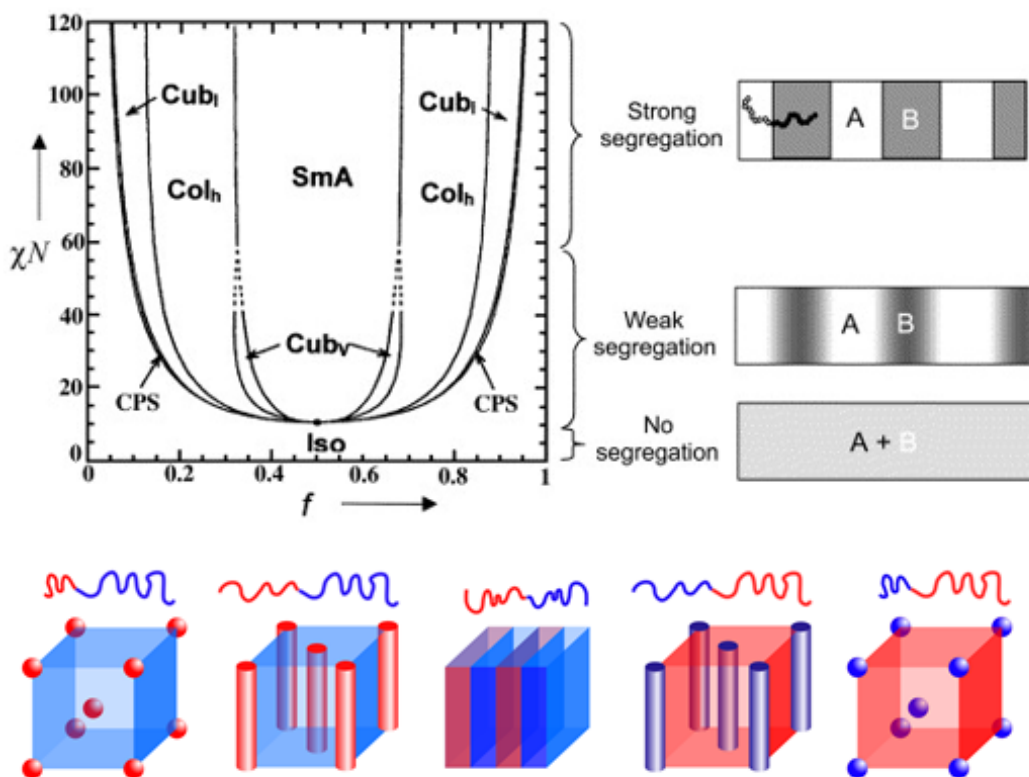


**Figure 1.6:** Bulk phases of diblock copolymers with no segregation, weak segregation, and strong segregation are shown as a phase diagram. The x-axis represents the volume fraction of one block, while the y-axis shows the product of the Flory-Huggins parameter ( $\chi$ ) and the degree of polymerization ( $N$ ). The segregation is visually depicted to the right, with full mixing, partial mixing (as gradients), and no mixing (sharp changes in intensity). Below are schematic depictions of selected block copolymer phases with varying volume fractions of each chain. From left to right: spherical close packed; hexagonally packed cylinders; lamellar; hexagonally packed cylinders; and spherical close packed. Phase diagram reprinted with permission from ref.<sup>[18]</sup> and adapted according to ref.<sup>[19]</sup> Copyright ©2006 American Chemical Society.

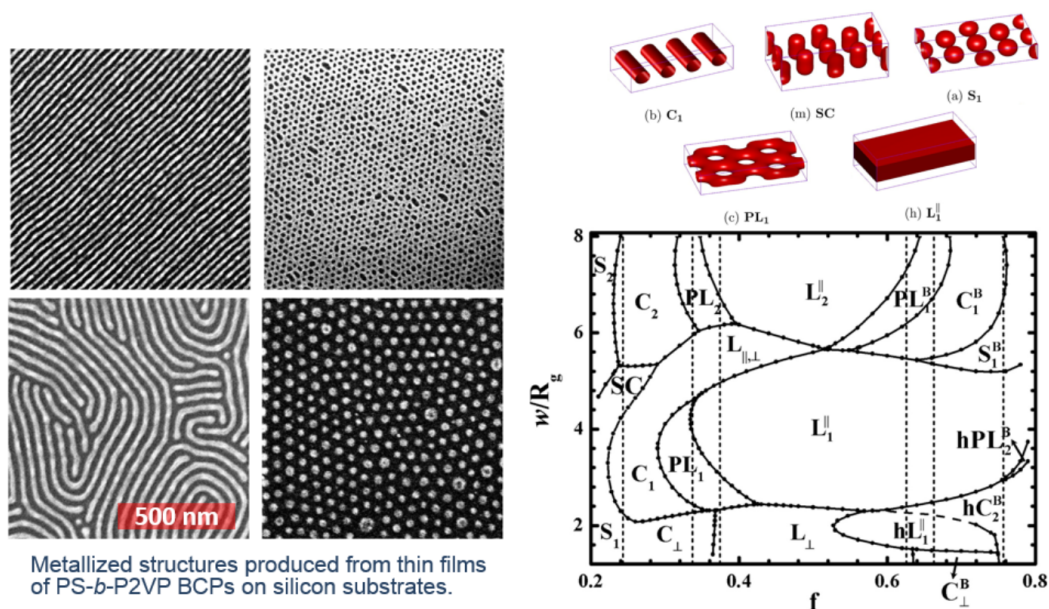


**Figure 1.7:** Left: Selected SEM images of platinum nanoattens templated from PS-*b*-P2VP block copolymer thin films: (top right) horizontally aligned cylindrical patterns with perfect and (bottom right) imperfect alignment; (top right) perforated lamellar structure; (bottom right) close packed spherical structure.<sup>[20]</sup> Right: (top) Computationally predicted structures. (bottom) A phase diagram for films with symmetric boundary conditions with preferential wetting of one block as a function of film thickness and volume fraction.<sup>[21]</sup> Reprinted with permission from refs.<sup>[20]</sup> and<sup>[21]</sup> and adapted. Copyright ©2011 and 2013 American Chemical Society.

accessed. Presently, synthetic methods for forming block copolymers *via* living or pseudo-living polymerizations include: anionic polymerization, cationic polymerization, nitroxide mediated radical polymerization (NMP), atom transfer radical polymerization (ATRP), Reversible addition-fragmentation chain-transfer (RAFT) polymerization, and ring-opening metathesis polymerization (ROMP). Methodologies have continued to improve in each area, with recent advances such as light-catalyzed polymerizations; metal-free methodologies; and others.

Vertically oriented lamellae or horizontally oriented cylinders are desired for their ability to template line arrays. In order for these to be useful, guiding features, either topographical or chemical are required to control registration and orientation and to limit defects. However such control features can be readily imparted using conventional lithographic processes combined with surface chemistry, as necessary, for appropriate wetting characteristics.

Such arrays can form the mask of devices such as synchronous dynamic random access memory (SDRAM) and tri-gate transistors, provided that other complementary patterning techniques are used to reduce line structures to shorter segments, as show in Figures 1.8 and 1.9. Orthogonally aligned bilayers or line patterns also could be used to create addressable “crossbar” arrays, suitable for memory or logic functions. Additionally there are other applications such as polarization

filters which can be developed with minimal modification of the features. Some of the possible device-oriented applications of BCP lithography are listed below:

- ▶ Memory structures:
  - Random-access memory (RAM)
  - Read-only memory (ROM)
  - Dynamic random-access memory (DRAM)
  - Synchronous dynamic random-access memory (SDRAM)
  
- ▶ Field-effect transistors (FET) architectures including:
  - FinFETs
  - Tri-gate FETs
  - Nanowire FET
  
- ▶ Memristive systems relying on crossbar arrays
  
- ▶ Polarization filters

With current chemoepitaxial methods, irregular morphologies and assemblies of the blocks can be induced. Device-relevant structures such as bends, jogs, junctions, periodic line arrays, and even isolated lines or spots can be formed with regularity and precision and on the same

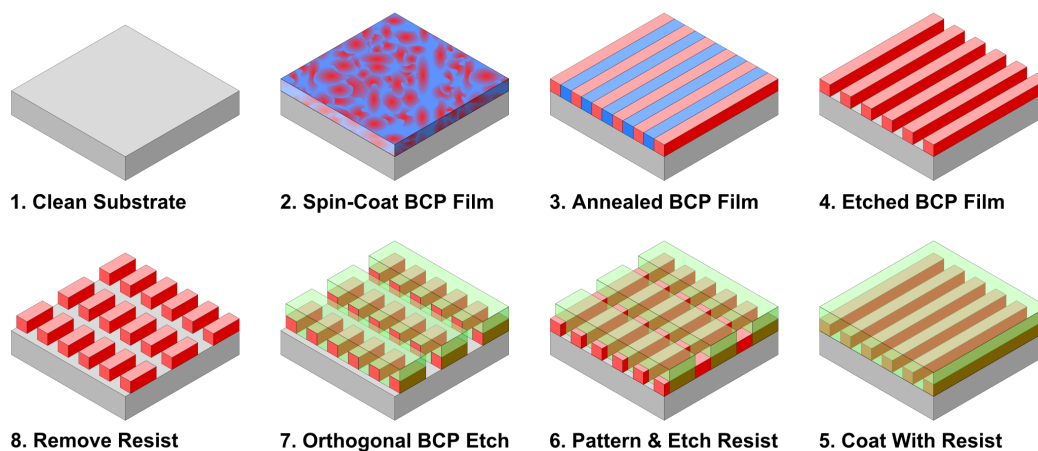


**Figure 1.8:** Process for using a combination of lamellar BCP lithography and conventional photolithography to pattern an array of truncated lines or rectangular features. Steps 1-4 represent the BCP pattern process where the substrate is prepared, coated via spin coating to create a thin film, which is then annealed, then etched to remove one of the phases. Steps 5-8 show the subsequent lithography process integrated to delimit the line lengths using a resist to coat the film, which is then patterned, exposing a limited region of the BCP lines for etching, followed by complete removal of the resist to reveal the mask of truncated line features. Although an edge-on lamellar pattern is depicted, the scheme is also possible for cylindrical BCPs.

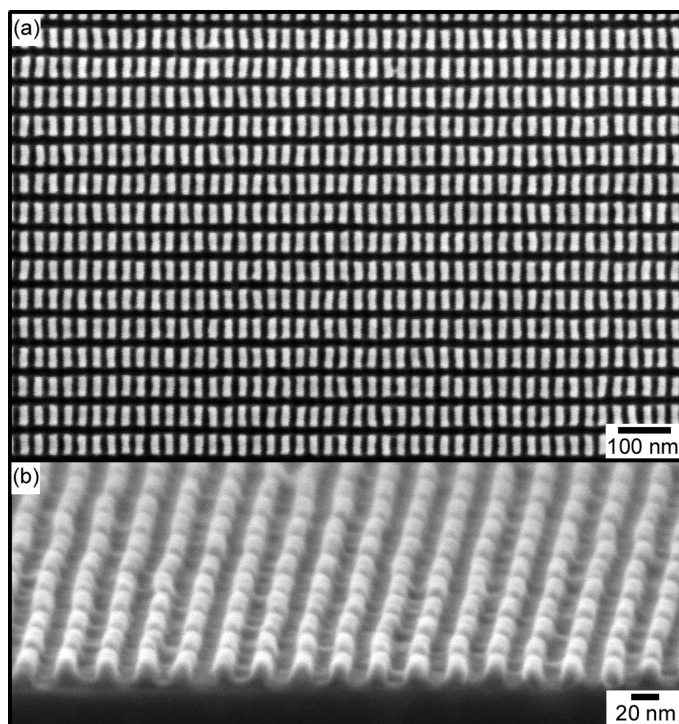


**Figure 1.9:** An example of lamellar PS-*b*-PMMA lines transformed into rectangular bits. Using an annealed, chemoepitaxially aligned PS-*b*-PMMA film, the PMMA was removed, then using electron beam lithography, the lines were cut to short rectangular segments. Phase diagram reprinted with permission from ref.<sup>[22]</sup>. Copyright ©2011 American Chemical Society.

scale as other block copolymer features, as shown in Figure 1.10. Irregular structures would greatly increase the breadth of designs that can be templated using BCPs. Presently chemoepitaxial methods are limited to patterning features based on striped lamellar patterns and vertically oriented cylinders, as it relies on a contrast in chemical potential on the surface of the substrate. Moreover, although it is possible to use sparse pre-patterned directing features, this still represents an additional step. Risks similar to those exhibited by contact printing lithography or large time investments, as in the case of pre-patterning with electron-beam lithography, could limit the technique. However, it is currently being studied and applied by several major manufacturers of electronics components.

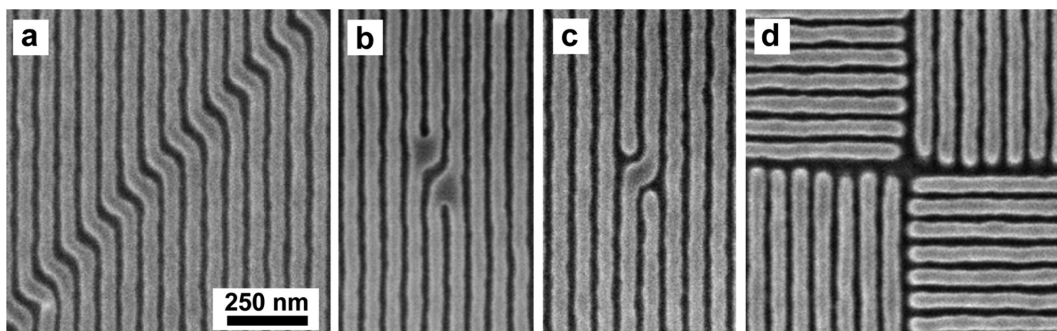


**Figure 1.10:** Irregular structures templated using vertically oriented lamellar domains of block copolymers, guided by chemoepitaxy. These include isolated lines; periodic lines; bends; jogs; T-junctions; Isolated spots; and periodic spots. Reprinted with permission from ref.<sup>[23]</sup>. Copyright ©2007 American Chemical Society.

## 1.4 Fundamental Challenges and the ITRS Objectives for Block Copolymer Lithography

Block copolymers are not without their own challenges to overcome. Several hurdles remain, including the problem of achieving an orders-of-magnitude decrease in the density of defects, obtaining sufficiently smooth lines, and with factors which top-down methods have long since overcome: predicting structure; optimizing pattern development time; registration; and metrology. Solving all of these barriers to achieve full integration with existing manufacturing processes is a mammoth task, beyond any single lab.

Note also that although numerous block copolymers have been synthesized in the course of the ever expanding repertoire of polymer chemistry, very few polymers have been fully examined for suitability as block copolymer templates. Much of the past and present work has focused on PS-*b*-PMMA as it is readily available, there exists an easy, simple method for selectively etching the PMMA phase, and the surface chemistry for chemoepitaxial approaches has already largely been optimized. Polystyrene, however, does not possess significant etch resistance under all circumstances; hence other polymers need to be explored. It is likely that polymers with greater Flory-Huggins interaction parameters would lead to more uniform lines, or that poly-

mers with a narrower distribution of molar masses could lead to more perfect ordering.

Hence, while it has been extensively investigated, block copolymer self-assembly is still a technology that continues to mature, with significant room to grow, develop, and improve. It is with this potential that many, both individually and corporately, have pursued it as a technology destined to shape the future, with the aim of overcoming present limitations.

The International Technology Roadmap for Semiconductors (ITRS) is a document produced by a collaboration of industry experts from five participating semiconductor industry associations: USA, Japan, Europe, Taiwan, and Korea. Its objective is to facilitate technological advances in the manufacture and performance of integrated circuits in a cost-effective fashion through the feedback of manufacturers, government labs, consortia, suppliers, and academic scientists and engineers.<sup>[24]</sup> These experts and stakeholders engage through working groups and community feedback to identify critical challenges, to quantify technology requirements, and identify areas of innovation. Consequently, the objectives described by the roadmap distill the cutting-edge advances and anticipated targets necessary for continued progression of semiconductor technologies, and frequently referenced in publications dealing with potential solutions to the monumental challenges at

the frontiers of nanolithography.

The ITRS is published online biennially, with brief updates typically published in the intervening years. The most recent edition of the ITRS is the 2013 edition, released on April 1, 2014. Additionally, the challenges and progress are disseminated through workshops such as the annual SPIE Advanced Lithography conference.

The “Emerging Research Materials” chapter addresses nascent materials solutions which are still in the phases of development where research challenges remain to be addressed in the laboratory. Within this category, block copolymer thin films are currently situated under “Directed Self-Assembly” (DSA).<sup>[11]</sup> With regards to the control of BCP self-assembly, the main challenges are listed in Table 1.1. These include questions and challenges among which there are fundamental thermodynamic questions; the need for modelling; metrology development and validation; defect control; and broader questions over the control of self-assembly in the context of integrated circuit lithography.

Many of these questions are focused on engineering the integration of BCP DSA structures with existing lithographic IC structures, design flows, and manufacturing processes. Registration control needs to be improved to ensure accuracy in the relative position of BCP features within the larger IC architecture. With this in place, models also need to be developed to accelerate and accurately predict BCP DSA struc-

Challenge	Summary of Issues
Fundamental thermodynamic stability and fluctuations of materials and structures.	Geometry, conformation, and interface roughness in molecular and self-assembled structures.
Accurate multiscale simulation for predictions of unit processes, structure, properties, and device performance.	Linkage between different scales in time, space, and energy bridging equilibrium and non-equilibrium phenomena.
Metrology to characterize structure and properties of materials at the nanometer scale.	Development of the method to evaluate the validity of the measurement result for each ERM.
Ability to control defects in material processing.	Methods to reduce directed self assembly based defects to $< 0.01 \text{ cm}^{-2}$ for litho extension.
Control of self-assembly to achieve desired properties reproducibly.	Required feature sizes in predetermined arrays with low anneal time, low defect density.
	Efficient CAD models to enable translating design features to guide structures on photomasks.
	Registration of self-assembled patterning materials in desired locations with control of geometry, conformation, interface roughness, and defects.
	Realistic device pattern with reduced pattern roughness and defects.
	Deterministically controlled locations of dopants conformally on 3D structures.

**Table 1.1:** Extracted items relevant to block copolymer DSA from the “Emerging Research Materials Difficult Challenges” table in the 2013 edition of the ITRS.<sup>[11]</sup>

tures within existing computer-assisted design (CAD) work flows. Then, the process needs to be integrated into the manufacturing process without sacrificing processing speed, while simultaneously maintaining pattern quality: correct conformation and geometry, good registration, line edge roughness, and low defectivity. To ensure quality, high-resolution, high-throughput metrology needs to be developed for routine inspection of integrated circuits bearing billions of features less than 20 nm. Engineering challenges await, while more fundamental objectives need to be addressed at the benchtop. BCP thin films, guided in various forms of directed self-assembly, need to be accessed for suitability and to determine whether the crucial targets set out by the ITRS for what can potentially be achieved for samples not yet embedded within IC layouts. For this, five primary metrics come into play: defect density, line width (and edge) roughness; feature size; feature placement; and annealing time. The targets for each of these is provided in Table 1.2. Whether any current block copolymer system can fully meet the thresholds described remains an open question. Consequently, we need to investigate and quantify whether present systems can be made amenable and determine if alternative systems' characteristics represent viable routes.

<b>Metric</b>	<b>Target</b>
Defect density	0.01 cm <sup>-2</sup>
Line width roughness ( $3\sigma$ )	1.1 nm
Annealing time	approx. 1 min
Minimum feature size	18 nm
Feature placement ( $3\sigma$ )	< 0.5 nm

*Table 1.2: Numerical targets for features templated by block copolymer directed self-assembly, extracted from the 2013 edition of the ITRS Emerging Research Materials chapter.<sup>[11]</sup>*

## 1.5 Application to Bit-Patterned Media

Integrated circuits may not be the only technology ready to benefit from block copolymer lithography: Hard drives designed with densely-patterned, individual magnetic domains could potentially be produced using block copolymer templates. Much of the research for block copolymers, both industrial and academic, has a concurrent focus on bit-patterned media on account of the potential for patterning large areas in a fast, parallel fashion. The monotonically decreasing cost of hard drives (shown in Figure 1.11), measured in price per gigabyte, has been a major factor in the rise of cloud storage, massive databases, and even personal electronic devices such as the first generation iPods. Hence there is a strong potential for cheap patterning technologies to be im-

plemented.

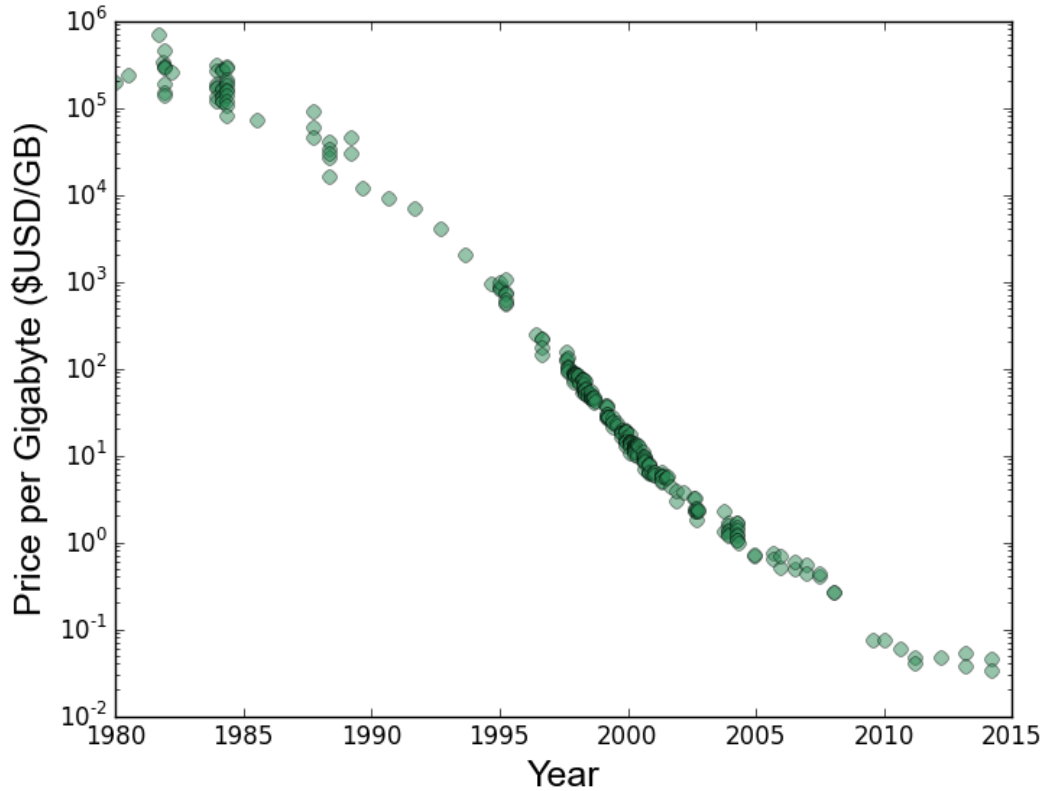


**Figure 1.11:** Hard drive prices expressed in dollars (USD) per gigabyte (GB). Cost has decreased exponentially since the early 1980s, when a 10 MB hard drive sold for \$3000 USD (\$300,000 USD/GB), to \$120 for a 3 TB hard drive (\$0.04 USD/GB) in 2014. Data adapted from ref.<sup>[25]</sup>

As hard drive storage capacities continue to increase, the aerial densities of magnetic disc drives consequently become greater. However, as density increases, the size of the magnetic domains will decrease. Smaller domains have a greater risk of superparamagnetic instability: the possibility that magnetization can randomly change direction with

ambient energy. The estimated information density limit for longitudinal recording is 200 Gbit/in<sup>2</sup>,<sup>[26]</sup> however perpendicular recording, the subsequent standard, permits densities of 1 Tbit/in<sup>2</sup>; shingled magnetic recording boosted the limit by about 25%. Continued increases in density will require circumvention of the superparamagnetic limit.

One means to mitigate the limit is heat-assisted magnetic recording (HAMR): By changing the magnetic properties of the disk to require a temperature change during the writing process, the superparamagnetic effect can be suppressed. This local heating is executed by a small laser that heats the active region of the disk as data is written.

The second major thrust for industrial hard drive research is to create bit-patterned media (BPM). Typically hard drives consist of continuous polycrystalline magnetic films; BPM entails patterning an array of nanoscale magnetic islands which are physically separated from adjacent bits. Individual grains within the island are strongly coupled, which results in the grain volume being the entire island, rather than an individual grain within a magnetic domain; the larger volume increases the thermal stability. On its own, BPM should enable aerial information densities up to 5 Tbit/in<sup>2</sup>, while in combination with HAMR estimates range from 20 Tbit/in<sup>2</sup> to 100 Tbit/in<sup>2</sup>, which at the high end would in physical terms correspond to one island within an area that is the equivalent of 20 surface atoms on a close-packed surface.

Block copolymers can be utilized to uniformly pattern large areas in a controlled fashion, provided that guiding features are incorporated. This can be effected through chemoepitaxy, graphoepitaxy or possibly other forms of imprinting and directing pattern development. Such patterning could be used to pattern complete hard drive plates.

For patterning magnetic bit features, either dot patterns or line patterns produced using block copolymers could be used to lithographically template magnetic domains. The densities attainable using BCPs could reach 1 terabit (or teradot) per square inch: specifically, HGST has demonstrated functional patterns of 1.2 trillion dots per square inch (1.2 Tbit/in<sup>2</sup>) in 2013 — twice the density of contemporarily available drives—using a pattern with 10 nm features. Currently all three major hard drive manufacturers—Seagate, HGST/Western Digital, and Toshiba — are engaged in research using block copolymer lithography to increase the areal density of dots for hard disk drives.

Given the low utilization per unit area, BCPs have the potential to make regular arrays of high density features at a cost comparable to drives currently on the market. Moreover, block copolymers might not be used directly, but rather to create masters for subsequent nanoimprint lithography to pattern disks, further extending their application.

## 1.6 Scope of the Thesis

This chapter sets the backdrop of the thesis to give a broad overview of nanopatterning in manufacturing applications and to give context to the relevance of block copolymer patterning as well as to indicate the dual potential and challenges faced.

Chapter 2 deals with the background to understanding defects, and their elimination, in block copolymers. This mini-review explains the various aspects of defects in block copolymers and how one can go about rectifying each aspect.

The development of an algorithm for automatically quantifying and studying defects in BCP thin films is described in Chapter 3. This is done using a particle-based and skeleton-based analyses of feature structures observed in images collected using scanning electron microscopy. A compilation of polymer molecular weights and annealing conditions are explored for overall features followed by a series of similarly annealed polymers to compare the specific effects of polymer molecular weight. Additionally, the results were analyzed over a range of resolution and image size to determine ranges for which results and data are valid. This work was originally published in *PLoS One* in 2015,<sup>[1]</sup> and the chapter adapted from the article.

The algorithm is applied in Chapter 4 to provide an overall understand-

ing of the features of horizontally aligned PS-*b*-P2VP thin films metallized and imaged using scanning electron microscopy. Films with different initial thicknesses were produced, characterized using ellipsometry, and annealed in order to study the effect of film thickness on the defectivity of monolayers of horizontally oriented cylindrical domains. AFM was also used to study the equilibrium thicknesses of layers which the films adopted during the annealing process.

Finally, a summary of conclusions and future directions for exploring the characteristics of BCP thin films is laid out in Chapter 5.

Additionally, two appendices are also provided to clarify the text: Appendix A provides a brief derivation of how particle size is used to determine line-width. Appendix B provides a section-by-section overview of the code and functions contained within it for reference to those engaging in future improvements. This is merely a description to assist in understanding the overall flow and function of the code, however the code is freely available in full online on GitHub and archived in the University of Alberta's institutional repository.

# 2

## Analysis of Defects in Block Copolymer Thin Film Structures

### **2.1 Introduction**

Block copolymer thin films are of significant interest to industries which rely upon lithographic patterning, as future technological advances are dependent on ever-smaller features which cannot be attained using conventional photolithography. Consequently, much time, effort,

and money has been invested in understanding the fundamental science behind these structures and how to apply that knowledge to creating perfect patterns which can be mobilized for use in integrated semiconductor circuits for the multi-billion dollar consumer electronics industry.

## **2.2 Structure of Thin Films**

The structure of block copolymer thin films is controlled by 6 primary parameters: the volume fraction of each block, the degree of polymerization, the Flory-Huggins interaction parameter, the film thickness, surface energies of each block relative to the surface and air (or confining layer), and the presence of guiding or confining features.

In bulk, strongly segregating diblock copolymers exhibit a range of morphologies, depicted in Figure 2.1, which for a given polymer pair, depends on the degree of polymerization and the volume fraction of each block. Typically, as the minority block increases in volume fraction, the sequence of phases goes from disordered, to body-centred cubic spherical domains, to hexagonally packed cylinders, to gyroidal or hexagonally perforated lamellar, and finally to the lamellar morphology. However bulk morphologies produced are often asymmetric, resulting in different regions of stability depending on which

block is the minority.<sup>[27]</sup>

When confined to a thin film, a geometric conformational asymmetry<sup>[28]</sup> is introduced: a lamellar film can be oriented with domains either or perpendicular parallel to the surface; the perpendicular orientation results in a 2D striped pattern, whereas a perfect parallel film will be featureless when viewed aurally. Likewise, cylindrical domains can be oriented to produce either an array of 2D dots with vertical pillars or 2D stripes with horizontal cylinders.

Striped patterns are primarily used for block copolymer templated nanopatterns for application in semiconductor nanolithography. Two-dimensional dot patterns have potential application as templates for bit-patterned media. While some defect features are common to both types of films, defectivity in each is treated differently. This chapter provides an overview primarily focused on striped patterns, given their utility and the challenges surrounding their application.

When confined in one dimension to a 2D film, the structures exhibited take on additional variety, depending on the preference of the interface with respect to each block<sup>[21]</sup>, as shown in the computed phase diagram in Figure 2.2. Consequently, in order to attain the desired morphology it is necessary to not only have the correct volume fraction for each block, but to also to control the interfacial energies of either the surface or of the polymer, along with the specified thickness.<sup>[21,29]</sup> As

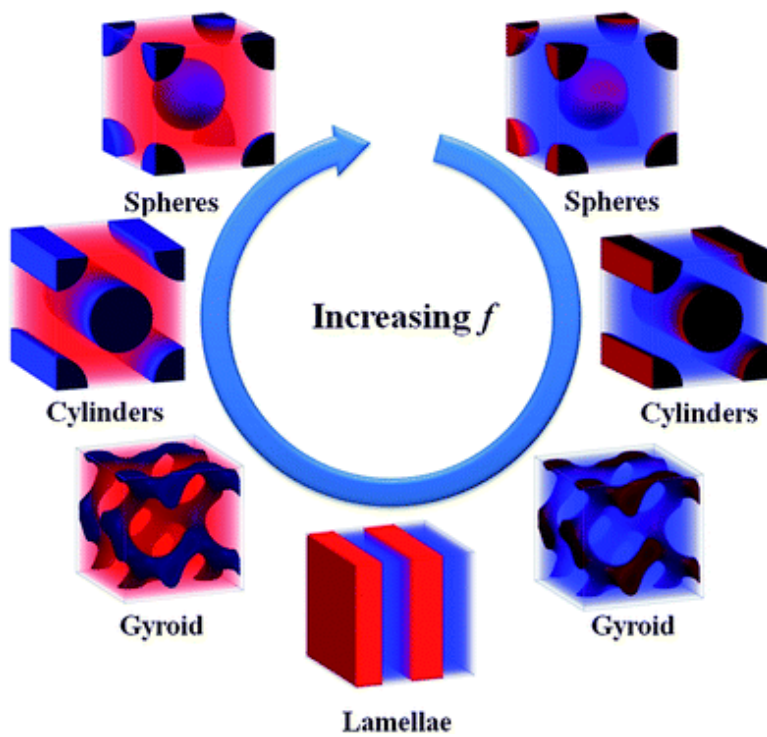


**Figure 2.1:** Bulk morphologies of block copolymers: BCC spheres; hexagonally packed cylinders; bicontinuous gyroidal; and lamellar. Hexagonally perforated lamellar and modulated lamellar are among the possible phases not shown. Reprinted with permission from ref.<sup>[19]</sup> Copyright ©2013 Royal Society of Chemistry

the latter is often not an option, the surface is tailored *via* interfacial layers, such as polymer brushes on the substrate,<sup>[30–33]</sup> or top-coats,<sup>[34]</sup> in order to either neutralize the attraction (often necessary to create vertically oriented lamellae) or to select for one block.<sup>[35]</sup>

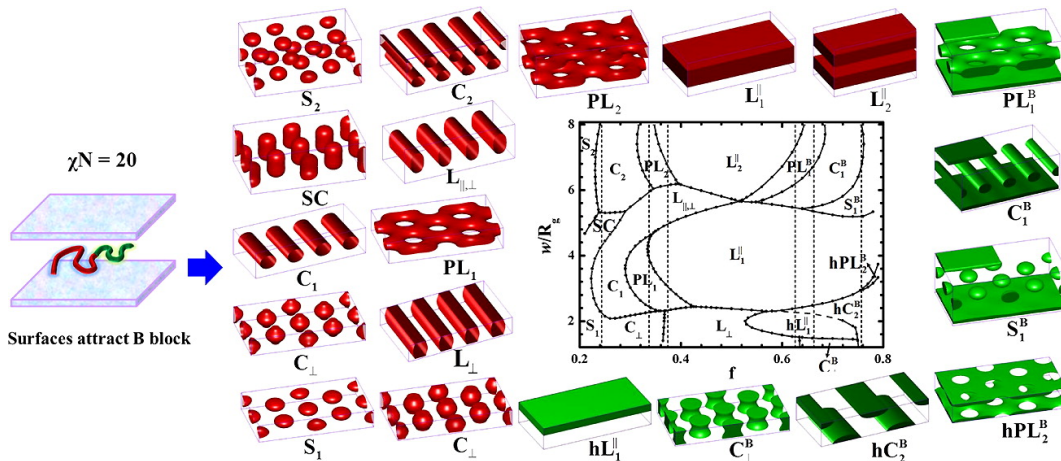


**Figure 2.2:** Morphologies simulated for a diblock copolymer of varying volume fraction, confined between two surfaces as a function of separation between the confining planes. The surfaces in this case both show preferential attraction of block B. Reprinted with permission from ref.<sup>[21]</sup> Copyright ©2013 American Chemical Society

## 2.3 Defects and their Characterization

The term “defect” can have a broad range of meanings in the context of block copolymer thin films: Defects are always qualified with respect to the desired outcome or the ideal pattern sought in a given appli-

cation. Here, we focus on the nanoscale domains of the block copolymer, where defects with respect to striped patterns derived from block copolymers, which represent departures from the linear, parallel, smooth, and continuous lines can form. Other larger-scale defects are also possible, resulting from incommensurate thickness, dewetting processes, or misorientation. When directing processes or structures are involved, defects also encompass the orientation, registration, and uniformity of line features.

### **2.3.1 General Considerations for Characterization of Defects**

Numerous tools are available for the characterization of defects in thin films. Electron microscopy is the workhorse for observing defect structures, given its ability to quickly survey large areas and to provide high resolution images down to  $\sim 0.5$  nm. The primary drawback is the limitation inherent in using electrons to image non-conductive soft matter. For this to work, the pattern must have at least one conductive component. This can be attained by: (A) selectively etching one block to reveal a conductive substrate or to create a surface with topographic relief; (B) pattern transfer to a conductive substrate; (C) metallization of one of the blocks to produce a conducting pattern.

Optical microscopy (and absorption spectroscopy) can also be used to directly characterize the nature of the film, in particular with regard to thickness defects. The interference pattern resulting from multilayer structures results in well-defined and predictable colours for layers of various thicknesses. Ellipsometry is more sensitive, despite the poor lateral resolution, it can provide information *via* modelling about the layer structure within the film, allowing the wetting preferences to be determined.

X-ray and neutron scattering techniques (GISAXS, SAXS, SANS, *etc...*) cannot directly measure topological defects, however they can be used to characterize in-plane deformations of the shape, as well as alterations to the size and spacing of domains. For some block copolymer nanostructures, it is either impossible or impractical to directly image defect structures, and in order to visualize them, a pattern transfer or contrast enhancement technique must be applied. Consequently, it can be uncertain whether defects observed (specifically topological and roughness) are the result of the annealing process and thermodynamic factors, or whether additional defects are introduced in the visualization stage. Similarly, in producing template nanostructures using block copolymers as a stencil, the template structures may contain defects introduced in the pattern transfer process.

### 2.3.2 Topological Defects

In the context of striped patterns, as formed by horizontal cylinders or vertical lamellae, “defects” primarily refer to topological defects in the pattern, resulting in a discontinuous pattern. Topological defects include disclinations and dislocations, which come in a variety of structures typified in Figure 2.3.

Counting defects has conventionally been done using software methods developed for nematic liquid crystal textures. Such methods require significant levels of filtering, which can be a problem. In particular, the method used by Harrison and coworkers is known to show a dependence on the radius of Gaussian smoothing applied.<sup>[36]</sup> Additionally Simao and coworkers have developed a method which appears to trace the contours of BCP patterns,<sup>[37,38]</sup> however certain results of the methodology and the lack of precise details have prevented widespread adoption.

One alternative means of assessing the topology of stripe networks is to use a skeleton of the pattern which has identical topology, thinned to a single pixel. This approach has been applied by two groups.<sup>[39,40]</sup> Rehse and coworkers applied it to a single domain, using skeleton as a graph, “characterized by its junctions and the number of edges originating from each junction”, following after the application of skeletonization

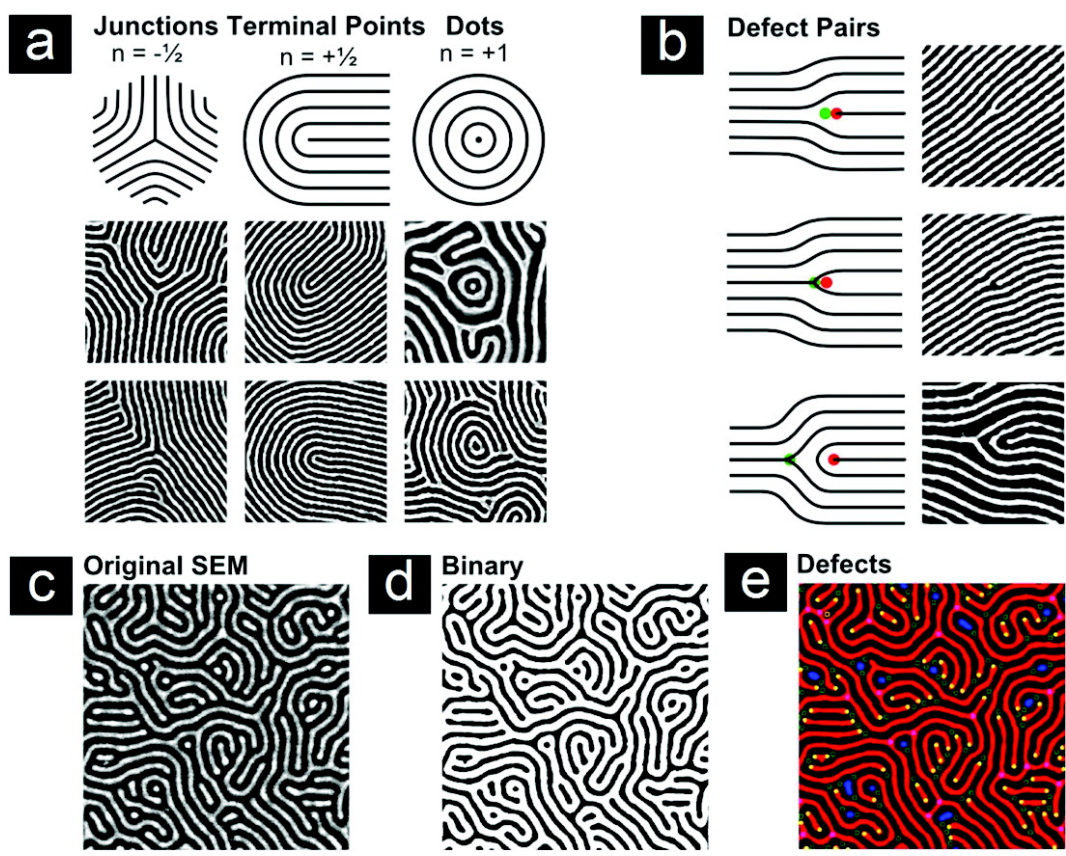


**Figure 2.3:** Defects observed in platinum-metallized cylindrical P2VP domains in PS-*b*-P2VP thin films. (a) Examples of junctions, terminal points, and dots. (b) Defect pairs forming disclinations or dislocations. Image processing of (c) the original SEM image, to produce (d) a binary version of the SEM image, from which (e) defects can be located and displayed. Reprinted with permission from ref.<sup>[20]</sup>. Copyright ©2011 American Chemical Society

to 3D gyroidal phases by Sherdel and Viglid.<sup>[41,42]</sup> Zhang and coworkers applied it to both domains, in order to calculate the total defectivity, dislocations and disclinations together,<sup>[40]</sup> following the suggestion of Kleman that striped patterns of liquid crystals can be decomposed into terminating lines and junctions.<sup>[43]</sup>

The annihilation of such defects is the basis for forming defect-free patterns. This requires either two dislocations or two disclination pairs to diffuse together, forming a quadrupole configuration whereupon they can cancel out, as shown in Figure 2.4.

### **2.3.3 Line-Edge Roughness and Line-Width Roughness**

The roughness of lines in BCP patterns is a point of concern for the application of directed self-assembly (DSA), due to the deleterious effect of line-edge roughness (LER) on device performance.<sup>[11,45]</sup> LER is defined as the “local line width variation ( $3\sigma$ , all frequency components included, both edges) evaluated along a distance equal to four times the technology node”.<sup>[46]</sup> Roughness of the lines can also be quantified in terms of line-width roughness (LWR), which describes the variation in the width of a line, whereas line-edge roughness (LER) describes the variation in the edge position of a line. Each is given as three times the standard deviation. One disadvantage of LWR is that it may not reflect

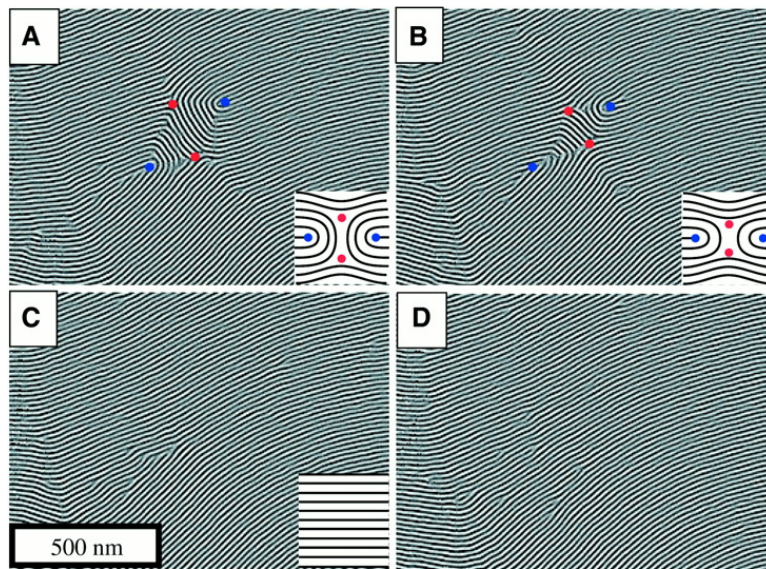


**Figure 2.4:** Defect annihilation BCP thin films: A quadrupole with two  $+1/2$  disclinations (blue) and two  $-1/2$  disclinations (red) diffuse together with annealing (A-B). Upon annihilation, dislocations are formed (C), which then separate due to repulsive forces. Reprinted with permission from ref.<sup>[44]</sup>. Copyright ©2000 American Association for the Advancement of Science.

the variation present in an undulating pattern, as shown in Figure 2.5 for a pattern with purely peristaltic roughness,  $LWR = 2LER$ .

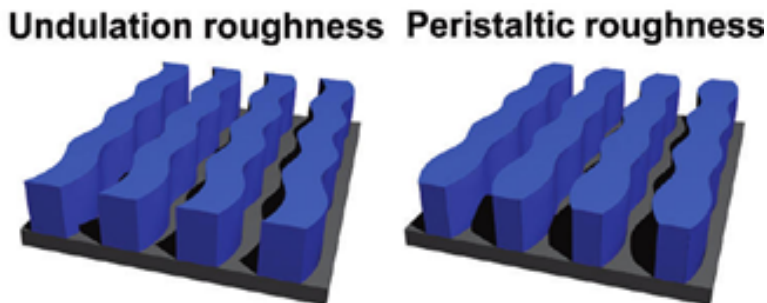


**Figure 2.5:** *Undulation roughness (left) and peristaltic roughness (right). Reprinted with permission from ref.<sup>[47]</sup>. Copyright ©2010 American Chemical Society.*

The interfacial width between blocks is proportional to  $\chi^{-0.5}$ ,<sup>[48]</sup> as the energetic cost of deforming the interface limits the LER,<sup>[49]</sup> hence increasing  $\chi$  is an obvious route to decreasing LER. Computational simulations seem to agree, in concluding that the interface is smoothest when the blocks have the greatest repulsive interaction<sup>[50]</sup>, shown in Figure 2.6. While the interfacial thickness in diblock copolymers scales with the degree of polymerization as  $N^{2/3}$ , the same simulations demonstrate that LER scales in the opposite direction: increasing for smaller chain lengths.<sup>[50]</sup> Hence the high- $\chi$  required to form small feature sizes may also be required to constrain LER for smaller domains.

Direct SEM imaging of graphoepitaxially-aligned BCP domains is the most typical means to assess LER, measuring deflections in the edge

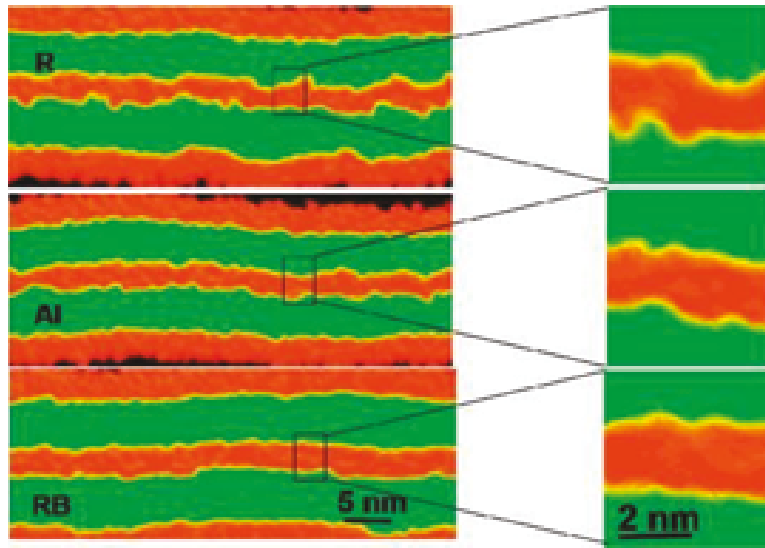


**Figure 2.6:** Simulation patterns showing LER, with three repulsive interaction potentials, increasing from top to bottom. Reprinted with permission from ref.<sup>[50]</sup>. Copyright ©2007 American Chemical Society.

position, for both left edge and right edge, relative to the average position determined by a linear fit. Summing the two edges :

$$LER = 3 \sqrt{\sigma_{left-edge}^2 + \sigma_{right-edge}^2}$$

In order to avoid sensitivity to sampling length, a minimum 2  $\mu\text{m}$  should be measured, otherwise the measured LER is underestimated as a function of the sampling length.<sup>[51]</sup> While typically done with aligned patterns, means to analyze curved patterns have been developed, employing the same skeletonization described for topology, in order to find the centre line to determine a centre position to reference the edges.<sup>[1,2,52,53]</sup> While likely not ideal for aligned films, LER measure-

ments are comparable, and enable comparisons between samples, and thus optimization strategies can be employed for the polymer structure, annealing process, and etching processes.

Additionally, LER should be analyzed using a power spectrum, which enables the components of LER to be deconvoluted, as demonstrated in Figure 2.7 as high frequency and low frequency components affect component performance differently. Figure 2.7 also demonstrates that LER in chemoepitaxial patterns can be partially rectified by the aligned BCP.

LER of solvent-annealed, metallized cylindrical domains of PS-*b*-P2VP films show promise for LER: patterns with 9 nm line width had LER measurements as small as 2.4 nm.<sup>[2]</sup> Similarly, immersion-based solvent annealing has resulted in 16 nm wide lines with LER of 2 nm.<sup>[54]</sup>

### **2.3.4 Feature Size Variation**

One less-often addressed issue is the overall uniformity of pattern features. This can, on occasion, be observed, in particular where confinement is employed. BCP patterns are able to distort, making small changes to the pitch in order to find a commensurate structure which will accommodate the available space. This can be noticed for patterns where lateral confinement is applied, as the example of graphoepitaxy

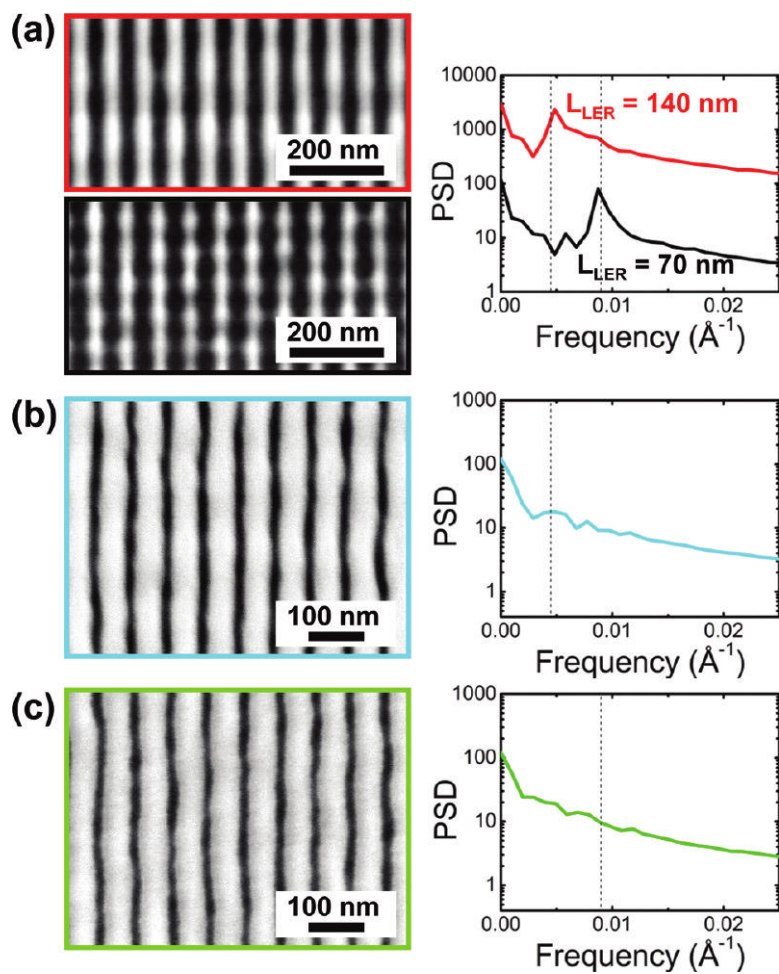


**Figure 2.7:** Comparison of LER measurements for (a) SEM images of chemical surface patterns with defined peristaltic roughness of 140 nm and 70 nm, and (b, c) SEM images of lamellar BCP self-assembled chemoepitaxially on the (b) 140 nm roughness and (c) 70 nm LER patterns. To the right are power spectrum density (PSD) plots showing the LER frequency components. Reprinted with permission from ref.<sup>[47]</sup>. Copyright ©9999 American Chemical Society.

in Figure 2.8.

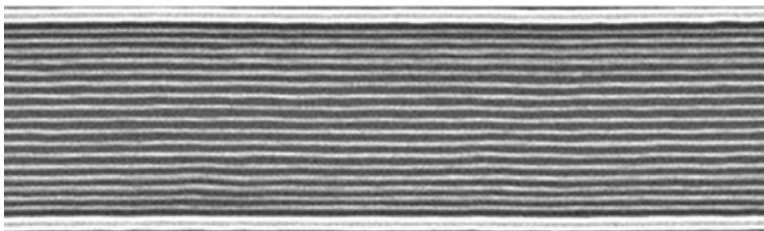


**Figure 2.8:** *Example of variation in line width and spacing for BCP cylinders confined via graphoepitaxy. Reprinted with permission from ref.<sup>[20]</sup>. Copyright ©2011 American Chemical Society.*

Even for regular structures there is typically a distribution in feature size and spacing, although a Gaussian distribution is often followed as seen in Figure 2.9. This has consequences for the reliability of registration, for which narrow tolerances are required to meet ITRS standards.<sup>[11]</sup>

### **2.3.5 Orientation and Registration**

In the absence of guiding features or directional annealing, the orientation of block copolymer nanostructures is random. Random orientation of striped domains results in a polycrystalline 2D surface, with associated grain boundaries. Moreover, even where graphoepitaxy is applied, features may not align as desired. Connected to this is the concept of controlling the position of one feature with respect to oth-

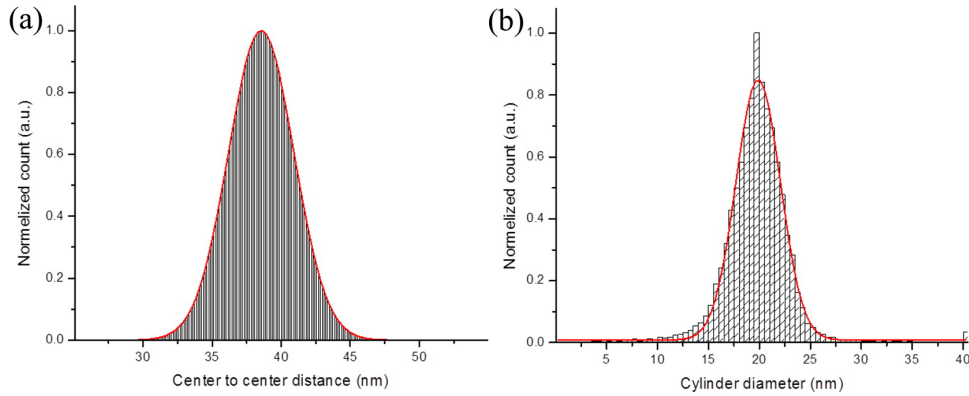


**Figure 2.9:** Normalized distributions of (a) centre-to-centre distance and (b) diameter for cylinders. Reprinted with permission from ref.<sup>[55]</sup>. Copyright ©2015 American Chemical Society.

ers: registration. Orientation of films is most commonly measured using imaging techniques, such as TEM, SEM, or AFM, with subsequent image analysis to determine the orientation of the film. Diffraction-based methods, such as small-angle X-ray scattering (SAXS)<sup>[56]</sup> are also widely utilized. One alternative is optical measurement of the birefringence<sup>[57]</sup> of a film,<sup>[58–60]</sup> which results from the anisotropic composition of domains. This can be used to observe the order-disorder transition and to follow the evolution of the orientational order parameter,  $S$ :

$$S = \frac{3}{2} \langle \cos^2\theta \rangle - \frac{1}{2}$$

which is calculated by taking the average value of  $\cos^2\theta$  for the orientation relative to a specified angle ( $\theta = \theta_i - \theta_{specified}$ ) at each point in the film pattern.

For extremely large block copolymers, it is even possible to image the defects directly using the instrumentation described in Figure 2.10.

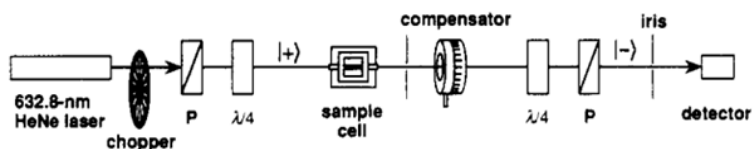


**Figure 2.10:** Optical set-up for finding defects in large BCP textures. Reprinted with permission from ref.<sup>[58]</sup>. Copyright ©1992 American Chemical Society.

Direct measurement from SEM or TEM images of the domains remains a standard technique for determining both orientational order, *via* the angular correlation length,<sup>[44,61]</sup> but also the size of grains.<sup>[62]</sup> Typically this involves sampling the texture of large, multi-grain images, to determine *via* fast Fourier transforms (FFTs) the local orientation, as shown in Figure 2.11. Orientation can also be determined directly from skeleton structures,<sup>[1]</sup> which avoids the problem of disordered regions not having a well-defined local orientation.<sup>[62]</sup>

FFT can also be used as a tool for filtering electron microscopy images, in order to remove noise and also to determine the period of the pattern, shown in Figure 2.12. This however has the disadvantage that disclinations and dislocations can be erased or created as a result of the filtering; limiting filtering to short distances tends to avoid this issue.

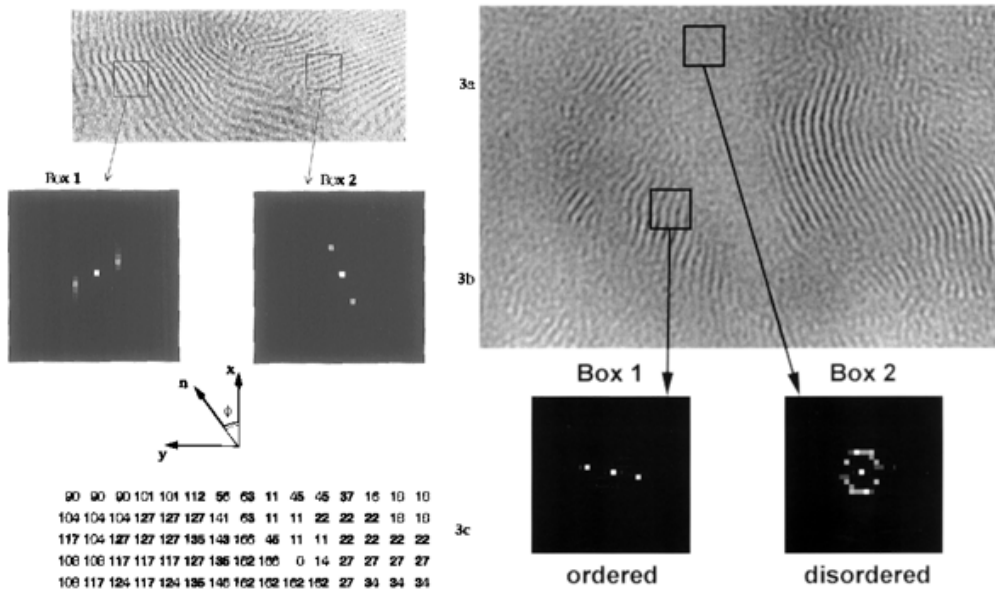


**Figure 2.11:** FFT sampling of orientations; disordered regions cannot produce an orientation measurement via this technique. Reprinted with permission from refs.<sup>[61]</sup> and<sup>[62]</sup>. Copyright ©1996 and 2002 American Chemical Society.

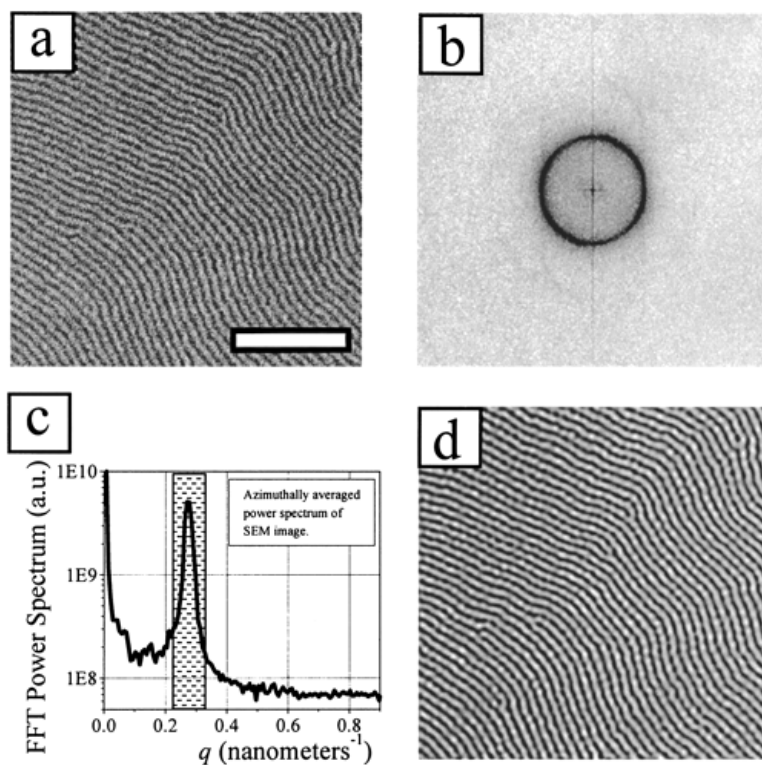


**Figure 2.12:** Fourier filtering of an SEM image. The fast Fourier transform (b) of an SEM image of the cylindrical domains of a block copolymer (a) can be azimuthally averaged to provide a power spectrum; the first peak corresponds to the inter-line spacing. By masking data outside of the window at  $\leq 20\% q_0$ , the area immediate to the peak, high frequency noise is removed and the contrast enhanced (d). Scale bar is 250 nm. Reprinted with permission from ref.<sup>[63]</sup>. Copyright ©2000 American Chemical Society.

### 2.3.6 Wetting and Misorientation

Given the typically significant difference in surface energies for each block, it is natural that preferential wetting behaviour can be observed.<sup>[64]</sup>

This may manifest itself over the whole film, for example turning what should be vertically oriented lamellar stripes into a featureless, flat, horizontally oriented lamellar layered structure. For lamellar films, preferential interfacial wetting can induce parallel orientation, however the influence only extends so far from the interface.<sup>[64]</sup>

It is also possible for the surface energy to result in dewetting of the block copolymer material from the surface resulting in a similar defect. Dewetting at high temperature can result in microdroplet formation, as in Figure 2.13, however this is typically an issue only for extremely thin films,<sup>[65]</sup> as polymer films show a thickness-dependent melting transition.<sup>[66]</sup> Solvent-annealed films, on the other hand, can de-wet as a result of excess solvent and high surface tension.<sup>[54]</sup>

Typically, neutral brush layers are applied to the substrate, while top-coat layers can be spin coated on top of the BCP film. Neutral brush layers are designed to control the delicate balance of surface energies, which determines the orientation of the BCP domains. While if undesired, misorientations are a defect, this can be used to intentionally pattern domain orientations.<sup>[67,68]</sup> In order to transform an inter-

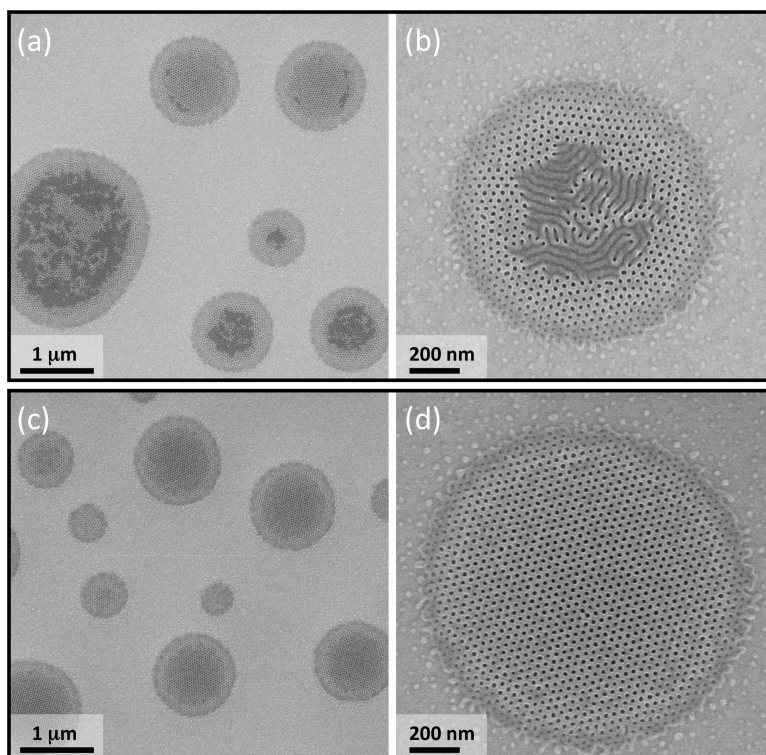


**Figure 2.13:** Microdroplet formation during rapid thermal processing from a 5 nm film of PS-*b*-PMMA ( $M_n = 67$  kg/mol; 0.71 PS unit fraction) on a 7nm brush layer of hydroxyl end-functionalized P(S-*r*-MMA) ( $M_n = 14.5$  kg/mol; 0.61 unit fraction PS) coated surface. Substrates were treated for 300 s at 270 celsius (a,b) and 250 celsius (c,d). Reprinted with permission from ref.<sup>[65]</sup>. Copyright ©2014 American Chemical Society.

facial layer into a chemoepitaxial pattern, interfacial material can be removed or chemically transformed, as by photolithography shown in Figure 2.14.

### **2.3.7 Contamination by Particulate Matter**

While much block copolymer research is carried out in typical bench-top conditions, industrial application of block copolymer nanolithography will require cleanroom conditions to prevent particulate contamination of thin films. Additionally, it is necessary to filter block copolymer solutions in order to exclude solids or incompletely dissolved material, such as residual filter paper fibres, from the spun films, as particulate defects<sup>[69–71]</sup> (as small as 20 nm<sup>[69]</sup>) can be an issue. Apart from this, particulate matter in the form of nanoparticles can be segregated selectively within a block copolymer domain, and even specifically within a block copolymer defect.

### **2.3.8 The Internal Structure of BCP Domains**

While block copolymers are primarily used as a 2D mask for lithography, they are three-dimensional systems with internal structure. So although in-plane defects considered here are typically more significant in terms of pattern disruption, the uniformity of the pattern through

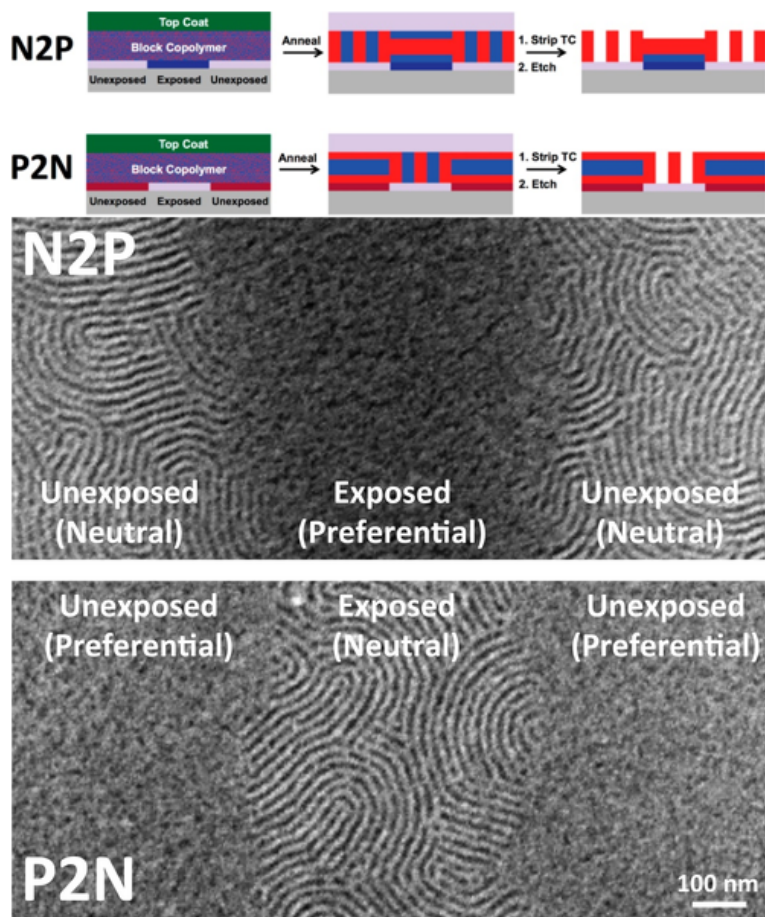


**Figure 2.14:** Preferential wetting can be induced using photopatternable interfacial layers, which exhibit different chemical compatibilities following light exposure. Hence one can either pattern (via exposure) neutral regions with vertically oriented lamellar domains or featureless regions with parallel domain orientations. Reprinted with permission from ref.<sup>[67]</sup>. Copyright ©2014 American Chemical Society.

the plane can also be a highly desirable feature, enabling formation of a uniform etch resist. Past work has utilized milling (*cf.* TOF-SIMS) of patterns in order to observe the structure of underlying layers, and scattering methods additionally give an indication of structure through the depth of the film. Edge-on SEM images provide some data, but it is typically limited to a small sample area. Hence these do not provide a full picture of the 3D structure of features embedded within the film and is both difficult and partly destroys any sample.

Recently, resonant critical-dimension small-angle X-ray scattering (res-CDSAXS)<sup>[72]</sup> has been developed as a new tool for determining the buried 3D structure of thin films, which aerial visualization techniques (SEM, TEM, and even AFM) are not able to observe. Using res-CDSAXS, surface wetting of vertically oriented lamellar patterns have been shown to result in a constriction at the substrate and surface interfaces, shown in Figure 2.15, resulting in through-plane inhomogeneity.<sup>[72]</sup>

Another complementary technique recently applied to BCP thin films is scanning transmission electron tomography, which provides a full 3D image of domains within the film.<sup>[55]</sup> Films are formed in order to allow removal from the substrate and transferred onto a silicon nitride membrane window and sequential infiltration synthesis is used to introduce Al<sub>2</sub>O<sub>3</sub> into the polar PMMA block of either cylindrical or lamellar PS-*b*-PMMA. This provides additional structural information about

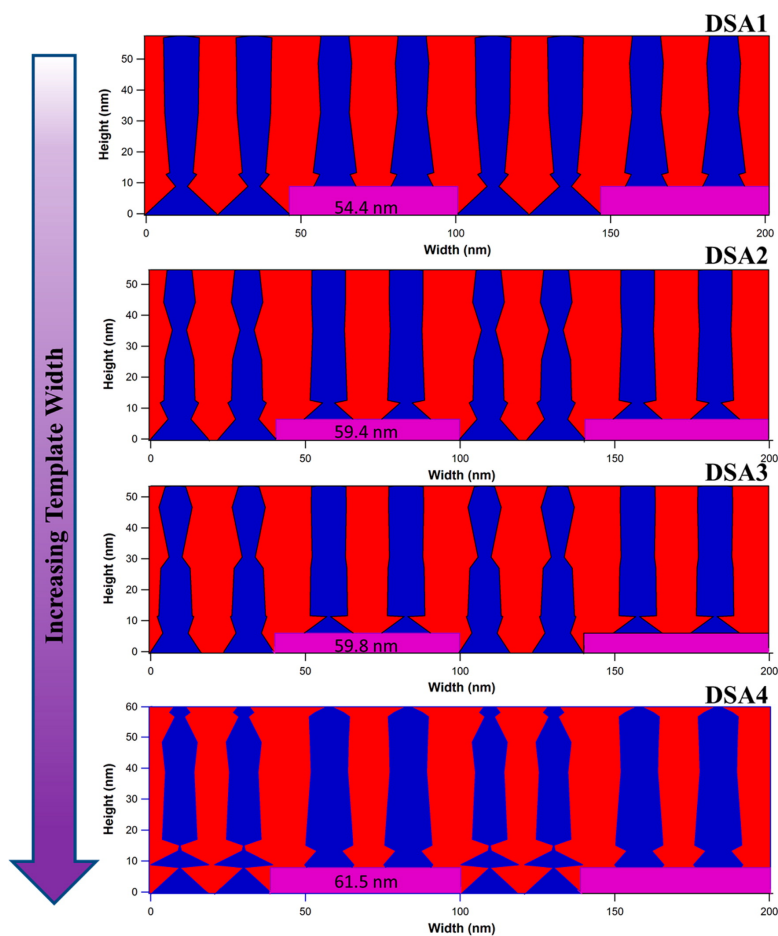


**Figure 2.15:** Through plane structures based on modelling with res-CDSAXS data. Increasing width of guiding, chemoepitaxial features results in greater constriction at the top-surface, while narrower features result in greater constriction at the lower-surface. Reprinted with permission from ref.<sup>[72]</sup>. Copyright ©2014 American Chemical Society.

disclinations and dislocations within the film, which are demonstrated to be non-uniform through the depth of the film, shown in Figure 2.16.

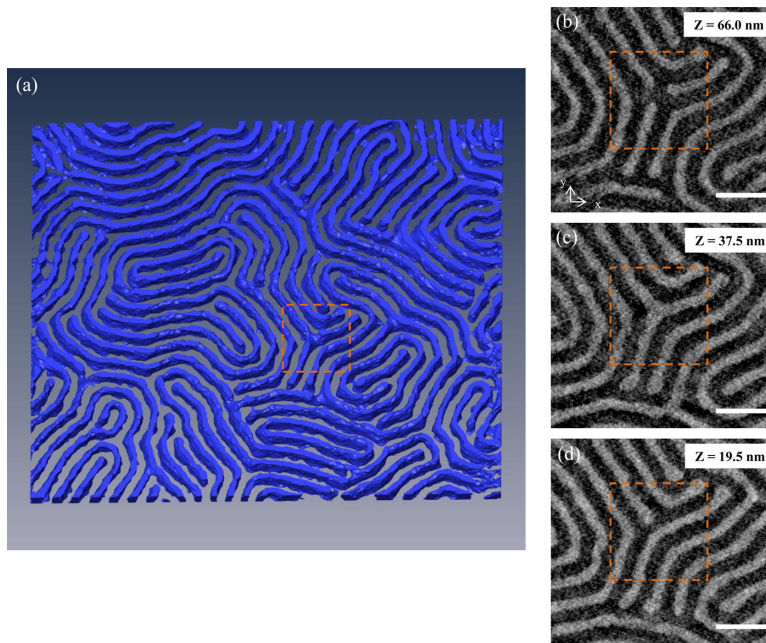


**Figure 2.16:** A. Structure of an 80 nm thick PS-*b*-PMMA/Al<sub>2</sub>O<sub>3</sub> film as a 3D reconstructed volume with PMMA/Al<sub>2</sub>O<sub>3</sub> domains coloured violet and PS domains transparent. Slices of the region marked with the orange selection are shown in B, C and D at Z = 66.0 nm (near top), Z = 37.5 nm (middle), and Z = 19.5 nm (near bottom). Scale bars are 200 nm. Reprinted with permission from ref.<sup>[55]</sup>. Copyright ©2014 American Chemical Society.

### 2.3.9 Tracking Sources of Defects

The ITRS target for production-grade defectivity is approximately 1 defect per 100 cm<sup>2</sup>, or, less than one defect per 100 mm wafer, con-

tributed from the BCP patterning process.<sup>[11]</sup> In order to quantify defects at or approaching this level, sampling is insufficient and whole-wafer characterization<sup>[71]</sup> must be performed. From a whole-wafer characterization, defect counts can be spatially defined, as in Figure 2.17.

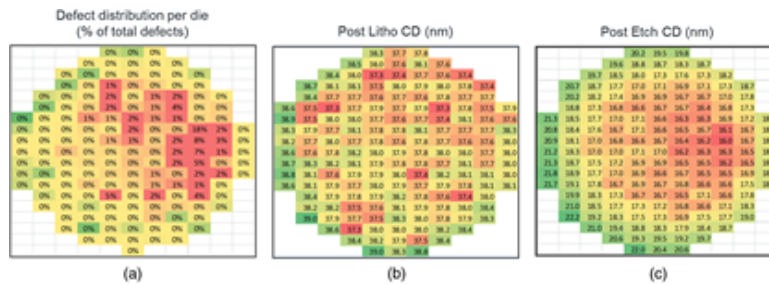


**Figure 2.17:** Whole-wafer defect analysis at various stages in the production process. Reprinted with permission from ref.<sup>[71]</sup>. Copyright ©2014 Society of Photo-Optical Instrumentation Engineers.

Using commercially available tools, defects can be tracked (with coordinates recorded to an accuracy of 1  $\mu\text{m}$ ) through each stage in the lithography process, in order to determine the underlying cause.<sup>[71]</sup> One major issue is the uniformity of the cross-linked polystyrene film which is etched to form a chemoepitaxial surface pattern. Regions left un-coated are termed “white spots” (after the parlance of paper-based lithography); these regions are thus without guiding patterns and thus susceptible to topological defect formation, as demonstrated in Figure 2.18.

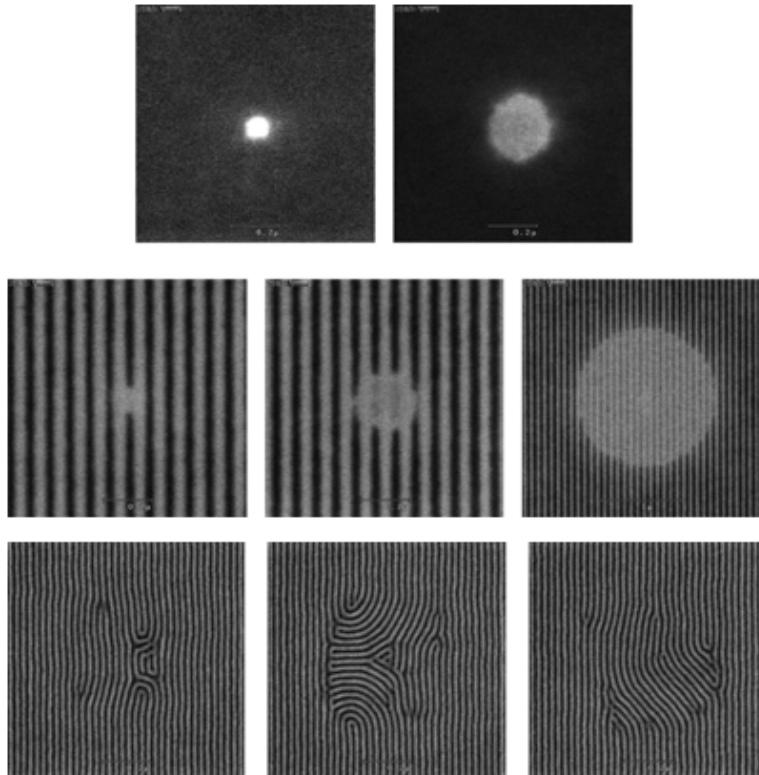


**Figure 2.18:** White spots observed (top 5 images), and defect regions (bottom 3 images) in the completed DSA patterns, resulting from the white spots. Reprinted with permission from ref.<sup>[71]</sup>. Copyright ©2014 Society of Photo-Optical Instrumentation Engineers.

## 2.4 Means of Eliminating Defects

Several methods have been developed for the purpose of eliminating topological defects from block copolymer thin films. These typically function by either applying a force to reorient domains, thus eliminating defects caused by grain boundaries, or by elevating the effective temperature above that required for phase segregation.

### 2.4.1 Thermal Annealing

Thermal annealing involves treating the BCP thin film at elevated temperature - above the glass transition temperatures of each of the blocks - while staying near or below the polymer melting temperature, in order to avoid de-wetting. Temperature increase decreases the Flory-Huggins parameter,  $\chi$ , which controls the segregation of the blocks as previously noted. Block copolymer domains strongly segregate if  $\chi N$  is above 20, the strong-segregation regime. However each Flory-Huggins parameter,  $\chi$  has a temperature dependence according to the equation:

$$\chi = A + \frac{B}{T}$$

Consequently, at some temperature,  $T_{ODT}$ , there will be an order-disorder transition. In solution,  $\chi$  is reduced on account of screening of the

blocks by solvent molecules permeating the domains, hence solvent annealing is effectively reducing the order-disorder transition temperature. For annealing both thermally and with solvent, defect elimination is most favoured at temperatures slightly below  $T_{ODT}$ .

BCP nanodomains are, upon casting a film, kinetically trapped in a local minima and thus unable to attain a lowest-energy configuration without energy input necessary to allow ordering of the nanostructures. Annealing processes, both thermal and solvent-based, provide two fundamental factors necessary for domain reorganization: First, mobility where the polymer chains are provided sufficient kinetic energy (or the energy barriers are decreased) enabling reptation and diffusion of the polymer chain. Second, the annealing process enables the chains to overcome the interaction energy barrier with the other block, which permits chains to transit through repulsive domains, thus permitting redistribution of polymer mass from one nanodomain to another.

Once  $\chi N$  is below  $\sim 20$ , the phases will begin to intermingle. Key to this is a gradual restoration to  $T_g$ , in order to prevent freezing in a non-equilibrium state with increased interfacial width. Methods used range from vacuum ovens, to hotplates, and thermal-energy emitting substrates.<sup>[73,74]</sup> Zone annealing, a technique borrowed from metallurgy, to create single-crystals for applications such as high-speed tur-

bines, has been applied to block copolymers to induce orientation by controlling the melt front within a constrained geometry and/or with thermal gradients.<sup>[74–76]</sup> Prior to thin films, it was applied to bulk BCPs. The thermal gradient creates a "time-dependent mobility gradient",<sup>[77]</sup> results in preferential orientation of domains and consequent reductions in defects arising from grain boundaries. Rates of heating and cooling play important effects,<sup>[74,76]</sup> one of the reasons, in addition to high throughput, why rapid-thermal processing has gained traction.<sup>[78,79]</sup>

## 2.4.2 Solvent Annealing

A room-temperature route to circumventing thermal issues while increasing order is solvent annealing. Solvent annealing for thin films has a long history of application to BCP films.<sup>[80]</sup> Upon exposure to solvent vapour, polymer thin films will swell, as shown in Figure 2.19; the degree depending on the solubility parameters of both solvent and polymer(s) and the vapour pressure. The morphology of the film will depend on the partitioning of solvents in each domain<sup>[81]</sup>, shown in Figure 2.20 as well as the overall thickness<sup>[2]</sup>, as in Figure 2.19. For block copolymers, where the swelling of both blocks is favourable (i.e. non-preferential swelling occurs),  $\chi$  will decrease as both phases become diluted.

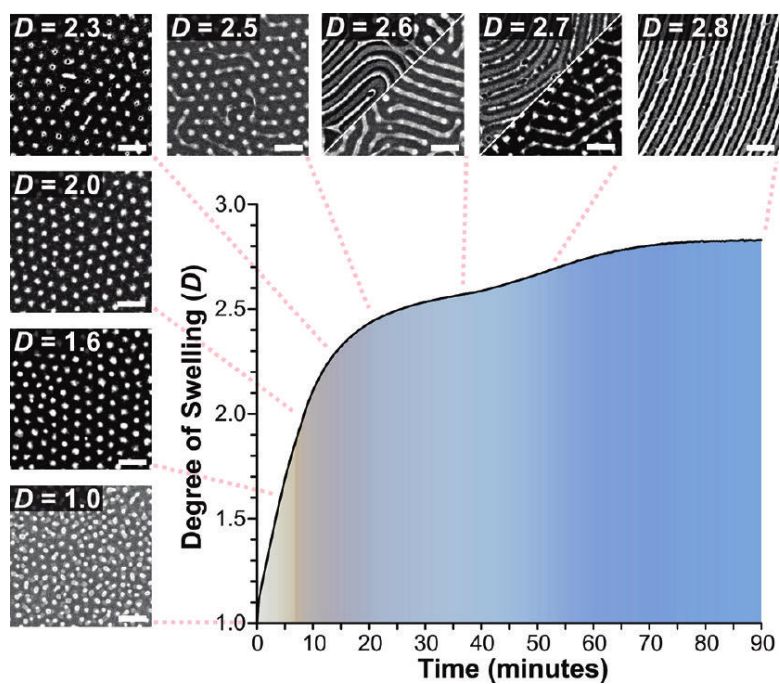


**Figure 2.19:** Effect of degree of swelling on the morphology of features in a PS-*b*-P2VP thin film annealed with a THF-water mixture. Reprinted with permission from ref.<sup>[2]</sup>. Copyright ©2012 American Chemical Society.

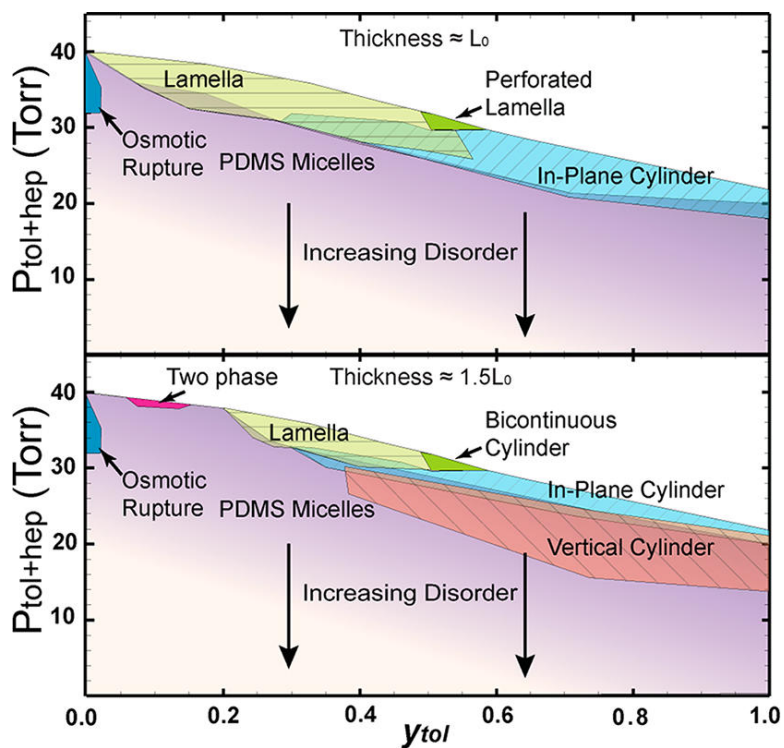


**Figure 2.20:** Experimental phase diagram for PS-*b*-PDMS annealed using heptane and toluene. Reprinted with permission from ref.<sup>[81]</sup>. Copyright ©2012 American Chemical Society.

Annealing with a non-preferential solvent has been demonstrated to be a *viable* route for polymers with high  $N$  - which are applicable to photonics and polarizers. This leads to structures with poorer phase separation and increased interfacial widths, however Ryu et al. have demonstrated that subsequent thermal annealing results in improved phase separation and decreased interfacial widths for high molecular weight PS-*b*-PMMA.<sup>[82]</sup> It may be feasible to introduce an all-solvent version of this low- $\chi$ -anneal  $\langle$  high- $\chi$ -anneal using a mass flow controller (MFC) system to change solvent compositions.<sup>[81,83]</sup> A handful of papers have utilized solvent gas flow systems to control annealing. Gotrik and coworkers introduced a three-component MFC system with streams of toluene/N<sub>2</sub>, heptane/N<sub>2</sub>, and N<sub>2</sub> to control the proportion of two selective solvents and overall vapour pressure.<sup>[81,84]</sup> This gave direct control over the observed morphology in PS-*b*-PDMS (polystyrene-block-polydimethylsiloxane) and maintained a higher  $\chi$  during the annealing process. Thus using a solvent flow system, shown in Figure 2.20, one may be able to switch from a stream of a single, non-selective solvent, to a stream containing two selective solvents, without interruption and without deswelling. Thereby defect elimination would take place first, followed by LER optimization without any trade-off to the defectivity. For this to work, the informed selection of solvents will be important.

One drawback in current applications of solvent annealing is that the majority of papers rely on common laboratory solvents available on hand, instead of other, potentially more appropriate solvents, for both casting and annealing BCP thin films. Toluene, tetrahydrofuran, chloroform, and benzene accounted for 72% of all instances of casting solvent use in a selection of 190 papers employing solvent annealing. Annealing solvents were more varied, however 69% of instances of annealing solvents were from a similar list (toluene, tetrahydrofuran, chloroform, water, benzene, and acetone). Furthermore, attempts at comparing multiple solvents as candidates for annealing are scant in the literature: only 5% of papers examine more than 3 annealing solvents. Analogously to thermal annealing, solvent annealing can be applied in a gradient or directional fashion to create a time-dependent mobility gradient *via* raster scanning<sup>[85]</sup> or directional permeation<sup>[86]</sup>. Moreover, “bulk” vapour phases are not the only means to introduce solvent: diffusion of solvent from a nearby polymer film can be used for “proximity injection”<sup>[87]</sup> or outright immersion in a solvent can be effective.<sup>[54]</sup>

### **2.4.3 Annealing Combinations**

Several approaches exist to combine solvent and thermal annealing processes. Sequential annealing, first with solvent, then thermally has

been shown to produce high quality patterns, even for extremely large BCPs.<sup>[82]</sup> Simultaneous application can also be effective.<sup>[88]</sup> Microwave annealing has utilized a combination of substrate-driven heating<sup>[73]</sup> and solvent vapour to solvothermally anneal BCP thin films.<sup>[20,40]</sup>

Thermal and solvent based annealing methods are not the only means of inducing morphological change and eliminating defects. Electric-fields can induce preferential orientation along the field lines<sup>[56,59,60,89-91]</sup>, which can stabilize a morphology sufficiently to change the  $T_{ODT}$  by 2 celsius.<sup>[60]</sup> Shearing applies a pressure gradient to the film, inducing preferential alignment.<sup>[85,92-94]</sup>

## 2.5 Using and Controlling Defects

While the primary goal presented here is the elimination of defects, they have useful application in their own right. The next step beyond regular arrays of repeating patterns is the formation of irregular, device-oriented structures using BCP self-assembly and lithography. Bends, junctions, and jobs are not BCP equilibrium morphology features, hence controlling features, either graphoepitaxy or chemoepitaxy need to be applied to ensure a favourable configuration and minimum energy of the defect in the desired location. Chemoepitaxy can induce bends set at various angles, demonstrated in Figure 2.21.

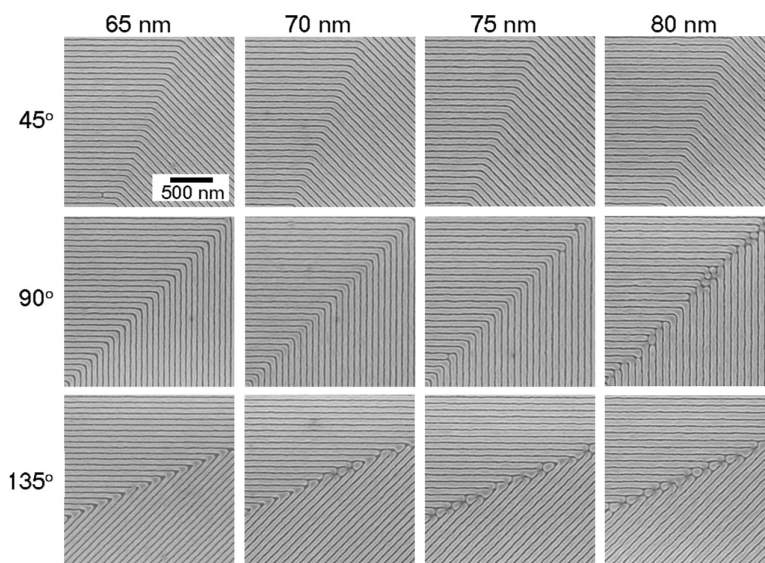


**Figure 2.21:** SEM images of PS-*b*-PMMA/PS/PMMA with a natural period ( $L_B = 70$  nm) blend registered on chemical surface patterns with different periods ( $L_S = 65, 70, 75,$  and  $80$  nm) with bends at  $45, 90,$  and  $135$  degrees. Reprinted with permission from ref.<sup>[95]</sup>. Copyright ©2005 American Association for the Advancement of Science.

Although chemoepitaxy has been the primary method employed to control defect generation, graphoepitaxy can also produce defects in a regular manner. Edge defects in circular confinement can produce a disclination at the centre of the circle,<sup>[96]</sup> while channel tapering can massage disclinations to occur at regular intervals along a tapered channel<sup>[97]</sup>, as shown in Figure 2.22. Precise control of thermally-generated, equilibrium defect structures such as these could be an alternative avenue to patterning functional junctions and terminating lines.

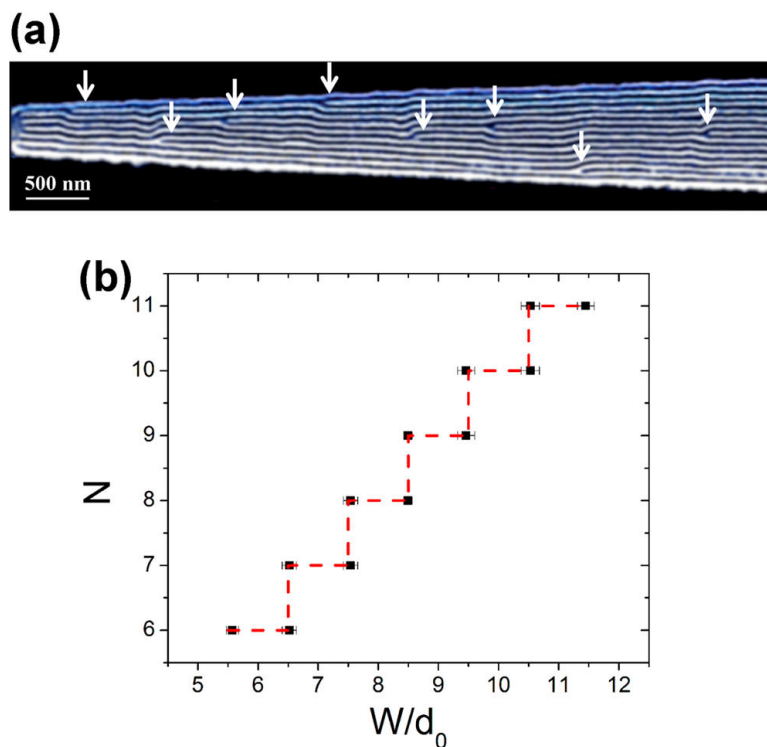


**Figure 2.22:** Disclinations generated at regular intervals along a tapered channel. Reprinted with permission from ref.<sup>[97]</sup>. Copyright ©2014 American Chemical Society.

### 2.5.1 Volume Fraction Modification and Blending

Additions of homopolymers can influence the proportion of line widths, and the flexibility of the system. However the broad region where lamellar is defined as the *most stable* does not preclude a difference in the level of defectivity with greater asymmetry. Similarly, the minimum in defectivity for cylindrical BCP line patterns has not been mapped, which may lead to significant differences in the defect annihilation rates measured for different polymers.

Finally, it has long been a mantra of the block copolymer self-assembly community that low polydispersity is necessary for good pattern formation. The polydispersity index (PDI) is one means of describing the broadness of a molecular weight distribution. It is defined as the ratio of the weight average molecular weight ( $M_w$ ) to the number average molecular weight ( $M_n$ ):

$$M_w = \frac{\sum_i N_i M_i^2}{\sum_i N_i M_i}$$

$$M_n = \frac{\sum_i N_i M_i}{\sum_i N_i}$$

$$PDI = \frac{M_w}{M_n} = \frac{N \sum_i N_i M_i^2}{(\sum_i N_i M_i)^2}$$

As such, the value of the PDI will always be greater than or equal to one, with a value of 1 being a perfectly monodisperse distribution, and larger numbers indicating a nonuniform distribution. It's important

to note that PDI does not completely describe the distribution and that other numeric tools are available for describing the distribution;<sup>[98]</sup> however, for polymers with and blends with similar  $M_w$ , it does offer a point of comparison.

Results from our experiments in controlling line width and spacing using blended pairs of BCPs caught my attention when we attained good patterns while having an overall calculated polydispersity of 2.36, as for the blend of PS(17k)-*b*-P2VP(9.8k) (A) with an equal mass of PS(125k)-*b*-P2VP(58.5k) (D) shown in Figure 2.23. Furthermore, among blends, these possessed the lowest defect density. Others had previously assessed BCP blends and demonstrated self-assembly in bulk up to a maximum polydispersity of 1.8, beyond which separate phases would form. I've begun utilizing ternary blends of homologous block copolymers where the ratio of the two blocks can be kept constant, along with either number-average molecular weight or weight-average molecular weight, while linearly varying polydispersity. This will enable us to tease-apart the influence of molecular weight and to determine whether it is simply an effect where one block acts as a "plasticizer" or whether it has to do with another feature or factor such as film thickness.

Additionally, homopolymers are typically blended with a BCP in order to enhance the flexibility with respect to forming irregular structures.<sup>[95]</sup> Solvent annealing can also be employed to control volume

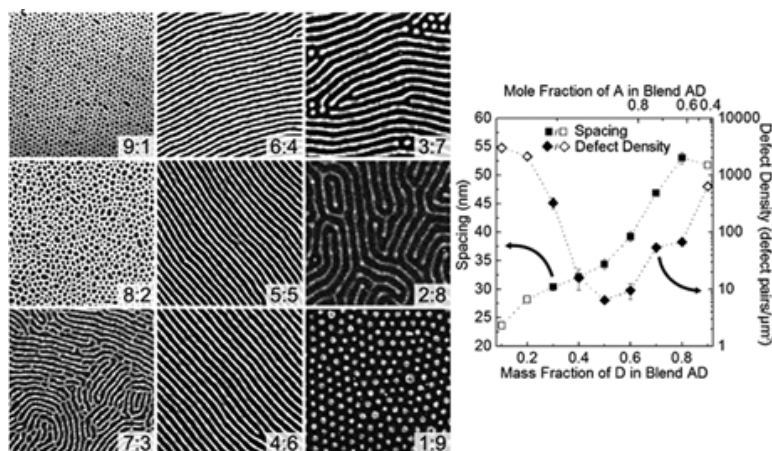


**Figure 2.23:** Equal masses of PS(17k)-*b*-P2VP(9.8k) (A) with PS(125k)-*b*-P2VP(58.5k) (D) are blended create a BCP with a minimum in the concentration of defects. Reprinted with permission from ref.<sup>[20]</sup> Copyright ©2011 American Chemical Society.

fraction in order to specify morphology and to access otherwise unfavourable structures while simultaneously annealing the film.<sup>[2,54,81,83]</sup> Typically experiments studying defects in lamellar-based striped patterns are set up as to provide near-equal volume fractions of each block. It has been noted previously that even for symmetric PS-*b*-PMMA lamellar diblock copolymers, defects may have a preference in one polymer phase over the other. By choosing off-symmetric compositions, these preferences may be further influenced to produce topologically distinct phases, where topological defects (junctions and terminal points) preferentially exist in one phase or the other, resulting in one phase possessing more fully connected networks, as shown in Figure 2.24.<sup>[99]</sup>

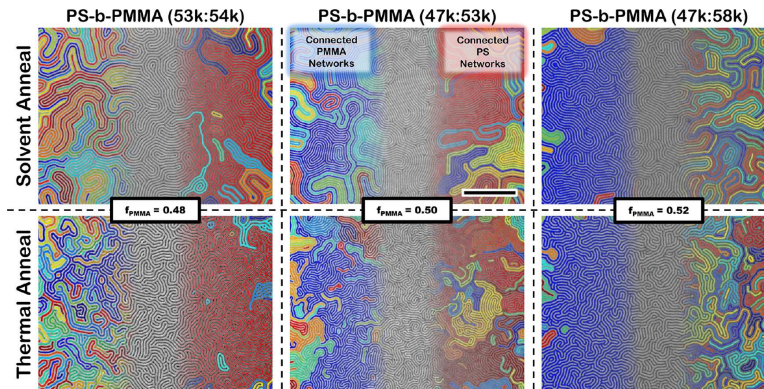


**Figure 2.24:** Topologically distinct lamellar patterns PS-*b*-PMMA showing connected PMMA networks and connected PS networks. Reprinted with permission from ref.<sup>[99]</sup>. Copyright ©2013 American Chemical Society.

## 2.6 Challenges

### 2.6.1 Minimum Level of Defects

The ITRS calls for a maximum of 1 topological defect (pair) per 100 cm<sup>2</sup>,<sup>[11]</sup> or roughly 2 defects on a 6 inch (150 mm) wafer. Such a daunting level of perfection has not yet been achieved,<sup>[70,71]</sup> however the combination of chemoepitaxial patterning with thermal annealing is gradually approaching this level. Annealed PS-*b*-PMMA has brought the level of thermally generated defects to within ~10 defects per 1 cm<sup>2</sup>.<sup>[70]</sup>

While analysis of defects in the ~10000 μm<sup>-2</sup> to ~0.1 μm<sup>-2</sup> regime is feasible through sampling with a relatively small number of SEM im-

ages,<sup>[1]</sup> to find 1 defect pair on a 100 cm<sup>2</sup> wafer would require ~10 billion SEM images, each 10 μm x 10 μm, which is orders of magnitude beyond feasibility for most academic labs, requiring specialized equipment.<sup>[71]</sup>

### **2.6.2 Timescale for Annealing**

A secondary challenge is to attain near-zero defectivity levels within an industrially relevant timescale of < 4 minutes.<sup>[20,40,73,100]</sup> Thus far, microwave annealing has been successful in attaining such times, however other annealing processes are being developed with equal or greater speeds,<sup>[74,76,78,79]</sup> hence the bar continues to be lowered. However for proper annealing

### **2.6.3 Multilayer Structures**

Moving beyond simple monolayer structures, next to nothing is known about the thermodynamics and kinetics of defects in bilayer structures,<sup>[2]</sup> or other morphologies with potential for lithographic application. Bilayer films exhibit a variety of defects, including junctions between layers. Analysis of patterns to obtain physically relevant data is complicated by the potential for features to cross over one another.

## 2.6.4 Flory-Huggins Parameter Trade-offs

As BCPs with larger  $\chi$  values will be required to further shrink feature size, it is important to understand what trade-offs this may have, in particular with reference to defectivity. It has been suggested that higher  $\chi$  may result in defects which are intractable and not amenable through current annealing processes; the result would be a trilemma of defectivity, resolution, and throughput due to slow annealing time.<sup>[101]</sup> However it may be possible to navigate around this by varying the  $\chi$  parameter over the course of the annealing process, as occurs with solvent annealing: solvent annealing has permitted the formation of well defined, low-defect striped patterns for high molecular weight BCPs, which exhibit improved LER upon thermal annealing.<sup>[82]</sup>

Both theoretical calculations and computational modelling of line-edge roughness<sup>[49]</sup> has shown a dependence on the Flory-Huggins parameter, with the  $\chi$  values for the commonly used PS-*b*-PMMA to be a factor of 30 below the necessary minimum of  $\chi \rightarrow 3$ , required to reduce LER. Such high LER however may result in greater thermodynamic stability of defects, leading to difficulty in their elimination. However no systematic, empirical study of the effect of the Flory-Huggins parameter on BCP features, or features templated from BCPs, has been performed, hence theoretical and computational results pointing to its importance, for the stability of dislocations and minimizing LER, require

more substantive investigation. This is understandably difficult, given that the necessary structural changes to the polymer would likely affect many other features of the system.

### **2.6.5 New Topologies and Large BCPs**

In addition to sequential solvent and thermal annealing, large block copolymers present an additional challenge for defectivity.<sup>[82]</sup> The large mass limits diffusion, slowing the defect annihilation process. Some progress may be made using brush BCPs, bearing a branched topology, which do not suffer as linear BCPs from entanglement, which severely limits the rate of annealing.<sup>[102–106]</sup> For BCPs with domains on the order of photonic crystals, near-field polarimetry may be an effective alternative for assessing defectivity.<sup>[107]</sup>

### **2.6.6 Effects of polydispersity on defects**

Polydispersity explored through mean field simulations has been shown to have negligible effect on line-edge roughness.<sup>[108]</sup> For defects, there has been at least one notable example where polydisperse systems were able to attain lower rates of defectivity compared to similar, less polydisperse systems.<sup>[20]</sup>

### **2.6.7 How the deposition method influence the evolution of defects**

It has been demonstrated that the morphology of a film controls the kinetics of solvent vapour uptake for non-selective solvents.<sup>[109]</sup> Hence the initial morphology can play an effect on the evolution of structure. Little has been done to investigate the effect of different initial states, where solvent exposure, dissolved states such as micelles, or pressure gradients regularly influence the initial state of a polymer film.

### **2.6.8 What is the minimum thermodynamic level of defects?**

It remains unclear what the minimum thermodynamic level of defects is. This is complicated in four parts: first, as graphoepitaxy (& chemoepitaxy) is quite effective, we may not be sampling enough. Second, there is a lack of kinetic studies for defect elimination with guiding patterns, and nothing truly bridging the kinetics of unpatterned samples with patterned ones. Optimal methodology remains an open question, and it will certainly depend on the polymer system used. Finally, theory simply does not answer the question. Moreover, if defects are interrelated, the effect of some local anomaly of LER may mani-

fest as an increased favourability of a dislocation or disclination elsewhere.

## 2.7 Additional Open Questions

There remain a number of holes present within the literature regarding studies of defects. Given that BCP structures must be translated to a different material *via etching*, direct imaging of the 3D, and even 2D structure of defects has been difficult. Hence there remains a quest for better techniques for analyzing the true morphology of defects, leaving the question of the exact structure still partially unsolved.

Greater applied, experimental work is required for relating the effects of defects in nanoscale BCP-templated features. While the ITRS has provided structural targets for features such as LER and LWR,<sup>[11]</sup> whether BCPs can meet the exact demands remains unanswered. And ultimately it may come down to whether the device performance can be achieved, and how LER and LWR affect this.

## 2.8 Conclusions

The analysis of defect structures in block copolymer thin films presently remains a maturing praxis, with greater attention paid than ever before. New techniques are available which complement previous methods for defect analysis and quantification, which enable observations of new defect features. For these, best practices need to be developed and widely disseminated, alongside shared tools and open software algorithms, to ensure consistency between results. With the continued advancing front of these techniques, many of the questions pertaining to defects in BCP thin films will soon be addressed.

# 3

## Automated Defect Analysis of Block Copolymer Thin Film Nanopatterns <sup>1</sup>

### 3.1 Introduction

The ability of block copolymers (BCPs) to self-assemble into periodic structures, with periods ranging from 5 nm to well over 100 nm, has

---

<sup>1</sup>Material in this chapter has been published under the CC BY 4.0 License in:

► Murphy, J.N.; Harris, K.D.; Buriak, J.M. "Automated Defect and Correlation Length Analysis of Block Copolymer Thin Film Nanopatterns" *PLoS One* **2015**, 10, 0133088.

prompted investigation into their potential applications for nanopatterning of integrated circuits,<sup>[95,110–112]</sup> bit-patterned media<sup>[22,112–114]</sup> for data storage, optical devices,<sup>[82,115]</sup> tissue interfacing,<sup>[116–118]</sup> and others. Lamellar or cylindrical domains of block copolymers can be used to create linear structures,<sup>[119,120]</sup> both large<sup>[82,103]</sup> and small,<sup>[121]</sup> when confined in one dimension as thin films on substrates with appropriate wetting characteristics.<sup>[31,34,122]</sup> Such patterns can be used as lithographic masks through etching or as scaffolds to create other nanostructured surfaces and materials.<sup>[123,124]</sup>

For application in semiconductor fabrication, the International Technology Roadmap for Semiconductors (ITRS) has, in its Directed Self-Assembly Critical Assessment<sup>[11]</sup> (where the term directed self-assembly is represented by the acronym DSA), identified challenges in 15 metrics, including: Feature sizes of under 10 nm, the ability to “add, exclude or trim individual DSA...features with simple lithography”,<sup>t[11]</sup> a low degree of line edge roughness (LER,  $3\sigma$ ) < 0.6 nm, defect density less than  $0.01 \text{ cm}^{-2}$ , and an annealing time of less than one minute. In addition, surfaces require appropriate wetting characteristics and surface energies in order to enable the process of self-assembly in the desired orientation with respect to the surface plane. These metrics have been correctly identified as challenges as they are daunting goals, but they represent very clear, quantified metrics that need to be attained.

Lacking, however, is a unified method of accurately determining each parameter ‘in the field’, with actual samples of surfaces patterned *via* block copolymer self-assembly (*vide infra*).

Much of the work to optimize BCP DSA has been carried out with a narrow range of polymers, namely polystyrene-*block*-poly(methyl methacrylate) (PS-*b*-PMMA),<sup>[23,95,125]</sup> polystyrene-*block*-polydimethylsiloxane (PS-*b*-PDMS),<sup>[110,126–128]</sup> and polystyrene-*block*-poly(2-vinylpyridine) (PS-*b*-P2VP).<sup>[2,40,116,120]</sup> Each of these polymers possesses favorable characteristics for nanopatterning, but many other block copolymer systems still remain to be designed, synthesized, and investigated, as the exploration of the space of possible systems, including structural classes and chemical motifs (monomers) is nowhere near complete<sup>[34,121,129–133]</sup> Dimensions of polymer-space available for exploration include triblock, comb, or other architectures<sup>[131–134]</sup> and topologies,<sup>[130]</sup> alternate chemical moieties such as silicon-containing polymers other than PDMS,<sup>[135,136]</sup> and oxygen-rich groups such as oligosaccharides and poly(lactic acid);<sup>[121]</sup> or tailoring polydispersity to modify morphological stability and domain sizes.<sup>[137–139]</sup> A consequence is that there remains much to be explored synthetically in order to optimize pattern formation, etch selectivity (or resistivity), polymer reactivity, surface energies, Flory-Huggins parameters,<sup>[140]</sup> LER, and annealing conditions. In particular, there is a persistent analytical barrier that synthetic chemists must overcome in

order to readily determine whether their polymeric creations may be applicable to novel DSA applications: they require access to a toolbox capable of analyzing critical features such as the defect density, correlation lengths, and LER of their patterns in order to determine whether their block copolymers have promise. The dearth of accessible tools remains a significant obstacle for the area of directed self-assembly.

Defects themselves also warrant a more in-depth investigation, which can only be achieved by studying defects “in the wild”, in the actual nanopatterns as they progress through various stages of annealing. While simulations can find matches to thin film defect structures,<sup>[141–143]</sup> automated analyses of defects in block copolymer thin films in an experimental setting allow access to statistical data about the frequency and distribution of various defects. Statistical data is generally inaccessible *via* modeling due to computational limits for defects beyond the simplest examples.<sup>[141]</sup> Furthermore, for cylindrical block copolymer domains, defects do not always have liquid crystal analogues,<sup>[142]</sup> rendering past defect-detection methods, originally developed for patterns formed in liquid crystal thin films,<sup>[144]</sup> inappropriate. Hence identification of structures beyond simple counting of disclinations and dislocations<sup>[44]</sup> would be advantageous.

Computerized analyses that are widely used to study images of BCP patterns include to determination of periodicity using azimuthally av-

eraged fast Fourier transform (FFT) images,<sup>[63]</sup> image filtering and regional analysis of domain orientation using FFTs<sup>[145]</sup> and defect density measurements. Less commonly measured is LER.<sup>[45]</sup> Rarely, however, are more than one or two methods packaged together in a published work, which leaves unanswered questions since there is typically a trade-off between factors such as defect density, orientation, nanostructure spacing, line-width, line-width roughness (LWR), LER, and correlation length (*i.e.*, grain size). Initially, in the course of investigating the process of microwave annealing of block copolymer thin films, we developed an in-house algorithm to quantify defects in block copolymer thin films, utilizing particle analysis and skeletonization to identify defect features.<sup>[20,40,73]</sup> Later, while analyzing density doubled cylindrical line patterns, a separate process for measuring the LER was created, which was limited to analyzing nearly-straight segments of nanowire structures.<sup>[2]</sup>

To remedy the lack of a readily available and straightforward analytical tool, we developed an accessible and free-to-download application for analyzing the defects in BCP thin films using a combined particle and skeleton based analysis of the pattern, called Automated Defect Analysis of Block Copolymers, or *ADAblock* for short (links to the tool provided in the Supplementary Materials). The application was constructed using the ImageJ platform, a free, open-source, Java-based im-

age analysis program, which provides a full and easy-to-understand output.<sup>[146,147]</sup> The tool identifies not only the type(s) of defects found in a sample, but also quantifies the density of defects over a range of length scales, accompanied by additional information regarding LER and LWR, as well as an alternate means of accessing the correlation length. In this work, we screened the *ADABlock* application against a range of nanopatterns prepared *via* block copolymer self-assembly and show the effects of polymer molecular weight on the defect densities of self-assembled BCP films. Additionally, we demonstrate how *ADABlock* can simultaneously track LER, defects, and correlation lengths. To our knowledge, no previous work analyzing 2D block copolymer line patterns has brought together data on defects, LER, LWR, and correlation lengths into one application or analysis. We believe that this omission is likely due, in part, to the lack of readily available, widely applicable, easy-to-use tools for analysis, and on occasion, may be a result of selection of the ‘makes-it-look-best metric’, rather than a complete description of pattern quality over larger areas of the sample. In this chapter, we show how such data can ideally be combined to better describe line patterns derived from BCP assembly in thin films. Images can be deceiving, and we hope that *ADABlock* will assist researchers in avoiding pitfalls resulting from performing incomplete defect density analyses.

## 3.2 Results and Discussion

Examples of four different nanopatterns derived from BCP self-assembled templates are shown in Figure 3.1. The patterns have been converted into easily visible platinum lines through a well-described platinization of three different PS-*b*-P2VP BCPs;<sup>[2,40,120]</sup> the Pt nanolines are derived from the P2VP blocks. Although these scanning electron micrographs (SEMs) are similar in appearance, each is subtly different, and thus the question to be posed is how to distinguish one pattern from another and to determine which is more defective. As shown in Figure 3.1 and Table 3.1, the pattern in 1A has 30% more defect pairs than the patterns in Figure 3.1C or 3.1D. Moreover, the correlation length of 1B is shorter than any of the others (in part due to the shorter period). Additionally, in terms of the line edge roughness (LER), they all appear at first glance to be quite smooth, but the measured roughness of these lines, as summarized in Table 1, would put them out of contention for ITRS targets. With respect to LER, the values of ~4 nm are significantly larger than the maximum 0.6 nm suggested,<sup>[11]</sup> but the feature size here is also ~2x larger than the 10 nm features sought by the ITRS; similarly, the defect density is ~10,000 times higher than ITRS goals. However the present samples lack any features to guide alignment, as is the case with graphoepitaxy, which assists in significantly lowering the observed defect density.<sup>[40,70,143]</sup>

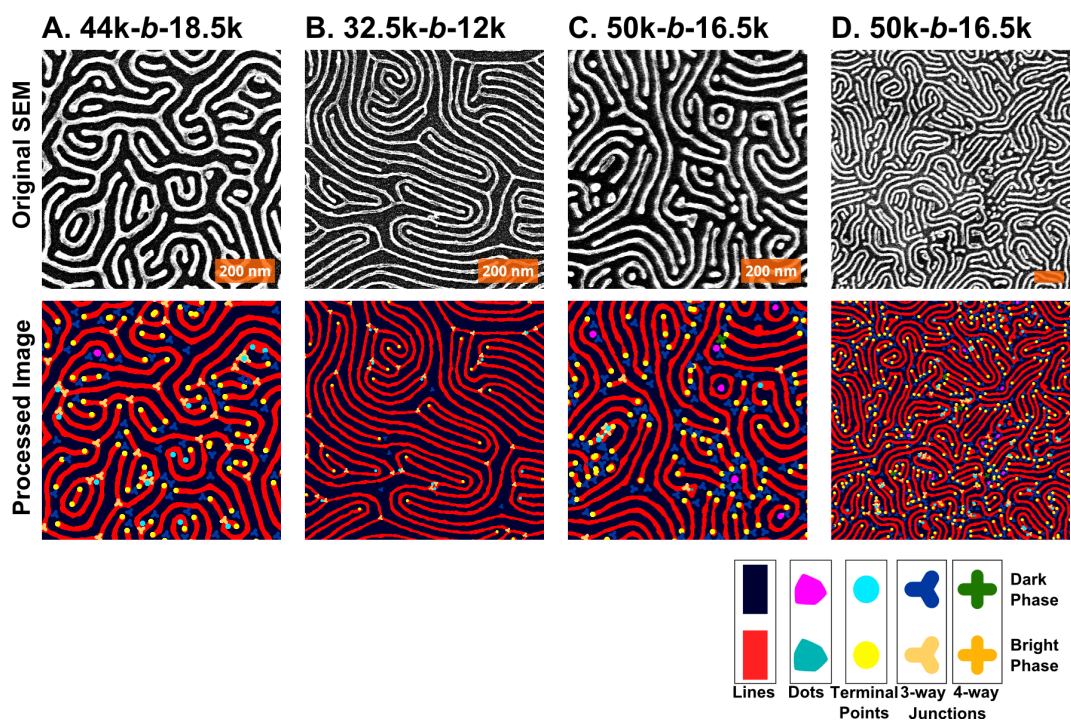


**Figure 3.1:** Sample SEM images for Pt line patterns derived from 3 different PS-*b*-P2VP polymers. The following molecular weights correspond to the polystyrene-*block*-poly(2-vinylpyridine) block copolymers used: (A) 44k-*b*-18.5k, (B) 32.5k-*b*-12k, (C & D) 50k-*b*-16.5k. Units are in kg/mol, hence 44k is 44 kg/mol. The first three images are taken at 50,000x magnification; the fourth at 25,000x. The orange scale bars all represent 200 nm.

Img	Mag	Polymer	Period	LER	LWR	$\kappa$	Defect Density
A	50k	44k- <i>b</i> -18.5k	41.4	4.2	6.8	41.5	140
B	50k	32.5k- <i>b</i> -12k	29.9	3.3	5.1	93.7	76
C	50k	50k- <i>b</i> -16.5k	38.5	5.3	9.2	70.1	187
D	25k	50k- <i>b</i> -16.5k	38.6	6.7	10.2	73.8	174

**Table 3.1:** Data for each of the four panels in Figure 1, including period, LER, LWR, correlation length ( $\kappa$ ), and defect density. Units are in nm, except for defect density, which is given as defect pairs $\cdot\mu\text{m}^{-2}$ . Line-edge roughness (LER) is given as three times the standard deviation ( $3\sigma$ ) in the edge position, relative to the center of the line; line-width roughness (LWR) is three times the standard deviation ( $3\sigma$ ) in the width of the line.

### 3.3 Outline of the Analysis

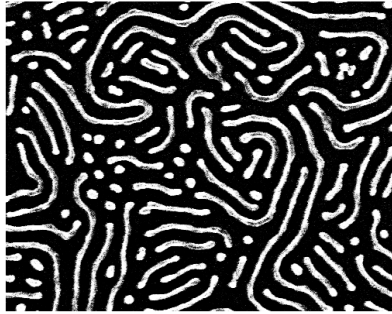
The analysis is briefly outlined in Figure 3.2, breaking down the *AD-Ablock* sequence into eight broad stages. Details of each stage are provided in detail, *vide infra*. The first stage is simply the representation of the original SEM image, which must be smoothed to reduce noise, while retaining all features of interest. Next, the smoothed image is thresholded, in order to produce a binary image from which data like area, perimeter, and shape can be determined. Next, the period and line-widths are calculated, followed by particle analysis to determine the shapes of the binary objects and to classify line and dot

features. The line features identified are then isolated and converted into a skeleton, from which the connectivity can be determined. This resulting structure is groomed and then analyzed for defects. Lastly, the data is recorded and confirmation images are produced for user inspection. All stages noted in the text correspond to the stages represented diagrammatically in Figure 3.2.

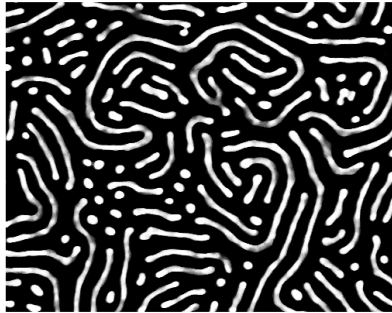
### **3.3.1 Stages 1 and 2: Input of original image and smoothing**

In order to extract information regarding defect density and LER (above, Table 1), a number of factors must be taken into account. Starting with the image itself, basic parameters must be adapted to (1) the image resolution [for instance, determination of how many nanometres are represented by each pixel (nm/px)]; (2) the contrast of the image, which can vary considerably image-to-image and instrument-to-instrument; (3) image noise, which creates artifacts not inherent to the actual structure under investigation; and (4) the period and line-width of the block copolymer. Given the nature of block copolymer patterns typically observed, certain presumptions about the structures observed within the images can be made. To begin, predominant structures within a given image are primarily limited to dots, lines, and meshes. Classification

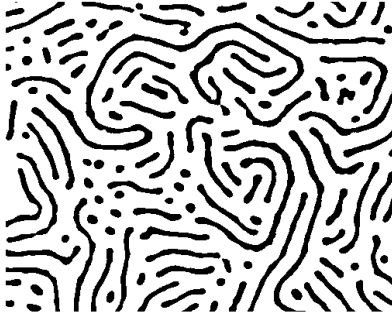
1. Original Image



2. Smoothing



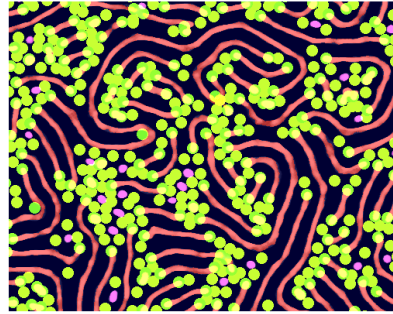
3. Threshold to Binary



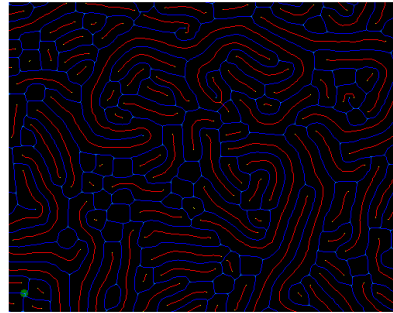
4. Obtain Linewidths



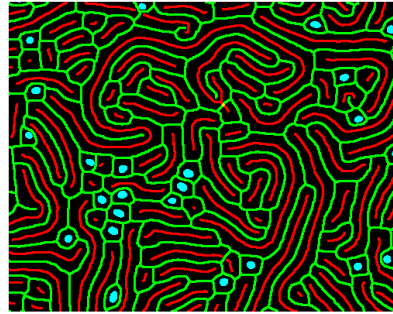
8. Draw Output Defects



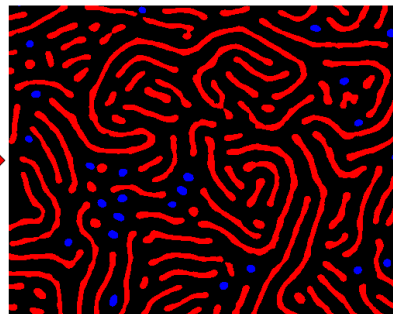
7. Groom + Analyze



6. Skeletonize Lines



5. Particle Analysis



into the basic families of structures in turn constrains certain shape characteristics for the features. Additionally, the period can be defined for a relatively narrow range (*e.g.* 20 to 40 nm for the samples described here, but modifiable for a given system), as block copolymer samples for a given image data set can be manually selected to those having similar period values. As preliminary background data, the period of a pattern can be obtained *via* azimuthal averaging of the image's fast Fourier transform before application of *ADABlock*.<sup>[63]</sup> The first item, the image resolution, is frequently embedded within the image's metadata and hence can be called by the program or input by the operator. The preponderance of our BCP pattern images were obtained using a Hitachi S4800 scanning electron microscope (SEM), which provided information in a legend at the bottom of the image; the consistency of this feature also provided a means for automated

---

**Figure 3.2 (preceding page):** *A brief visual outline of the analysis undertaken by the ADABlock application, broken into 8 major stages in sequential order. (1) The original SEM image; (2) Smoothing of the image to reduce noise; (3) Thresholding the image to produce a binary image suitable for particle analysis; (4) Analysis of period and line-widths in order to set parameters in subsequent analyses; (5) Particle analysis of the binary image to find lines and dots; (6) Skeletonization of the lines; (7) Grooming and analysis of the skeletons; and (8) Compiling visual and other data files for output.*

extraction of resolution parameters.

Combined with its high resolution and high throughput, SEM can be the ideal imaging tool for BCPs, although it does have some drawbacks: For our work, smoothing was necessary due to random noise, charging effects, and edge effects. In the case of SEM images, edges can possess enhanced brightness,<sup>[2,20,40,120]</sup> and white noise results in speckling of the image with bright and dark pixels. Without some smoothing, such salt-and-pepper noise can result in unwanted extra features. SEM owes much of its brilliance to edge effects, which result in objects protruding from the surface (such as Pt nanowires on Si) appearing much brighter than surrounding substrate.<sup>[2,20,40,120]</sup> Typically, smoothing images involves trial-and-error, but linking the smoothing to the period of the pattern and the image resolution gives consistent results: Gaussian and/or median filtering are automatically applied with filter radii calculated in proportion to the period of the pattern to avoid under- and over-smoothing. Median filtering typically is best, as it can preserve and even enhance the structure of the line pattern, as shown in Figure 3.3.

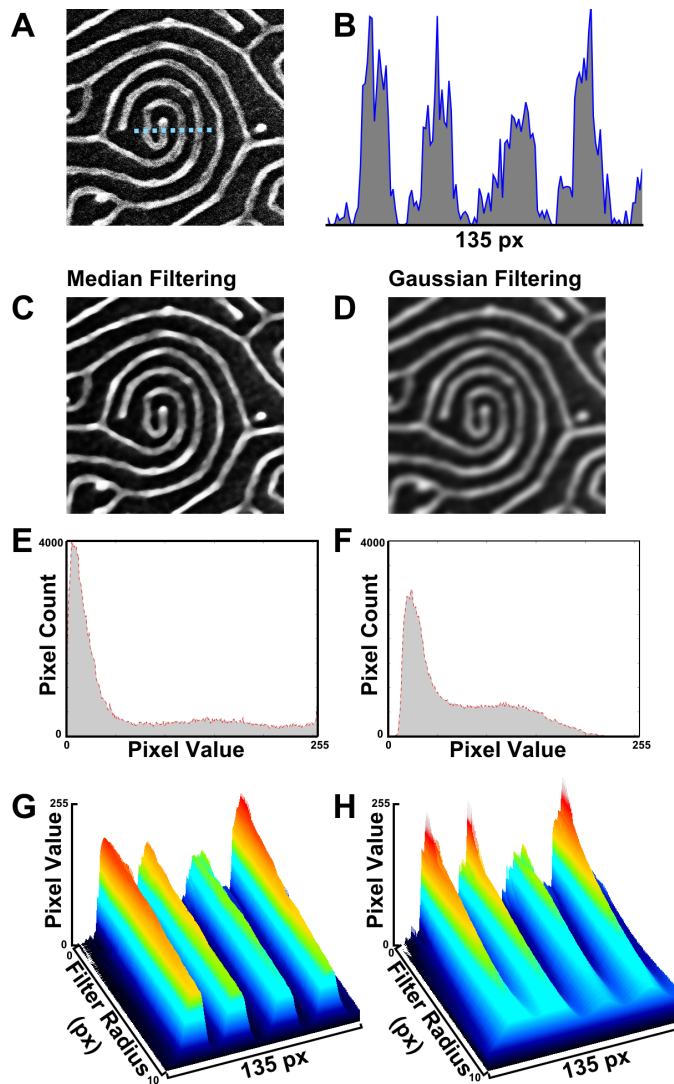


**Figure 3.3:** Median filtering and Gaussian filtering used to reduce noise. (A) Sample image with blue dotted line of (B) intensity profile. The left series (C,E,G) shows the effect of a median filter; the right series (D,F,H) shows the effect of a Gaussian filter. (C,D) Each filter applied at a 5-pixel radius. (E,F) Histograms of each filtered image. (G,H) The smoothing observed for filtering in a range of 0 to 10 pixels, shown in series: (H) Gaussian-filtered profile loses contrast more quickly than (G) the median-filtered profile.

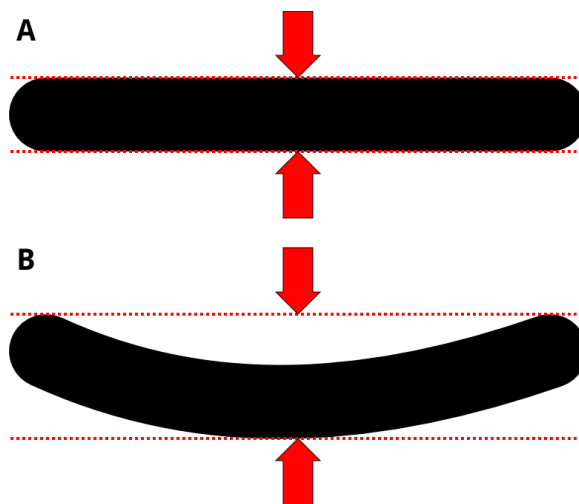
### 3.3.2 Stage 3: Threshold to binary

In order to analyze the pattern, the two phases, each corresponding to one of the blocks, must be clearly identified and separated by thresholding. This assigns each feature in the image to one of the two phases, referred to herein as positive (*i.e.* bright) and negative (dark). Contrast enhancement and thresholding typically requires manual intervention as well. For SEM and atomic force microscopy (AFM) images, which are typically used for block copolymer thin films and patterns, however, a bimodal histogram is either typical or attainable given the nature of the pattern. Such a bimodal histogram can occur either globally (*i.e.*, over the whole image) or locally (over smaller sub-regions); a suitable thresholding filter can be applied on either scale. Several “auto-local” thresholding plugins are available for ImageJ; analysis of our images typically works best utilizing an auto-local threshold which applies Otsu’s clustering method<sup>[148]</sup> locally across the image, however, other thresholds implemented in ImageJ are available options.<sup>[149]</sup> When the surface is not uniformly covered by features (*e.g.* featureless regions), however, automated thresholding can result in additional artifacts, hence subsequent steps are taken to remove noise and incorrectly phased features.

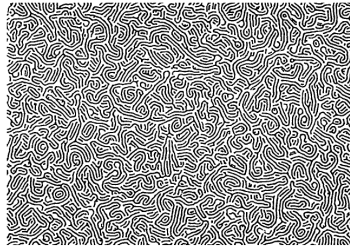
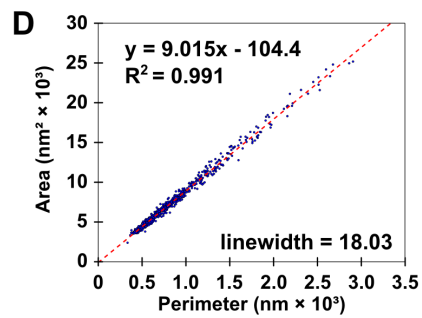
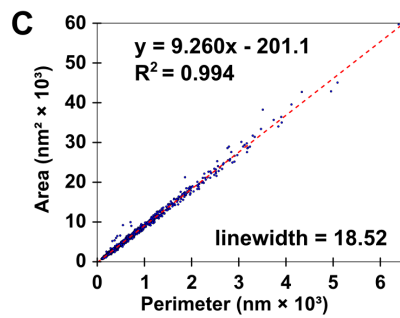
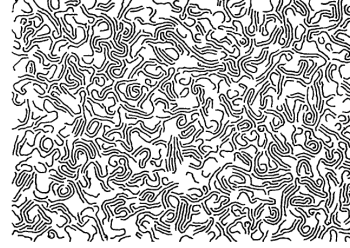
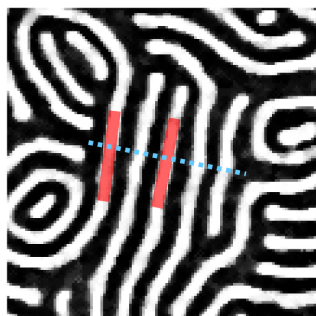
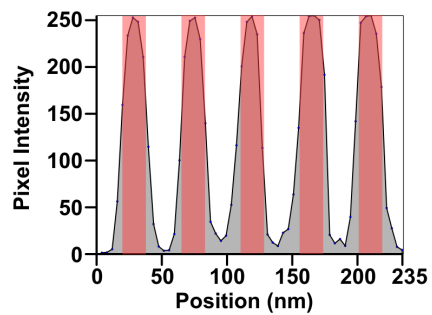
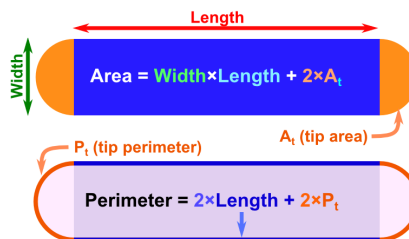
### 3.3.3 Stage 4: Initial Line-Width Analysis

The first pieces of data that must be determined are the dimensions. While period can be readily and automatically measured from azimuthally averaged FFT patterns,<sup>[63]</sup> line-widths and spacings cannot be derived directly from the image of the BCP nanopattern. Profile plots can make for easy manual measurement of these features when patterns are regular and aligned, but that is not always the case. Knowledge of the dimensions is useful, even necessary, in contexts where the pattern is poorly ordered. Particle analysis can measure the area and perimeter of each particle accurately. While Feret measurements (See Figure 3.4) work for simple particles, the tortuous nature of BCP “lines” calls for more nuanced measurement. Imagine a spaghetti noodle shape confined in 2D; there exists a relationship between the perimeter of the noodle’s edge and the area covered by the noodle. Using these easily measurable geometric quantities—particle area and perimeter—the width of lines can be calculated, straightness and degree of branching notwithstanding. Provided there are enough lines available, the particle area plotted as a function of perimeter is linear as shown in Figure 3.5; the slope of the plot is half of the width of the line.

For lines without junctions and only uniform tips, perimeter,  $P$ , can be broken into



**Figure 3.4:** Feret measurement for curved objects. (A) ImageJ can measure the calliper width of objects (shown by the arrows), however only using a MinFeret measurement, which is obtained using a rotating callipers method of rotation the objects perimeter to find the minimum height occupied by the selection. (B) For curved or bent line objects, this would result in a width greater than the line-width, thus making this method inapplicable to highly disordered block copolymer systems.

**A** Original Binary Image**B** Dots & Junctions Removed**E** Profile Line on Greyscale**F** Calculated Line Width on Binary**G** Profile Intensity Plot**H** Line Shape Model

$$P = 2P_t + 2L$$

where  $P_t$  is the perimeter of each tip region (see Figure 3.5H) and  $L$  is the length of the main portion of the line. The area can be calculated similarly

$$A = 2A_t + wL$$

where  $w$  is the width and  $A_t$  is the area of the line's tip region. Area as a function of perimeter can be calculated by substituting

$$L = \frac{P - 2P_t}{2}$$

into the area equation, giving

$$A(P) = 2A_t + \frac{w}{2}(P - 2P_t)$$

$$A(P) = \frac{w}{2}P + 2A_t - wP_t$$

As previously stated, the slope is  $0.5w$ . For patterns where junctions

---

**Figure 3.5 (preceding page):** Process for determining line width and period directly from binary patterns. (A) Unmodified binary image of platinized PS(50k)-b-P2VP(16.5k) and (B) simplified binary image; (C) fit of particle area as a function of perimeter for the unmodified image and (D) fit for the simplified image. (E) Demonstration that a fit of 18 nm for line-width is reasonable for the filtered greyscale image, (F) the thresholded binary image, and (G) a profile of the filtered image. (H) Line diagram showing the relationship between particle area, perimeter, and length.

rather than terminal points are predominant,  $P_t$  becomes zero, and the intercept is positive (due to an additional area term derived from the junction). In practice the contribution of the ends (thus intercepts) is negligible relative to the segment lengths ( $L \gg w$ ) for images with junctions. With exclusively semicircular terminal points or triangular junctions, one would expect intercepts of  $0.785w^2$  and  $0.289w^2$  respectively. (See SI for calculation.)

Intermediate combinations can be avoided by temporarily excluding junctions and breaking down the binary pattern into smaller, junctionless particles, as shown in Figure 3.5B. By excluding the junctions, along with excessively small particles and sections of particles on the edge, a better fit can be obtained, providing a better estimate of the line-width. (See Fig. S11 for a schematic depiction of how junction exclusion achieves this.) The value of the intercept in Figure 3.5A is given as approximately  $-200 \text{ nm}^2$ , which is reasonably close to the predicted value of  $-250 \text{ nm}^2$ , detailed in Appendix A.

Repeating the process for the negative phase, separately, gives a measure of the spacing between lines. Summing the two measurements to approximate the period has, in most cases, been found to come within 5% of the period measured by FFT, usually slightly greater. It appears that this discrepancy may be due, in part, to the particle perimeters being larger than non-discrete analogues, and also due to the approxi-

mations made herein. Alternatively, knowledge of the line-width and the period would give the line spacing by difference.

### **3.3.4 Stage 5: Particle analysis**

In the course of annealing spin-coated BCP thin films, the pattern may evolve from a dot pattern, or similarly disconnected collection of features, into an array of lines, with numerous defect-rich intermediate states. The binary image can be analyzed using ImageJ's built-in particle analysis routine to determine characteristics of particle size and shape descriptors such as circularity and Feret measurements, mean pixel values, and relationships to the image boundary for each feature. Particle analysis is done separately for the positive and negative phases in order to access all the features. Particle analysis data is then used to separate dots (or other objects), which cannot be accurately treated as lines, and identifies them as a specific type of defect. It can also provide information on the evolution of particles in the course of the annealing process (*e.g.* increases in the average size or length of lines). Moreover, the creation of a binary pattern further enables distinction between noise and misclassified particles.

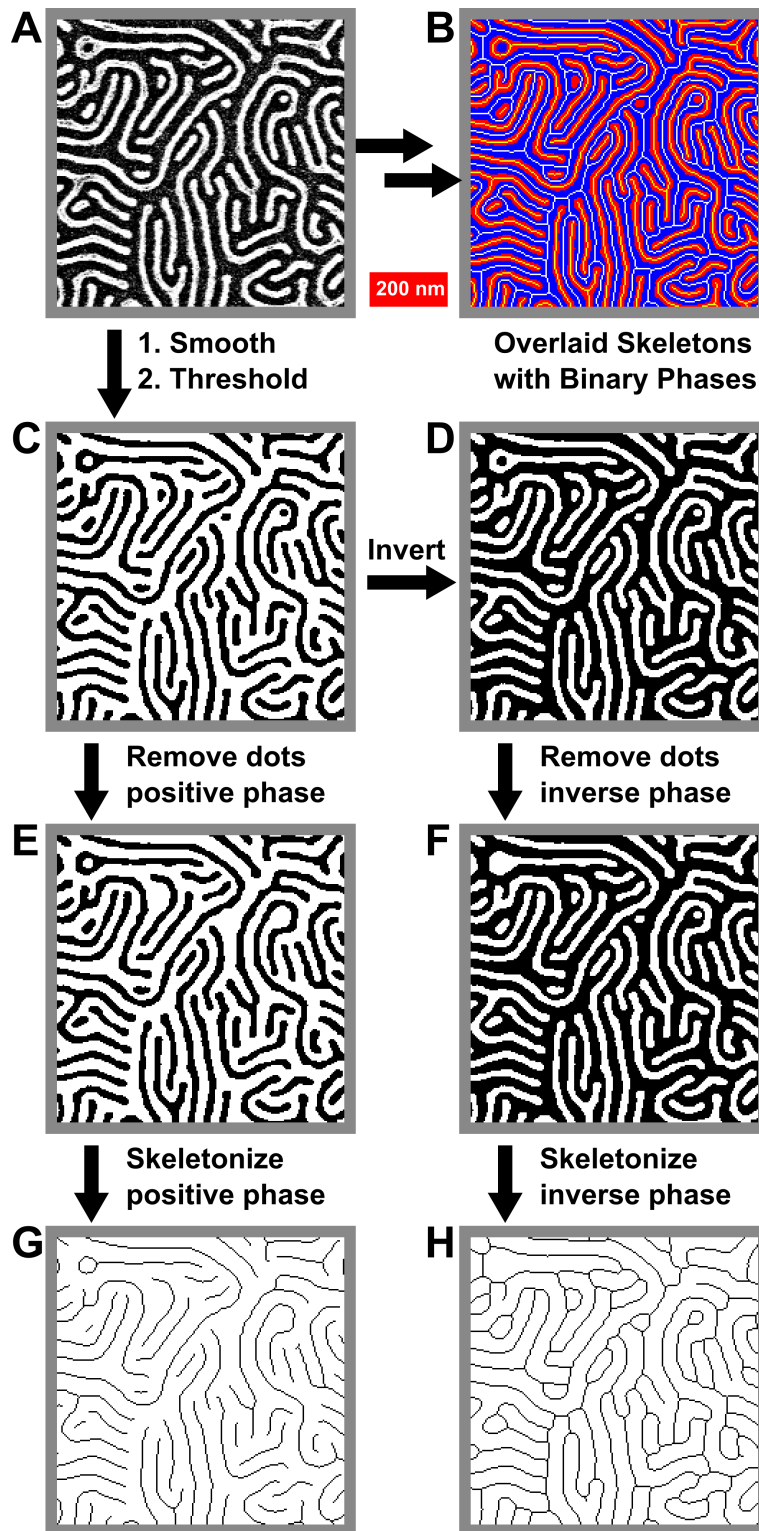
### 3.3.5 Stage 6: Skeletonization

The most effective means to analyze the topology of lines and meshes is *via* analysing the connectivity of the pattern by creating a skeleton of it. Skeletonization reduces lines or meshes to binary objects which maintains the connectivity of the original by “thinning” the pattern to create a simplified, single-pixel-wide version of the shape, suitable for pixel-by-pixel analysis. Skeletonization algorithms and skeleton analysis has been widely used in other fields to study the topology of structures, from text recognition algorithms in computer science to numerous subfields in biology, including bone analysis (“bonej”),<sup>[150]</sup> and studying the structure of neurons, as well as for the recognition of typographic characters. In all cases, skeletonization is used to simplify collections of interconnected shapes and objects into networks to study their properties. Although other algorithms do exist, the default technique is implemented in ImageJ:<sup>[151]</sup> the skeletonize function in ImageJ uses a lookup table to progressively thin the structure based on each pixel’s 3x3 neighbourhood, leaving a 1-pixel wide topological skeleton.<sup>[151]</sup> At least two other groups have applied skeletonization as a means to interpret BCP thin film patterns.<sup>[39,41]</sup> Rehse and coworkers utilized skeletonization of one phase of the polymer pattern to study frame-to-frame correlations between junctions as a measure of BCP dynamics;<sup>[39]</sup> their work followed that of Scherdel<sup>[41]</sup> and Vigild<sup>[42]</sup> who

used 3D interpenetrating skeletons to describe gyroidal phases.

The skeletonization process itself is quite straightforward, as shown in Figure 3.6: to skeletonize a binary image (Figure 3.6C), first dots are removed (Figure 3.6E), leaving only line features, then the image is thinned as described above (Figure 3.6G). It is important to skeletonize both phases of the image, so the original binary image is then inverted (Figure 3.6D), dots from the negative phase are removed (Figure 3.6F), and the inverted image skeletonized (Figure 3.6F). Overlaying the skeletons with the binary images (Figure 3.6B) shows that skeletonization indeed preserves the connectivity found in the original image (Figure 3.6A).

In order to actually access the defects in striped BCP patterns, it is necessary to investigate each phase separately, thus requiring parallel particle analysis and skeletonization of each phase. It is worth noting that for BCPs, certain kinds of defects will prefer one phase to the other, resulting in a surplus of terminal points or junctions in either phase. This tends to limit the frequency of spatially paired defects. Figure 3.7 shows some examples of this effect. In the images on the left of Figure 3.7B, there are ample junctions in the positive phase; in the images on the right, there are almost no junctions in the positive phase, despite having more defects overall. Similarly in Figure 3.7C, there is a greater proportion of terminals in the negative phase than in the correspond-



ing image on the right side. Such features contribute to the topology of the pattern, which can be affected by the means of annealing.<sup>[99]</sup>

### 3.3.6 Stage 7: Groom and analyze

This stage is the most complicated, and it is divided up into separate sections, (a)-(d) based upon the type of analysis.

#### Locating Defects

The ideal, defect-free line pattern derived from lamellar or cylindrical domains of block copolymers, consists of perfectly parallel straight lines extending across the entire substrate without interruption, as by breaks or junctions in the lines. It is with respect to this ideal that topological defects are defined. The analogy between block copolymers and liquid crystals (nematic and lyotropic phases in particular)

---

**Figure 3.6 (preceding page):** Process for the skeletonization of both positive and negative phases of a binary image. (A) Original image. (B) Overlay of binary and skeletonised images showing retained connectivity. (C) Binary image. (D) Inverted binary image. (E) and (F) Processed images (C) and (D), with dots in respective phases removed. (G) and (H) Skeleton images derived from (E) and (F). Images are all 735 nm × 735 nm.

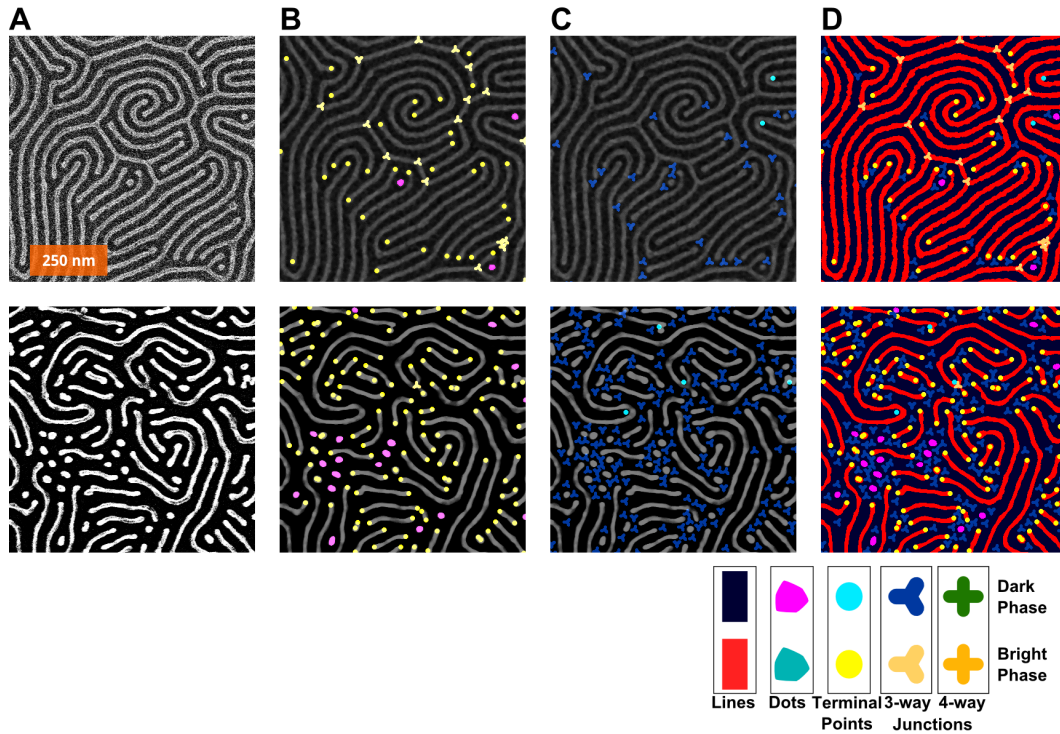


**Figure 3.7:** How the defects, depending on phase (bright = “positive”; dark = “negative”), tend to be of different types. Analysis of two images are shown in parallel with corresponding images in two columns. (A) The original images. (B) Defects in the positive phase marked. (C) Defects in the negative phase marked. (D) All defects. Legend at the bottom shows colours and shapes used for each feature: Bright phase: red lines, teal dots, yellow circles at terminal points, and 3- and 4-connected junctions. Dark phase: navy blue lines, magenta dots, aqua terminal points, and 3- and 4-connected junctions represented by shapes with an equal number of branches.

inspired previous defect analyses<sup>[152]</sup> utilizing winding numbers to identify and measure topological defects. While this does work in principle, and many previous analyses have utilized it and other defect-detection methods,<sup>[39,44]</sup> these methods typically are published without full working details or code. Kléman suggested in 1983 that defects in two-dimensional line patterns could be simplified to junctions, terminal points, and dots, shown in Figure 3.8, rather than the more conventional approach using winding numbers to determine the type of defect.<sup>[43]</sup> While such methods correctly describe the type of defect,<sup>[44]</sup> high levels of defects and variability of the patterns, including variations in line-width (or LER) can make it difficult to correctly identify and quantify defects. One author noted an order of magnitude change in the density of defects for one particular image depending on the amount of Gaussian filtering applied; the filtering parameters ultimately selected appeared to be arbitrary.<sup>[144]</sup> Furthermore, images depicting disclinations and dislocations suggest imprecision in the identification of closely associated dislocations.<sup>[44]</sup> Moreover, while such methods provide the magnitude of each defect, they do not provide information about the connectivity of defects or orientation of surrounding features.

Many frequently encountered defect structures are not isolated dislocations (junction-terminal point pairs immediately adjacent) or discli-

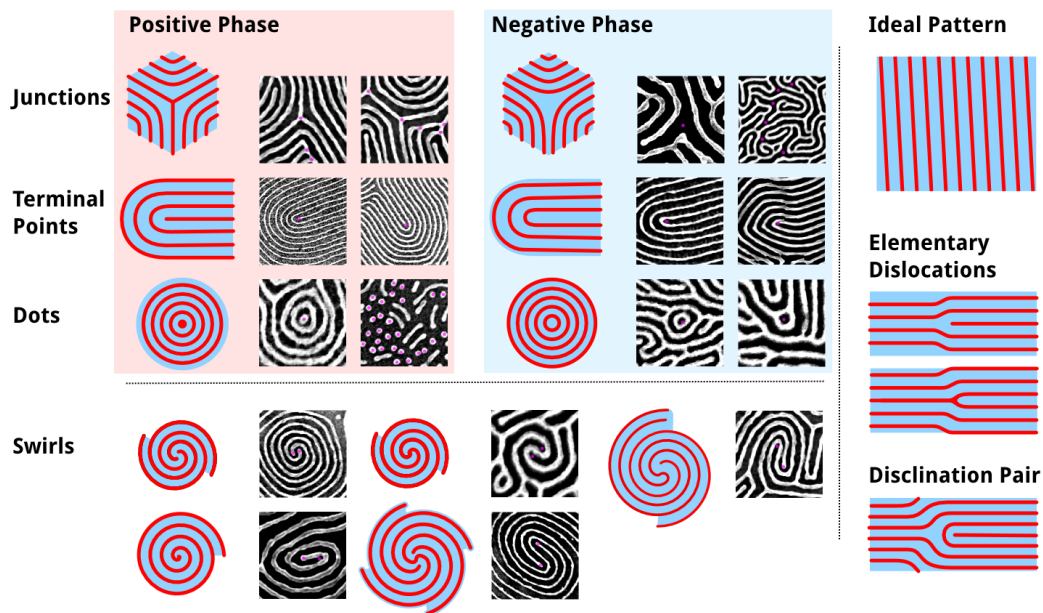


**Figure 3.8:** Table of topological defect components typically found in BCP thin film nanopatterns. Shown are each major type of component defect, as exists in either the positive (e.g. P2VP) phase or the negative (e.g. PS) phase. For each, 3-branch junctions, terminal points, and dots, examples are given with defects highlighted by a magenta dot. This analysis is done relative to an ideal striped pattern without any interrupting features, save for the edge of the image.

nations (either terminal points or junctions), but are part of more complex defect structures. These structures can be broken down into component dots, junctions, and terminal points, the elementary components of defects shown in Figure 3.8. Dots can be determined best using the particle analysis data, so from the skeleton analysis we locate and characterize the junctions and terminal points.

At this point in the analysis, the skeleton is a binary object where lines are represented by a series of 2-connected pixels in any of the 8 directions; terminal points are singly-connected pixels; and junctions occur where more than 2 pixels are neighbouring a given pixel. Dots do not, however, always reduce to single-pixel objects and hence they are treated separately. Furthermore, junctions exist in numerous possible configurations, often with multiple (3+)-connected pixels per junction, hence there will not be a one-to-one correspondence between junction pixels and either the number of junctions or junction types (see Figure 3.9). Identification of defects is done in a manner, which is, in essence, analogous to playing the Minesweeper-type games, by knowing how many adjacent pixels exist, as shown in Figure 3.9.

At its simplest, any connection or disconnection that breaks the 2-connected topology of the skeleton, resulting in a new local topology (or connectedness), is a defect with a corresponding value. For junctions, with each additional branch beyond two (which, on its own, would consti-

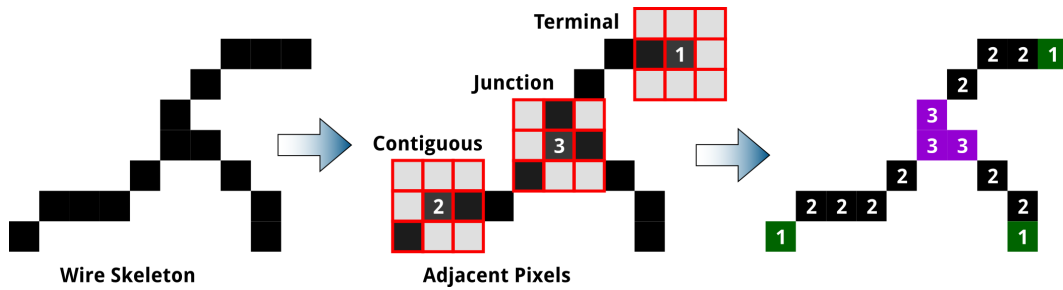


**Figure 3.9:** Pixels of a typical junction and three associated terminal points showing the analogy to Minesweeper. Highlighted are pixels representing (i) terminal points at the end of the line or branch, each adjacent to only 1 pixel, (ii) contiguous points along the line, each with 2 neighbour pixels, and (iii) junction points where three or more branches meet, having 3 or more neighbour pixels.

tute a line without topological defect), the defect increases in magnitude by  $\frac{1}{2}$ :

$$n_{jp} = \frac{1}{2}(B - 2)$$

where B is the number of branches. Typically junctions come with only 3 branches, but 4-way, or even 5-way, intersections can be found, on occasion, between clusters of dots or other complex features. A 4-way intersection would be  $n_{jp} = -1$ , which can be imagined as being derived from two adjacent junctions, each with  $n_{jp} = -\frac{1}{2}$ , with a common line-segment, where the intervening line segment's length decreases to zero; the same approach can be generalized for any number of additional line segments (as shown in Figure 3.10).

Terminal points possess only one configuration, hence their value is

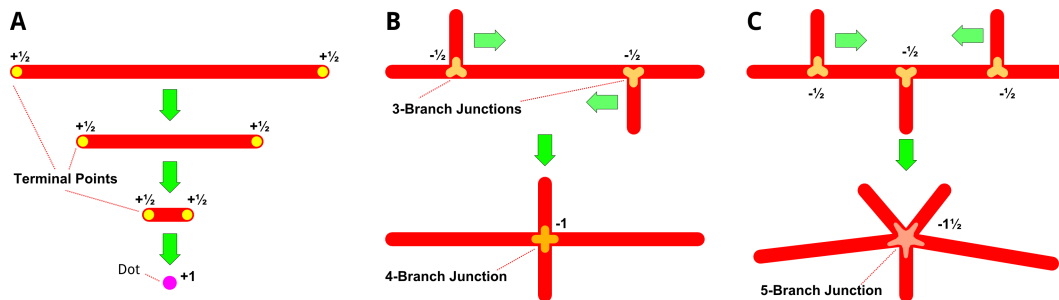


**Figure 3.10:** Equivalency justification for determining the defect value for each disclination. (A) A dot can be thought of as being a junctionless line which has been reduced in length to its width. The  $+1/2$  defect value associated with each of the two terminal points can be viewed as combining to give the  $+1$  value of the dot. This can also be seen when the dots are paired with  $-1/2$  defects. The 3-branch junction has a value of  $-1/2$ . Although 3-branch junctions are the most common, (C) 4-branch junctions ( $-1$ ) and (C) even 5-branch junctions ( $-1 1/2$ ) can, on rare occasion, be observed. For each additional branch, the value decreases by  $1/2$ ; this can be viewed as being equivalent to sliding an additional branch from a 3-branch junction to increase the junction by 1 branch.

assigned:

$$n_{tp} = +\frac{1}{2}$$

Dots can be considered as a line with two terminal points, collapsed to a single point (as depicted in Figure 3.10), hence their value is twice that of a terminal point:

$$n_{dot} = 2n_{tp} = 2(+\frac{1}{2}) = +1$$

Other more complex structures, such as spirals (containing terminal point dislocations) can be counted *via* their component structures in this regard. Large, solid spots in the bright phase or large regions without any pattern (*i.e.*, large spots in the dark phase) possibly formed due wetting (or other causes) may exist, these regions may be treated as dots with radiating arms, however, we found it was more effective to separate the core of the dot prior to skeletonization. The result treats the dot as a kind of enlarged junction, with defects existing only at the periphery.

For all defects to be counted, skeletons for both phases must be generated and connectivity analyzed separately. This raises an important point for defect analysis: that defects exist in a particular phase. The phase dependency of defects has not been sufficiently explored, however hints are seen in the literature, as it directly controls the topology of a system.<sup>[153]</sup> The dual phase analysis brings about an addition

rule for description of the system: on average, the sum of all defects in the pattern should be zero. Alternatively, this can be stated that every defect is “paired”, hence for every junction there is a terminal point; Moreover, for every dot, there will be two junctions: consider this an analogue of a unit cell (see Figure 3.11), as two defect pairs are produced if spontaneously generated and two are required to cancel out through annihilation.<sup>[44]</sup> Typically there exists a small imbalance between the two measures, which others have observed as well.<sup>[144]</sup> The pairing of defects does not imply however that the number of defects in the two phases of the block copolymer will be equal.

Skeletons also provide a description of the connectivity of defects, which merits further exploration. Defects can also be associated with particles using this method, but perhaps the greatest benefit is derived from the ability to search for and positively identify particular clusters of defects. One such example is an H-junction, which results from a break in the line or a bridging of two adjacent lines, shown in Figure 3.12. These junctions are supposedly not the result of a defect in the actual thin film structure, but result from (a) incomplete metallization or other means of pattern transfer, (b) image noise, or (c) the smoothing-thresholding process. Hence it may be prudent to recognize them and count them separately or to “correct” such errors in the binary image itself.

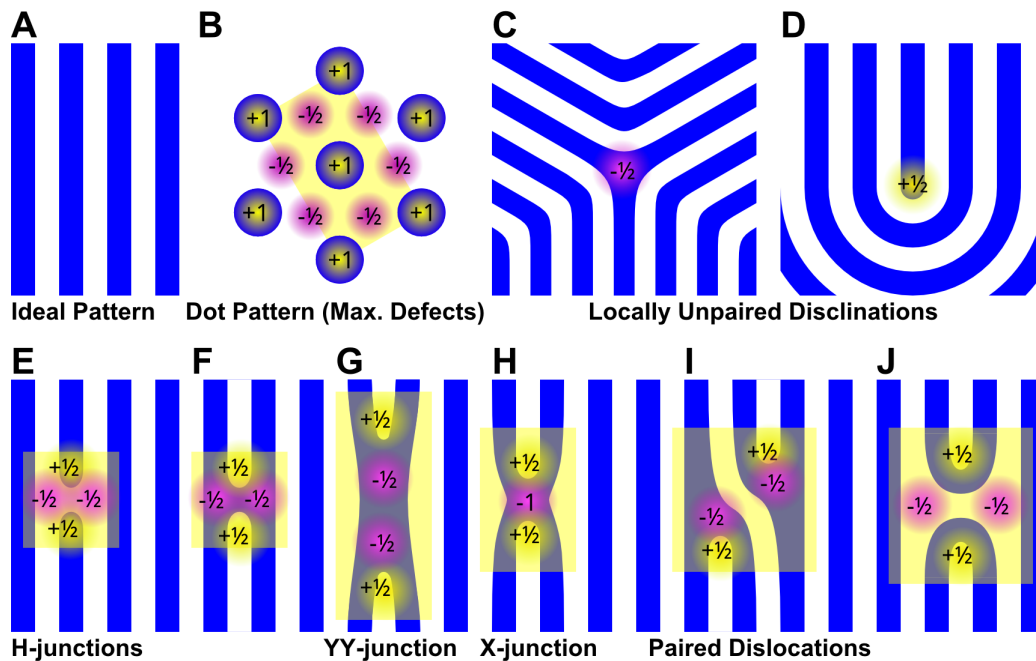


**Figure 3.11:** Pairing of defects and defect unit cells. Negative defects are noted with magenta dots, while positive defects are identified with yellow dots. The defect unit cells, shown in yellow, are drawn to indicate the parts of the defect required for the defect pairs to be part of an otherwise homogeneous, ideal pattern. (A) Region with an ideal pattern. (B) Region of dot pattern, which represents the maximum possible defect density for a stripe pattern made from a misoriented cylindrical BCP. (C) An isolated junction, which cannot be part of a unit cell on its own. (D) An isolated terminal point, also not part of a unit cell on its own. (E) H-junctions formed either from a line break or (F) from a bridging of two lines. (G)/(H) Junctions created by two adjacent lines coming into contact. (H) is similar to (G), except that the defect at the centre is 4-connected. (I) Paired dislocations. (J) Paired disclination pairs, where positive and negative components are in the same phase.

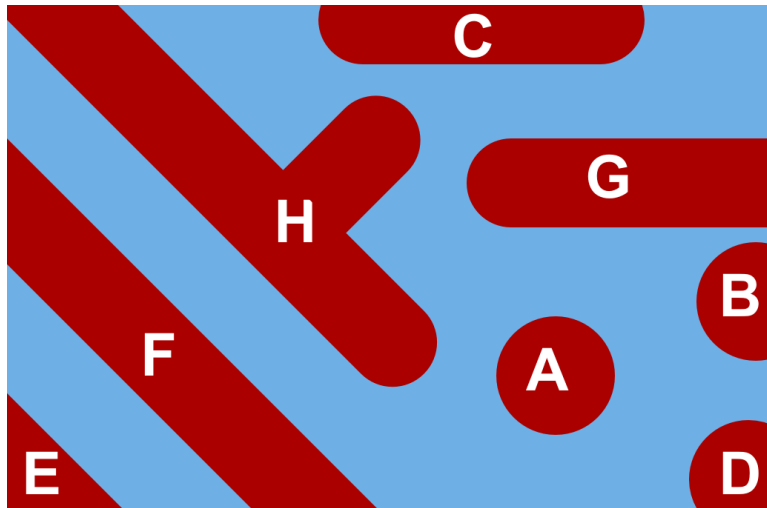


**Figure 3.12:** Rules regarding defects with regard to their location in the image frame. (A) Dots not touching the edge are counted in full. (B) Dot-sized features touching the edge are counted as half-dots, equivalent to terminal points. (C) For line features which lie on the edge, they do not count, as the terminal points are not within the frame of the image. (D) Dots touching two edges do not count, as these can be considered equivalent to lines touching two edges as in (E) and (F), which do not contribute to the defectivity of the image. (G) and (H) Only the terminal points and junctions within the frame of the image are counted for any given lines.

## Grooming the Skeleton

Grooming the skeleton consists of trimming away short branches, which may result as artifacts from small “bumps” on the edge of a line. With the dimensions determined in Stage 5, we can create a metric to selectively prune away any branches resulting from variations in line-width or simply from sharp points or edge effects that can influence the skeletonization algorithm. It may be a point for philosophical debate what constitutes a branch, justifying a junction and terminal point, but objectivity can be introduced by basing the grooming procedure on the measured LER. For this purpose, any end point separated from a junction by less than  $1.5 \times$  line-width (for a given phase) is considered roughness, rather than an additional defect pair, and is hence pruned, as shown by the example in Figure 3.13.

Because any image represents a finite sample of a larger structure, defects at image edges must be carefully treated. Depending on the resolution of the image and the domain size of the block copolymer, these can for smaller images, represent a significant fraction of defects; additionally, in otherwise low-defect patterns, features cut off at the edge may appear as additional defects. In particular, three rules must be applied:

1. Any “dot” (or sufficiently small object without junctions) touching

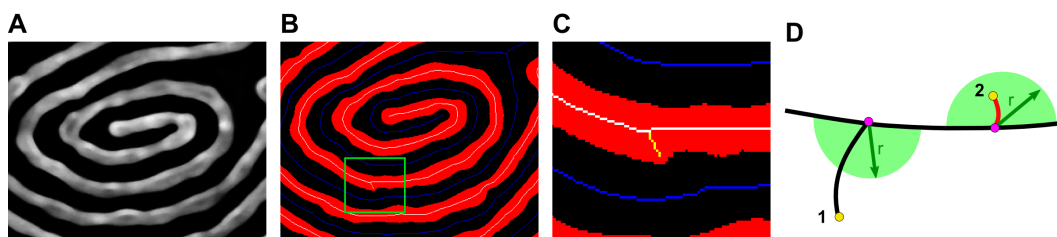


**Figure 3.13:** Grooming the skeleton to remove junctions formed as an artifact from variations in line width or from edge effects. (A) Image of metallized PS(50k)-b-P2VP(16.5k) nanowire. (B) Image of skeletonized image, with positive lines in red and skeleton in white, and negative lines in black and skeleton in blue. (C) Detail of region identified by green box in (B), showing a branch, yellow, trimmed from the skeleton. (D) Schematic showing radius-based trimming of branches: (1) a branch that exceeds the radius does not undergo trimming and (2) a branch that terminates within the radius is trimmed.

2 edges is not a defect. (See Figure 3.12)

2. Lines that run roughly parallel to the edge, touching at all times, are not defects.
3. Lines that terminate at the edge of an image are not defects, as it is not a true terminal point.

The third rule requires some manipulation of skeleton points & component terminal points near edges, as ImageJ's native skeletonize algorithm can produce limited edge artifacts. What these rules do not address is particulate matter; other analysis methods tend to default

to manual identification or require equipment unavailable to most researchers.<sup>[70]</sup>

### **Line-Edge Roughness and Line-Width Roughness**

One of the chief questions posed for BCP lithography is whether lines can be produced with sufficient uniformity and with smooth edges. LER measures the variation in the position of the edge of a line, which can have different frequency components, leading to undulation of the edge and variation in the width of the line, or LWR (Figure 3.14). The variation in position is measured as the standard deviation in the position of the edge, and LER is reported as  $3\sigma$ . Such variations are deleterious for circuit elements: For transistor gate features with widths  $< 85$  nm, line roughness causes significant variations in the off-current, as well as affecting threshold voltages.<sup>[154,155]</sup> For nanometre-scale interconnects, line roughness increases both resistance and capacitance,<sup>[156,157]</sup> resulting in degraded transistor performance.

The line roughness of block copolymer nanostructures has been considered theoretically and has been shown to depend on  $\chi N$ ,<sup>[49,108,158]</sup> and polymer polydispersity;<sup>[108]</sup> results have suggested that the Flory-Huggins  $\chi$  parameter may need to be increased by a factor of 3 to 4, relative to that of PS-*b*-PMMA,<sup>[49]</sup> in order to decrease LER sufficiently to

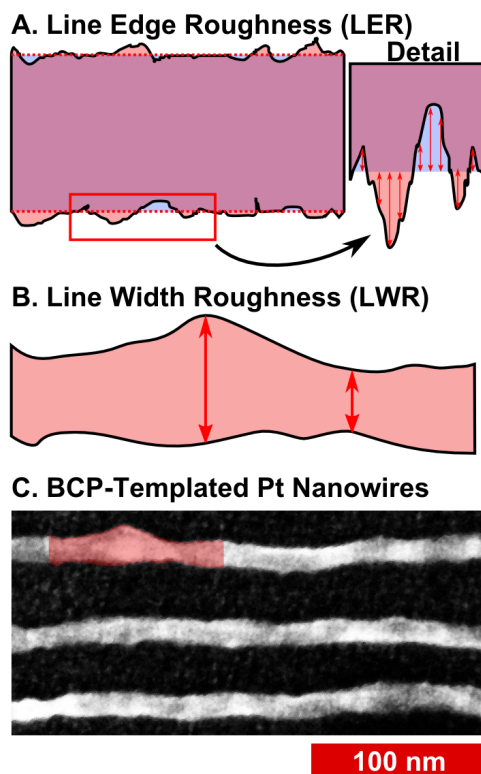


**Figure 3.14:** Diagrams depicting measurement of line-edge roughness and line-width roughness. (A) Sketch to conceptually demonstrate line edge roughness, where the variation in edge position of the line (shown in rose with black edge) varies with respect to the ideal (shown overlaid in blue) or, in this case, the average edge position. Each individual displacement is measured with respect to the average, and the LER calculated as 3 times the standard deviation. (B) Sketch of line-width roughness, which is the variation in line-width. The sketch is adapted from the bulges and pinches shown in the SEM image below. (C) SEM image of block copolymer templated Pt nanowires on a Si wafer, using PS(44k)-*b*-P2VP(18.5k), annealed at 200 °C for 20 minutes.

accommodate ITRS targets.<sup>[100]</sup> It has been specifically noted that there are few reports on the topic of LER/LWR in the literature;<sup>[45]</sup> typically, the actual position of the edge is measured relative to the ideal or average edge position for straight or aligned lithographic patterns. In order to achieve the same measurements for block copolymers, films aligned *via* graphoepitaxy would typically be required in order to have linear lines representing ideal edges. However, we<sup>[2,53]</sup> and others<sup>[52]</sup> have taken the approach of measuring LER for unaligned patterns. One may measure edge positions relative to the centre of the line, rather than with respect to a linear ideal edge position; the standard deviation in the edge position will be the same either way. As lines get narrower, however, the influence of pixel position can begin to slightly increase the measured LER, up to 0.5 nm in our previous work using high resolution (ca. 100,000x) BCP patterns. We mitigate this, in part, by smoothing both the centre line of the skeleton and the outer edge, while constraining the positions of the edge points. Edge-to-skeleton distances are determined for all points on the smoothed line edge, matching with the nearest points (shown in Figure 3.15A) on the smoothed skeleton line which satisfy:

$$(x_{edge} - x_{skel} + slope_{skel}(y_{edge} - y_{skel})) = 0$$

As derived from the dot product of the vector on the edge-to-skeleton distance and the orthogonal vector (1, slope) of the skeleton at that

point, an interpolated point on the skeleton can be obtained (shown in Figure 3.15B).

Line-width measurements can be made in conjunction with edge-to-skeleton measurements by finding a line segment on the opposing edge, which is intersected by the vector made between the edge point and skeleton point of the previous step (shown in Figure 3.15C). The solution exists at a point on the line segment formed by the vector between the edge  $(x_{edge}, y_{edge})$  and the skeleton  $(x_{skel}, y_{skel})$  is scaled by a factor,  $a$ , and on the line segment formed by the vector between two consecutive points on the transverse edge  $(x_{trans1}, y_{trans1})$  &  $(x_{trans2}, y_{trans2})$ , scaled by a factor,  $b$  (shown in Figure 3.15D). Provided that the two vectors are not parallel, the equations<sup>[159]</sup> for the scalars,  $a$  and  $b$ , are:

$$d = (x_{trans2} \quad x_{trans1})(y_{skel} \quad y_{edge}) - (x_{skel} \quad x_{edge})(y_{trans2} \quad y_{trans1})$$

$$a = d^{-1}((x_{edge} \quad x_{trans1})(y_{trans2} \quad y_{trans1}) - (y_{edge} \quad y_{trans1})(x_{trans2} \quad x_{trans1}))$$

$$b = d^{-1}((x_{edge} \quad x_{trans1})(y_{skel} \quad y_{edge}) - (y_{edge} \quad y_{trans1})(x_{skel} \quad x_{edge}))$$

An intersection is considered valid when  $1 < a < 4$ , indicating that the side opposite would have a width ranging from 0 to 3 times the width of the first side. The limit,  $a < 4$ , prevents identification of points on parallel segments, as with a hairpin, from being identified as valid; typically the period is on the order of 2 times the width of a given line, hence 4 times the half-width of a line. In practice, the values of  $a$  are

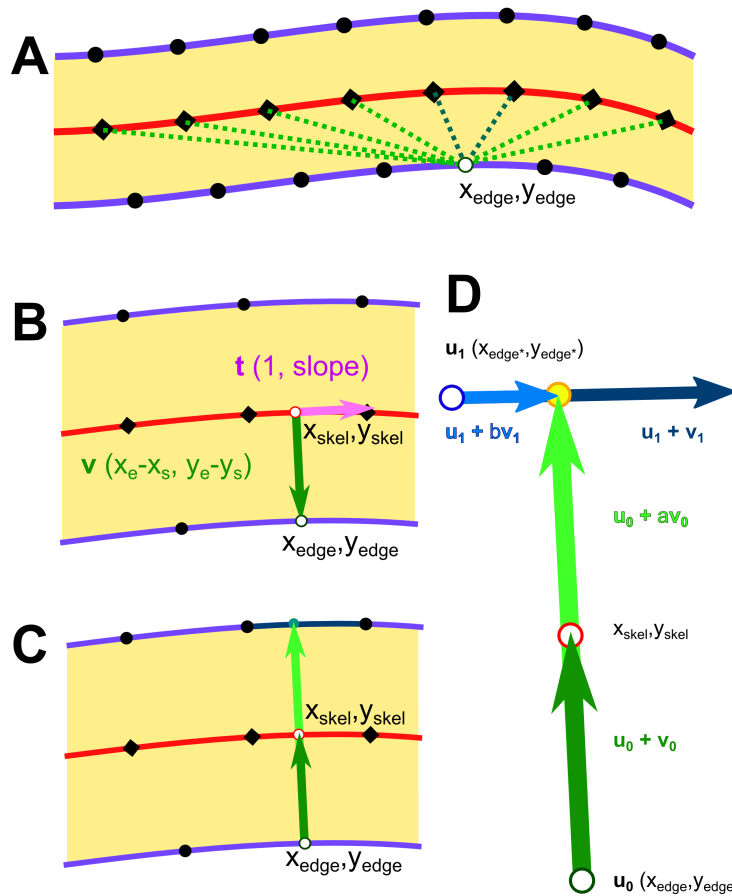


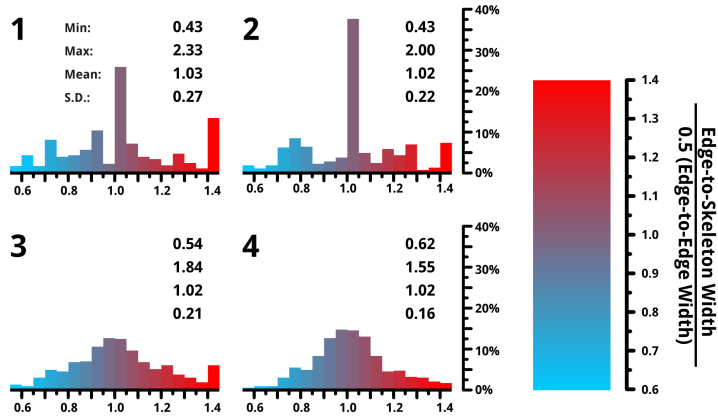
**Figure 3.15:** Diagram showing relationship between line edge points, skeleton points, and the vectors used to determine edge positions and line-widths for LER and LWR. (A) Outline of a line, showing edge points (black dots) and skeleton points (black diamonds) on the centre line. One edge point ( $x_{edge}, y_{edge}$ ) is selected and distances to nearest skeleton points are checked. (B) Interpolation to nearest orthogonal point from the edge point to a point on the skeleton segment. (C) Extension of edge-to-skeleton vector to intersection with transverse edge segment. (D) Expanded, with parameterization as scalable, intersecting vectors.

in the range  $1.5 < a < 2.5$ , as can be seen typified in Figure 3.16 via the histograms. The second limit for valid points is that  $0 \leq b \leq 1$ , which ensures that the point of intersection is within the line segment formed by the two consecutive edge points.

In order to obtain reasonable measurements of LER and LWR, the blocky structures of binary lines and skeletons need to be smoothed. The smoothing process, which we have utilized here, involves 4 stages:

1. Centring of the skeleton points by adding 0.5 px to each x and y coordinate. This accounts for the slight truncation from the skeletonization process and makes the edge-to-skeleton distances more equidistant on each side.
2. Shifting all edge points to the midpoints between consecutive points. This averaging reduces roughness introduced by the shape of individual pixels.
3. Smoothing the skeleton by iteratively averaging the positions of points, while limiting the displacement to within 0.25 pixels. This provides a smooth, continuous, reasonably centred skeleton line.
4. Smoothing the edges likewise provides a smooth edge while maintaining the shape and deviations in width, from which roughness can be measured.

### A. Distribution in Edge Widths as a Proportion of Half-Width



### B. Curved Line with Modified Coordinates

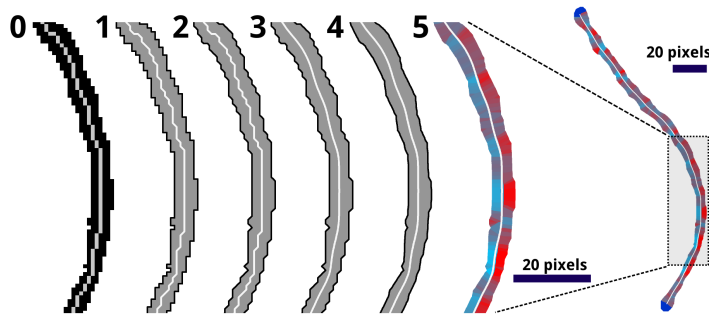


*Figure 3.16: Histograms show the smoothing process used to partially eliminate roughness resulting from pixelation of the lines. The labels 1, 2, 3, and 4 mark the line subject to each of the four stages of smoothing described. All images with the cyan-to-red colour scheme show the relative width of the opposite side of the line, from the skeleton centre, to the edge; if a side is wider in proportion it is shown in red; narrower is shown in cyan. A colour scale is given provided. (A) The histograms represent the edge to skeleton widths relative to the half widths for each point. (B) Last, the original skeleton (0), along with the 4 stages of smoothing (1,2,3,4) are shown for a re-drawn line, along with a the distribution of edge widths via colouration (5).*

Figure 3.17 shows the data for a single line as it is modified by each of these four smoothing processes (1, 2, 3, 4). By the fourth stage (4), the data shows considerably less noise, as demonstrated by the point-to-point colour variations in Figure 3.17A. In particular, the histograms of edge widths, depicting which edge is further from the skeleton, for each point on the edge, begins to approach a normal distribution, as one would expect for a line with random variations in width. Visually, the line becomes sufficiently smooth that pixels are no longer apparent, while variations in width are in keeping with the original image, and the sequential widths and edge positions measured do not have large point-to-point changes in displacement. While the skeletonization algorithm is largely effective in finding the centre line, it is imperfect. In particular for lines with pixelated widths less than 7 pixels, the centre will tend to be skewed preferentially depending on the orientation of the line. However this does not affect LWR measurements and smoothing does help to limit the impact on LER.

In order for BCPs to be relevant in industrial manufacturing, they must achieve a low frequency LWR ( $3\sigma$ ) of 1.1 nm on features 16 nm wide; in order to “significantly exceed” conventional lithography, the patterns would need to be better than 0.6 nm LWR on features 9 nm wide.<sup>[100]</sup> Presently our best measured samples have a LER ( $3\sigma$ ) of 2 to 3 nm,<sup>[2]</sup> however, no aspect of the process has, as of yet, been explored with re-

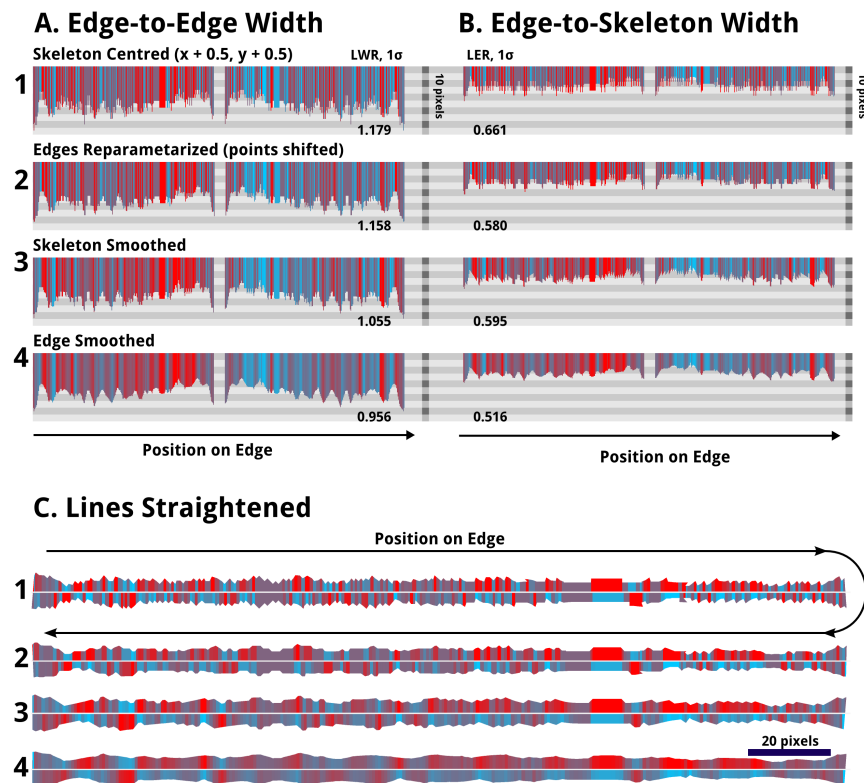


**Figure 3.17:** The smoothing process here is shown on a straightened version of the line, as in Figure 3.16, with the same colour scheme. The labels 1, 2, 3, and 4 mark the line subject to each of the four smoothing stages. (A) The top left shows the edge-to-edge width, following both sides of the edge of the line (C1), hence it is roughly symmetric; (B) the edge-to-skeleton widths are plotted similarly, but with roughly half of the displacement. (C) Next, the lines are shown replotted in a straightened fashion. Note that the lengths have been scaled to be equal, as smoothing of the skeleton shortens the length measured along the skeleton, as expected, due to smaller point-to-point displacements. In the above 3 cases, the more smoothed lines show smaller variations in colour.

spect to minimizing LER or LWR. To avoid the local effects of junctions and to increase the speed of the calculation, the lines are modified, as shown in Figure 3.5B, to render all lines junction-free. Additionally, points where lines contact image edges are selectively modified, erasing large contacts, to prevent any effects of the image edge.

### **Correlation Lengths & Order Parameters**

Correlation lengths (or orientational persistence lengths) are typically calculated for large images, often with low resolution (pixels/nm), by subdividing the area into overlapping squares, for which azimuthal angles are derived from two-dimensional FFTs of each region.<sup>[61]</sup> Lack of clarity for such images sometimes necessitates filtering in order to avoid disordered regions. In this work we implemented an alternative means of determining the 2D correlation function using the skeletonized lines. Skeletons are groomed to remove junctions and loops are broken to provide isolated lines. Orientation along the skeletonized lines can be calculated using a rolling average of each line's tangent to provide smoothly varying angles along the lines. In a typical image, there can be over 20000 points in the lines; calculating the correlation length using every point is feasible, however for expediency, the set of points can be downsampled or randomly sampled to a smaller set of 4000 points, which provides faster calculation with minimal trade-

off in terms of accuracy. From the set of orientation angles,  $\phi(r)$ , the correlation function,  $C(r-r')$ , can be calculated.

$$C(r-r') = \langle \cos[2\phi(r) - \phi(r')] \rangle$$

Advantages of this method include ease of applicability to higher resolution, smaller-area images and images with disordered regions where, due to defects, line segments are particularly short, and  $\phi(r)$  might not be determinable *via* FFT. This is demonstrated in Figure 3.18.

The correlation function is fit using an exponential function,

$$C(r-r') = \exp\left(-\frac{r}{\kappa}\right)$$

where  $\kappa$  is the correlation length, a characteristic measure of the degree of ordering in the film, which describes the average distance over which orientational order is preserved. The correlation length should be proportionate to the grain size, as illustrated by the circles in Figure 3.18, which are approximately keeping in proportion with the domains visible in the orientationally-colour-mapped pattern image. However the circles are unquestionably smaller than the observed domains.

One disadvantage of this method of determining  $\kappa$  *via* skeletonization is that one observes a periodic variation (corresponding to the periodicity of the pattern) in the correlation function, as shown in Figure 3.18. This periodic variation is a result of features separated by non-integer line spacings tending toward greater disorder than points separated by

integer spacings. This appears to be due to influence by neighbouring defects. The large undulation in the curve can be partially compensated by using both the positive phase and negative phase skeletons (thus reducing the period and amplitude of the variation, however exclusion of non-line areas may be necessary), by binning measurements, as is typically done in FFT-based methods,<sup>[62,160]</sup> or by smoothing, as we apply in the algorithm.

Herman's orientational parameter,  $S$ ,<sup>[161]</sup> gives a measure of how uniformly oriented the lines within an image frame are. It can also be readily calculated using the set of orientational data:

$$S_{2D} = \frac{1}{2} \frac{\langle \cos^2(\phi) \rangle}{\langle \cos^2(\phi) \rangle - \langle \cos(\phi) \rangle^2}$$

The reference angle can be set as the average orientation for the whole image, thus giving the best orientation parameter for a disordered image. Because it is widely used, we implemented this calculation into our code, however, Herman's orientation parameter tends to be less useful than the correlation length, as it can be significantly influenced by the size of the area sampled. That is to say one can typically choose a sample area small enough to give  $S_{2D} \approx 1$  (perfect net order) or an area large enough to give  $S_{2D} \approx 0$  (no net order). The code may, however, be adapted to set an angle where a particular direction is induced *via* processes such as directional annealing<sup>[161]</sup> or graphoepitaxy; in such cases,  $S_{2D} = 0.5$  is a possibility for samples where the line orientation

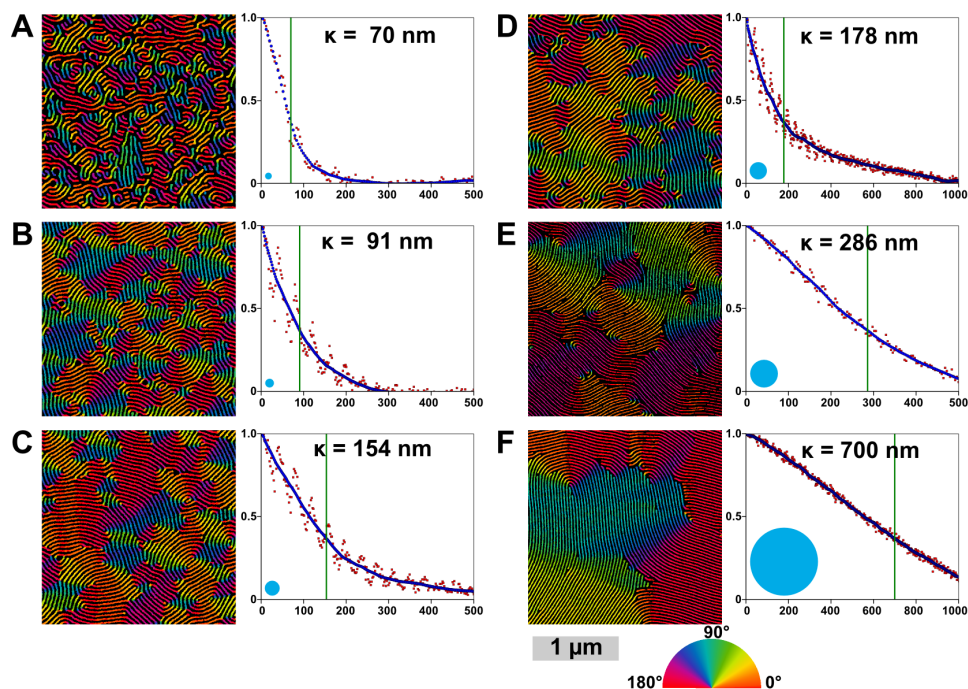


**Figure 3.18:** Correlation lengths and orientation maps for six SEM images of metallized PS-*b*-P2VP (50k-*b*-16.5k, 44k-*b*-18.5k, and 32.5k-*b*-12k) patterns with different degrees of thermal annealing. SEMs are shown in false colour to display the angle of each wire as used in the calculation of the correlation functions, shown right. The raw correlation data is shown in red, the smoothed data is blue, and the calculated correlation length ( $\kappa$ ) is marked with a green line and noted on each plot. Beside each image is a blue circle whose radius is equal to the correlation length, as the correlation length is often given as a measure of average grain size. Each image is shown cropped here to 2  $\mu\text{m}$  wide. The scale bar is 1  $\mu\text{m}$ . (See Figure 3.19 for full images). The labels (A-F) correspond to the same labelled images in Figure 3.21.

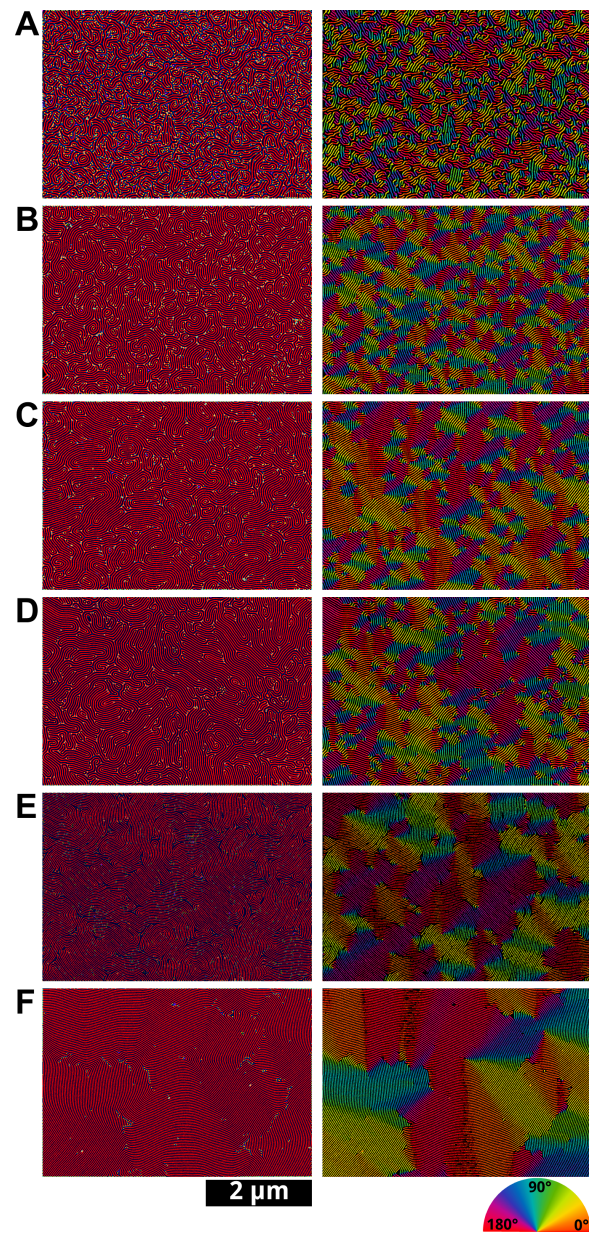


**Figure 3.19:** Full, processed images shown cropped in Figures 3.15 and 3.18. Full resolution images with labels (A-F) corresponding to those in Figures 3.15 and 3.18.

is orthogonal to the desired orientation.<sup>[110]</sup>

Finally, this skeleton-based approach facilitates generation of pseudo-coloured orientation maps, as in Figure 3.18, which also avoid grain-edge averaging problems exhibited with other methods.<sup>[162]</sup> Such images may assist researchers in qualitatively grasping the orientational ordering in their system. Such visual checks, can provide researchers with an accessible means of confirming numeric results, as it allows for a qualitative, direct measure of grain size on the image.

### **3.3.7 Stage 8: Output and confirmation images.**

Finally, as a result of these considerations, we seek to provide self-assurance and quality control by creating confirmation images, wherein features described numerically are mapped onto real images to provide visual feedback of the accuracy of the measurement, as shown in Figure 3.21, which shows the defects found alongside the associated SEM images. This step is ultimately the means to determine whether the defects identified are (1) a true representation of the pattern and (2) are in the correct location. Such images of pattern orientation, line roughness, defects, and thresholding provide visual confirmation that all stages of the analysis proceeded correctly. Specifically, one can check simultaneously whether the thresholding, connectivity, groom-

ing, and defect identification have all functioned as expected.

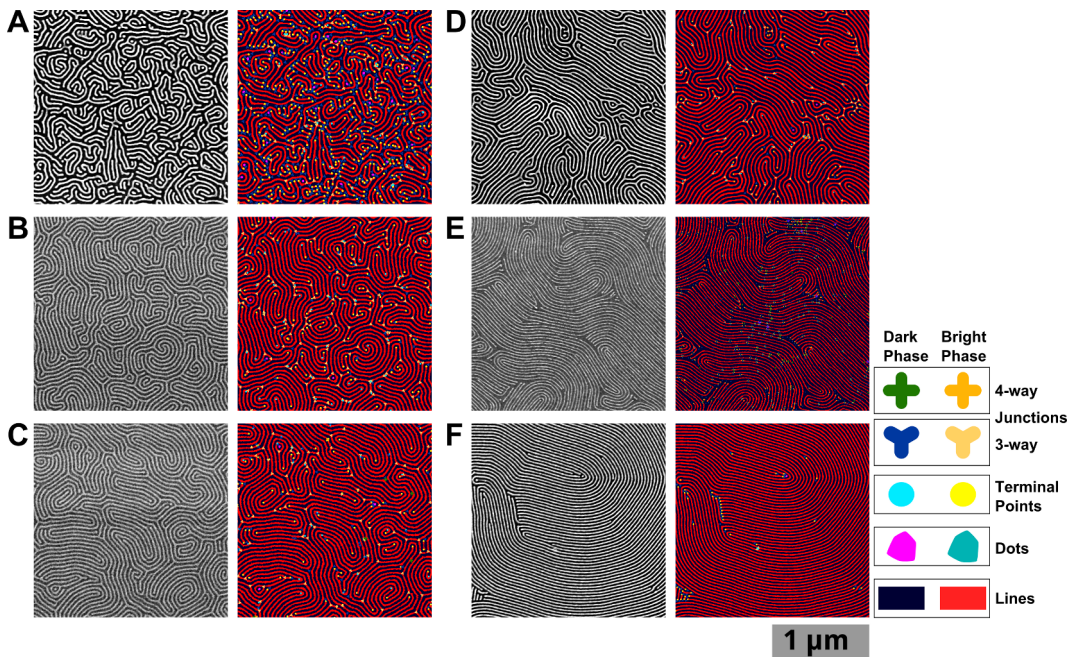


**Figure 3.20:** Original and defect analysis images for six SEM images of metalized PS-*b*-P2VP (50k-*b*-16.5k, 44k-*b*-18.5k, and 32.5k-*b*-12k) patterns with different degrees of thermal annealing. SEM images on left, and confirmation images with defects identified shown right. These images are spectacular only upon a close-up. Each image is shown cropped here to  $\sim 2 \mu\text{m}$  wide. The scale bar is  $1 \mu\text{m}$ . (See Figure 3.19 for full images). The labels (A-F) show correspondence to the same processed images in Figure 3.18.

Such visual feedback also lets researchers, particularly those presently involved in synthetic work, to tangibly grasp the important aspects of the pattern quality. By encoding the information spatially with colours and shapes rather than relying purely on the abstraction of defect den-

sities and correlation lengths, *ADAblock*'s visual feedback can function as a guiding indicator for selection of optimum structures and conditions. The data output, both numerical and visual, make it possible to engage in exploratory data analysis<sup>[163]</sup> to discover new trends, motifs, and outliers in the data available, as demonstrated in Figure 3.21 and later in Figure 3.23 and Figure 3.25.

### **3.4 Application of *ADAblock***

In order to demonstrate the utility and versatility of this application, two different scenarios and questions are posed. First, what is the effect of image resolution, and the area sampled, on the measured defect densities, LER, and other parameters of a self-assembled BCP thin film? Secondly, what can we learn from investigating the data provided by these samples, by examining the relationships between different features, to identify features that warrant further investigation—and what does this suggest about the resulting properties of a self-assembled BCP film?

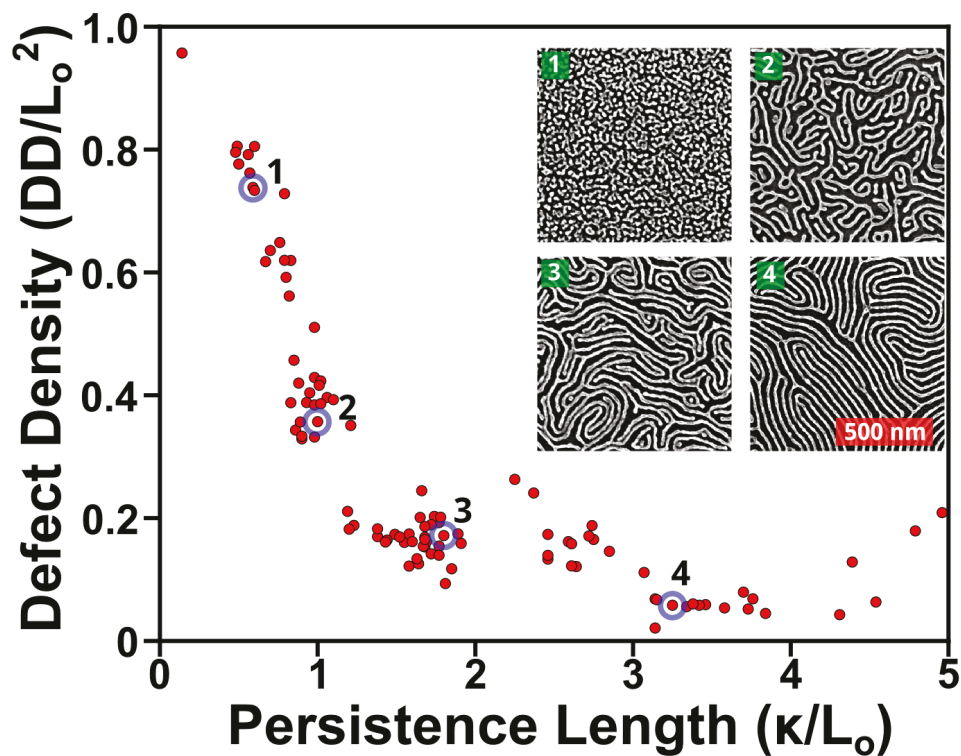


*Figure 3.21: Relationship between correlation lengths, plotted here as persistence length ( $\kappa/L_o$ ) versus the defect density, normalized per unit period squared. Based on data for a variety of annealed, neat and blended, cylinder-forming, PS-b-P2VP polymer thin films of a variety of molecular weights including blends, using images of the metallized P2VP domains on Si substrates. This enables direct comparison between different polymers, which result in patterns with different periodicities. Defects initially show a dramatic decrease, as structures move away from dot arrays, for which the normalized, defect metric would be 1. Inset displays four representative images. Respectively, their periods are 32, 43, 36, & 37 nm; their correlation lengths are 19, 43, 65, & 121 nm; their defect densities are 744, 195, 134, & 42 defect pairs  $\mu\text{m}^{-2}$ .*

### 3.4.1 Effect of Resolution and Sampling Area

When measuring defect densities, correlation lengths, LER, and LWR, the area sampled and the resolution can potentially affect the measured results. Ideally, for any measurement, the effect of sample size must be analyzed and understood in order to obtain reliable results. To develop a general sense of how this and different polymer sizes are affected in the analysis, we annealed 5 different polymer types, each with approximately ideal thicknesses, for 20 minutes at 200 °C and imaged the resulting metallized patterns at different magnifications.

The effect of resolution in the LWR measurements in Figure 3.23A appears to be minimal, although there is a slight downward trend with increasing resolution (smaller image area) for the two smallest polymers, where the LWR ( $1\sigma$ ) values decrease from 0.18 to 0.14. The increase in LWR is primarily observed for those samples with the smallest period, which would likely be on account of pixelation of the lines, as suggested by Figure 3.22. A confounding effect may also result from the decreased length of line sampled for images of higher resolution. LER data, on the other hand, shows a more consistent trend of decreasing LER with increasing resolution in Figure 3.23B. LER is likely more affected by pixelation due to the inability of the skeletonization process to precisely locate the line center, in particular when line-widths are a small, even number of pixels. In contrast, the line-width is not

strongly constrained by the determination of the line centre. The magnitude of the decrease (-0.03 to -0.05 pixels) here is still small, given that image area changes by a factor of up to 100.

Sampling effects can be observed in the measurement of defect pair density at various resolutions in Figure 3.23C. High resolution images, depending on the distribution of defects, can completely avoid defects or oversample them. Here the smallest BCP (23.6k-*b*-10.4k) is most affected, due to having a larger grain size. The same effect can be observed for correlation length measurements in Figure 3.23D, although this affects all of the polymers. In order for the correlation length measurement to be meaningful, the measured value should be shorter than the dimensions of the image. The linear decrease in correlation length as a function of the image area suggests that one may be able to estimate the true value based on the size of the image. The plot of 23.6k-*b*-10.4k is particularly telling because it shows the effect of sampling within a single grain or few grains (at low resolution) and the sudden decrease once more grains become involved.

As shown in Figure 3.24, images with few, large grains, measurement within a single image tends to result in a bimodal distribution of measurements, either over-estimating or under-estimating the actual grain size, depending on whether the image falls inside a grain or on the boundary between two grains. The limitation of large grains may be

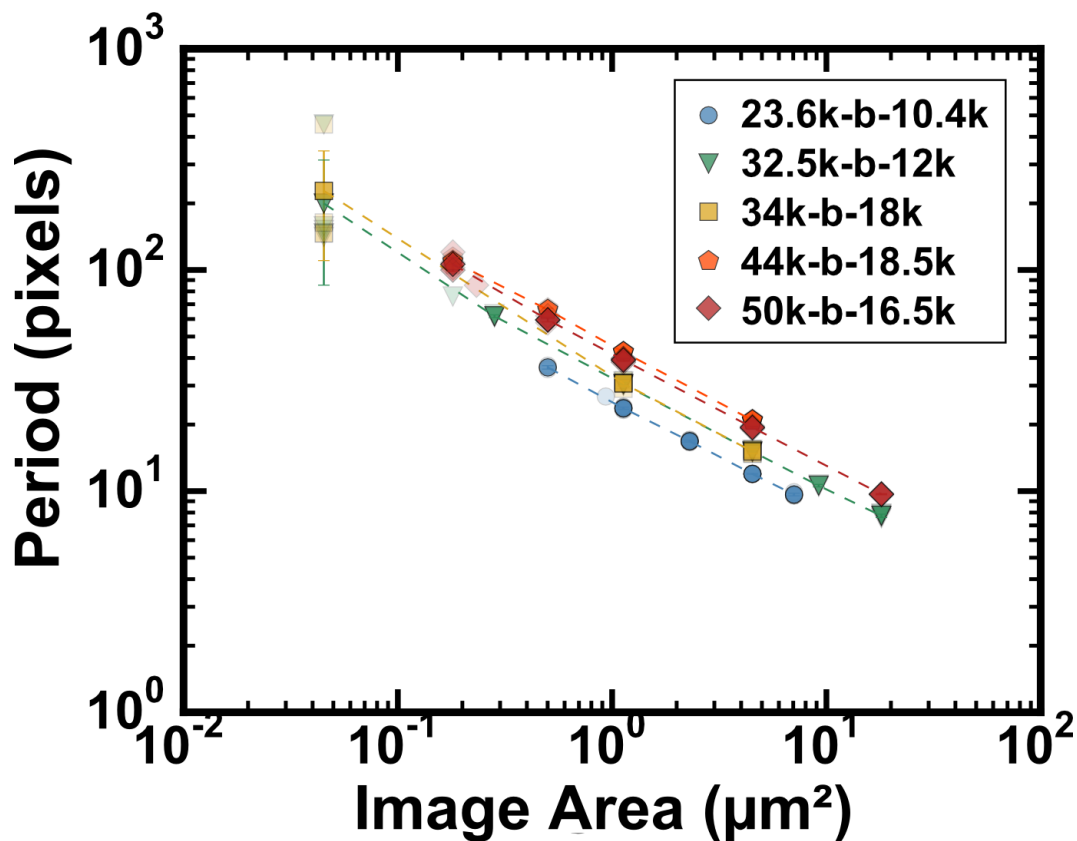
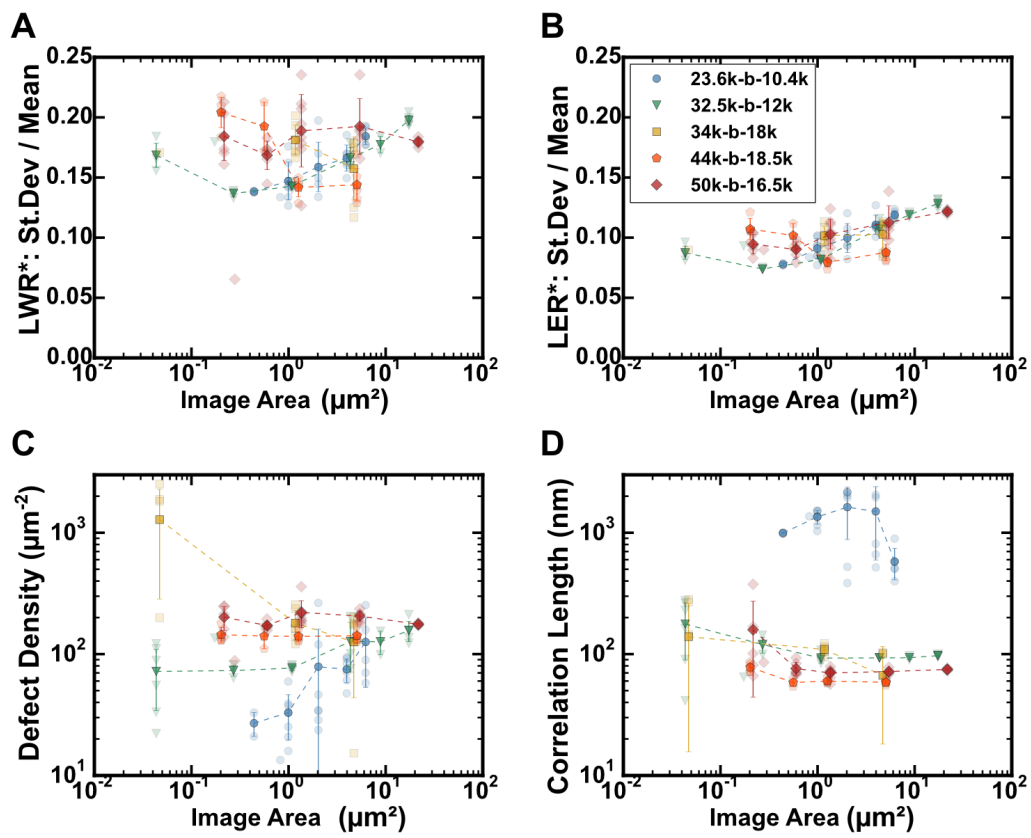


*Figure 3.22: Pattern period in pixels as a function of image area. Using images with constant dimensions (1280 pixels wide by 896 pixels high), and various image resolutions (500k magnification to 20k magnification), pattern periods were determined automatically from azimuthally averaged fast Fourier transform images. The relationship, within these constraints, for each of the 5 polymers is shown, with individual measurements shown as lighter markers; the dark markers are the averaged data. Dashed lines function as a guide for each set.*



partly avoided by using automated data collection (avoiding user bias), combined image stitching, which has been demonstrated to be effective for imaging large areas with electron microscopy, however as ordering approaches perfection, grain sizes become infinite, and the correlation function will approach unity.

---

**Figure 3.23 (preceding page):** Data showing effect of sampling area and resolution for BCP pattern metrics: LWR, LER, defect density, and correlation length. All images had areas of 1280 x 896 pixels, taken with different magnification factors. Five cylinder-forming PS-*b*-P2VP block copolymers, each identically treated, were imaged: PS(23.6k)-*b*-P2VP(10.4k) [blue circles], PS(32.5k)-*b*-P2VP(12k) [green triangles], PS(34k)-*b*-P2VP(18k) [yellow squares], PS(44k)-*b*-P2VP(18.5k) [orange pentagons], and PS(50k)-*b*-P2VP(16.5k) [red diamonds]. Average values are indicated by dark markers and standard deviation error bars; data from individual images are shown with light markers. A. Standard deviation for line-width (LWR,  $1\sigma$ ) divided by the line-width for various resolutions and plotted as a function of real image area,  $\mu\text{m}^2$ . B. Standard deviation for line edge position (LER,  $1\sigma$ ) divided by the line-width for various resolutions and plotted as a function of real image area,  $\mu\text{m}^2$ . C. Defect pair density as a function of real image area,  $\mu\text{m}^2$ . D. Correlation length measured as a function of real image area,  $\mu\text{m}^2$ .

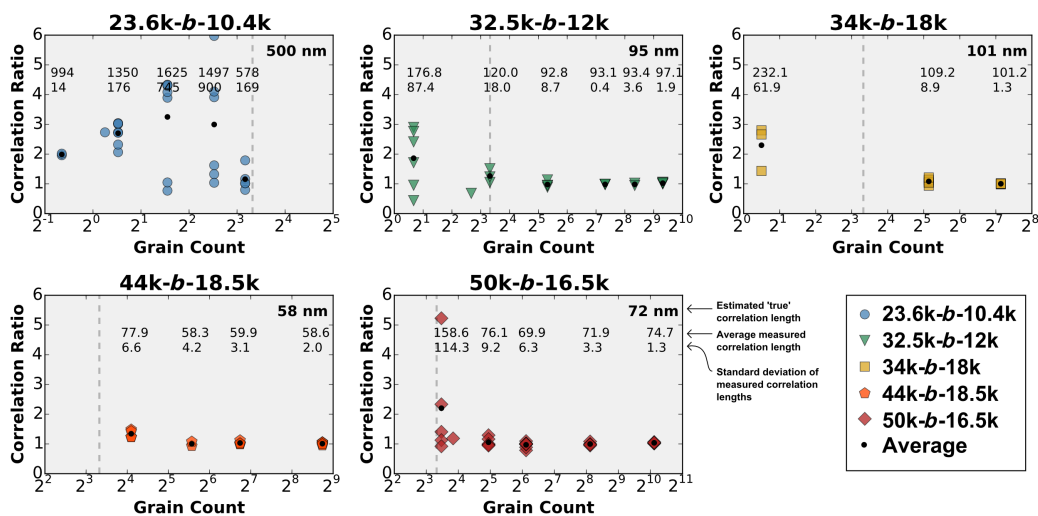


**Figure 3.24:** Grain count affects estimates of correlation length. Using data from Figure 3.23D, the number of grains in each image is approximated by dividing the image area by the grain size, taking the average grain area to be a circle with radius equal to the correlation length. Correlation lengths are also normalized, dividing the measured correlation length for each image by an estimate of the “true” correlation length (listed on each subplot) which would be measured for an image of the entire surface. A vertical dashed line on each image at 10 grains serves a reference point. The following values were used as estimates of the “true” correlation length for each image: PS(23.6k)-b-P2VP(10.4k): 500 nm, PS(32.5k)-b-P2VP(12k): 95 nm, PS(34k)-b-P2VP(18k): 101 nm, PS(44k)-b-P2VP(18.5k): 58 nm, and PS(50k)-b-P2VP(16.5k): 72 nm.

### 3.4.2 Feature Relationships

In order to derive lessons from the data, we undertake a form of exploratory data analysis to chart the relationships of different parameters observed; in particular, whether parameters such as LER and LWR are independent of the feature size, and what relationship exists between line-widths, polymers, and periods.

Taking all of the data (across resolutions) for each polymer, we note that as a proportion of the line-widths, the standard deviations in the edge position (LER,  $1\sigma$ ) and line-width (LWR,  $1\sigma$ ) stay constant, about 10% and 16% respectively, indicating that the LER and LWR scale with the line-width dimension of the polymer, as shown in Figure 3.25A and 3.25B. The set point may be a property of a given BCP's Flory-Huggins parameter, indicating that a higher Flory-Huggins parameter ( $\chi$ ) is required. However we must caution that other factors, such as the processing, metallization, plasma treatment, and lack of alignment are convoluted with the roughness inherent to the polymer, preventing a direct conclusion. However this method should enable comparison between polymer templates and patterns translated from the BCP via etching or other means. The values observed here would however all exceed LWR targets set by the ITRS for LWR ( $3\sigma$ ) of less than 6%: 1.1 nm for patterns with 18 nm feature size; or <0.6 nm for patterns with 10 nm feature size.<sup>[11]</sup> For aligned patterns, solvent annealed with wa-

ter as a co-solvent, we have observed significantly better LER and LWR values.<sup>[2]</sup> We hypothesize that it may be the result of the water selectively partitioning inside of the P2VP block during annealing, resulting in a higher effective  $\chi$ , leading to a smoother interface than we attain here with thermal annealing.

Line-width in Figure 3.25C and 3.25D shows the expected relationship of being proportionate to the period, although there does appear to be a greater spread in the width of lines than in the FFT-measured periods. This is likely an effect of thresholding, which needs to be done relative to each image. It may be possible for a specific polymer or a series of images to constrain the threshold, as a fraction of area, in order to obtain a narrower distribution of line-widths.

### **3.4.3 Limitations of the code**

As with any programmed analysis, there are drawbacks and trade-offs made in analysis to optimize for speed or accuracy. The approximations we implemented are one reason that necessitates a full sharing of the code. ImageJ's macro language is interpreted, hence it is slower in processing compared to plugins or other compiled programs. It is, however, easily edited and modified, which enables adaptation where modification may be required. The code was written so that it can

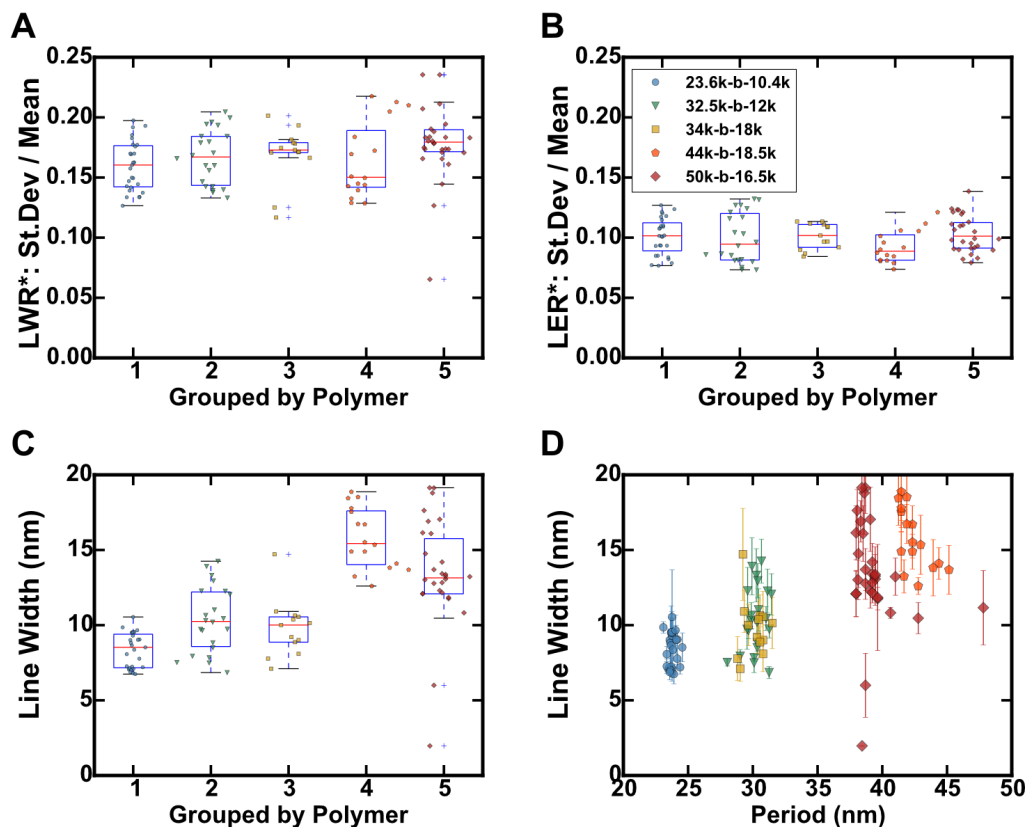


**Figure 3.25:** Boxplots of calculated BCP pattern metrics for SEM images with various resolutions for 5 cylinder-forming PS-*b*-P2VP block copolymers, each identically treated. Data from all resolutions shown. Data from individual images are shown with dark markers. A. Boxplot of the standard deviation for line-width (LWR,  $1\sigma$ ) divided by the line-width for various resolutions, grouped by polymer. B. Boxplot of the standard deviation for line edge position (LER,  $1\sigma$ ) divided by the line-width for various resolutions, grouped by polymer. C. Boxplot of measured line-widths for polymer groups by polymer. D. Same data, plotted as a function of BCP period (nm), all resolutions included; the error bars are standard deviations for the line-widths from measuring the lines separately.

be operated in a batch mode to process a folder of images, meaning that a series of images can be processed overnight, or while attending to other tasks. It should be cautioned that in the present state, as *ADABlock* continues to be developed, the code may produce a reproducible error for ~4% of images at present. Further refinement should reduce this error rate, but at present may limit a series from being completed. With manual intervention, however, the image can be skipped, or the settings modified, and the queue re-continued.

Typically an image with dimensions of 1280 x 896 pixels (the default of our SEM, for example) requires ~7 minutes to process when run on the standard personal computers that we used for testing. Higher pixel-resolution (*e.g.* 2560 x 1792) images require more time to process, roughly in proportion to the number of pixels. Given the automated nature of the program, it's possible to run a queue of images overnight, rendering the increased processing time irrelevant.

In addition to images showing the locations of defects, the code saves several check images to act as references to help determine whether any errors have taken place or other undesirable operations. Consequently, ~16 MB is recorded to the disk for each image processed, as presently configured, although non-graphic data only accounts for less than 300 kB.

## 3.5 Conclusions

We have developed a facile, automated, and reliable analysis for striped patterns derived from the self-assembly of BCP thin films, that integrates both conventional and newly developed techniques. This analysis is done in order to quantify defects and their types using a skeletonization-based method; to measure line-edge roughness; and to calculate Herman's order parameter and the correlation length in a novel fashion, based upon the skeletonized structure. Moreover, the skeletonized structure provides information about the connectivity of patterns. We expect that this will be of use to others carrying out annealing studies and preliminary characterizations of novel self-assembling polymeric materials. Finally, for 5 block copolymers of similar composition, we have found the metallized patterns to have LER and LWR in roughly constant proportion to the line-width.

Ultimately, no one measurement provides a "complete description" of pattern quality; typically they are complementary. Hence this work represents an attempt to broaden the scope of analysis and to make tools which may not be readily accessible to all. Additionally, having shared protocols, or at least protocols derived from a common origin, we might be able to standardize a broad toolset, providing consistent analysis *via* fully shared code.<sup>[164,165]</sup> We hope this aids comparisons

between polymers, between papers, and between scientists seeking to understand the characteristics of block copolymers, and in addressing the numerous critical issues associated with block copolymer lithography.<sup>[35]</sup>

## 3.6 Materials and Methods

PS-*b*-P2VP block copolymers were obtained from Polymer Source Inc. (Dorval, QC), in weight-averaged molecular weights of 23.6k-*b*-10.4k, 32.5k-*b*-12k, 34k-*b*-18k, 44k-*b*-18.5k, and 50k-*b*-16.5k and all with polydispersity below 1.1. Toluene was purchased from Fisher Scientific (Mississauga, ON); concentrated H<sub>2</sub>SO<sub>4</sub> from Caledon Laboratories (Georgetown, ON); 30% H<sub>2</sub>O<sub>2(aq)</sub> from Sigma-Aldrich (Oakville, ON); and Na<sub>2</sub>PtCl<sub>4</sub> · xH<sub>2</sub>O from Strem Chemicals (Newburyport, MA). Silicon wafers were obtained from University Wafer (Boston, MA).

### 3.6.1 Substrate Preparation

100 mm diameter, single-side polished silicon wafers were diced into squares with dimensions 1.0 cm ± 1.0 cm. Prior to cleaning, substrates were scribed, on the unpolished side, with a diamond-tip, to mark the identity of each substrate as part of a set of 10. The samples were then

immersed in methanol and sonicated for 15 minutes in glass beakers. Next, after rinsing each substrate square in a series of beakers filled with 18.2 M $\Omega$  cm water, the substrates were placed polished-side-up in PTFE beakers, and immersed in 6.0 mL of concentrated H<sub>2</sub>SO<sub>4</sub>, to which was added 2.0 mL of 30% H<sub>2</sub>O<sub>2</sub>, before placing the beaker to stand in an 80 °C hot water bath for 20 minutes. The piranha solution was then decanted to a glass flask to cool prior to neutralization.

Following several rinses with water, the substrates were immersed in aqueous 1% NH<sub>4</sub>OH solution for 5 minutes to remove any surface sulfonate groups, prior to a final decant and replacement of the solution with 18 M $\Omega$  cm water. Typically samples were stored immersed in water with the top sealed with paraffin wax.

### **3.6.2 Solutions and Spin Coating**

Immediately prior to spin coating, each wafer was dried under a nitrogen stream. Once dry, the sample was analyzed using fixed-angle, single-wavelength ellipsometry (632.8 nm) to determine the thickness of the thermal oxide at the center; typically 2 nm. Spin coating was carried out under argon or nitrogen gas. Each substrate's polished side was evenly coated with 10  $\mu$ l of 10-15 g/L BCP solution; any bubbles were manually removed; then the substrates were spun for up to 15 s,

between 3000 rpm and 4000 rpm, with an initial acceleration of 1500 rpm/s. Following this, the film was reanalyzed by ellipsometry, prior to quartering the sample and annealing.

### **3.6.3 Annealing**

Thermal annealing was carried out in ambient atmosphere on a hot-plate covered with a thin aluminum sheet. Temperature was monitored directly at the wafer using an OSENSA (Coquitlam, BC) fiber-optic fluorescence-based temperature probe. For the thickness measurements and for the comparison of the 5 polymers, the substrates were annealed for 20 minutes at 200 °C.

### **3.6.4 Metallization**

A solution of 20 mM  $\text{Na}_2\text{PtCl}_4$  in aqueous 0.9 M HCl was used for metallizing the P2VP block of PS-*b*-P2VP samples. Samples were submerged for at least 2-3 hours prior to removal and rinsing with 18.2 M $\Omega$  cm water.

### 3.6.5 Plasma processing

Following metallization, sample sets were placed together in a plasma chamber, and the chamber was evacuated to  $< 200$  mTorr to remove contaminant gases or adsorbates. Finally,  $O_2$  gas was leaked into the chamber to a pressure of  $\approx 750$  mTorr. The RF coils were then energized and a faint lavender-blue  $O_2$  plasma was maintained for  $\approx 60$  s (depending on the film thickness) to etch the organic materials from the substrate. Finally, samples were imaged using a Hitachi S-4800 scanning electron microscope, sampling regions near the centre of each substrate.

### 3.6.6 Computation

For image analysis, ImageJ,<sup>[146]</sup> version 1.49 and above, was used. It is freely available at <http://imagej.nih.gov/ij/>. The code for performing the analyses is available on our institutional repository; updated versions will be available on GitHub. Python scripts used in preparing the data shown here are also available to assist with processing and plotting output from multiple runs. They are available under an MIT license, allowing users to freely copy, redistribute, and modify the code.

## 3.7 Abbreviations

BCP: block copolymer; PS-*b*-P2VP: polystyrene-*block*-poly(2-vinylpyridine);  
SEM: scanning electron microscopy; JP: junction point; TP: terminal  
point; LER: line-edge roughness; LWR: line-width roughness; PX: pixel.

# 4

## Effect of Film Thickness on Defect Density of Monolayers of Self-Assembled Block Copolymers

### 4.1 Introduction

Block copolymer (BCP) self-assembly as a means of producing lithographic masks or templates presents an attractive route to patterning surfaces with nanoscale features, ranging from 5 nm to greater than 100 nm, on account of their potential to create highly ordered patterns over large areas with minimal external intervention.<sup>[82,103,121]</sup> Research is underway to integrate BCP lithography into a variety of commercial

technologies, including hard drives,<sup>[22,127,166]</sup> integrated circuits,<sup>[11,167]</sup> sensors,<sup>[168,169]</sup> linear polarizers,<sup>[82]</sup> surfaces for cellular adhesion,<sup>[116]</sup> and other devices or applications. One constant challenge to the adoption and integration of BCP lithography is the presence of defects in the nanostructured morphology. In order to produce ordered structures and eliminate defects, BCP thin films must be annealed in order to reach an equilibrium structure.<sup>[11]</sup> Annealing is primarily effected using thermal treatment with temperatures above the glass transition temperature<sup>[44,73]</sup>, exposure to solvent vapours<sup>[80,170]</sup>, or combinations of the two<sup>[20,40,82,84]</sup>. Although the defect density of a self-assembled BCP film may be further reduced through the use of graphoepitaxial,<sup>[171,172]</sup> and chemoepitaxial pre-patterning,<sup>[125,173]</sup> controlling or preventing defects in a pattern is a challenge, particularly for BCPs with smaller domain sizes.<sup>[174]</sup>

Several critical factors affect the defectivity, including the mode of annealing, along with time, temperature, and the innate characteristics of the BCP (such as polydispersity, Flory-Huggins parameters). External to these factors is the nature of the environment in which self-assembly occurs, as influenced by lateral constraints as in graphoepitaxially aligned patterns,<sup>[172]</sup> the defects and topology in those structures,<sup>[96]</sup> and surface interfacial energies.<sup>[31,34,63,175-177]</sup> The film thickness of block copolymers is recognized as a critical issue in optimiz-

ing defect levels.<sup>[174]</sup> It has long been known that the structure of a self-assembled BCP film is directly dependent on the thickness of the film,<sup>[178–181]</sup> in addition to interfacial energies and wetting characteristics.<sup>[175,182]</sup> The computationally-derived phase diagram by Li and coworkers of thin films of block copolymers shows that a variety of morphologies are possible, depending on the volume fraction of each block and the relative thickness of the film.<sup>[21]</sup> In work by Mishra, Fredrickson and Kramer,<sup>[174]</sup> defects were identified in PS-*b*-P2VP thin films by atomic force microscopy (AFM), and order-disorder transition temperatures and average block spacings were measured using grazing incidence small angle X-ray scattering (GISAXS); they showed a dependence of the order-disorder transition temperature on the film thickness for cylindrical domains in confined in graphoepitaxial troughs, which directly influences the defect levels observed via AFM.<sup>[174]</sup> In confined monolayer BCP films, the formation energy of a point defect can decrease substantially, meaning that there may be a high defect density well below the order-disorder temperature (ODT). Consequently an incommensurate thickness has the potential to lead to increased defectivity relative to an ideal striped pattern, composed of either horizontally aligned cylinders or vertically aligned lamellae. A low formation energy of a point defect could therefore dramatically affect the results obtained via the screening of BCPs with respect to their resulting

nanopatterns for a given set of conditions, since a ‘one size fits all’ set of common conditions may not exist. That the defect density may be high, well below the order-disorder temperature, would also be important for studies of block copolymer defect kinetics and thermodynamics, since the results would be dependent upon external parameters for each system in question.

Determination of the relationship between defect density and film thickness (and other parameters) is thus important for next steps in directed self-assembly applications since the success of a BCP patterning process in a manufacturing setting may have only a small window for error with respect to film thickness. Defect density measurements can provide detailed information regarding the kinetics of self-assembly and defect annihilation,<sup>[40,44,183]</sup> the effect of BCP composition,<sup>[20]</sup> substrate-presented chemical and topographic environment,<sup>[63], [97]</sup> and other aspects of pattern formation. In this work, we investigate the details of how thickness of thin films of cylindrical block copolymers affects the level and distribution of topographic defects in striped patterns.<sup>[43]</sup>

While changing the initial film thickness outside of some optimal value will result in micro-scale defects in the form of islands and holes, the main question here is what happens to the remaining cylindrical monolayer: Do defects within that monolayer stay constant, as suggested in Figure 4.1, with additional topological defects solely arising from the

nanostructures of the island and hole features? Or do the island and hole features further perturb the level of topological defects in the continuity of the BCP nano-domains outside of the region immediate to the islands and holes?

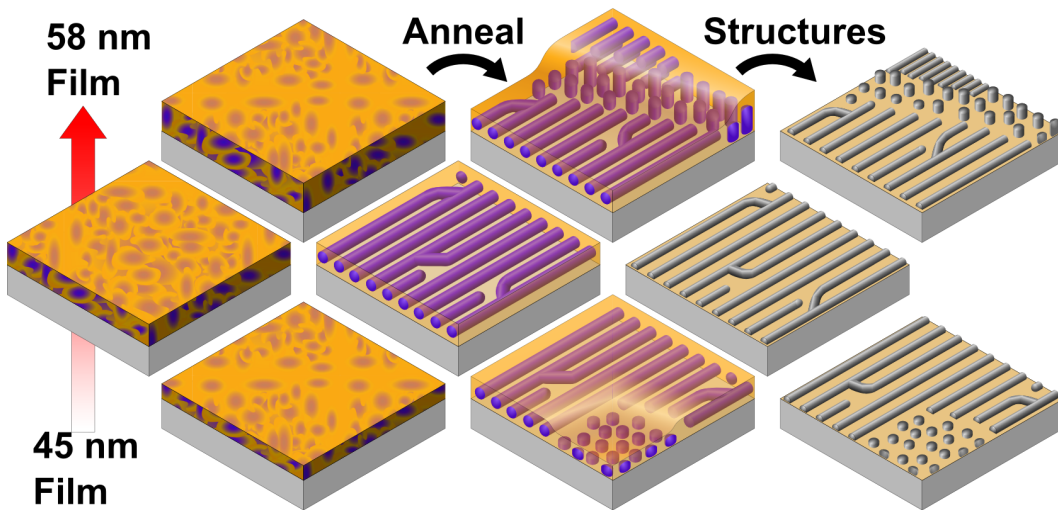


**Figure 4.1:** BCP thin films of varied initial thicknesses form islands and holes upon annealing, resulting in micro-scale defects. What is not certain is whether the remaining monolayer regions maintain a constant level of defectivity.

## 4.2 Results and Discussion

To investigate the relationship between film thickness and defect density, the BCP system of PS(34k)-*b*-P2VP(18k) on a native oxide (SiO<sub>x</sub>) surface of silicon wafers was selected. A schematic outline of the procedure is drawn in Figure 4.2. Films of different thicknesses, ranging

from 40 to 57 nm, as measured by ellipsometry, were prepared via spin-coating, and thermally annealed at 200 °C for 20 minutes, and subsequently platinized and plasma treated for visualization of the self-assembled P2VP block, followed by analysis of defects present in the pattern. [2,20,40,73,96,120]

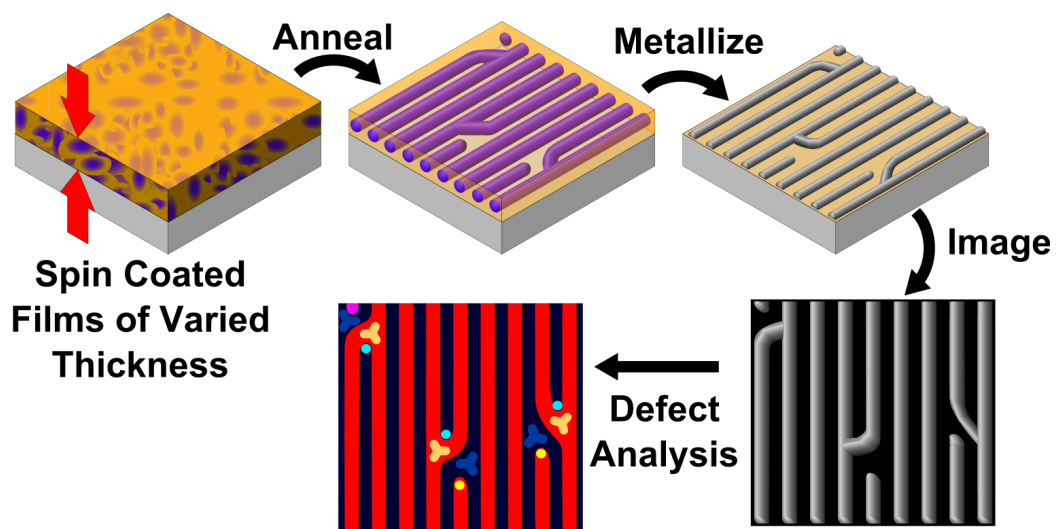
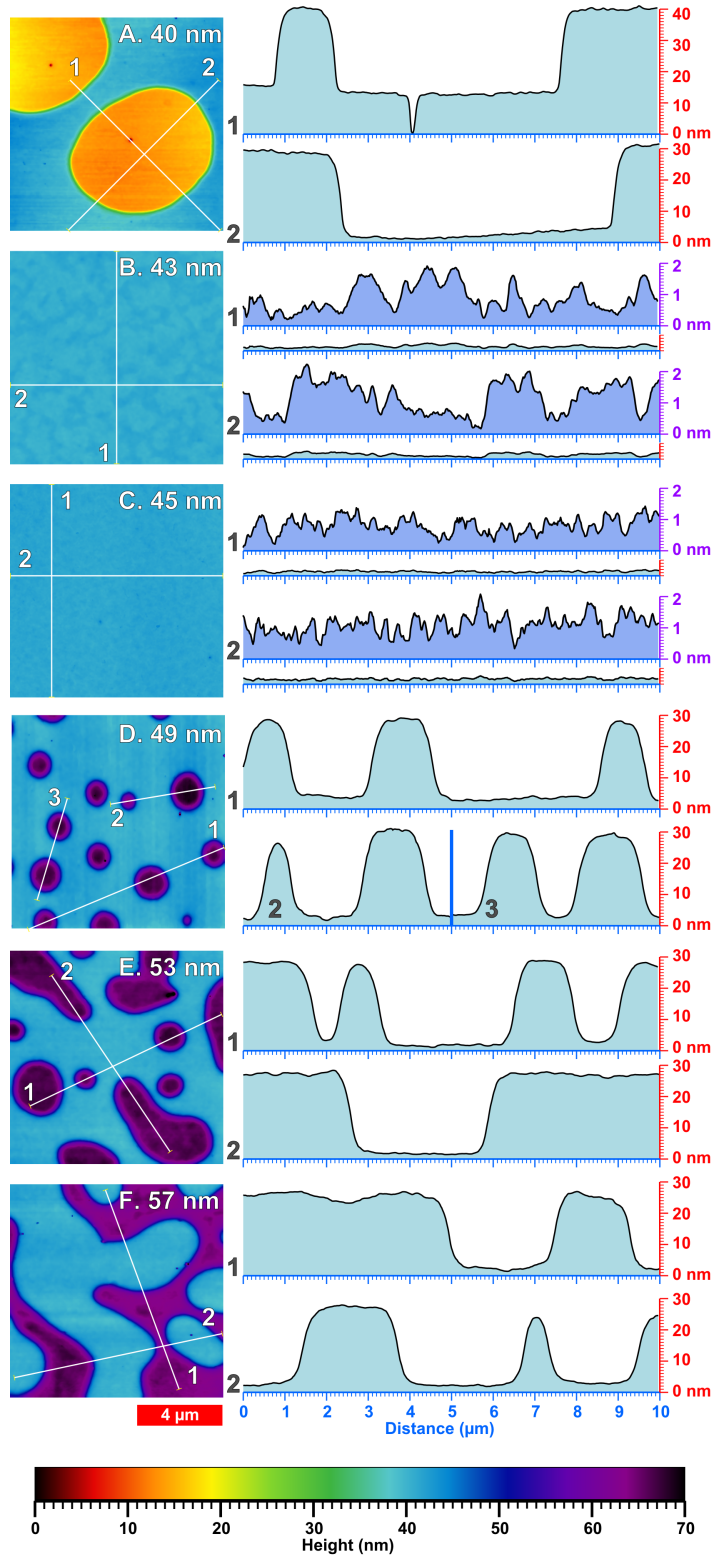


**Figure 4.2:** Schematic of the processing of BCM thin films using cylindrical PS-*b*-P2VP. First the thin film is spin coated onto a native oxide-capped silicon wafer. Thermal annealing then results in nanoscale phase segregation, and self-assembly, of the P2VP blocks into cylindrical structures embedded in a PS matrix. The structures are then platinized/plasma treated, and imaged using SEM. The SEM images are then analyzed using an automated algorithm called ADABlock to determine defectivity in the monolayer regions.

### 4.2.1 Polymer Film Structure

AFM measurements of the original PS-*b*-P2VP films after annealing, but prior to platinization, show a series of plateaus, each representing a different structure for the underlying polymer film. Starting with an initial thickness of 40 nm, the annealed film appears smooth, with roughly 27 nm deep holes that are several microns wide (Figure 4.3A). PS-*b*-P2VP films are known to form a polymer brush layer due to the interaction of the P2VP block with SiO<sub>x</sub>/SiOH at the surface,<sup>[184-186]</sup> moreover, with SEM, we observe corresponding regions with an absence of any nanopatterned features (see Figure 4.14) hence we conclude that the BCP structures observed are all formed upon a common brush layer.

The annealed films with initial thicknesses of 43 and 45 nm appear continuous over the entire surface, with no holes or islands observed. A subtle texture can be observed in the surface of the 43 nm film, while the 45 nm film lacks a discernable texture, as shown in Figures 4.3B-C. The textured nature of the 43 nm film is clearly different from the relatively smooth surface of the 45 nm film when the histogram of heights is analyzed (see Figure 4.4); the 45 nm film clearly has a unimodal distribution well-fit by a single normal function, whereas the 43 nm film has a broad shoulder indicating bimodality and requiring two normal functions to fit well. Analyzing AFM profiles, the height difference in



the texture is  $\sim 1.2$  nm (see Table 4.4 and Figure 4.22).

One notable feature in Figure 4.3 is the patchy appearance of the surface, corresponding to the mixed pattern of line and dot features. Overall, the dot features present a higher profile when metallized, as one might expect from the vertical orientation of the cylinders (see Figure 4.5). This same patchwork texture can be observed in Figure 4.4, although with difficulty owing to the expanded vertical scale. These features are examined in Figure 4.4, comparing the height distributions of the 43 nm and the 45 nm polymer films. The 45 nm film is, in images of metallized samples, a nearly pure line pattern, while the 43 nm film is a mixture of dots and brushstroke patches of lines. The mixed nature of the 43 nm film is reflected in the AFM image which appears to show

---

**Figure 4.3 (preceding page):** AFM images showing the progression of profiles of starting film thickness of annealed PS-*b*-P2VP films, from 40 nm to 57 nm, after annealing (but before platinization and plasma treatment). All AFM images are  $10\ \mu\text{m} \times 10\ \mu\text{m}$  (512 px  $\times$  512 px), Two profile plots of each image are shown to the right. A. 40 nm. Within the large holes are pin-sized punctures of the underlying PS-*b*-P2VP brush layer on SiO<sub>2</sub> likely caused by the AFM tip. B 43 nm. C 45. D 49 nm. E 53 nm. F 57 nm. A median filter (6 px radius) has been applied to remove noise and particulate dust for the profiles shown. Images are offset with respect to the look-up table (vertical scale, shown at bottom) in order to provide a consistent scale across the images by matching plateau heights.

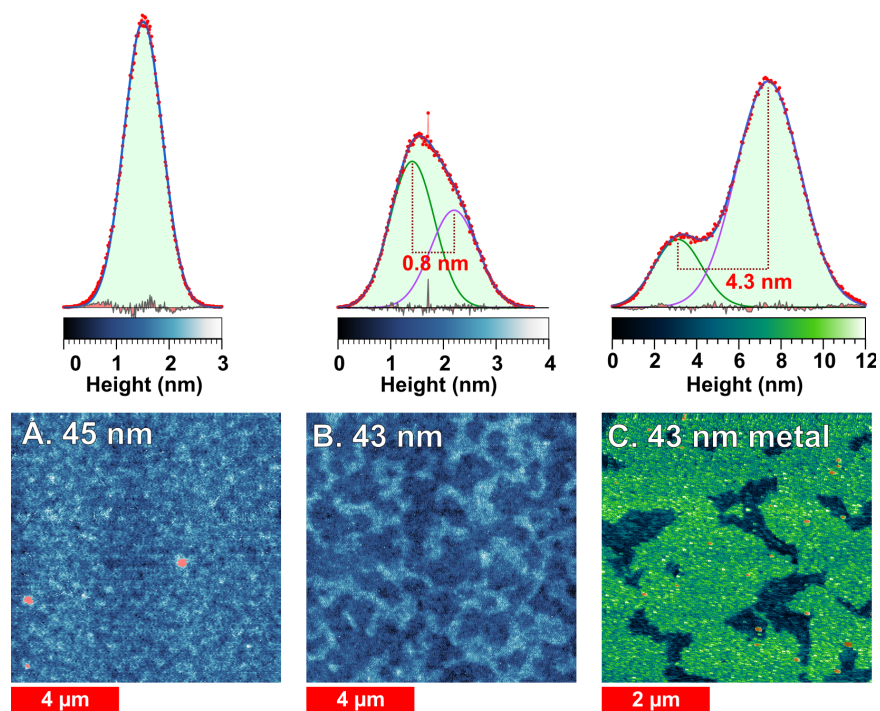


**Figure 4.4:** Plots of subtle differences in the heights in AFM images, along with corresponding height distributions. All AFM images (right) are  $512 \text{ px} \times 512 \text{ px}$ . Masked regions, excluded due to debris or irregular features, are marked with a red overlay. Height distribution data are shown with red dots; overall fitting curve in blue; separate component distributions in green or purple; and residuals in grey with red fill at the bottom. A. 45 nm polymer film ( $10 \mu\text{m} \times 10 \mu\text{m}$ ), fit with a single normal function ( $\mu = 1.5077$ ,  $\sigma = 0.3654$ ,  $A = 1.0845$ ). B. 43 nm polymer film ( $10 \mu\text{m} \times 10 \mu\text{m}$ ), fit with two normal functions ( $\mu_1 = 1.4078$ ,  $\sigma_1 = 0.4213$ ,  $A_1 = 0.5550$ ,  $\mu_2 = 2.2026$ ,  $\sigma_2 = 0.4466$ ,  $A_2 = 0.3700$ ). C. Metal nanostructures from an adjacent section of the 43 nm sample, fit with two normal functions ( $\mu_1 = 3.1095$ ,  $\sigma_1 = 1.1327$ ,  $A_1 = 0.0644$ ,  $\mu_2 = 7.3922$ ,  $\sigma_2 = 1.5179$ ,  $A_2 = 0.2144$ ).

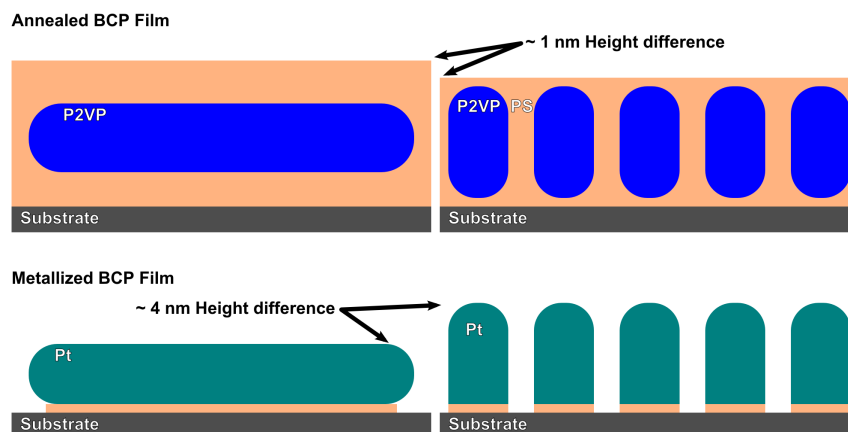


**Figure 4.5:** Schematic of proposed polymer structures showing relative height of nanostructures within the polymer film prior to annealing (above) with horizontally oriented cylinders (left) and vertically oriented cylinders (right). Below are the corresponding metal nanostructures.

a patchwork of small plateaus, approximately 1 nm higher than surrounding areas. The proportion of the two plateaus, as measured with the AFM histogram, varies with sampling and across the film, likely as a result of an initial gradient in thickness in the film prior to annealing, resulting from the spin coating process. Similar results were observed for repeat experiments with additional films.

Plotting the distribution of heights, as measured by AFM for the 43 nm film, shows a non-normal distribution of heights, fit with two Gaussian curves, the mean values of each separated by 0.8 nm, and the plateaus covering 40% of the surface. This can be compared to the height distribution for the 45 nm polymer film, which shows a normal distribution,

with 99% of measured values within  $\pm 1$  nm of the mean. Sigma values for each of the distributions in Figure 4.4A and 4.4B are comparable, indicating that the fits are reasonable and that variations in height result from the same sources, whether physical variations in the polymer film or errors in measurement.

The metallized 43 nm film has a more clearly bimodal height histogram, when compared to that of 4.3. The difference is clearly seen in the side-by-side 3D projections in Figure 4.6. Here the height difference is measured to be 4.3 nm, with the lines covering 23% of the surface; the exact coverage of lines varies across the surface, and is estimated from SEM data, measuring more regions with larger areas, average  $\sim 27\%$  for the 43 nm film. The greater, and inverted, height difference is due to the orientation of the cylindrical metal nanostructures having a greater height profile compared to the more embedded, horizontal cylinders in the line-patterned regions. What is surprising is that the preference of one structure versus the other is effected by a height difference on the order of approximately 1.2 nm, as indicated by the height distribution in Figure 4.22 and Table 4.4 and the profile plots in Figure 4.3.

Increasing the initial film thickness from 49 nm to 57 nm, islands appear that are about 26 nm in height; coverage of the islands gradually increases and they become continuous when the initial thickness reaches 58 nm. We note that the thickness of the polymer plateaus as

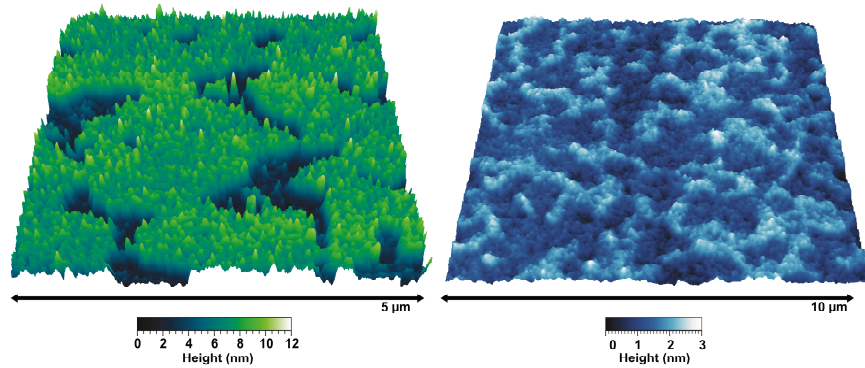


**Figure 4.6:** 3D projections of the the surfaces of 43 nm samples as a polymer film (right) and metallized (left). Vertical scales are matched to show the relative height difference. A 4-pixel median filter has been applied to each image (both 512 px × 512 px) to minimize noise in each case.

measured by AFM, combined with the area fractions of various features measured with SEM, accords well with data from ellipsometry measurements of the film thicknesses prior to annealing. Summing the area fraction of each component, as measured using SEM (over areas of > 100 μm<sup>2</sup>; see Figures S13-S18 in Appendix #), multiplied by the thickness of each plateau, as measured with AFM (see Tables 4.3, 4.4, and Figure 4.22), provides an effective means of estimating the initial film thickness, as shown in Table 4.1. This is given by the equation:

$$d_{calc} = \sqrt[n]{\sum_{i=1}^n a_i \times d_i}$$

where  $d_i$  is the thickness of a given layer and  $a_i$  is the area fraction which is at least the height of the layer; as such, in a layer with islands and monolayer lines, the monolayer lines would have  $a_{lines} = 1.0$ , while

$$0 \sim a_{islands} \sim 1.0.$$

Sample	Solution (mg/mL)	Thickness	Thickness	Brush (area)	Dots (area)	Lines (area)	Islands (area)
		Ellipso. (nm)	Calc. (nm)				
A (40 nm)	10	39.6	39.5	1.0	0.901	0.0	0.0
B (43 nm)	11	43.2	42.4	1.0	1.0	0.272	0.0
C (45 nm)	12	45.5	43.3	1.0	1.0	1.0	0.0
D (49 nm)	13	48.7	46.2	1.0	1.0	1.0	0.113
E (53 nm)	14	52.8	48.8	1.0	1.0	1.0	0.214
F (57 nm)	14.5	57.0	55.2	1.0	1.0	1.0	0.461

**Table 4.1:** Estimated contributions to thickness based on SEM-measured area fractions of each feature and the AFM-measured thickness of each layer. The products of each layer’s thickness, multiplied by the area fraction which that layer covers, provides an calculated value for the original ellipsometry measurement, as compared to the original value as measured by ellipsometry. The AFM-measured thicknesses for each layer is as follows: Brush (16.3 nm), dots (26.8 nm), lines (1.2 nm), islands (25.8 nm), except for the 57 nm film, where the islands were thinner (23.7 nm), as described in Table 4.4.

## 4.2.2 Brush Coating Thickness

Underlying the nanostructured layers is a brush layer, with P2VP in close association with the SiO<sub>2</sub> surface. In order to obtain a direct measurement of the thickness of the brush, the polymer film shown in Figure 4.3A was scraped using either the tip of a steel needle or the edge

of a steel scalpel; the resulting surface is shown in Figure 4.7. AFM height profiles of the film give the thickness of the annealed brush layer was found to be ~16 nm, relative to the mechanically-cleaned surface regions, as shown in Figure 4.8. Note that the distribution of heights shown in Figure 4.22 is likely the result of the cleaned surface having some residual mater, causing the skew toward smaller height differences.

In order to futher investigate the annealed film structure, samples of the 43 nm and 45 nm films were analyzed with ToF-SIMS, in order to obtain a depth profile. The 45 nm film shows a symmetrical peak for nitrogen (CN) from the P2VP slightly below the surface as seen in Figure 4.9, as well as a second peak at the substrate interface where the Si surface is oxidized, forming  $\text{SiO}_x$ , as is evident from the O, and OH peaks observed here. Much smaller OH, O, and  $\text{Si}_2$  peaks can be observed, when the data is plotted logarithmically, coincident with the upper P2VP peak, indicating the presence of a small amount of  $\text{H}_2\text{O}$  and possibly  $\text{SiOH}_4$  within the P2VP domains.

The data in Figure 4.9 comports with the understanding of PS-*b*-P2VP coating the  $\text{SiO}_x$  with the P2VP block in closely associated with the surface. An illustration of this is presented in Figure 4.10. The surface of hydrated  $\text{SiO}_x$  bears silanol groups,  $\text{O}_n\text{Si}(\text{OH})_{(4-n)}$  (for  $n = 1-4$ ), capable of forming hydrogen bonds. These would be able to hydrogen

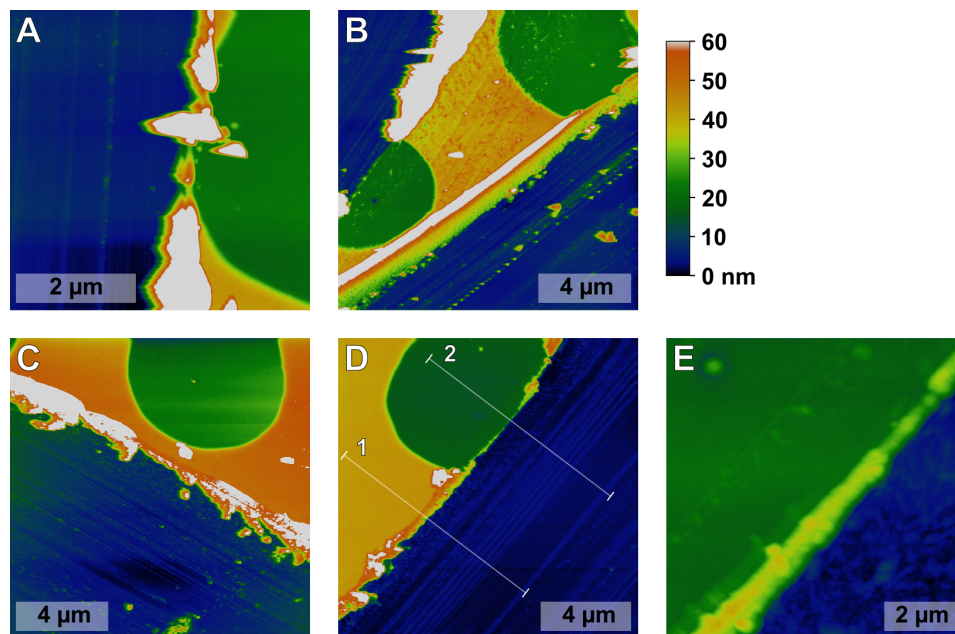


**Figure 4.7:** In order to obtain profiles of the brush layer, scratch tests were performed using either the tips of tweezers (steel) or the blade of a an X-Acto knife, leaving the  $\text{SiO}_x$  thermal oxide of the substrate intact while removing most adsorbed polymer. Images (A—E) are all presented with the same 60 nm colour scale, which shows that the scraping procedure reaches approximately the same level, relative to both the “holes” coated by the brush layer, and the thicker dot-layer regions. As not all of the material comes cleanly off, the white patches observed are the residue material which is taller than the 60 nm colour profile used in the images. Panel E is a higher resolution scan, zooming in on the region in D, where the edge of the brush layer is adjacent to the scraped surface and is not obscured by significant residue.

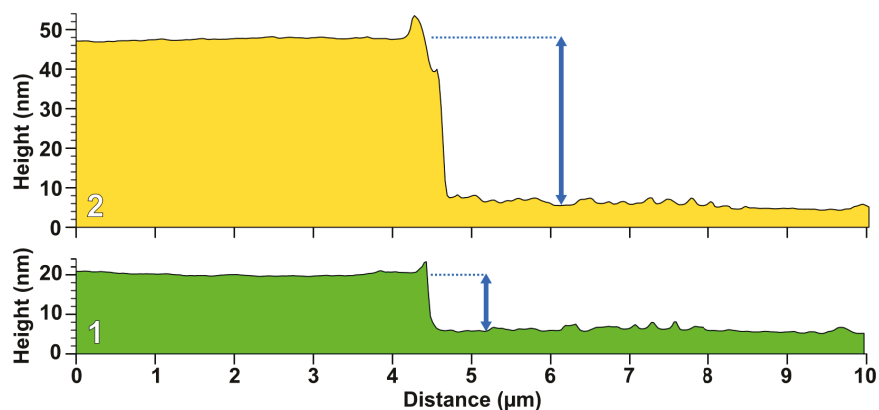


**Figure 4.8:** Two AFM height profiles from Figure 4.7 are shown. Profile 1 (above) shows the step from the top of the dots layer to the scraped-clean SiO<sub>2</sub> substrate below is approximately 42.5 nm; Profile 2 (below) shows the step from the top of the brush layer to the scraped-clean SiO<sub>2</sub> substrate surface, which is ~14.5 nm for this profile.

bond with pyridine, however given the sterically hindered nature of the nitrogen lone pair in poly(2-vinylpyridine), it would make sense for bridging water molecules to function as a hydrogen bond bridge between the surface and the P2VP. It should be noted that H<sub>2</sub>O is observed to be present, even in the P2VP domains which are not in contact with the surface, as evident by the OH<sup>+</sup> ion peak in the ToF-SIMS data in Figure 4.9.

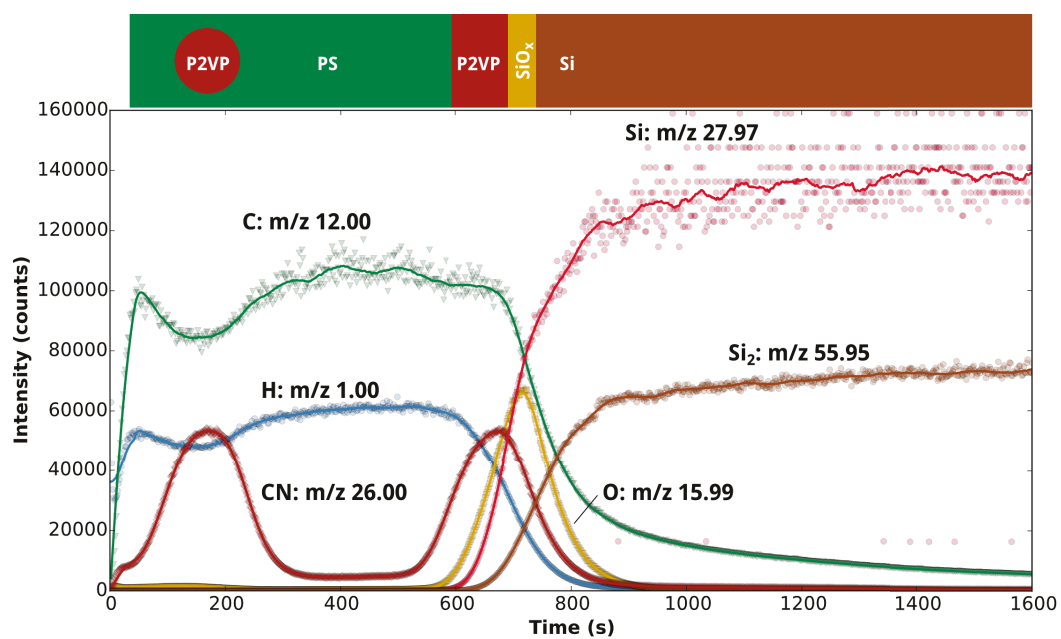


**Figure 4.9:** TOF-SIMS data for PS-*b*-P2VP with horizontal cylindrical P2VP domains on Si/SiO<sub>x</sub>.

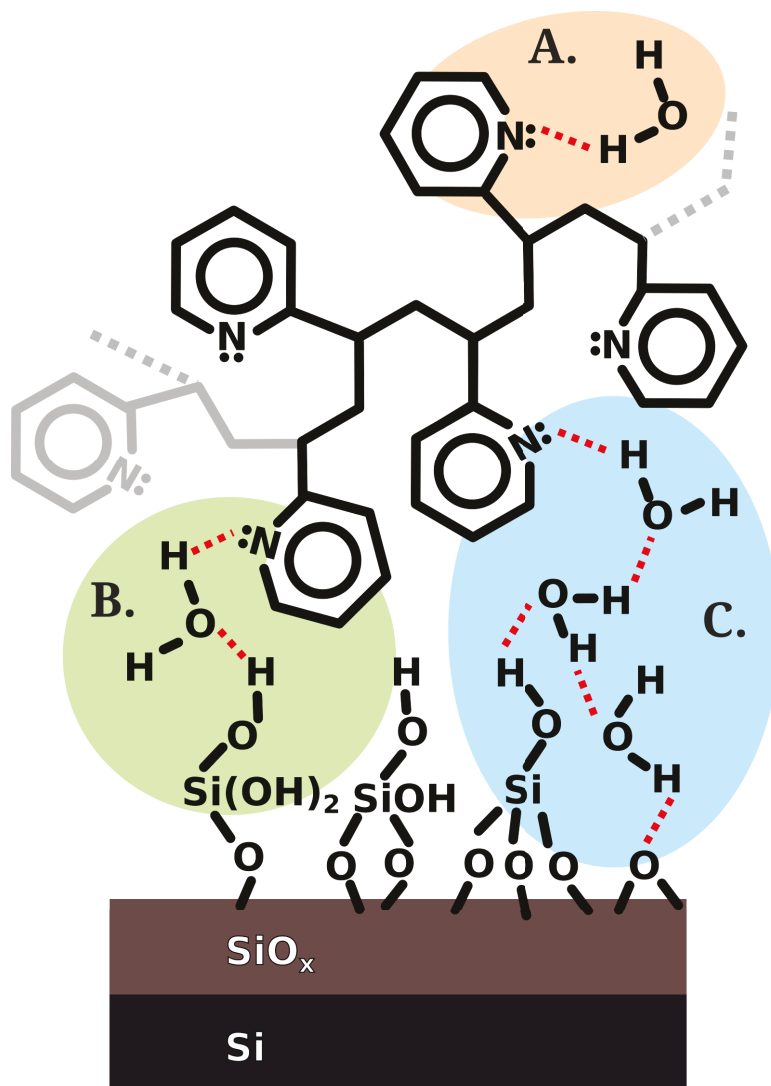


**Figure 4.10:** Illustration of P2VP in association with the SiO<sub>x</sub> surface via hydrogen bonding. A segment of P2VP from a larger PS-*b*-P2VP BCP chain is shown with 3 proposed modes of hydrogen bonding: A. isolated water molecules hydrogen bonded to the pyridine nitrogen lone pair; B. pyridine bridged to the surface via a single bridging water molecule; C. multiple water molecules in a cluster bridging between the hydroxyl-terminated surface and the pyridine moieties.

### 4.2.3 Metallized P2VP Domains

Following platinization and plasma treatment, the nanoscale patterns of the self-assembled BCPs become apparent as shown in the AFM micrographs in Figure 4.11, and the cross-sectional thickness measurements in Figure 4.12. The thicknesses, as before, refer to the starting thickness of the BCP film before annealing, as determined by ellipsometry. In the thinnest film, the 40 nm-thick sample, the hole features that are speckled across the surface are regions that appear completely pattern-free, surrounded by random dots (Figure 4.11A), with a height difference of  $\sim 8$  nm (Figure 4.12A). The holes apparently result from dewetting due to redistribution of polymer, leaving the hole-region devoid of any BCP-templated Pt pattern, as the region was covered only by the PS-*b*-P2VP brush layer. All parts of the otherwise homogeneous region surrounding the holes are covered by a uniform layer of dots, with no lines present.

As the film increases in thickness to 43 nm (Figures 4.11 and 4.12B), regions of ordered parallel lines appear, separated by large regions of dot-patterns; lower resolution imaging of this film shows no dewetting, and a uniform thickness. The regions of parallel lines are  $\sim 3$  nm lower than the random dot regions (Figure 4.12B and Figure 4.4). The thicker film of 45 nm (Figures 4.11 and 4.12C) consists of almost entirely of lines with a characteristic fingerprint line pattern, with only

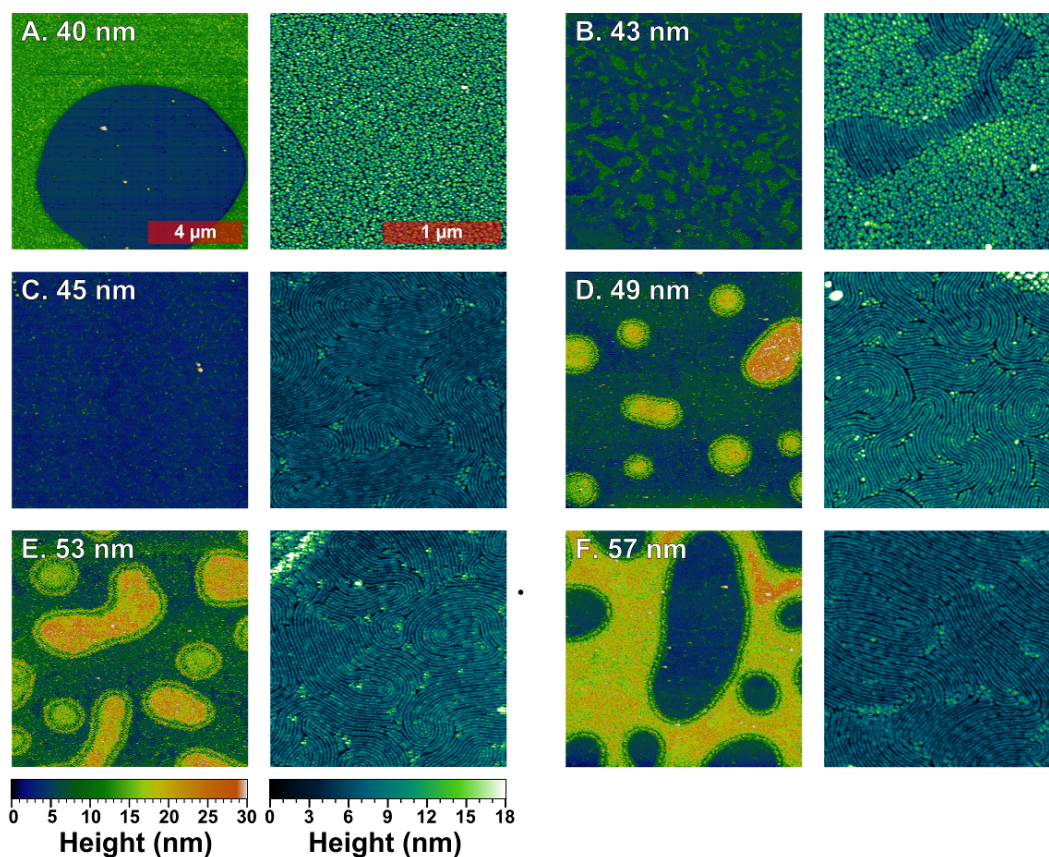
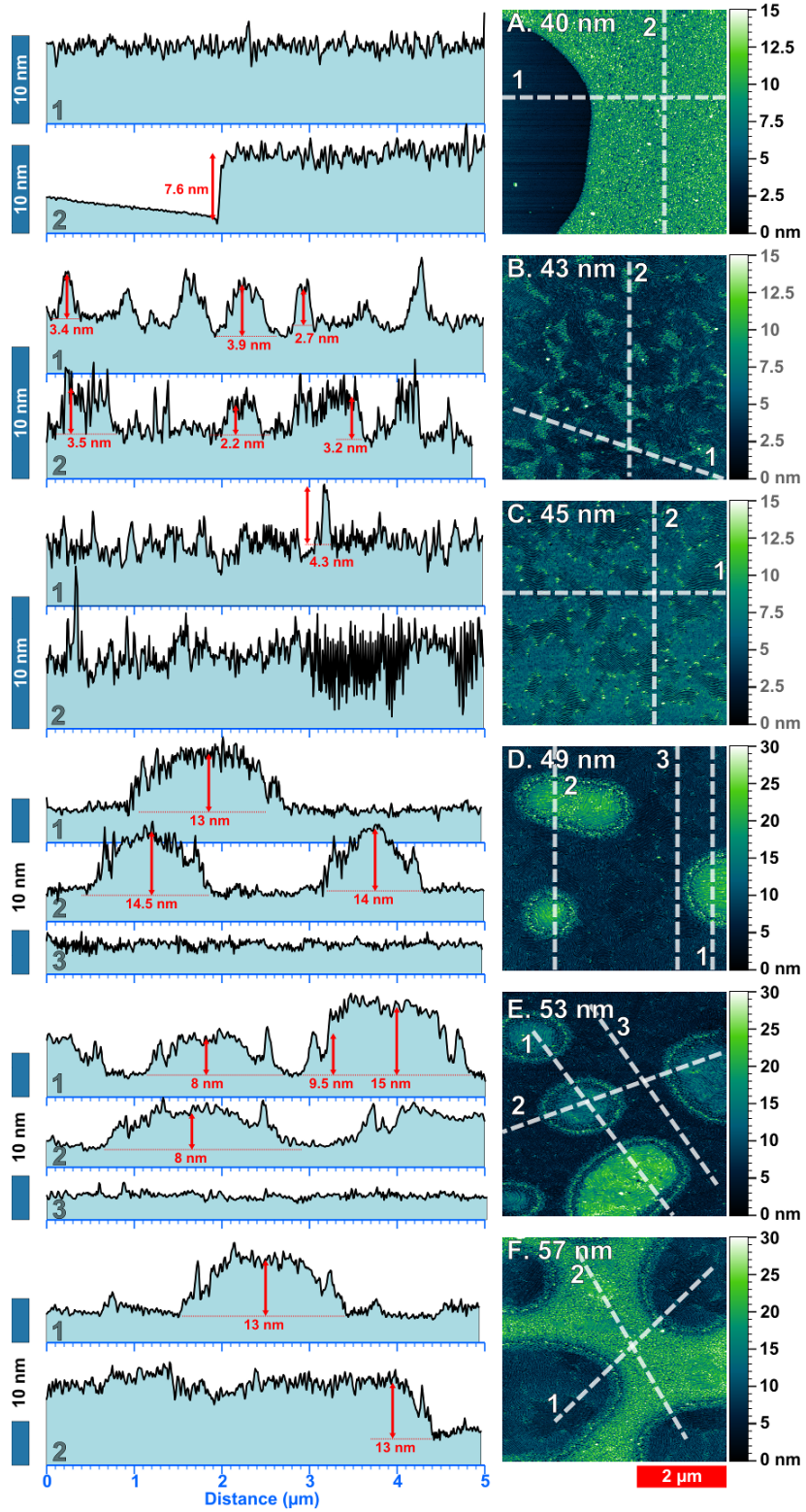


**Figure 4.11:** AFM images of the platinum nanopatterns after platinization and plasma treatment, for different initial film thicknesses, from 40 nm – 58 nm. All left-hand side images are lower resolution images,  $10\ \mu\text{m} \times 10\ \mu\text{m}$  (512 px x 512 px), intended to capture all visible features. All right-hand side images are higher resolution images  $2\ \mu\text{m} \times 2\ \mu\text{m}$  (512 px x 512 px), of monolayer regions, exclusively. A 40 nm. B 43 nm. C 45. D 49 nm. E 53 nm. F 57 nm.



a few stray dots, and no other texture resulting either from dewetting or island formation, as shown in the AFM images in Figure 4.13, taken over a range of length scales.

Within each of the images, the features remain consistent. Similar periods (accounting for thermal drift of the AFM) can be found from the profiles of lines in each possible configuration: within a dot layer; as part of a monolayer of horizontally oriented cylinders; and on islands. Where compression from thermal drift is absent, the line period matches the period observed *via* SEM, 30 nm.

Increasing the film thickness further to 49 nm and above (Figures 3D and 4D) resulted in the observation of islands comprised of double layer films,<sup>[2]</sup> about 13-14 nm higher than the surrounding monolayer areas, surrounded by a buffer of thick vertical cylinders or dots. Be-

---

**Figure 4.12 (preceding page):** *AFM measurements of the thickness of the platinum nanopatterns, with different initial thicknesses: A. 40 nm. B. 43 nm. C. 49 nm. D. 53 nm. E. 57 nm. All AFM images (right) are 512 px × 512 px and 5 μm × 5 μm. Corresponding profiles, each 20 px wide, are marked on the AFM with a dashed white line; the numbers identify each profile (left) and indicate the origin. Profiles are approximately 5 μm each, and have been scaled vertically, as indicated by the 10 nm tall blue bars on the left. Heights of particular features are indicated with a red double-headed arrow.*

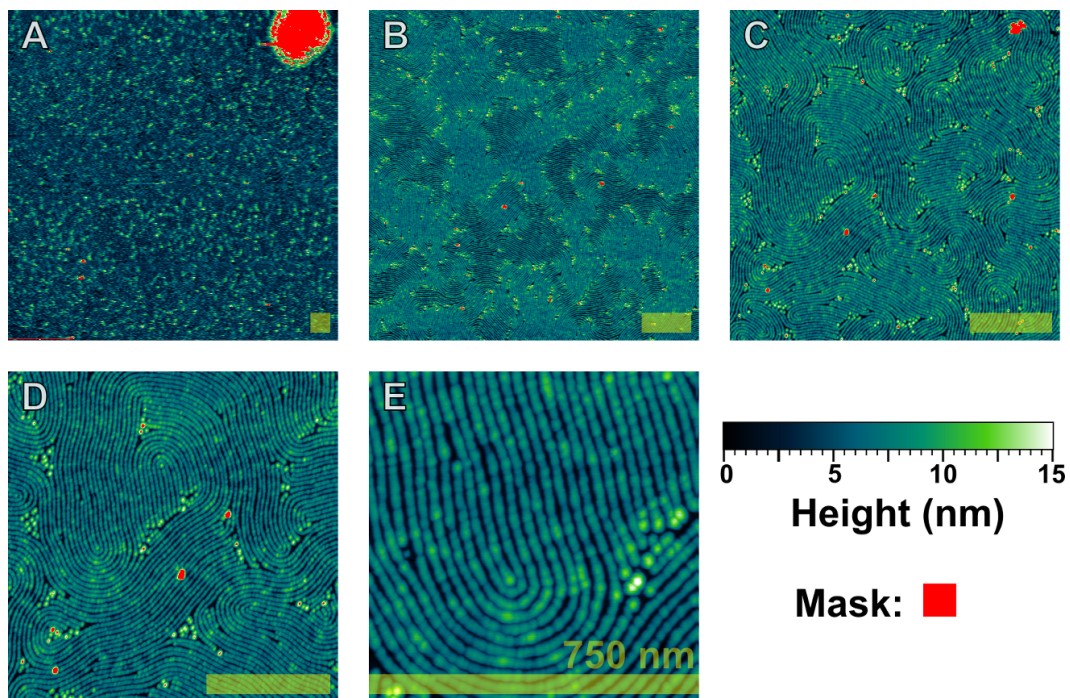


**Figure 4.13:** AFM images of the same region of 45 nm film at five different resolutions. To provide a relative sense of scale, the yellow scale bar on each image is 750 nm wide and all images are set on a 15 nm scale, with anomalies masked in red. At the top right of the lowest resolution image (A) is a rare double-layer island. Bright features forming a faint texture can be observed in images A-C, which are observed to be the dots clustered with the terminal points of lines in the pattern.

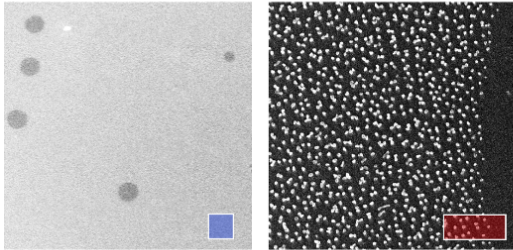
tween these isolated features, a monolayer line pattern was observed, which was otherwise consistent with that observed at 45 nm. The islands increase in size as the initial layer thickness increases to 53 nm and 57 nm, and these thicker films possess largely the same features as that at 49 nm (Figures 4.11E and F, 4.12E and F).

The islands of the 57 nm-thick films largely consist of a dot pattern (see Figure 4.23), interspersed with patches of double layer lines. AFM of the polymer films show that the height of these islands is ~24 nm higher than the monolayer cylinders of the second dot pattern. Within this pattern can be observed small patches ~2 nm higher, corresponding to the patches of double layer lines (see 4.22 and Table 4.4).

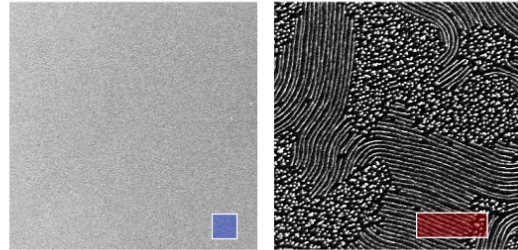
The overall trend from brush regions without a nanoscale pattern, to dots, to horizontal cylinders, to vertical cylinders/dots, to double layer cylinder regions, is consistent with previous reports.<sup>[2,29]</sup> The trend observed for bilayer islands in the thickest films, at 49 nm, 53 nm, and 57 nm, which as the film thickness increases progress from circular islands (49 nm) to stretched out islands (53 nm) and finally to become a continuous network with only pockets of single layer regions within (57 nm), has been previously described.<sup>[181]</sup> This trend is consistent with what is observed in SEM images of the films, shown in Figure 4.14.

As can also be seen in close-up SEM images of these non-uniform fea-

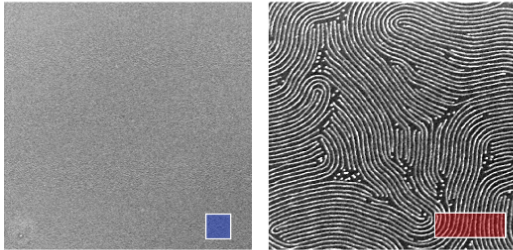
**A. 40 nm**



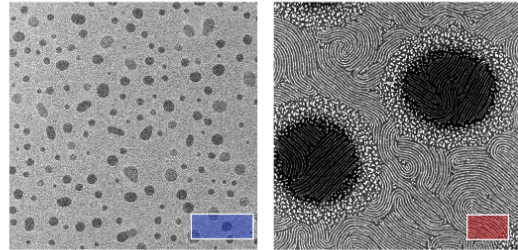
**B. 43 nm**



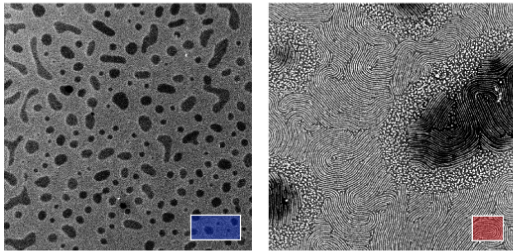
**C. 45 nm**



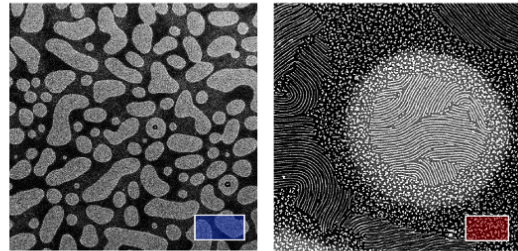
**D. 49 nm**



**E. 53 nm**



**F. 57 nm**



10  $\mu$ m

500 nm

tures in Figure 4.3, the dark patches, viewed at low resolution, are either holes or islands in the BCP thin films that result from relaxation and redistribution of the PS-*b*-P2VP on the SiO<sub>2</sub> surface. The dark appearance is an SEM effect which results from either the lack of surface

---

**Figure 4.14 (preceding page):** SEM images of the surface showing the texture of each surface corresponding to the thickness of the spin-coated film. Images on the left of each column show the texture at low magnification (blue scale bars 10 μm wide) as well as the corresponding features corresponding in the right of each column at higher magnification (red scale bars 500 nm wide). A (40 nm) shows scattered dark holes with no Pt nanoscale features present, while the bright areas are covered with a uniform dot pattern. B (43 nm) is uniform at low magnification, however higher magnification shows a textures surface with regions of parallel Pt nanolines (brushstroke-like appearance) surrounded by dot regions. C (45 nm) The surface is largely uniform and on close inspection is covered by a line pattern with very few dots interspersed. D (49 nm) Dark islands appear on the surface, which correspond to double-layer lines surrounded a corona of dots. Regions between the islands are covered by uniform monolayer line patterns. E (53 nm) The pattern is similar to D, except for a larger coverage of the surface by islands and the islands becoming more elongated in shape. F (57 nm) The dark “island” plateaus are continuous with isolated regions of monolayer cylinders. The island regions’ dot patterns are not limited to the corona, and the surface of the dark region has patches of double-layer lines.

features (holes) or from the lack of electrical contact with the surface (islands) compared to monolayer regions where lines and dots exist in good contact with the surface; The lack of contact is primarily the result of the plasma process not being optimized for bilayer films.<sup>[2]</sup>

While the islands and holes observed are obvious defects in the film, the question remains, as to the defectivity *within* the monolayer regions in the midst of these islands and holes. Examination of the uniform monolayer regions, excluding any neighbouring islands or holes, would reveal whether the defectivity of the annealed BCP thin film is influenced in any way by the initial thickness condition imposed when spin-coating, or by the presence of large neighbouring defects such as micrometre-wide islands.

#### **4.2.4 Accessing Defectivity**

In order to accurately determine defect densities, sampling the regions exclusive of these islands and holes might provide a better measure of the defectivity for these monolayer areas of the films, with respect to any annealing process. Consequently, unoptimized films of non-ideal thicknesses could remain suitable for defect density and periodicity measurements, whereas bulk analyses of order, such as small angle x-ray scattering (SAXS) and GISAXS would lead to inaccurate measure-

ments of the film due to averaging over all areas. In order to accurately determine defect densities of the monolayer regions, an open-source, freely available algorithm, called *ADABlock*, written for use with ImageJ,<sup>[146,147]</sup> was used on the corresponding SEM images (Figure 4.15). Information about obtaining *ADABlock* is provided in the Supplementary Information.

Images analysed for defect quantification are generally taken to exclude the regions that are not monolayers as they represent a different film thickness and corresponding structure. Selection of regions in this manner is often necessary for spin-coated samples, as films at substrate edges, comet tail defects, or dewetted areas, for example, are not uniformly thick. Such selectivity, avoiding regions of variable thickness, may result in apparently contradictory observations between more averaged “bulk” measurements of pattern quality and local defect analysis counting. Moreover, in the bilayer regions, the algorithm is unable to provide an accurate measure of defect density, largely due to lower contrast and the level of etching, and may also not be meaningful as a measurement, given the different nature compared to the target monolayer line region where two overlapping and sometimes interconnected patterns exist.<sup>[53]</sup>

Application of the open source *ADABlock* defect quantification algorithm on monolayers regions is shown in Figure 4.15. The total pro-

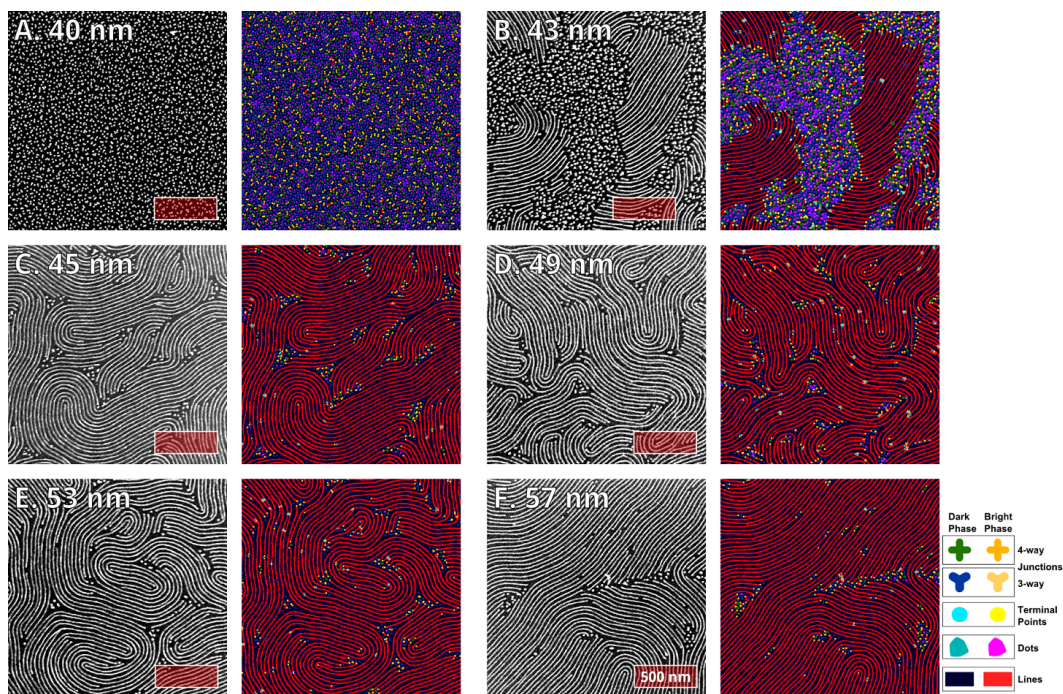


**Figure 4.15:** High resolution SEM images (left) of monolayer regions observed in each of the samples, with different initial monolayer thicknesses. On the right of each SEM image is a depiction of the defects, identified by colour and defects by colour and shape using the ADABlock algorithm. The bright phase lines are in red; dots in magenta; junctions in peach (3-way trifoil) and gold (4-way plus sign); terminal points as yellow circles. The dark phase lines are in dark navy blue; dots in turquoise; junctions in blue (3-way trifoil) and green (4-way plus sign); terminal points as aqua circles.

portion of surface coverage for island and hole regions, along with the corresponding coverage of lines and dots, is plotted in Figure 4.16A as a function of film thickness, as a reference. Only the monolayer regions were analyzed for defectivity. With thicknesses below 45 nm, the defectivity is dominated by thinner regions of dots, which increase the defectivity to  $\sim 1000$  defect-pairs $\cdot\mu\text{m}^2$  for fully covered regions, and a roughly interpolated defect level depending on the coverage of lines and dots for the mixed surfaces with mixed dot/line textures, as is the case at an initial film thickness of 45 nm (Figures 4.15-B, Figure 4.16B). The measured maximum of  $\sim 1000$  defect-pairs $\cdot\mu\text{m}^2$  value would correspond to a period-normalized defectivity metric of  $\sim 0.9$ , with 0 being a defect-free striped pattern, and 1 representing a layer of hexagonally packed dots, which presents the maximum defectivity possible for the pattern, corresponding to a domain consisting purely of dots at a 30 nm period. At or above the monolayer thickness ( $\sim 45$  nm), the defectivity of these monolayer regions remains constant: 92 to 128 defect-pairs  $\times\mu\text{m}^2$ , with all values falling within 1.5 standard deviations.

The measured period, shown in Figure 4.16C, is also consistent for uniform-monolayer regions covered by pure lines, which indicates that the monolayer lines do not stretch or compress in width to accommodate the thickness variation; island formation is sufficient to allow

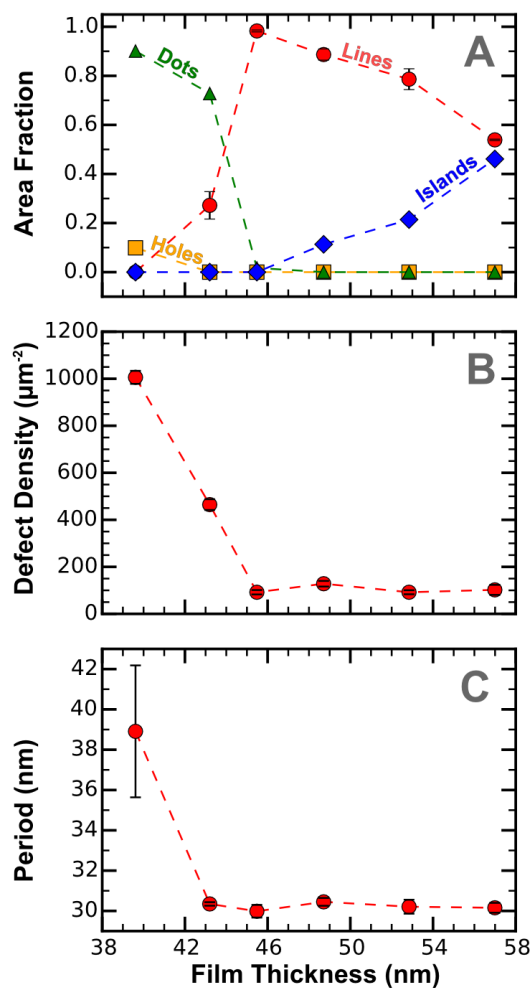


**Figure 4.16:** Data for metallized patterns of PS(34k)-b-P2VP(18k), thermally annealed at 200 °C for 20 minutes. A. Proportion of the surface covered by each region-type in the annealed films as a function of as-cast film thickness: dots (green triangles), lines (red circles, with standard deviations marked), holes (yellow squares), and islands (blue diamonds). B. Measured defect density for monolayer regions, excluding islands and holes, as a function of as-cast film thickness. Standard deviations indicated by error bars. C. Azimuthally-measured period for monolayer regions as a function of as-cast film thickness. Dashed lines connecting data points.

for modulation of film thickness to correct for the film's non-integer layer thickness. On the other hand, areas covered by the pure dot texture show a significantly increased period, as observed by others.<sup>[174]</sup> A similar example of films forming terraces of monolayers, bilayers, and trilayers has been observed in the course of solvent annealing as films swell<sup>[2,53]</sup>, where redistribution of the polymer across the surface eliminates regions of non n-layer thickness. Gradations of thickness are limited to narrow regions at the edges of islands and holes, leaving the rest of the polymer film a uniform thickness, as depicted in the model in Figure 4.17.

#### **4.2.5 Defectivity Near Island Features**

Finally, the possibility exists that the presence of holes and islands could influence the defectivity of nearby regions. Examples of the complexity of structures observed near holes and islands are shown in Figure 4.18. One curious and notable feature in these AFM images, in Figures 4.18B-D, is the bright ring around the islands. These rings are comprised of bright dot (vertical cylinder) features that extend ~9 to ~12 nm higher than features on either the outside (lines) or the inside (dots). It may be that these perpendicular cylinders are at an optimal point on the edge of the island where metallization is facile or it could represent a change of phase beyond that point to a multilayer of

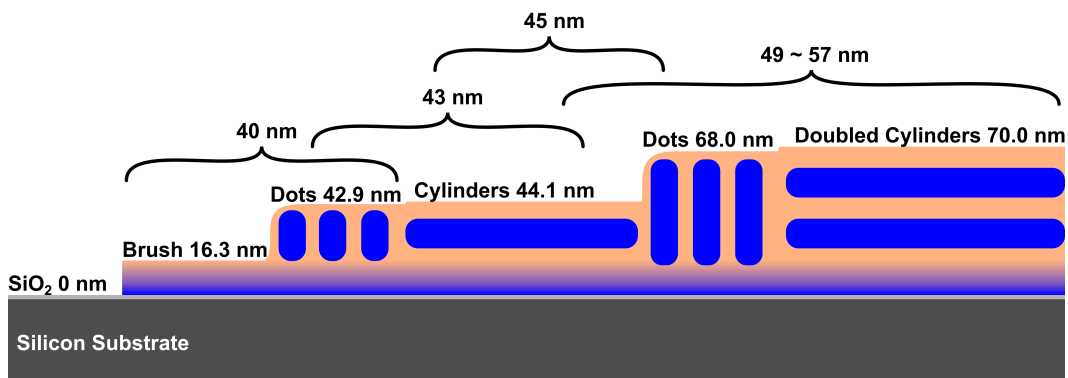


**Figure 4.17:** The schematic shows a simple model of the block copolymer thin film, with each of the plateaus observed labelled and the cumulative thickness provided. The plateaus result from the film adopting different equilibrium thicknesses, corresponding structures of the P2VP phase, which is shown in blue, against the orange color coding of PS. The structures formed, in order of increasing thickness: a brush layer plateau (16 nm), a plateau of dots (43 nm), a plateau of cylinders (45 nm), a second plateau of dots (68 nm), and finally a plateau of a bilayer of cylinders. Above are provided the film thicknesses measured, in films as-cast, measured using ellipsometry, with brackets identifying the range of structures observed.

spheres, which do not metallize equally well.

Profiles of lines at the top of islands show nearly regular longitudinal spacing, but more irregular vertical position, possibly owing to either the morphology of underlying cylinders, or the degree of metallization. On the other hand, cylinders in monolayer regions show highly regular heights except at terminal points, which typically appear higher. Although it was not observed for the AFM scans of the BCP islands, in some AFM images of the first dot layer, we observed hexagonally packed protrusions ( $\sim 1$  to 3 nm above the background) along the edge between the brush layer and the dot layer, shown in Figure 4.19. Such structures may be more accessible to solution for metallization.

In order to assess the impact of islands on the defect density in their immediate vicinity, an analysis of defects in areas adjacent to the double-layer islands was performed. While the defect measurements in Figure 4.15 were taken using SEM images collected from regions not immediately adjacent to islands or holes, SEM images where either the entirety of islands or the edges of islands were contained were also collected. Using manually created selections, as shown in Figure 4.20, chosen to follow the edges of the islands, defects were determined as a function of minimum distance to the edge, and the counts normalized numerically according to the distance. As the coronal dot regions show up well in SEM, two edge choices were selected: the inner boundary

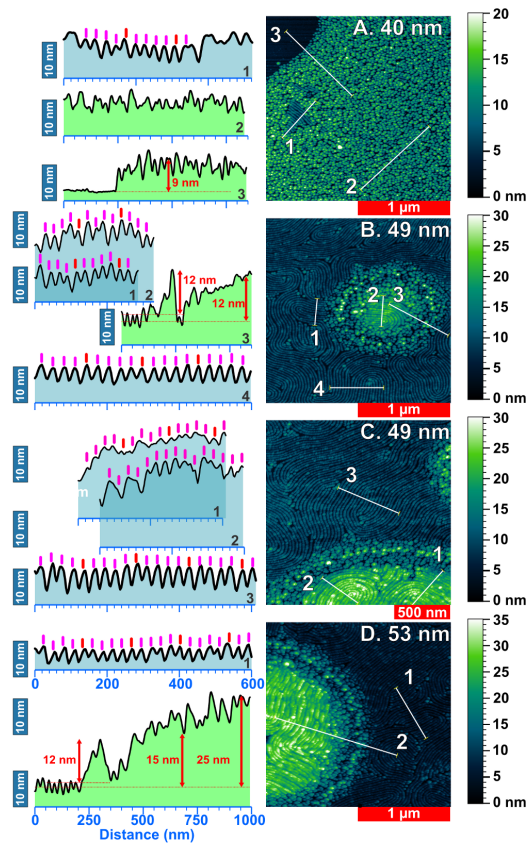


**Figure 4.18:** AFM images of the film near islands and holes, along with profiles. Blue profiles and green profiles have different lateral scales as indicated at the bottom, but all have the same vertical axis, as indicated by the scale bars, however some compression is evident in the y-axis due to thermal drift. All AFM images (right) are  $512 \text{ px} \times 512 \text{ px}$  and  $2 \text{ } \mu\text{m} \times 2 \text{ } \mu\text{m}$  (A,B,D) or  $1.65 \text{ } \mu\text{m} \times 1.65 \text{ } \mu\text{m}$  (C). Corresponding profiles, each 4 px wide. A. (40 nm initial thickness), the dot pattern film near a hole, showing a rare region with lines. B. (49 nm initial thickness), a small island. C. (53 nm initial thickness), edge of a larger island. D. (49 nm initial thickness), edge of an island roughly twice the height of the island in B.

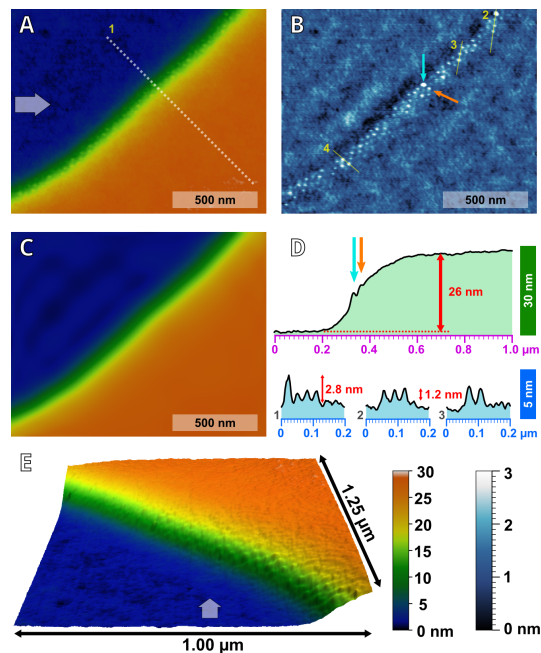


**Figure 4.19:** A. AFM and profile of 40 nm PS-*b*-P2VP thin film showing the edge of an isthmus of vertically oriented cylinders between two holes. At the edge, the cylinders can be observed protruding, revealing the underlying structure of the film. B. Pseudo-hexagonally packed cylinders can be observed after background subtraction. C. Background resulting from fitting the surface with a polynomial equation in  $x$  and  $y$ . D. Profiles of the bumps, observed in A and C, range from  $\sim 0.5$  nm to 3.0 nm in height. The bumps in the line profile of A are marked with cyan and orange arrows in B, where the corresponding bumps can be clearly seen. E. A 3D projection of the edge; the white arrow shows the orientation relative to A.

of the coronal dot region, which interfaces with the double-layer lines; and the outer boundary of the coronal dot region, which interfaces with the monolayer lines region.

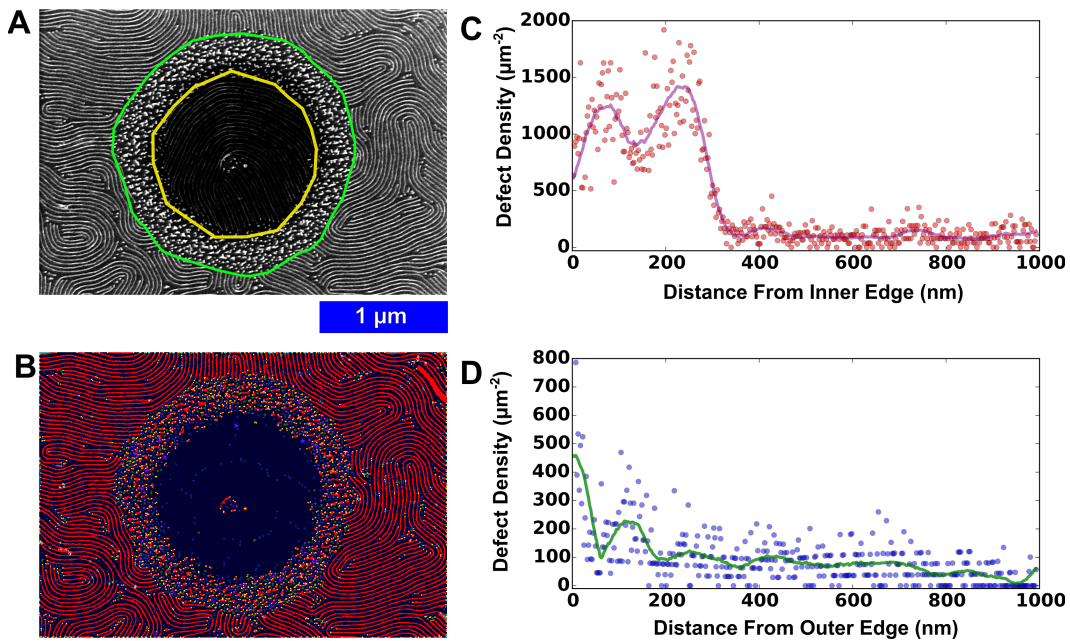


**Figure 4.20:** Influence of islands on defectivity of neighbouring regions. *A.* Original Image with a coronal region dots encompassed by an inner boundary edge (yellow)  $\sim 1250$  nm diameter and an outer boundary edge (green)  $\sim 2000$  nm diameter. *B.* Defect analysis image, with phases marks, as in Figure 4.15. *C.* Defect density as a function of distance from the inner edge boundary; data smoothed using Savitzky Golay filter<sup>[187]</sup> shown as line. *D.* Defect density as a function of distance from the outer edge; smoothed data shown as line.

Inspecting the profile of the defect density from the inner coronal boundary, the coronal region has a defect density on the order of a region uniformly covered by dots,  $\sim 1100$  defect pairs  $\cdot \mu\text{m}^{-2}$ , across a width

of  $\sim 300$  nm. Beyond the edge of the region, at  $\sim 330$  nm, an average defect density of  $\sim 120$  defect pairs $\cdot\mu\text{m}^{-2}$  is observed, with no significant slope relative to the boundary. As the width of the coronal dot region is not entirely uniform, the edge observed in the data is likely a convolution of the actual edge of the outer coronal boundary and the line region in the immediate vicinity. In order to tease out the effect on regions immediately external to the coronal boundary, the outer edge was selected and the analysis repeated. Within the first 50 nm of the edge, there is a sharp drop off in the density of defects whereas in the nearby region, from  $\sim 50$  nm to  $\sim 200$  nm, we do observe a level of defectivity roughly double the background level in regions beyond 200 nm, where the defect density remains relatively uniform.

This thin buffer zone is likely dictated by the correlation length of the patterns, which range from  $\sim 200$  nm to  $\sim 300$  nm in most cases, hence they would have no influence on the defectivity beyond such a narrow buffer zone. It is worth noting that patterns in the thickest films exhibited correlation lengths of  $\sim 500$  nm in some cases, which appears to be a consequence of the confinement of these patterns inside patches surrounded by the continuous double layer “islands”. Confinement in small spaces, allowing for greater alignment within, is one of the principles of graphoepitaxy, and the same appears at work here. The islands themselves typically present a well-ordered arrangement of

cylinders at the surface, possibly also an effect of their confinement.

### 4.3 Summary

In summary, we observed a consistent defect density for the monolayer line pattern component of annealed BCP thin films above a threshold thickness for initial thickness following spin coating, which in this case is 45 nm, when evaluating the monolayer regions. An increase in the coverage by islands containing thick dot/double-layer equilibrium structures for thicker films above the optimal thickness needs to be considered for large areas, but does not result in a change in defect density within the monolayer regions, except within a narrow periphery, as directed by the correlation length. These observed transitions, from almost exclusive dots at thin initial thicknesses, to double layer regions at higher initial thicknesses are consistent with predictions from confined structures, where a transition from vertical cylinders, to monolayer horizontal cylinders, to vertical cylinders or bilayer dots, to bilayer horizontal cylinders, has been predicted computationally,<sup>[21]</sup> however such numerical methods for block copolymers have not yet provided prediction of the formation of well-defined islands in preference to forming films of intermediate thickness.

In addition, very small changes in the thickness of the block copoly-

mer result in different phases: 1.2 nm less than the ideal thickness for a film of monolayer horizontal cylinders, and 2.0 nm less for a double layer of cylinders results in vertically oriented cylinders, substantially increasing the defectivity of the overall film. However, so long as the ideal thickness is met or overshot, regions of monolayer cylinders will have a consistent level of defectivity. These finding should be of use in making the analysis of block copolymer thin films outside of directing features more widely accessible as a screening tool for characterizing pattern quality, as a greater margin of error in the thickness of cylinder-forming BCPs would still allow for consistent defect measurements.

## 4.4 Materials and Methods

The PS(34k)-*b*-P2VP(18k) (PDI 1.05) block copolymer was obtained from Polymer Source Inc., QC. Toluene (HPLC grade; >99.8%) was purchased from Fisher Scientific; concentrated H<sub>2</sub>SO<sub>4</sub> (reagent grade) from Caledon Laboratories; 30% aqueous H<sub>2</sub>O<sub>2</sub> from Sigma-Aldrich (ACS reagent); and Na<sub>2</sub>PtCl<sub>4</sub> · xH<sub>2</sub>O from Strem Chemicals. Silicon wafers were obtained from University Wafer.

#### **4.4.1 Substrate Preparation**

100 mm diameter, single-side polished silicon wafers were diced into squares with dimensions 1.0 cm x 1.0 cm. Prior to cleaning, substrates were scribed, on the unpolished side, with a diamond-tip, to mark the identity of each substrate as part of a set of 10. The samples were then immersed in methanol and sonicated for 15 minutes in glass beakers. Next, after rinsing each substrate square in a series of 18.2 M $\Omega$  cm water beakers, the substrates were placed polished-side-up in PTFE beakers, and immersed in 6.0 mL of concentrated H<sub>2</sub>SO<sub>4</sub>, to which was added 2.0 mL of 30% H<sub>2</sub>O<sub>2</sub>, before placing the beaker to stand in an 80 celsius hot water bath for 20 minutes. The piranha solution was then decanted to a glass flask to cool prior to neutralization.

Following several rinses with water, the substrates were immersed in aqueous 1% NH<sub>4</sub>OH solution for 5 minutes to remove any surface sulfonate groups, prior to a final decant and replacement of the solution with 18 M $\Omega$  cm which was repeated twice. Typically samples were stored immersed in water with the top sealed with paraffin wax.

#### **4.4.2 Solutions and Spin Coating**

Immediately prior to spin coating, each wafer was dried under a nitrogen stream. Once dry, the substrate was analyzed using fixed-angle,

single-wavelength ellipsometry (632.8 nm) to determine the thickness of the thermal oxide at the center; typically 2 nm. Spin coating was carried out under argon or nitrogen gas. Each substrate's polished side was evenly coated with 10  $\mu$ L of 10-15 g/L BCP solution: 10 g/L for 41 nm; 11 g/L for 45 nm; 12 g/L for 47 nm; 13 g/L for 50 nm; 14 g/L for 54 nm; and 14.5 g/L for 58 nm. Solutions were each prepared by weighing a small mass of solid BCP (*circa* 50.0 mg) in a glass vial (8 mL; 17x60 mm), adding a specified volume of toluene (*circa* 5.000 mL), weighed, followed by addition of a small PTFE-coated stirbar and sealing tightly with a PTFE-lined cap. Solutions were stirred for a minimum 12 hours at 50 °C. Any bubbles in the toluene-BCP solution on deposition were manually removed by inducing a pressure wave within the spin coating chamber prior to spinning by manually tapping on the lid of the spin coating chamber; then the substrates were spun for up to 15 s, between 3000 rpm and 4000 rpm, with an initial acceleration of 1500 rpm/s. Following this, the film was reanalyzed by ellipsometry, prior to quartering the sample and annealing, to determine the thickness of the polymer film on top of the SiO<sub>2</sub> surface layer.

#### **4.4.3 Ellipsometry Measurements**

Ellipsometry measurements for each of the substrates was collected to determine the thickness of the freshly cleaned SiO<sub>2</sub> layer prior to spin

coating. Then after spin coating the PS-*b*-P2VP film on the substrate, the film was again measured with ellipsometry to determine the thickness of the polymer layer. The psi ( $\psi$ ) and delta ( $\delta$ ) values are reported in Table 4.2.

#### **4.4.4 Annealing**

Thermal annealing was carried out in ambient atmosphere on a hot-plate covered with a thin aluminum sheet. Temperature was monitored directly at the wafer using an OSENSA fiber-optic fluorescence-based temperature probe. The substrates were annealed for 20 minutes at 200 celsius.

#### **4.4.5 Metallization and Plasma Processing**

A solution of 20 mM  $\text{Na}_2\text{PtCl}_4$  in 0.9 M aqueous HCl was used for metallizing PS-*b*-P2VP samples. Samples were submerged for 3 hours prior to removal and rinsing with 18 M $\Omega$  cm water.

Following metallization, sample sets were placed together in a plasma chamber, and the chamber was evacuated to < 200 mTorr. Gas lines emptied via vacuum drawing to remove any contaminant gases or adsorbates, again bringing the pressure down to < 200 mTorr. Finally,  $\text{O}_2$

Label	Solution	d(SiO <sub>2</sub> )	Psi	Delta	d(Film)	Psi	Delta
nm	mg/mL	nm	deg.	deg.	nm	deg.	deg.
40	10.0	2.85	10.5248	170.9060	39.61	21.5024	95.5026
43	11.0	2.73	10.5168	171.2480	43.20	22.7648	92.3162
45	12.0	2.74	10.5300	171.2198	45.48	23.5408	90.3584
49	13.0	2.72	10.5332	171.2720	48.71	24.6226	87.7966
53	14.0	2.72	10.5302	171.2684	52.84	26.0290	84.7998
57	14.5	2.63	10.5358	171.5164	56.99	27.4292	82.1352

**Table 4.2:** Ellipsometry measurements of thin films on SiO<sub>2</sub>/Si substrates. Concentrations of solutions used and values of psi and delta are provided for corresponding substrates before and after spin coating. Each psi and delta value pair was measured 5 times and the average taken. Values of thickness were determined using standard multilayer ellipsometry models for single wavelength ( $\lambda = 632.8$  nm) measurements taken at 70° from the normal, with the following layers: Si substrate ( $n_s = 3.85$ ,  $k_s = -0.02$ ); SiO<sub>2</sub> native oxide ( $n_{SiOx} = 1.457$ ,  $k_{SiOx} = 0$ ); PS-b-P2VP ( $n_{PS-b-P2VP} = 1.587$ ,  $k_{PS-b-P2VP} = 0$ ); air ( $n_{air} = 1.000$ ,  $k_{air} = 0$ ). The refractive index of the PS-b-P2VP film was approximated as that of the PS block, however this is not greatly different from the value of P2VP, which has an index of refraction of approximately 1.59 ~1.62.

gas was continuously leaked into the chamber to a steady-state pressure of  $\sim 750$  mTorr while under vacuum. The RF coils were then energized and a faint lavender-blue  $O_2$  plasma was maintained for  $\sim 60$  s (depending on the film thickness) to etch the organic materials from the substrate.

#### **4.4.6 AFM Imaging**

Tapping mode AFM images of both annealed polymer films and metallized, plasma-treated samples were obtained in ambient conditions using a Digital Instruments / Veeco Nanoscope IV equipped with commercially available Si cantilevers from MicroMasch (HQ:NCS15/AL BS). Immediately prior to imaging, the samples were briefly swept with a nitrogen gas stream to remove any non-embedded particulate matter. AFM images were processed using Gwyddion 2.40 (<http://gwyddion.net/>) to level data and subtract background prior to analysis.

Step heights were determined from line profiles collected using Gwyddion. Each profile was 4-8 pixels wide. Profile data was exported to Excel for determination of step heights, as depicted in Figure 4.21.

The values measured using this method are reported in Table 4.3.

The trend of observed heights was partially convoluted, as small steps can, in certain instances, either increase or decrease the average val-

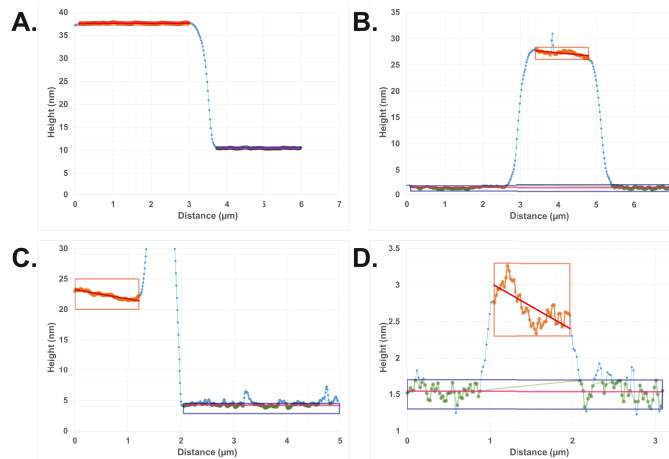


**Figure 4.21:** Example plots showing semi-automated fitting used to determine step-heights. For steps with no baseline overlap (A and C), the step height was measured at the midpoint, in the region between the two flat, fitted regions. For steps with a baseline overlap, the height was taken as the mean value of the fitted upper fitted region, relative to the flattened baseline.

Layer	Base	d	St.Dev.	$\Sigma d$	$\Sigma St.Dev.$
(Upper)	(Lower)	(nm)	( $\sigma$ , nm)	(nm)	( $\sigma$ , nm)
Brush / Holes	SiOx	16.27	0.40	16.3	0.4
Dots	Brush / Holes	26.64	0.64	42.9	0.8
Cylinders	Dots	1.20	0.14	44.1	0.8
Island (Dots)	Cylinders	23.72	0.84	68.0	1.1
Island (Cylinders)	Island (Dots)	2.06	0.63	70.1	1.3
Islands (Cylinders)	Cylinders	25.77	0.72	70.1	1.1

**Table 4.3:** Heights for each plateau, as measured by AFM, with reference to the underlying reference layer. Profiles were plotted for several images and heights measured by fitting the data, as shown in Figure 4.21.

ues observed. Bumps with a narrow height distribution can be observed in some plateaus, and these were profiled separately, where possible. Using kernel density estimate for each set of data, the contributions of these secondary plateaus to the overall height can be deconvoluted as shown in Figure 4.22, with data in 4.4. From the figure, the distribution of thicknesses measured for the brush layer in 4.22A skews toward 16 nm, which suggests that residual material from the scraping is likely responsible for the lower measured values, hence the maximum value (16 nm) is used as a proxy measurement. Similarly, 4.22E shows a bimodal distribution, indicating that the islands have both dot nanostructures (at 23-24 nm) bilayer cylinders nanos-

structures (at 26 nm).

Ref.	Sample	Description	Average	St.Dev.	Median	Min	Max	N
			(nm)	(nm)	(nm)	(nm)	(nm)	
A	40 nm	SiO <sub>2</sub> Surface to Brush	15.35	0.86	15.71	13.42	16.29	19
B	40 nm	Brush to Dots-1	26.80	0.60	26.78	25.38	28.93	40
C	43 nm	Dots-1 to Cylinders-1	1.21	0.14	1.19	0.95	1.63	40
D	49 nm	Cylinders-1 to Cylinders-2	25.77	0.72	25.91	24.58	27.17	15
E	53 nm	Cylinders-1 to Dots-2 / Cylinders-2	24.92	1.44	25.44	21.99	26.84	42
F	53 nm	Dots-2 to Cylinders-2 (Uncertain)	1.93	0.29	1.97	1.54	2.25	4
G	57 nm	Cylinders-1 to Dots-2	23.72	0.84	23.82	21.55	24.91	26
H	57 nm	Dots-2 to Cylinders-2	2.06	0.63	1.90	1.27	3.68	26

**Table 4.4:** Step-height averages measured for each sample, along with data on the distribution including the standard deviation, median, maximum, and minimum values, along with the number of profiles measured. References correspond to plots in Figure 4.22.

The apparent smaller step height observed in thicker films can be understood in terms of the texture of such film observed *via* SEM. In the thickest films, the now-continuous islands are primarily dots, with small regions of bilayer lines. The step regions are almost entirely comprised of dots, as seen in Figure 4.23

#### 4.4.7 TOF-SIMS Data

Time-of-flight secondary-ion mass spectrometry (TOF-SIMS) depth profiling was performed, using Cs<sup>+</sup> ions, in order to obtain the depth-dependent

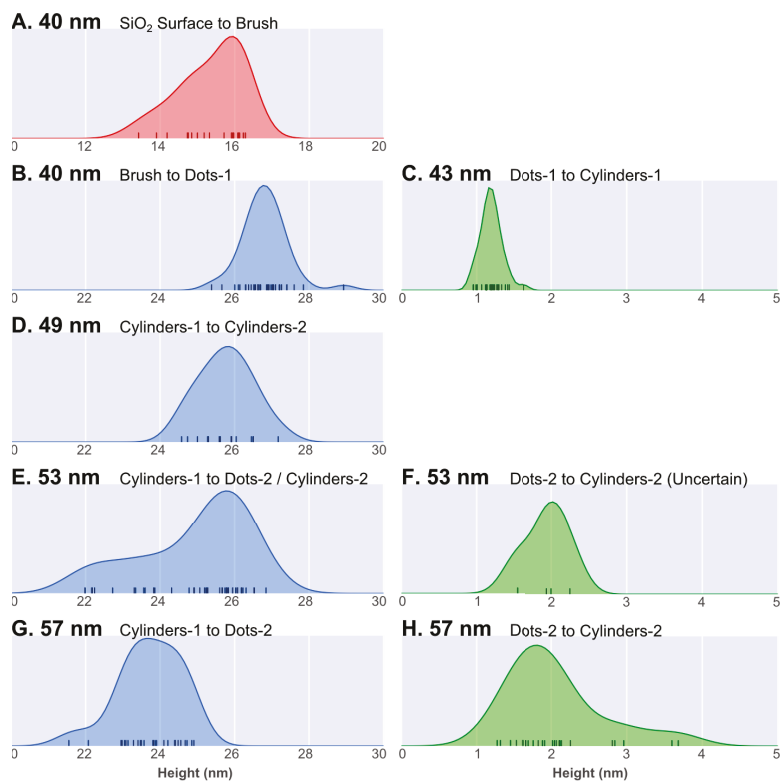


**Figure 4.22:** Kernel density estimates distributions of the data summarised in Table 4.3 to show the relationships between each measure. Green profiles are plotted on a 1-5 nm horizontal scale; blue profiles on a 20-30 nm scale; and red on a 10-20 nm scale. A. SiO<sub>2</sub> substrate to the brush layer. B. Brush layer to dot layer 1. C. Dot layer 1 to cylinder layer 1. D. Cylinder layer 1 to cylinder layer 2. E. Cylinder layer 1 to dot layer 2 (23 ~24 nm) or cylinder layer 2 (~26 nm). F. Small bumps (few observed) which may be dots layer 2 to cylinders layer 2. G. Cylinders layer 1 to dots layer 2. An example of the 57 nm film is shown in Figure 4.23. H. Dots layer 2 to cylinders layer 2.

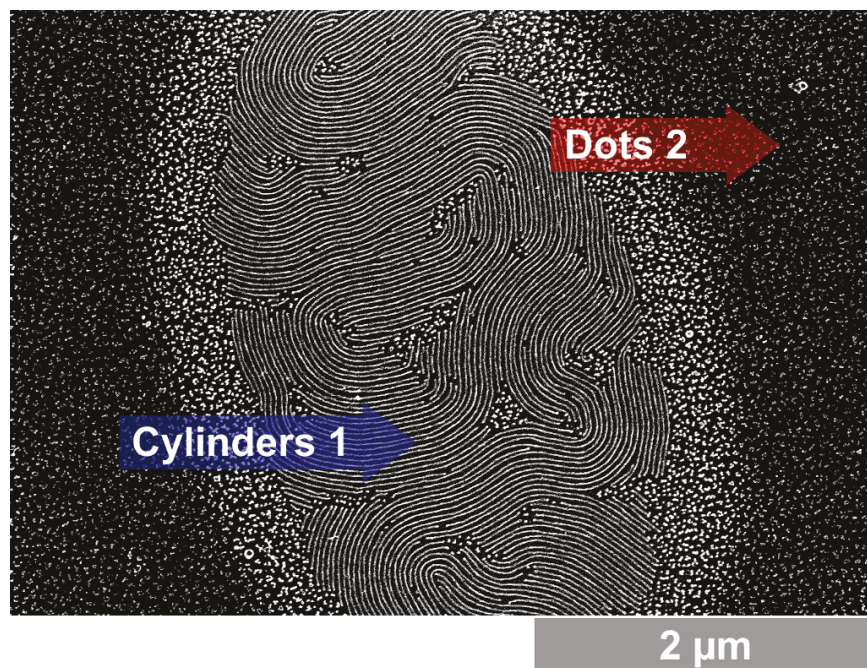


**Figure 4.23:** An SEM image of a platinized 57 nm sample, showing a region with a monolayer of cylinders and surrounded by the second level of the dot pattern. (See Figure 4.22, panel G)

composition of the 45 nm and 43 nm films. Due to the mixed morphology of the 43 nm films, the first nitrogen peak (CN) is skewed toward the surface.

#### **4.4.8 SEM Imaging**

SEM images of metallized, plasma-treated samples were collected using a Hitachi S-4800 scanning electron microscope using an electron energy 15k eV under high vacuum (pressure  $< 1 \pm 10^{-8}$  Torr). Sampling was limited to regions near the center of each substrate and far from any macroscopic features (such as comet tails) to avoid extraneous effects.

#### **4.4.9 Computation**

Defect analysis (in Figure 4.12) was performed for several images of each thickness, each without any island or hole features present, and typically selected from a region further than 1  $\mu\text{m}$  from any such feature, except where the effect of such features was of interest (in Figure 4.16). ADAblock, an algorithm designed to run in ImageJ was utilized to determine the number of topographic defects - dots, terminal points, junctions, and so forth - as previously described<sup>[20,40]</sup>. ImageJ,<sup>[146]</sup> version 1.49 and above, was used; it is available at <http://imagej.nih>.

gov/ij/. The code for performing the defect analysis is available on our institutional repository, including the distribution of defects with respect to the boundary; the main defect analysis used here is fully described in paper published in PLoS ONE<sup>[1]</sup>; the entire source code is freely available and updated versions will be available on GitHub at: <https://github.com/MurphysLab/ADAblock>.

# 5

## Summary and Outlook

### 5.1 Thesis Summary

The overarching goal of this thesis is to extend the analysis of defects in striped patterns formed from self-assembled block copolymer thin films. This was executed by first developing an open source, freely available algorithm, *ADABlock* to assess topological defects in the line patterns, as well as to measure the correlation lengths, and the roughness of the lines, measured as LER or LWR. In developing any new or

adapted metrology, the limits of these measurements were explored; here in conjunction with SEM images of metallized nanostructures derived from PS-*b*-P2VP. Using this tool, the effect of film thickness on topological defects in BCP thin films was explored in order to understand, fundamentally, when measurements are valid: insufficiently thick films possess a substantial admixture of dot regions, however once the film has sufficient thickness, the defectivity, island features excluded, remains roughly constant. This enables subsequent studies of annealing and composition, safe in the knowledge that small variances in the thickness of the film do not bear upon the defectivity of the monolayer regions which are sampled.

### **5.1.1 Chapter 1**

The first chapter provided the context which underlies the purpose of this thesis: The drive to make smaller features has exceeded the ability of conventional photolithography to keep shrinking. To sate the desire for smaller, nanoscale patterning, a variety of alternatives have been explored in academia and in industry: extreme ultraviolet (EUV) lithography; electron-beam lithography; nanoimprint lithography; scanning tip methods; and block copolymer (BCP) lithography. Each has its drawbacks, but BCP patterning succeeds in being rapid, massively parallel, inexpensive, and fully compatible with conventional

lithography.

### **5.1.2 Chapter 2**

As defects present one of the major challenges to directed self assembly with BCP lithography, the second chapter explores the current understanding of defects in BCP thin films and the challenges which they present. It starts with an introduction to the structure of block copolymers, specifically lamellar and cylindrical morphologies, which can be used to form striped patterns with thin films. The various types of defects and their effects are described, along with methods employed to analyze and quantify them. The key prevent their occurrence or to eliminate them through numerous annealing strategies.

### **5.1.3 Chapter 3**

*ADABlock* and its function is the subject of the third chapter. The algorithm used is described, both in text and visually, in order to communicate how the code works in a sequential fashion. The program was designed with visual output in mind, illustrating defects and orientation of the lines. *ADABlock* is then demonstrated using a variety of metal nanopatterns templated from cylinder-forming PS-*b*-P2VP, measuring the line-edge roughness (LER), line-width roughness (LWR), cor-

relation length, and defectivity as a function of image resolution and size. The code is summarized in Appendix [[[NUMBER]]] and is freely available on GitHub.

#### 5.1.4 Chapter 4

Chapter 4 addressed three aspects of the effect of initial film thickness on cylinder-forming PS-*b*-P2VP and the nanostructures formed from it: First, how the initial film thickness affects the overall film structure. Second, how this affects the metal nanostructures formed following metallization. Third, how the defectivity varies *within* the regions where monolayers of horizontally oriented P2VP cylinders predominate as a function of film thickness. And fourth, whether there is a local effect on the density of topological defects in the monolayer regions neighbouring where bilayer islands are present. Using the BCP, PS(34k)-*b*-P2VP(18k), with a period of 30 nm, we found the proportion of islands and holes was readily predicted from the initial thickness, once the heights of each plateau was known: the brush layer (16.3 nm); vertically oriented cylinders, or dots (42.9 nm); horizontally oriented cylinders, or lines (44.1 nm); vertically oriented cylinders, or dots (68.0 nm); and bilayer horizontally oriented cylinders, or double lines (70.0 nm). Given the small difference in height required to switch from dots to lines, it would be better to be able to slightly overshoot the ideal

thickness. Thus we assess the defectivity as a function of thickness, and find that the monolayer of cylinders, once established, maintains a constant defectivity. Moreover, the presence of islands in an annealed film has minimal effect locally on the number of defects (excluding the island itself). This sets up a convenient design for future experiments, where a slightly thicker film could be deposited, while knowing that the defectivity of the monolayer remains constant with respect to thickness.

## 5.2 Directions for Future Work

### 5.2.1 Further Refinement of ADABlock

Having developed a tool for analysis of defects has opened up many avenues of exploration using it. Already, we have utilized the *ADABlock* algorithm, both in its current form as well as earlier prototypes, to study the effect of microwave annealing<sup>[20,40,73]</sup> and blending<sup>[20]</sup> on the defectivity of striped patterns formed from cylindrical PS-*b*-P2VP, as well as on the line edge roughness of solvent-annealed single- and double-layer patterns.<sup>[2]</sup> However further refinements and additional features can yet be made. It is with an eye to this continuing work that the project is being hosted on GitHub, in order to enable collaboration

with others and continued improvement.

### **Grain Boundaries**

One improvement is developing better ways of recognizing typologies of defects, such as the variable, yet humanly-recognizable features of a grain boundary, as in Figure 5.1. This would not necessarily need to be done in ImageJ along with the *ADABlock*, but could be implemented in Python, either within ImageJ, or as a data post-processing using the connectivity and locations of features.

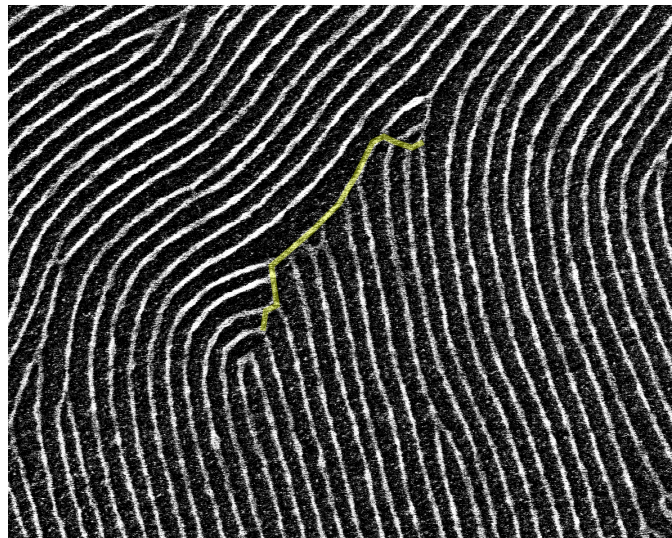


**Figure 5.1:** *Metallized PS-b-P2VP BCP pattern with a grain boundary highlighted in yellow.*

Finding a reasonable, deterministic means of identifying and counting grains using data for the orientation of lines, combined with infor-

mation on the location of defects and grain boundaries, would enable better interpretation of the correlation length, as well as the overall structure of the film. It would also provide a means to quantify the size distribution of grains and to perhaps take a better view of annealing as a grain-ripening process.

### **Loops and Spirals**

Another point of curiosity is the role of spirals and loops in the pattern, shown by examples in Figure 5.2. While loops are not a topological defect — although loops do contain a defect at their centre — it has not been investigated what barrier they present, if any, to the elimination of defects. Likewise, with spirals and whorls, commonly observed in the BCP "fingerprint" patterns, although the defects at the centre are measured and counted, the effect of the wound structure on enhancing or retarding defect elimination is unknown, hence a robust identification of such features may be worthwhile.

### **H-Junctions**

Junction pairs, formed bridging two lines, or by breaking a line (as shown in Figure 5.3), we term H-junctions. These can be viewed as tightly paired dislocations, however it may be useful to classify them

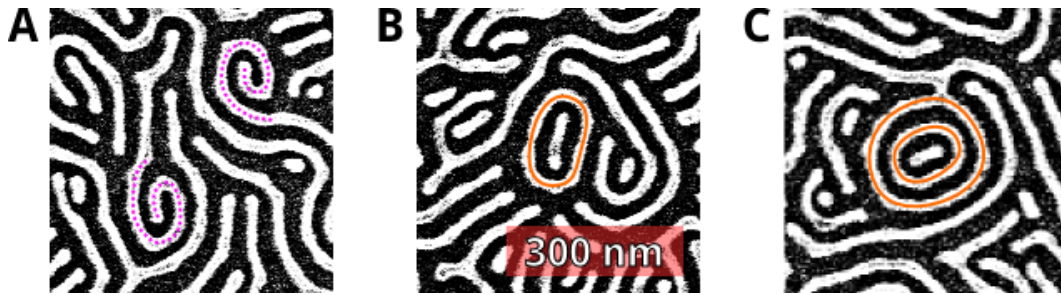


**Figure 5.2:** A. Two spirals marked with dotted magenta. B. Single loop, marked with an orange line. C. Concentric loops, marked with orange lines.

with a separate typology. For metallized P2VP domains and other methods of pattern transfer, it appears that such junctions can be formed by (1) incomplete metallization of domains or (2) other issues in the pattern transfer process and those which result from pinching of lines; alternatively (3) two (metal) lines can be bridged by some extraneous feature, creating a bridge between them. Hence it would be useful to find a way to differentiate between such features from thermally generated dislocations, and to understand them as a separate contribution.

### **Blobs and Featureless Regions**

Blobs, or large features, and regions without texture, formed from film misorientation or locally different morphology, are a challenge to identify and to define. At present, *ADABlock* is optimized to find, and translate into a binary pattern, uniformly textured regions. Features or ob-

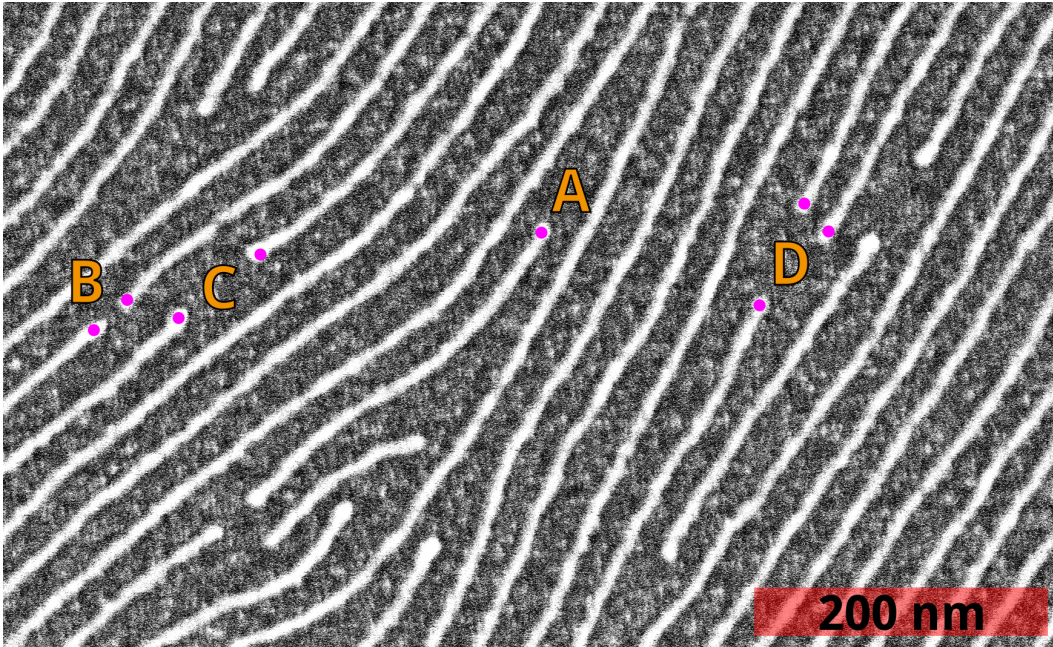


**Figure 5.3:** A. Shows a terminal point (marked in magenta) which is not part of an H-junction, but rather a dislocation. B. Shows two proximal terminal points, possibly from a "broken" line. C. Shows two distant terminal points, possibly from a "broken" line. D. Shows three terminal points, which cannot be simply paired.

jects without a periodic can be difficult to identify without human intuition: *Is this just a region with low contrast? Or is it something different?* In the context of local thresholding, necessary for nonuniform images, such features can be misinterpreted and incorrectly assigned or result in artifacts being generated.

### **Translating AFM Patterns**

Although the *ADABlock* algorithm can be used to analyze AFM patterns, it is not optimized for such, in particular, in creating a binary mask from such patterns. Thus AFM-specific thresholding which takes into account the physical shape and height differences accessible through such images would be useful. Additional 3D information on the shape of junctions and terminal points might also be gleaned from the defects, which cannot be accessed from flat SEM images. One example would be how the height of dot features in such films might be used to determine whether the feature results from a vertically aligned cylinder or from a more spherical domain.

While some additional information is available from AFM images, other information may be sacrificed. In particular, the limitation of AFM images however is the decrease in LER and LWR due to tip convolution. Hence SEM and He-ion microscopy will likely continue to be the pre-

ferred image acquisition techniques.

### **5.2.2 Use of Image Stitching**

Automated acquisition and stitching of SEM images has been a growing interest in biology for the comprehensive imaging of small organisms in order to study them in a holistic manner.<sup>[188,189]</sup> The technique is less frequently used in materials science, where surfaces are generally presumed to be homogeneous, hence appropriate for sampling, at some scale; for nanomaterials the scale is typically well within the maximum frame of reference or image size. BCP patterns, with increasing order, will require larger and larger areas in order to be sampled correctly. While *ADABlock* is designed primarily for sampling the range of reference frames accessible *via* SEM, it could, in principle, be extended slightly further with automated collection of stitched images. This, in turn, may require an effective routine to break large images into smaller pieces, followed by re-assembly of the data, to achieve suitably time-efficient processing.

### **5.2.3 Controlling Island Defects**

While islands and holes may not be topological defects, in the same fashion as disclinations and dislocations, they are defects nonetheless.

Such defects would be detrimental to the effective construction of integrated circuit architectures using BCP lithography. This has largely been overcome for *lamellar* BCP thin films, through the use of interfacial layers and top coats concocted to present neither block with a preferential attraction or repulsion. Block copolymers based on cylindrical domains are somewhat limited in this regard, as they have a very narrow range of ideal thicknesses which produce horizontal cylinders. They do however have the distinct advantage of enclosing one block within the cylinders, hence each interface needs only a single preferential interaction.

There may be a simple solution to the issue of thickness for cylindrical BCP thin films: It is observed, from work done with Wu<sup>[2]</sup> as well as my own work studying film thickness, that islands tend to nucleate on bits of dust or particles in the film. Thus it should be feasible to provide a set nucleation points by lithographically patterning posts on the substrate. Such posts could be positioned in order to control the location of island nucleation, as shown in Figure 5.4, removing the island defects from areas where the block copolymer pattern is desired, to locations where the islands may be selectively etched or removed by other means.

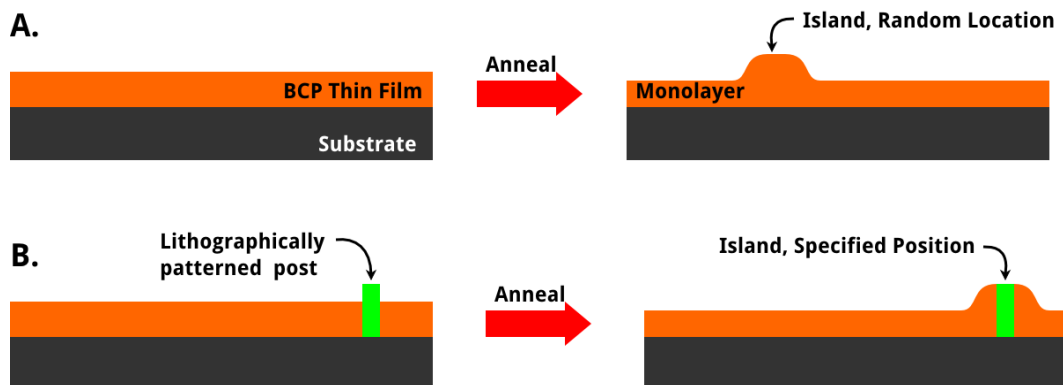


**Figure 5.4:** Illustration of A. how islands will randomly nucleate at some set density across the film surface, and B. how a lithographically patterned post, or an array of posts, could be used to designate locations for island formation.

## 5.2.4 Pattern Transfer Fidelity

Ultimately, for lithographic purposes, unmodified BCPs are a sacrificial structure, functioning as a template, rather than as the functional product. Consequently, a pattern transfer process is necessary. However the pattern transfer itself may introduce additional defects depending in the fidelity of the process. The metallization of P2VP domains in films of cylinder-forming PS-*b*-P2VP is a pattern transfer pertinent to this thesis, and, repeatedly, questions have been raised as to the fidelity of the metal nanostructures to the original P2VP domains. Although pinning of the metallized domains by PS certainly conserves most features of the P2VP domains and prevents some transformations of the pattern, other more subtle changes may be relevant. In partic-

ular, while the LER and LWR of the final metallized product can be assessed, it is difficult to assess the LER or LWR of the original P2VP domains. Strategies such as comparing TEM images of I<sub>2</sub>-stained P2VP domains to metallized domains may yield an answer; such experiments could be feasible with current silicon nitride membrane windows. It is also possible that the topology may change with the metallization process, breaking (or bridging) lines, and forming "H-junctions" as previously noted; again, it is difficult to determine from the metal nanostructures alone whether it is an issue.

### **5.2.5 Defects and LER**

There remains a relative paucity of studies on LER and LWR in BCP derived patterns; typically the focus has been on controlling orientation, managing registration, and eliminating defects. As it is possible, using *ADABlock*, to determine the LER and LWR for curved line patterns, it should be feasible to explore the evolution of LER and LWR during the annealing process, to see what influence defects have on roughness, and whether the two share any interaction. Additionally, although complicated, it may be possible to analyze positional data for defects in thin films to determine how their presence locally affects the roughness of lines and variations in both position and size.

## 5.2.6 Effects of Composition, Polydispersity, and Tacticity

Much of the initial work in improving *ADABlock* was in service of studying the morphological changes in binary blends of PS-*b*-P2VP after microwave annealing.<sup>[20]</sup> One curious result of that study was that the blend with the highest polydispersity attained the lowest level defects within the annealing parameters. This raised questions regarding the competing effects of composition & polydispersity. Presently in the initial stages of investigation, a complete and accurate determination of the effect has been limited due to thickness effects, which were resolved through the experiments described in Chapter 2. Hence it should be possible to fully deconvolute the two effects.

One additional avenue for future research is the exploration of block tacticity as an architectural parameter for controlling the morphology, roughness, and defect evolution properties of BCP domains in thin films. BCPs utilized in this thesis, and in the majority of BCP thin film research papers, are typically atactic, containing no stereochemical order. However syndiotactic and isotactic polymers, with regular stereochemical order, can have significantly different properties compared to atactic analogues. Typically this results in increased melting points and glass transition temperatures, but it could also affect the inter-

block interfacial area on account of increased rigidity and helicity. Similarly, improved packing of like chains could lead to minimization of line-edge roughness.

### 5.3 Conclusion

Having developed *ADABlock* to study topological defects, correlation lengths, LWR, and LER, we have applied the algorithm to the study of annealing. In order to ensure good data, we have tested the results from *ADABlock* and determined appropriate parameters for data collection. Then, determining the effect of thickness, as pertains to the parameters, the stage has been set to fully apply *ADABlock* to improving our understanding of morphology and defects in BCP thin films. Numerous questions remain, such as the effects of composition, polydispersity, and metallization. As the algorithm is improved and added upon, we can anticipate additional answers to each complex question.

# References

- [1] Murphy, J. N.; Harris, K. D.; Buriak, J. M. *PLoS ONE* **2015**, *10*, e0133088.
- [2] Wu, N. L. Y.; Zhang, X.; Murphy, J. N.; Chai, J.; Harris, K. D.; Buriak, J. M. *Nano Letters* **2012**, *12*, 264–268.
- [3] Moore, G. E. *Electronics* **1965**, *38*, 114–117.
- [4] Garner, C. M. *Philosophical Transactions of the Royal Society A: Mathematical, Physical and Engineering Sciences* **2012**, *370*, 4015–4041.
- [5] Feynman, R. P. *The pleasure of finding things out: the best short works of Richard P. Feynman*; Penguin: London, 2007; pp 117–140.
- [6] Transistor count. 2015; [http://en.wikipedia.org/w/index.php?title=Transistor\\_count&oldid=643524573](http://en.wikipedia.org/w/index.php?title=Transistor_count&oldid=643524573), Page Version ID: 643524573.
- [7] Smith, A. R. How Pixar Used Moore's Law to Predict the Future. 2013; <http://www.wired.com/2013/04/how-pixar-used-moores-law-to-predict-the-future/>.
- [8] Lasseter, J. To John Lasseter, for his inspired leadership of the Pixar "Toy Story" team, resulting in the first feature-length computer-animated film. 1996; <http://aaspeechesdb.oscars.org/link/068-25/>.
- [9] Ito, H.; Willson, C. G.; Frechet, J. M. J. Positive- and negative-working resist compositions with acid generating photoinitiator and polymer with acid labile groups pendant from polymer backbone. 1985.

- [10] Mack, C. A. *Field Guide to Optical Lithography*; SPIE: 1000 20th Street, Bellingham, WA 98227-0010 USA, 2006.
- [11] *International Technology Roadmap for Semiconductors, 2013 Edition*; SEMATECH: Albany, NY, 2014.
- [12] Yokoo, A.; Namatsu, H.; Oda, M. Nanoelectrode Lithography. Symposium O – Nanostructured and Patterned Materials for Information Storage. 2006.
- [13] Yokoo, A. *Journal of Vacuum Science & Technology B* **2003**, *21*, 2966–2969.
- [14] A Boy And His Atom: The World’s Smallest Movie. 2013; <https://www.youtube.com/watch?v=oSCX78-8-q0>.
- [15] Moving Atoms: Making The World’s Smallest Movie. 2013; <https://www.youtube.com/watch?v=xA4QWwaweWA>.
- [16] McCracken, H. *Time* **2013**,
- [17] Johnson, D. IBM’s Millipede Project, Social Networking and How Semiconductor Technology Can Save the World - IEEE Spectrum. 2011; <http://spectrum.ieee.org/nanoclast/semiconductors/nanotechnology/ibms-millipede-project-social-networking-and-how-semiconductor-technology-can-save-the-world>.
- [18] Cochran, E. W.; Garcia-Cervera, C. J.; Fredrickson, G. H. *Macromolecules* **2006**, *39*, 2449–2451.

- [19] Koo, K.; Ahn, H.; Kim, S.-W.; Ryu, D. Y.; Russell, T. P. *Soft Matter* **2013**, *9*, 9059–9071.
- [20] Zhang, X.; Murphy, J. N.; Wu, N. L. Y.; Harris, K. D.; Buriak, J. M. *Macromolecules* **2011**, *44*, 9752–9757.
- [21] Li, W.; Liu, M.; Qiu, F.; Shi, A.-C. *The Journal of Physical Chemistry B* **2013**, *117*, 5280–5288.
- [22] Ruiz, R.; Dobisz, E.; Albrecht, T. R. *ACS Nano* **2011**, *5*, 79–84.
- [23] Stoykovich, M. P.; Kang, H.; Daoulas, K. C.; Liu, G.; Liu, C.-C.; de Pablo, J. J.; Müller, M.; Nealey, P. F. *ACS Nano* **2007**, *1*, 168–175.
- [24] About the IRTS. 2014; <http://www.itrs.net/about.html>.
- [25] Komorowski, M. A History of Storage Cost. 2009; <http://www.mkomo.com/cost-per-gigabyte>.
- [26] Kryder, M. Magnetic recording beyond the superparamagnetic limit. Magnetics Conference, 2000. INTERMAG 2000 Digest of Technical Papers. 2000 IEEE International. 2000; pp 575–575.
- [27] Bates, F. S.; Schulz, M. F.; Khandpur, A. K.; Förster, S.; Rosedale, J. H.; Almdal, K.; Mortensen, K. *Faraday Discussions* **1994**, *98*, 7–18.
- [28] Nikoubashman, A.; Register, R. A.; Panagiotopoulos, A. Z. *Macromolecules* **2014**, *47*, 1193–1198.
- [29] Knoll, A.; Horvat, A.; Lyakhova, K. S.; Krausch, G.; Sevink, G. J. A.; Zvelin-

- dovsky, A. V.; Magerle, R. *Physical Review Letters* **2002**, *89*, 035501.
- [30] Huang, E.; Pruzinsky, S.; Russell, T. P.; Mays, J.; Hawker, C. J. *Macromolecules* **1999**, *32*, 5299–5303.
- [31] In, I.; La, Y.-H.; Park, S.-M.; Nealey, P. F.; Gopalan, P. *Langmuir* **2006**, *22*, 7855–7860.
- [32] Ji, S.; Liu, G.; Zheng, F.; Craig, G. S. W.; Himpsel, F. J.; Nealey, P. F. *Advanced Materials* **2008**, *20*, 3054–3060.
- [33] Kim, S.; Yoo, M.; Baettig, J.; Kang, E.-H.; Koo, J.; Choe, Y.; Choi, T.-L.; Khan, A.; Son, J. G.; Bang, J. *ACS Macro Letters* **2015**, *4*, 133–137.
- [34] Bates, C. M.; Seshimo, T.; Maher, M. J.; Durand, W. J.; Cushen, J. D.; Dean, L. M.; Blachut, G.; Ellison, C. J.; Willson, C. G. *Science* **2012**, *338*, 775–779.
- [35] Bates, C. M.; Maher, M. J.; Janes, D. W.; Ellison, C. J.; Willson, C. G. *Macromolecules* **2014**, *47*, 2–12.
- [36] Harrison, C. K. Block copolymer microdomains in thin films. Ph.D. Thesis, Princeton University, Princeton, New Jersey, United States, 1999.
- [37] Simão, C.; Tuchapsky, D.; Khunsin, W.; Amann, A.; Morris, M. A.; Sotomayor Torres, C. M. Defect analysis and alignment quantification of line arrays prepared by directed self-assembly of a block copolymer. Proc. SPIE 9050. San Jose, California, United States, 2014; pp 905028–905028–10.

- [38] Simão, C.; Tuchapsky, D.; Khunsin, W.; Amann, A.; Morris, M. A.; Sotomayor Torres, C. M. Order and defectivity nanometrology by image processing and analysis of sub-20 nm BCPs features for lithographic applications. Proc. SPIE 9110. Baltimore, Maryland, United States, 2014; pp 91100R–91100R–10.
- [39] Rehse, S.; Mecke, K.; Magerle, R. *Physical Review E* **2008**, *77*, 051805.
- [40] Zhang, X.; Harris, K. D.; Wu, N. L. Y.; Murphy, J. N.; Buriak, J. M. *ACS Nano* **2010**, *4*, 7021–7029.
- [41] Scherdel, S.; Schoberth, H. G.; Magerle, R. *The Journal of Chemical Physics* **2007**, *127*, 014903.
- [42] Vigild, M. E.; Almdal, K.; Mortensen, K.; Hamley, I. W.; Fairclough, J. P. A.; Ryan, A. J. *Macromolecules* **1998**, *31*, 5702–5716.
- [43] Kleman, M. *Points, lines, and walls: in liquid crystals, magnetic systems, and various ordered media*; J. Wiley: Chichester; New York, 1983.
- [44] Harrison, C.; Adamson, D. H.; Cheng, Z.; Sebastian, J. M.; Sethuraman, S.; Huse, D. A.; Register, R. A.; Chaikin, P. M. *Science* **2000**, *290*, 1558–1560.
- [45] Tseng, Y.-C.; Darling, S. B. *Polymers* **2010**, *2*, 470–489.
- [46] *International Technology Roadmap for Semiconductors, 2001 Edition*; SEMATECH: Albany, NY, 2002.
- [47] Stoykovich, M. P.; Daoulas, K. C.; Müller, M.; Kang, H.; de Pablo, J. J.;

- Nealey, P. F. *Macromolecules* **2010**, *43*, 2334–2342.
- [48] Bates, F. S.; Fredrickson, G. H. *Annual Review of Physical Chemistry* **1990**, *41*, 525–557.
- [49] Patrone, P. N.; Gallatin, G. M. *Macromolecules* **2012**, *45*, 9507–9516.
- [50] Srinivas, G.; Swope, W. C.; Pitera, J. W. *The Journal of Physical Chemistry B* **2007**, *111*, 13734–13742.
- [51] Gabriel, C.; Choo, B.; Morales, C.; Singh, B. Measuring and Minimizing Line Edge Roughness in BEOL Damascene Dielectric Patterning. 2003; [http://www.avusergroups.org/pag\\_pdfs/PEUG\\_04\\_2003\\_05.pdf](http://www.avusergroups.org/pag_pdfs/PEUG_04_2003_05.pdf).
- [52] Isawa, M.; Sakai, K.; Rincon Delgadillo, P. A.; Gronheid, R.; Yoshida, H. Line edge roughness measurement technique for fingerprint pattern in block copolymer thin film. Proc. SPIE 8681. San Jose, California, USA, 2013; pp 868114–868114–6.
- [53] Wu, N. L.-Y. Self-Assembly of Block Copolymers for Nanopatterning. Ph.D. Thesis, University of Alberta, Edmonton, Alberta, Canada, 2014.
- [54] Park, W. I.; Kim, J. M.; Jeong, J. W.; Jung, Y. S. *ACS Nano* **2014**, *8*, 10009–10018.
- [55] Segal-Peretz, T.; Winterstein, J.; Doxastakis, M.; Ramírez-Hernández, A.; Biswas, M.; Ren, J.; Suh, H. S.; Darling, S. B.; Liddle, J. A.; Elam, J. W.; de Pablo, J. J.; Zaluzec, N. J.; Nealey, P. F. *ACS Nano* **2015**, *9*, 5333–5347.

- [56] Böker, A.; Knoll, A.; Elbs, H.; Abetz, V.; Müller, A. H. E.; Krausch, G. *Macromolecules* **2002**, *35*, 1319–1325.
- [57] Folkes, M. J.; Keller, A. *Polymer* **1971**, *12*, 222–236.
- [58] Amundson, K.; Helfand, E.; Patel, S. S.; Quan, X.; Smith, S. D. *Macromolecules* **1992**, *25*, 1935–1940.
- [59] Amundson, K.; Helfand, E.; Quan, X.; Smith, S. D. *Macromolecules* **1993**, *26*, 2698–2703.
- [60] Kathrein, C. C.; Kipnusu, W. K.; Kremer, F.; Böker, A. *Macromolecules* **2015**, *48*, 3354–3359.
- [61] Garetz, B. A.; Balsara, N. P.; Dai, H. J.; Wang, Z.; Newstein, M. C.; Majumdar, B. *Macromolecules* **1996**, *29*, 4675–4679.
- [62] Chang, M. Y.; Abuzaina, F. M.; Kim, W. G.; Gupton, J. P.; Garetz, B. A.; Newstein, M. C.; Balsara, N. P.; Yang, L.; Gido, S. P.; Cohen, R. E.; Boontongkong, Y.; Bellare, A. *Macromolecules* **2002**, *35*, 4437–4447.
- [63] Harrison, C.; Chaikin, P. M.; Huse, D. A.; Register, R. A.; Adamson, D. H.; Daniel, A.; Huang, E.; Mansky, P.; Russell, T. P.; Hawker, C. J.; Egolf, D. A.; Melnikov, I. V.; Bodenschatz, E. *Macromolecules* **2000**, *33*, 857–865.
- [64] Weith, V.; Krekhov, A.; Zimmermann, W. *The Journal of Chemical Physics* **2013**, *139*, 054908.
- [65] Ferrarese Lupi, F.; Giammaria, T. J.; Volpe, F. G.; Lotto, F.; Seguíni, G.;

- Pivac, B.; Laus, M.; Perego, M. *ACS Applied Materials & Interfaces* **2014**, *6*, 21389–21396.
- [66] Wojtczak, L. *Physica Status Solidi (B)* **1967**, *23*, K163–K166.
- [67] Maher, M. J.; Bates, C. M.; Blachut, G.; Carlson, M. C.; Self, J. L.; Janes, D. W.; Durand, W. J.; Lane, A. P.; Ellison, C. J.; Willson, C. G. *ACS Macro Letters* **2014**, *3*, 824–828.
- [68] Onses, M. S.; Song, C.; Williamson, L.; Sutanto, E.; Ferreira, P. M.; Alleyne, A. G.; Nealey, P. F.; Ahn, H.; Rogers, J. A. *Nature Nanotechnology* **2013**, *8*, 667–675.
- [69] Bencher, C.; Smith, J.; Miao, L.; Cai, C.; Chen, Y.; Cheng, J. Y.; Sanders, D. P.; Tjio, M.; Truong, H. D.; Holmes, S.; Hinsberg, W. D. **2011**, 79700F–79700F.
- [70] Bencher, C.; Yi, H.; Zhou, J.; Cai, M.; Smith, J.; Miao, L.; Montal, O.; Blitshtein, S.; Lavi, A.; Dotan, K.; Dai, H.; Cheng, J. Y.; Sanders, D. P.; Tjio, M.; Holmes, S. Directed self-assembly defectivity assessment. Part II. 2012; pp 83230N–83230N.
- [71] Delgadillo, P. R.; Suri, M.; Durant, S.; Cross, A.; Nagaswami, V. R.; Heuvel, D. V. D.; Gronheid, R.; Nealey, P. *Journal of Micro/Nanolithography, MEMS, and MOEMS* **2013**, *12*, 031112–031112.
- [72] Sunday, D. F.; Hammond, M. R.; Wang, C.; Wu, W.-l.; De-longchamp, D. M.; Tjio, M.; Cheng, J. Y.; Pitera, J. W.; Kline, R. J.

*ACS Nano* **2014**, *8*, 8426–8437.

- [73] Jin, C.; Murphy, J. N.; Harris, K. D.; Buriak, J. M. *ACS Nano* **2014**, *8*, 3979–3991.
- [74] Majewski, P. W.; Yager, K. G. *ACS Nano* **2015**, *9*, 3896–3906.
- [75] Zhang, R.; Singh, G.; Dang, A.; Dai, L.; Bockstaller, M. R.; Akgun, B.; Satija, S.; Karim, A. *Macromolecular Rapid Communications* **2013**, *34*, 1642–1647.
- [76] Singh, G.; Yager, K. G.; Smilgies, D.-M.; Kulkarni, M. M.; Bucknall, D. G.; Karim, A. *Macromolecules* **2012**, *45*, 7107–7117.
- [77] Bosse, A. W.; Douglas, J. F.; Berry, B. C.; Jones, R. L.; Karim, A. *Physical Review Letters* **2007**, *99*, 216101.
- [78] Perego, M.; Lupi, F. F.; Ceresoli, M.; Giammaria, T. J.; Seguini, G.; Enrico, E.; Boarino, L.; Antonioli, D.; Gianotti, V.; Sparnacci, K.; Laus, M. *Journal of Materials Chemistry C* **2014**,
- [79] Lupi, F. F.; Giammaria, T. J.; Ceresoli, M.; Seguini, G.; Sparnacci, K.; Antonioli, D.; Gianotti, V.; Laus, M.; Perego, M. *Nanotechnology* **2013**, *24*, 315601.
- [80] Kim, G.; Libera, M. *Macromolecules* **1998**, *31*, 2569–2577.
- [81] Gotrik, K. W.; Hannon, A. F.; Son, J. G.; Keller, B.; Alexander-Katz, A.; Ross, C. A. *ACS Nano* **2012**, *6*, 8052–8059.

- [82] Kim, E.; Ahn, H.; Park, S.; Lee, H.; Lee, M.; Lee, S.; Kim, T.; Kwak, E.-A.; Lee, J. H.; Lei, X.; Huh, J.; Bang, J.; Lee, B.; Ryu, D. Y. *ACS Nano* **2013**, *7*, 1952–1960.
- [83] Chavis, M. A.; Smilgies, D.-M.; Wiesner, U. B.; Ober, C. K. *Advanced Functional Materials* **2015**, *25*, 3057–3065.
- [84] Gotrik, K. W.; Ross, C. A. *Nano Letters* **2013**, *13*, 5117–5122.
- [85] Luo, M.; Scott, D. M.; Epps, T. H. *ACS Macro Letters* **2015**, *4*, 516–520.
- [86] Cui, G.; Fujikawa, M.; Nagano, S.; Shimokita, K.; Miyazaki, T.; Sakurai, S.; Yamamoto, K. *Macromolecules* **2014**, *47*, 5989–5999.
- [87] Jeong, J. W.; Hur, Y. H.; Kim, H.-j.; Kim, J. M.; Park, W. I.; Kim, M. J.; Kim, B. J.; Jung, Y. S. *ACS Nano* **2013**, *7*, 6747–6757.
- [88] Park, W. I.; Kim, K.; Jang, H.-I.; Jeong, J. W.; Kim, J. M.; Choi, J.; Park, J. H.; Jung, Y. S. *Small* **2012**, *8*, 3762–3768.
- [89] Liedel, C.; Schindler, K. A.; Pavan, M. J.; Lewin, C.; Pester, C. W.; Ruppel, M.; Urban, V. S.; Shenhar, R.; Böker, A. *Small* **2013**, n/a–n/a.
- [90] Olszowka, V.; Hund, M.; Kuntermann, V.; Scherdel, S.; Tsarkova, L.; Böker, A.; Krausch, G. *Soft Matter* **2006**, *2*, 1089–1094.
- [91] Tong, Q.; Sibener, S. J. *The Journal of Physical Chemistry C* **2014**, *118*, 13752–13756.
- [92] Angelescu, D. E.; Waller, J. H.; Adamson, D. H.; Deshpande, P.; Chou, S. Y.;

- Register, R. A.; Chaikin, P. M. *Advanced Materials* **2004**, *16*, 1736–1740.
- [93] Davis, R. L.; Chaikin, P. M.; Register, R. A. *Macromolecules* **2014**, *47*, 5277–5285.
- [94] Kim, S. Y.; Nunns, A.; Gwyther, J.; Davis, R. L.; Manners, I.; Chaikin, P. M.; Register, R. A. *Nano Letters* **2014**, *14*, 5698–5705.
- [95] Stoykovich, M. P.; Müller, M.; Kim, S. O.; Solak, H. H.; Edwards, E. W.; de Pablo, J. J.; Nealey, P. F. *Science* **2005**, *308*, 1442–1446.
- [96] Chai, J.; Buriak, J. M. *ACS Nano* **2008**, *2*, 489–501.
- [97] Tong, Q.; Zheng, Q.; Sibener, S. J. *Macromolecules* **2014**, *47*, 4236–4242.
- [98] Rogošić, M.; Mencer, H. J.; Gomzi, Z. *European Polymer Journal* **1996**, *32*, 1337–1344.
- [99] Campbell, I. P.; He, C.; Stoykovich, M. P. *ACS Macro Letters* **2013**, *2*, 918–923.
- [100] *International Technology Roadmap for Semiconductors, 2011 Edition*; SEMATECH: Albany, NY, 2011.
- [101] Herr, D. J. *Journal of Materials Research* **2011**, *26*, 122–139.
- [102] Sveinbjörnsson, B. R.; Weitekamp, R. A.; Miyake, G. M.; Xia, Y.; Atwater, H. A.; Grubbs, R. H. *Proceedings of the National Academy of Sciences* **2012**, *109*, 14332–14336.

- [103] Hong, S. W.; Gu, W.; Huh, J.; Sveinbjornsson, B. R.; Jeong, G.; Grubbs, R. H.; Russell, T. P. *ACS Nano* **2013**, *7*, 9684–9692.
- [104] Macfarlane, R. J.; Kim, B.; Lee, B.; Weitekamp, R. A.; Bates, C. M.; Lee, S. F.; Chang, A. B.; Delaney, K. T.; Fredrickson, G. H.; Atwater, H. A.; Grubbs, R. H. *Journal of the American Chemical Society* **2014**, *136*, 17374–17377.
- [105] Zhao, L.; Goodman, M. D.; Bowden, N. B.; Lin, Z. *Soft Matter* **2009**, *5*, 4698–4703.
- [106] Runge, M. B.; Bowden, N. B. *Journal of the American Chemical Society* **2007**, *129*, 10551–10560.
- [107] Fasolka, M. J.; Goldner, L. S.; Hwang, J.; Urbas, A. M.; DeRege, P.; Swager, T.; Thomas, E. L. *Physical Review Letters* **2003**, *90*, 016107.
- [108] Peters, A. J.; Lawson, R. A.; Ludovice, P. J.; Henderson, C. L. Effects of block copolymer polydispersity and  $\chi_N$  on pattern line edge roughness and line width roughness from directed self-assembly of diblock copolymers. Proc. SPIE 8680. San Jose, California, USA, 2013; pp 868020–1–868020–8.
- [109] Stenbock-Fermor, A.; Rudov, A. A.; Gumerov, R. A.; Tsarkova, L. A.; Böker, A.; Möller, M.; Potemkin, I. I. *ACS Macro Letters* **2014**, *3*, 803–807.
- [110] Jung, Y. S.; Ross, C. A. *Nano Letters* **2007**, *7*, 2046–2050.

- [111] Black, C. T.; Guarini, K. W.; Milkove, K. R.; Baker, S. M.; Russell, T. P.; Tuominen, M. T. *Applied Physics Letters* **2001**, *79*, 409–411.
- [112] Tavakkoli K.G., A.; Gotrik, K. W.; Hannon, A. F.; Alexander-Katz, A.; Ross, C. A.; Berggren, K. K. *Science* **2012**, *336*, 1294–1298.
- [113] Yang, X.; Wan, L.; Xiao, S.; Xu, Y.; Weller, D. K. *ACS Nano* **2009**, *3*, 1844–1858.
- [114] Ruiz, R.; Kang, H.; Detcheverry, F. A.; Dobisz, E.; Kercher, D. S.; Albrecht, T. R.; de Pablo, J. J.; Nealey, P. F. *Science* **2008**, *321*, 936–939.
- [115] Mistark, P. A.; Park, S.; Yalcin, S. E.; Lee, D. H.; Yavuzcetin, O.; Tuominen, M. T.; Russell, T. P.; Achermann, M. *ACS Nano* **2009**, *3*, 3987–3992.
- [116] Deeg, J. A.; Louban, I.; Aydin, D.; Selhuber-Unkel, C.; Kessler, H.; Spatz, J. P. *Nano Letters* **2011**, *11*, 1469–1476.
- [117] Kruss, S.; Wolfram, T.; Martin, R.; Neubauer, S.; Kessler, H.; Spatz, J. P. *Advanced Materials* **2010**, *22*, 5499–5506.
- [118] Adutler-Lieber, S.; Zaretsky, I.; Platzman, I.; Deeg, J.; Friedman, N.; Spatz, J. P.; Geiger, B. *Journal of Autoimmunity* **2014**, *54*, 100–111.
- [119] Park, S.; Kim, B.; Wang, J.-Y.; Russell, T. P. *Advanced Materials* **2008**, *20*, 681–685.
- [120] Chai, J.; Wang, D.; Fan, X.; Buriak, J. M. *Nature Nanotechnology* **2007**, *2*, 500–506.

- [121] Cushen, J. D.; Otsuka, I.; Bates, C. M.; Halila, S.; Fort, S.; Rochas, C.; Easley, J. A.; Rausch, E. L.; Thio, A.; Borsali, R.; Willson, C. G.; Ellison, C. J. *ACS Nano* **2012**, *6*, 3424–3433.
- [122] Mansky, P.; Liu, Y.; Huang, E.; Russell, T. P.; Hawker, C. *Science* **1997**, *275*, 1458–1460.
- [123] Park, M.; Harrison, C.; Chaikin, P. M.; Register, R. A.; Adamson, D. H. *Science* **1997**, *276*, 1401–1404.
- [124] Jeong, C. K.; Baek, K. M.; Niu, S.; Nam, T. W.; Hur, Y. H.; Park, D. Y.; Hwang, G.-T.; Byun, M.; Wang, Z. L.; Jung, Y. S.; Lee, K. J. *Nano Letters* **2014**, *14*, 7031–7038.
- [125] Ouk Kim, S.; Solak, H. H.; Stoykovich, M. P.; Ferrier, N. J.; de Pablo, J. J.; Nealey, P. F. *Nature* **2003**, *424*, 411–414.
- [126] Wu, N. L. Y.; Harris, K. D.; Buriak, J. M. *ACS Nano* **2013**, *7*, 5595–5606.
- [127] Bitá, I.; Yang, J. K. W.; Jung, Y. S.; Ross, C. A.; Thomas, E. L.; Berggren, K. K. *Science* **2008**, *321*, 939–943.
- [128] Ross, C. A.; Jung, Y. S.; Chuang, V. P.; Ilievski, F.; Yang, J. K. W.; Bitá, I.; Thomas, E. L.; Smith, H. I.; Berggren, K. K.; Vancso, G. J.; Cheng, J. Y. *Journal of Vacuum Science & Technology B* **2008**, *26*, 2489–2494.
- [129] Kim, Y.; Pyun, J.; Fréchet, J. M. J.; Hawker, C. J.; Frank, C. W. *Langmuir* **2005**, *21*, 10444–10458.

- [130] Poelma, J. E.; Ono, K.; Miyajima, D.; Aida, T.; Satoh, K.; Hawker, C. J. *ACS Nano* **2012**, *6*, 10845–10854.
- [131] Hawker, C. J.; Bosman, A. W.; Harth, E. *Chemical Reviews* **2001**, *101*, 3661–3688.
- [132] Hawker, C. J.; Wooley, K. L. *Science* **2005**, *309*, 1200–1205.
- [133] Hawker, C. J. *Accounts of Chemical Research* **1997**, *30*, 373–382.
- [134] Bates, F. S.; Fredrickson, G. H. *Physics Today* **1999**, *52*, 32–38.
- [135] Gopalan, P.; Yang, S. *Material Matters* **2006**, *1*, 6.
- [136] Fukukawa, K.-i.; Zhu, L.; Gopalan, P.; Ueda, M.; Yang, S. *Macromolecules* **2005**, *38*, 263–270.
- [137] Beardsley, T. M.; Matsen, M. W. *Macromolecules* **2011**, *44*, 6209–6219.
- [138] Lynd, N. A.; Hillmyer, M. A. *Macromolecules* **2005**, *38*, 8803–8810.
- [139] Lynd, N. A.; Hillmyer, M. A. *Macromolecules* **2007**, *40*, 8050–8055.
- [140] Sweat, D. P.; Kim, M.; Larson, S. R.; Choi, J. W.; Choo, Y.; Osuji, C. O.; Gopalan, P. *Macromolecules* **2014**, *47*, 6687–6696.
- [141] Nagpal, U.; Müller, M.; Nealey, P. F.; de Pablo, J. J. *ACS Macro Letters* **2012**, *1*, 418–422.
- [142] Horvat, A.; Sevink, G. J. A.; Zvelindovsky, A. V.; Krekhov, A.; Tsarkova, L. *ACS Nano* **2008**, *2*, 1143–1152.

- [143] Takahashi, H.; Laachi, N.; Delaney, K. T.; Hur, S.-M.; Weinheimer, C. J.; Shykind, D.; Fredrickson, G. H. *Macromolecules* **2012**, *45*, 6253–6265.
- [144] Harrison, C. K. Block copolymer microdomains in thin films. Ph.D., Princeton University, United States – New Jersey, 1999.
- [145] Qiang, Z.; Zhang, Y.; Groff, J. A.; Cavicchi, K. A.; Vogt, B. D. *Soft Matter* **2014**, *10*, 6068–6076.
- [146] Rasband, W. S. ImageJ. 1997-2014; <http://imagej.nih.gov/ij/>.
- [147] Schneider, C. A.; Rasband, W. S.; Eliceiri, K. W. *Nature Methods* **2012**, *9*, 671–675.
- [148] Otsu, N. *IEEE Transactions on Systems, Man and Cybernetics* **1979**, *9*, 62–66.
- [149] Landini, G. Auto Local Threshold. 2013; [https://github.com/fiji/Auto\\_Threshold/tree/master/src/main/java/fiji/threshold](https://github.com/fiji/Auto_Threshold/tree/master/src/main/java/fiji/threshold).
- [150] Doube, M.; Klosowski, M. M.; Arganda-Carreras, I.; Cordelières, F. P.; Dougherty, R. P.; Jackson, J. S.; Schmid, B.; Hutchinson, J. R.; Shefelbine, S. J. *Bone* **2010**, *47*, 1076–1079.
- [151] Zhang, T. Y.; Suen, C. Y. *Communications of the ACM* **1984**, *27*, 236–239.
- [152] Abukhdeir, N. M.; Rey, A. D. *New Journal of Physics* **2008**, *10*, 063025.
- [153] Campbell, I. P.; Hirokawa, S.; Stoykovich, M. P. *Macromolecules* **2013**, *46*, 9599–9608.

- [154] Kim, H.-W.; Lee, J.-Y.; Shin, J.; Woo, S.-G.; Cho, H.-K.; Moon, J.-T. *IEEE Transactions on Electron Devices* **2004**, *51*, 1984–1988.
- [155] Asenov, A.; Kaya, S.; Brown, A. *IEEE Transactions on Electron Devices* **2003**, *50*, 1254–1260.
- [156] Stucchi, M.; Bamal, M.; Maex, K. *Microelectronic Engineering* **2007**, *84*, 2733–2737.
- [157] Steinhögl, W.; Schindler, G.; Steinlesberger, G.; Traving, M.; Engelhardt, M. *Microelectronic Engineering* **2004**, *76*, 126–130.
- [158] Patrone, P. N.; Gallatin, G. M. Modeling line-edge roughness in lamellar block copolymer systems. 2012; pp 83232Q–83232Q–9.
- [159] templatetypedef, Answer to: Determining if two line segments intersect? 2011; <http://stackoverflow.com/a/4977569>.
- [160] Hu, X.; Zhu, Y.; Gido, S. P.; Russell, T. P.; Iatrou, H.; Hadjichristidis, N.; Abuzaina, F. M.; Garetz, B. A. *Faraday Discussions* **2005**, *128*, 103–112.
- [161] Qiang, Z.; Zhang, L.; Stein, G. E.; Cavicchi, K. A.; Vogt, B. D. *Macromolecules* **2014**, *47*, 1109–1116.
- [162] Berry, B. C.; Bosse, A. W.; Douglas, J. F.; Jones, R. L.; Karim, A. *Nano Letters* **2007**, *7*, 2789–2794.
- [163] Brillinger, D. R. International Encyclopedia of Political Science. 2011; <http://knowledge.sagepub.com/view/intlpoliticalscience/n128.xml>.

- [164] Ince, D. C.; Hatton, L.; Graham-Cumming, J. *Nature* **2012**, *482*, 485–488.
- [165] Niemeyer, K. Nature Editorial: If you want reproducible science, the software needs to be open source. 2012; <http://arstechnica.com/science/2012/02/science-code-should-be-open-source-according-to-editorial/>.
- [166] Griffiths, R. A.; Williams, A.; Oakland, C.; Roberts, J.; Vijayaraghavan, A.; Thomson, T. *Journal of Physics D: Applied Physics* **2013**, *46*, 503001.
- [167] Stoykovich, M. P.; Nealey, P. F. *Materials Today* **2006**, *9*, 20–29.
- [168] Shin, D. O.; Jeong, J.-R.; Han, T. H.; Koo, C. M.; Park, H.-J.; Lim, Y. T.; Kim, S. O. *Journal of Materials Chemistry* **2010**, *20*, 7241–7247.
- [169] Jung, Y. S.; Jung, W.; Tuller, H. L.; Ross, C. A. *Nano Letters* **2008**, *8*, 3776–3780.
- [170] Albert, J. N. L.; Bogart, T. D.; Lewis, R. L.; Beers, K. L.; Fasolka, M. J.; Hutchison, J. B.; Vogt, B. D.; Epps, T. H. *Nano Letters* **2011**, *11*, 1351–1357.
- [171] Fasolka, M. J.; Harris, D. J.; Mayes, A. M.; Yoon, M.; Mochrie, S. G. J. *Physical Review Letters* **1997**, *79*, 3018–3021.
- [172] Ruiz, R.; Ruiz, N.; Zhang, Y.; Sandstrom, R. L.; Black, C. T. *Advanced Materials* **2007**, *19*, 2157–2162.
- [173] Jeong, S.-J.; Moon, H.-S.; Kim, B. H.; Kim, J. Y.; Yu, J.; Lee, S.; Lee, M. G.;

- Choi, H.; Kim, S. O. *ACS Nano* **2010**, *4*, 5181–5186.
- [174] Mishra, V.; Fredrickson, G. H.; Kramer, E. J. *ACS Nano* **2012**, *6*, 2629–2641.
- [175] Maher, M. J.; Bates, C. M.; Blachut, G.; Sirard, S.; Self, J. L.; Carlson, M. C.; Dean, L. M.; Cushen, J. D.; Durand, W. J.; Hayes, C. O.; Ellison, C. J.; Willson, C. G. *Chemistry of Materials* **2014**, *26*, 1471–1479.
- [176] Mansky, P.; Russell, T. P.; Hawker, C. J.; Pitsikalis, M.; Mays, J. *Macromolecules* **1997**, *30*, 6810–6813.
- [177] Willson, C. G.; Blachut, G.; Maher, M. J.; Durand, W. J.; Bates, C. M.; Carlson, M. C.; Self, J. L.; Lane, A. P.; Asano, Y.; Sirard, S.; Hayes, C. O.; Ellison, C. J. *Journal of Photopolymer Science and Technology* **2014**, *27*, 415–418.
- [178] Smith, A. P.; Douglas, J. F.; Meredith, J. C.; Amis, E. J.; Karim, A. *Physical Review Letters* **2001**, *87*, 015503.
- [179] Yang, Y.-B.; Park, S. J.; Kim, P.; Kim, J. U. *Soft Matter* **2013**, *9*, 5624–5633.
- [180] Tsarkova, L. *Macromolecules* **2012**, *45*, 7985–7994.
- [181] Green, P. F.; Limary, R. *Advances in Colloid and Interface Science* **2001**, *94*, 53–81.
- [182] Bates, C. M.; Strahan, J. R.; Santos, L. J.; Mueller, B. K.; Bamgbade, B. O.; Lee, J. A.; Katzenstein, J. M.; Ellison, C. J.; Willson, C. G. *Langmuir* **2011**,

27, 2000–2006.

- [183] Tong, Q.; Sibener, S. J. *Macromolecules* **2013**, *46*, 8538–8544.
- [184] Webber, R. M.; Anderson, J. L. *Langmuir* **1994**, *10*, 3156–3160.
- [185] Toomey, R.; Mays, J.; Tirrell, M. *Macromolecules* **2004**, *37*, 905–911.
- [186] Pelletier, E.; Stamouli, A.; Belder, G. F.; Hadziioannou, G. *Langmuir* **1997**, *13*, 1884–1886.
- [187] Savitzky, A.; Golay, M. J. E. *Analytical Chemistry* **1964**, *36*, 1627–1639.
- [188] Faas, F. G. A.; Avramut, M. C.; van den Berg, B. M.; Mommaas, A. M.; Koster, A. J.; Ravelli, R. B. G. *The Journal of Cell Biology* **2012**, *198*, 457–469.
- [189] Williams, E. H.; Carpentier, P.; Misteli, T. *The Journal of Cell Biology* **2012**, *198*, 271–272.

# A

## Particle Analysis Calculation of Line-Width

One can imagine several different scenarios for the “tips” of lines, and how they would contribute to the overall relationship between line perimeter and line area. A structure consisting entirely of junctions—and analyzed as such, without breaking lines apart—would have junctions contributing a small area without any additional contribution to the perimeter. We can approximate this by junctions coming to meet in an equilateral triangle, as shown in the following, Figure A.1:

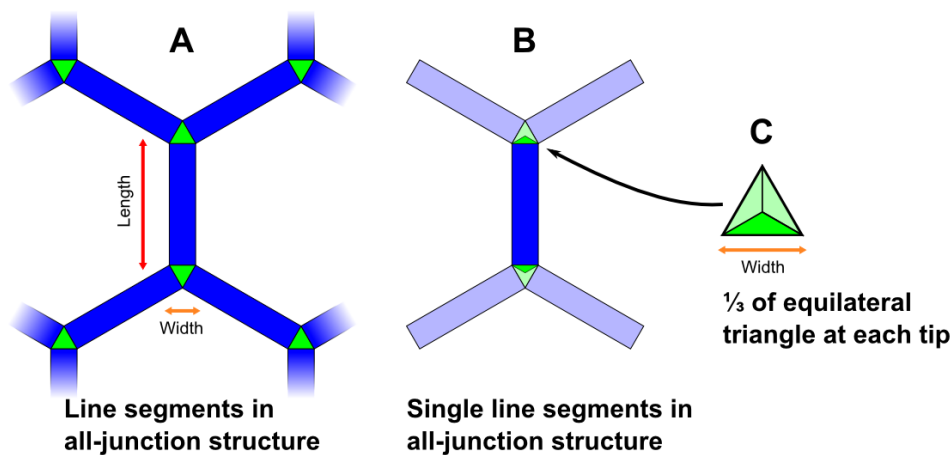


**Figure A.1:** A. Shows part of a hypothetical infinite array of connected line segments; such lines could be parallel, however the hexagonal layout simplifies depiction. B. Shows an isolated line, with associated area from the triangular region at each junction. C. The area at each tip can be approximated as one third of an equilateral triangle.

For this continuous network, we can calculate the area as a product of the

length of each segment, multiplied by its width, plus two triangular pieces, each third of an equilateral triangle, for which the edge length is equal to the width:

$$A = Lw + 2\frac{A_{\Delta}}{3}$$

Substituting the area of an equilateral triangle for  $A_{\Delta}$ , we have:

$$A = Lw + \frac{\sqrt{3}w^2}{6}$$

The perimeter is simply twice the length of the line segment, as the junctions contribute no area in this case:

$$P = 2L$$

Rearranging to make the area depend on perimeter, one obtains:

$$A(P) = 12wP + \frac{\sqrt{3}}{6}w^2 \rightarrow \frac{1}{2}wP + 0.289w^2$$

The slope remains  $0.5w$ , however the intercept is  $0.289w^2$ , which for a line of width 18 nm, were it to only have junctions and arbitrary lengths, one would expect an intercept of  $93.5 \text{ nm}^2$ .

For samples with lines that terminate and do not possess junctions, the equation can be modified to presume a semi-circular tip at the end. As shown in Figure A.2:

From this we can contrive, using the usual equations for a circle, an equation for area,

$$A = Lw + A_{circle} = Lw + \pi r^2 = Lw + \frac{1}{4}\pi w^2$$

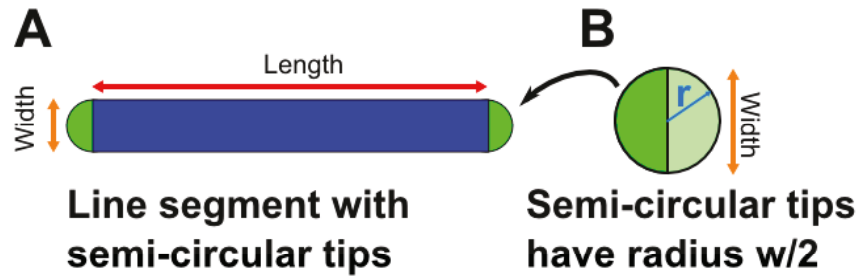


**Figure A.2:** A. Lines without any junctions can be approximated as having semicircles for tips. B. These would correspond to circles with a radius half the width of the line.

and similarly for the perimeter,

$$P = 2L + P_{circle} = 2L + w$$

of the line segment. Converting the equation for area to a function of perimeter gives:

$$A = \frac{P - \pi w}{2} \sum w + \frac{1}{4} \pi w^2 = \frac{1}{2} w P - \frac{1}{4} \pi w^2 \rightarrow \frac{1}{2} w P - 0.785 w^2$$

The intercept for a structure with semicircular tips would be  $-0.785w^2$ , which for a line of width 18 nm, would correspond to a value of  $-254.5 \text{ nm}^2$ , for a collection of lines of constant width and tip structure, but arbitrary length.

Finally, perhaps the simplest case would be for the lines to have a simple rectangular structure with no tip-area that is unaccounted for by the length, as drawn:

The area would simply be the product of the length and the width,

$$A = Lw$$

while the perimeter would be twice the sum of the length and the width,

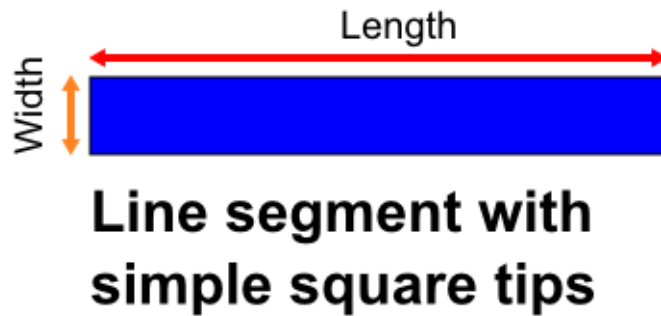


**Figure A.3:** Depiction of a line segment with no junctions and regular, square tips.

$$P = 2L + w$$

Rearranging to give the area as a function of perimeter:

$$A = \frac{1}{2}wP - w^2$$

The intercept would be  $-w^2$ , which for a 18 nm wide line would be  $-324 \text{ nm}^2$ . Figure 3.5 provides examples for one such image, where the intercept, after removing junction-containing structures, is  $-104.4 \text{ nm}^2$ , indicates that the semi-circular tips would be a better model, on average.

Furthermore, for such a sample image, the magnitude of the change makes for a scatter which is small compared to the typical particle areas: on a range of  $5000 \text{ nm}^2$  to  $30000 \text{ nm}^2$ ,  $\pm 300 \text{ nm}^2$  represents  $\pm 0.06 \%$  to  $0.01 \%$ .

Typically samples with moderate levels of defects will have a mixture of particles with varying levels of junctions and terminal points. Larger particles tend to characteristically have a greater number of junctions and a greater contact with the image edge; smaller particles fewer junctions and likely zero contact with the image edge. In order to accurately measure line-width, re-

removal of junctions provides an improved estimate.

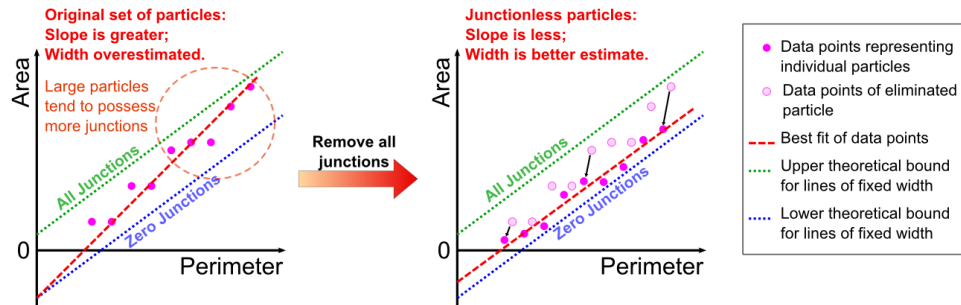


**Figure A.4:** Schematic graphs depicting the effect of removing junctions and particles touching the edge of an image. On the left, larger particles tend to bias the slope higher, due to the increase in area for samples of an equivalent perimeter; overall there is greater scatter of the data points. On the right, removal of junctions results in a smaller scatter in the data points, and places them closer to the theoretical slope, as dependent on the width.

# B

## Summary of the "ADAblock" Defect Analysis Code

The following section provides a brief summary of the *ADAblock* code (version 1.00, as published) and the functions contained. The code itself is approximately 5600 lines, hence inclusion in would add nearly 175 pages, however the full code can be inspected and tested using copies contained in the *University of Alberta* institutional repository, the *Education & Research Archive* at <https://hdl.handle.net/10402/era.41438> or on *GitHub*, with updated versions, at <https://github.com/MurphysLab/ADAblock>. The current, published version is archived through *Zenodo* at <https://doi.org/10.5281/zenodo.19644>.

- 1–11** Prefatory material
- 13–36** Settings and modifiable defined variables
- 38–51** Check for missing dependencies and required plugins
- 53–1860** **Functions defined for reuse in the macro**

*ImageJ* comes with numerous pre-defined macro functions which are described on the *ImageJ* website: <http://imagej.nih.gov/ij/>. User-defined functions enable further extension of the macro language. Numerous functions were written to facilitate a more compressed code; the drawback is that user-defined functions are slower

*than hard-coded operations. The following entries are functions which I have added to this code, however as the macro language has expanded, some have become redundant.*

- 55      **Function 000:** Output tags & output data
- 67      **Function 001:** Append-to-array
- 81      **Function 002:** Check-in-array
- 93      **Function 003:** Coordinate indexer
- 102     **Function 004:** Coordinate de-indexer
- 112     **Function 005:** Circuit value
- 129     **Function 006:** Four-connected circuit value
- 152     **Function 007:** Neighbour value
- 169     **Function 008:** Neighbour value, exact
- 195     **Function 009:** Follow-two
- 225     **Function 010:** Follow-erase
- 274     **Function 011:** Set foreground index
- 282     **Function 012:** LUT operations
- 309     **Function 013:** Weighted least squares algorithm
- 484     **Function 014:** Edge walk pixels

540	<b>Function 015:</b> Check inside
630	<b>Function 016:</b> Conditions true
723	<b>Function 017:</b> Colour particles
783	<b>Function 018:</b> XY coder (encoder-decoder)
803	<b>Function 019:</b> Centre pixel
828	<b>Function 020:</b> Is-point-in-path
880	<b>Function 021:</b> Get selection pixels
922	<b>Function 022:</b> Defect encoder / decoder
948	<b>Function 023:</b> Integer string
963	<b>Function 024:</b> Shift values
994	<b>Function 025:</b> Distance from edge
1001	<b>Function 025:</b> Junction degree
1035	<b>Function 026a:</b> LER (line-edge roughness)
1345	<b>Function 026b:</b> LWR (line-width roughness)
1461	<b>Function 027:</b> Downsample
1524	<b>Function 028:</b> Base-62 converter
1558	<b>Function 029:</b> Array-smooth (median & window filters)
1644	<b>Function 030:</b> Object histogram

**1716**      **Function 031:** OPA Components & follow-two-encode-vs

**1772**      **Function 032:** Particle analysis excerpt

**1819**      **Function 033:** Defect drawing tools & shapes

**1864–2070** **Interactive user options and input**

*This is what the sub-paragraph comments will look like*

**1866**      Batch processing

*User chooses "Single" or "Multi" mode and whether the ImageJ "Batch Mode" option should be used.*

**1878**      Image resolution

*User selects method for determining resolution or supplies a universal resolution.*

**1893**      Line period determination

*User selects method for determination of line period along with a valid range, or provides a specified line period.*

**1911**      Smoothing & noise

*User selects method for smoothing. Median or Gaussian, with radius selected relative to the line period.*

**1925**      Thresholding

*User selects a method for thresholding, based on defaults in ImageJ or using the Auto-Local Thresholding plugin.*

- 1952** Additional operations  
*User selects additional analyses to perform. Creation of an orientational domain map is time-consuming, hence it is made optional.*
- 1960** Cropping  
*User specifies whether cropping should be performed on the image and at which stage (1) or (2).*
- 2003** Image lists  
*User selects a directory for obtaining images if "Multi" mode is selected. Images in the selected directory are extracted from the files in the user-selected directory if the "Multi" mode is chosen.*
- 2034** Output folder creation  
*User selects a "save location". Output folder is created based on the location selected by the user and the time when the process is started.*
- 2049–2067** Log file is created
- 2074–2080** Multiple-image data storage  
*Summarizes key data for multiple images.*
- 2082–5585** **Multiple-image looping**
- 2086–2095** Import image(s)
- 2097–2101** Image viability

*Checks image type to ensure process can be run. Otherwise, skip to line 5576.*

**2103–5575 Algorithm process**

**2106–2112** Data structures

**2114–2115** Subfolder creation

**2119–2131** Image log

**2133–2270** Determine image resolution

*Image resolution is determined either using embedded values or other means. A custom method for determining resolution for images from NINT's Hitachi S-4800 SEM is implemented.*

**2272–2316** Optional cropping (1)

**2318–2473** Period estimate by WFFT

*Period is initially estimated using data from FFT image processing; azimuthal averaging provides a radial function of intensity, from which the peak can be found. The data is first smoothed using a weighting function (hence "WFFT") to aid in determining the peak position.*

**2477–2500** Smoothing

**2502–2551** Optional cropping (2)

**2553–2581** Thresholding

**2583–2720** Binary grooming

**2722–3102** Particle analysis

**3105–3141** Divide images

*Separating images into components with only lines, dots, or other regions.*

**3143–3727** Skeleton analyses

**3729–4353** Correlation function & order parameter

**4355–5021** Line-width and line-edge roughness

**5024–5042** Recording results

*Position, phase, and value for all defects is tabulated and recorded.*

**5045–5453** Creating composite images

*Composite images are made, marking locations and types of defects.*

**5456–5513** Final calculations & logging

*Defectivity calculations are added to the output and values are logged.*

**5515–5522** Multi-image data logging

**5524–5567** Safe files

*Various images are saved, along with defect coordinates. Output data and labels are exported to CSV files for future analysis.*

**5569–5572** Close superfluous images

**5576–5581** Non-viable images

**5583–5585** Close images

**5587–5594** Multi-image results summary

**5596** Completion notification